



**HAL**  
open science

# Looking for Short-Range Correlations in proton-induced QFS reactions in inverse kinematics

Andrea Lagni

► **To cite this version:**

Andrea Lagni. Looking for Short-Range Correlations in proton-induced QFS reactions in inverse kinematics. Atomic Physics [physics.atom-ph]. Université Paris-Saclay, 2024. English. NNT : 2024UP-ASP095 . tel-04759783

**HAL Id: tel-04759783**

**<https://theses.hal.science/tel-04759783v1>**

Submitted on 30 Oct 2024

**HAL** is a multi-disciplinary open access archive for the deposit and dissemination of scientific research documents, whether they are published or not. The documents may come from teaching and research institutions in France or abroad, or from public or private research centers.

L'archive ouverte pluridisciplinaire **HAL**, est destinée au dépôt et à la diffusion de documents scientifiques de niveau recherche, publiés ou non, émanant des établissements d'enseignement et de recherche français ou étrangers, des laboratoires publics ou privés.

# Looking for Short-Range Correlations in proton-induced QFS reactions in inverse kinematics

*Recherche de corrélations à courte portée dans les  
réactions QFS induites par des protons  
en cinématique inverse*

**Thèse de doctorat de l'université Paris-Saclay**

École doctorale n° 576, PHENIICS :  
Particules, Hadrons, Énergies et Noyau,  
Instrumentation, Imagerie et Simulation  
Spécialité de doctorat: Physique nucléaire  
Graduate School : Physique. Référent : Faculté des Sciences d'Orsay

Thèse préparée dans l'unité de recherche  
**Département de Physique Nucléaire (Université Paris-Saclay, CEA)**,  
sous la direction d'**Anna CORSI**, Ingénieure de recherche,  
et la co-direction d'**Aldric REVEL**, Ingénieur de recherche

**Thèse soutenue à Paris-Saclay, le 27 Septembre 2024, par**

**Andrea LAGNI**

## **Composition du jury**

Membres du jury avec voix délibérative

<b>David VERNEY</b> Professeur IPN Orsay, IJClab, Université Paris-Saclay, France	Président
<b>Alexandre OBERTELLI</b> Professeur TU Darmstadt, Allemagne	Rapporteur & Examineur
<b>Olivier SORLIN</b> Directeur de recherche GANIL, University of Caen, France	Rapporteur & Examineur
<b>Marlène ASSIÉ</b> Chargée de recherche IJCLab-CNRS, Université Paris-Saclay, France	Examinatrice



**Titre:** Recherche de corrélations à courte portée dans les réactions QFS induites par des protons en cinématique inverse.

**Mots clés:** Corrélations à courte portée, noyaux exotiques, structure nucléaire, QFS induite par le proton, cinématique inverse.

**Résumé:** Les systèmes à plusieurs corps composés de fermions sont courants dans la nature, tels que les supraconducteurs à haute température, les liquides de Fermi, les noyaux atomiques, la matière de quarks et les étoiles à neutrons. La complexité des interactions entre les particules rend difficile la résolution des équations de la dynamique des particules dans ces systèmes quantiques. Pour simplifier, on modélise souvent ces systèmes en utilisant des particules indépendantes dans un potentiel de champ moyen effectif. Cependant, les interactions résiduelles révèlent des corrélations significatives qui affectent l'occupation des états en dessous et au-dessus du niveau de Fermi.

Les noyaux atomiques, avec leurs interactions à courte portée, sont particulièrement intéressants. La physique des corrélations à courte portée (SRC) découle des interactions à courte distance et se manifeste sous la forme de paires de nucléons. Les paires SRC ont une impulsion relative élevée et une impulsion de leur centre de masse faible par rapport à l'impulsion de Fermi ( $k_F = 250$  MeV/c). Ces paires forment des fluctuations temporaires de haute densité, limitées par l'interaction nucléon-nucléon répulsive à des distances inférieures à environ 1 fm.

La plupart des connaissances sur les SRC proviennent d'expériences de diffusion d'électrons et de protons. Les études indiquent qu'environ 20% des nucléons liés occupent cette région à haute impulsion. La première preuve expérimentale des SRC a été apportée par la mesure d'une queue à haute impulsion dans les distributions d'impulsions des protons lors d'expériences de diffusion d'électrons. Pour étudier les SRC dans les noyaux riches en neutrons, nous avons utilisé des réactions de Quasi-Free Scattering (QFS) en cinématique inverse, avec des faisceaux d'ions radioactifs sur une cible de protons à l'installation  $R^3B$  de GSI en Allemagne. Cette méthode a permis d'étudier les propriétés des SRC, y compris les rapports de

paires  $np/pp$  et les distributions d'impulsion, en se concentrant sur les noyaux  $^{12}\text{C}$  et  $^{16}\text{C}$  avec une énergie de faisceau de 1,25 GeV/u.

Les principaux objectifs étaient de développer une méthodologie pour différencier les réactions de diffusion sur des paires SRC des réactions sur un proton suivies par des interactions finales (FSI) et d'étendre les études des SRC aux noyaux riches en neutrons, en particulier les noyaux exotiques comme  $^{16}\text{C}$ . L'analyse consistait à identifier les événements SRC produits via les réactions  $^{12}\text{C}(p, 2pN)A-2$  et  $^{16}\text{C}(p, 2pN)A-2$ . Des rapports de paires  $np/pp$  inférieurs aux prédictions du Generalized Contact Formalism et aux résultats expérimentaux antérieurs ont été extraits, suggérant une interférence des FSI et des effets de champ moyen.

Des difficultés sont apparues pour isoler les événements SRC, et nous avons supposé que la section efficace pour la rupture de paires SRC pourrait être réduite à l'énergie de 1,25 GeV/u. De plus, la résolution limitée en impulsion a réduit notre capacité à séparer les événements SRC des autres canaux concurrents, indiquant la nécessité d'améliorer le système de détection. Les faibles statistiques utilisables et les limites d'acceptance de l'équipement expérimental ne nous ont pas permis de réaliser une mesure exclusive des SRC, mais ont fourni des informations essentielles pour améliorer les études futures à  $R^3B$ .

Cette recherche constitue une étape fondamentale dans l'étude des SRC en cinématique inverse. Malgré les difficultés, la méthodologie développée fournit des informations importantes pour mieux identifier la physique des SRC. Les futures expériences devraient envisager des énergies de faisceau plus élevées ou de meilleures techniques de détection pour mieux isoler les événements SRC.

**Title:** Looking for Short-Range Correlations in proton-induced QFS reactions in inverse kinematics.

**Keywords:** Short-range correlations, Exotic nuclei, Nuclear structure, proton-induced QFS, inverse kinematics.

**Abstract:** Many-body systems composed of fermions are common in nature, such as high-temperature superconductors, Fermi liquids, atomic nuclei, quark matter, and neutron stars. The complexity of interactions between particles makes it difficult to solve the equations governing particle dynamics in these quantum systems. To simplify, these systems are often modeled using independent particles in an effective mean-field potential. However, residual interactions reveal significant correlations that affect the occupation of states below and above the Fermi level.

Atomic nuclei, with their short-range interactions, are particularly interesting. The physics of short-range correlations (SRC) arises from short-distance interactions and manifests as nucleon pairs. SRC pairs have a high relative momentum and a low center-of-mass momentum compared to the Fermi momentum ( $k_F = 250$  MeV/c). These pairs form temporary high-density fluctuations, limited by the highly repulsive nucleon-nucleon interaction at distances less than about 1 fm.

Most of our knowledge about SRC comes from electron and proton scattering experiments. Studies indicate that about 20% of bound nucleons occupy this high-momentum region. The first experimental evidence of SRC was provided by measuring a high-momentum tail in the proton momentum distributions during electron scattering experiments.

To study SRC in neutron-rich nuclei, we used Quasi-Free Scattering (QFS) reactions in inverse kinematics, with radioactive ion beams on a proton target at the  $R^3B$  facility of the GSI accelerator in Germany. This method allowed us to study

SRC properties, including  $np/pp$  pair ratios and momentum distributions, focusing on the  $^{12}\text{C}$  and  $^{16}\text{C}$  nuclei with a beam energy of 1.25 GeV/u.

The main objectives were to develop a methodology to differentiate between scattering reactions on SRC pairs and reactions on a proton followed by final-state interactions (FSI) and to extend SRC studies to neutron-rich nuclei, particularly exotic nuclei like  $^{16}\text{C}$ . The analysis involved identifying SRC events produced via  $^{12}\text{C}(p, 2p\text{N})A-2$  and  $^{16}\text{C}(p, 2p\text{N})A-2$  reactions. We extracted  $np/pp$  pair ratios lower than the predictions of the Generalized Contact Formalism and previous experimental results, suggesting interference from FSI and mean-field effects.

Difficulties arose in isolating SRC events, and we hypothesized that the cross-section for SRC pair breaking might be reduced at the 1.25 GeV/u beam energy. Additionally, limited momentum resolution reduced our ability to separate SRC events from other competing channels, indicating the need to improve the detection system. The limited usable statistics and acceptance limits of the experimental setup did not allow us to achieve exclusive SRC measurements but provided essential information for improving future studies at  $R^3B$ .

This research constitutes a fundamental step in studying SRC using inverse kinematics. Despite the difficulties, the developed methodology provides important information to better identify SRC physics. Future experiments should consider higher beam energies or better detection techniques to better isolate SRC events.

*Per Daniela,  
per Alberto,  
per Anna,  
per Davide,  
per Elisa  
e per tutte le persone  
che mi hanno supportato e ispirato.*





# Acknowledgements

As I complete this thesis, I find myself deeply grateful to the many people who have supported, encouraged, and guided me along this journey. This work would not have been possible without their contributions, both professionally and personally.

First and foremost, I would like to express my deepest gratitude to the esteemed members of my PhD defence panel: David Verney, Alexandre Obertelli, Olivier Sorlin, and Marlène Assié. It was a true privilege to engage in such a stimulating discussion with you. I sincerely appreciate the time and attention you devoted to my work, allowing me to present the culmination of my efforts over these years. Your thoughtful insights and constructive feedback were invaluable, and I believe they will greatly enrich the content of this thesis and also my personal knowledge. Thank you for your support and encouragement throughout this journey.

I owe immense gratitude to my PhD supervisors, Anna Corsi and Aldric Revel. Their knowledge, patience, and encouragement have been invaluable throughout my research. From the early stages of my studies to the final touches on this thesis, they offered me their time, wisdom, and support. Anna, with her keen insight and careful guidance, taught me the importance of precision and perseverance in scientific inquiry. Aldric, with his contagious enthusiasm and innovative thinking, pushed me to explore beyond the boundaries of conventional approaches. Together, they have been inspiring mentors, and I am profoundly thankful for the opportunity to learn from them.

To my family, my mum Daniela, my dad Alberto, my sister Anna, and my brother Davide, I extend my deepest gratitude. Your unwavering love and belief in me have been the foundation of everything I have accomplished in this work. Mamma, your endless encouragement, patience, and guidance have been my constant sources of motivation, especially in moments of doubt. Papà, your quiet strength and unwavering inspiration have taught me the true value of hard work and dedication. Anna and Davide, your support, infinite love and perspective have grounded me through the most challenging times, giving me always the strength and motivation to keep going. I am profoundly grateful for the faith you all have shown in me, even when I struggled to find it within myself. I love you all.

Elisa, you have been a true pillar of support throughout this journey. Thank you for being there through the late nights and long days, for understanding the sacrifices required by this journey, and for always encouraging me to keep pushing forward. Your love, patience, and optimism have been a constant source of strength.

To my grandparents, aunt, uncle and cousins thank you for your support and encouragement. You have been a constant presence in my life, always interested in my progress and eager to celebrate each step forward. Knowing that I had such a supportive network behind me has been an invaluable comfort.

---

I am especially grateful to my colleagues and friends who have shared this journey with me, offering infinite fun, laughter, valuable lessons and inspiration. Antia, Christine, Eleonora, Ivana, Martina, Antoine, Enis, Gabriel, Hans, Leandro, Manuel, Nikhil, and Tomas, I want to thank you for the insightful discussions, mutual encouragement, and shared moments of both hard work and humor. Each of you has made these years of research a more rewarding and meaningful experience.

My heartfelt appreciation goes to the LENA group and my collaborators at CEA, especially Barbara, Valerie, Marine, Vittorio, Thomas, Alain, Emanuel and Gilles. Working with you has been an inspiring and rewarding experience, and I am grateful for the collaborative atmosphere and mutual respect that defined our interactions. Your expertise and enthusiasm for nuclear physics have greatly enriched my research experience, and your readiness to support and challenge me has helped shape my understanding of this field.

During my time at CEA, I have been fortunate to form strong friendships with many incredible people who helped make these years both productive and enjoyable. Borana, Benjamin, Alberto, Andrea, Andrii, Mathéo, Michael, Paul, and Pierre you have all played a significant role in my PhD journey. Benjamin, thank you especially for your friendship, for the many shared moments, and, of course, for all the coffee breaks that kept us energized. You were always there to chat, offer advice, and provide support, and it has been a privilege to work alongside you.

Completing this thesis has been a demanding journey, and the support of everyone mentioned here has made it possible. I am deeply grateful to each of you for your kindness, encouragement, and belief in me. Thank you for helping me reach this milestone and for making this experience as rewarding as it has been.



Andrea Lagni

València, 27 October 2024

Handwritten signature of Andrea Lagni in black ink.

# Contents

<b>1</b>	<b>The Atomic nucleus</b>	<b>19</b>
1.1	Nuclear models	24
1.1.1	Independent particle model (IPM)	26
1.1.2	The N-N interaction	29
	Long Range Correlations (LRC)	29
	Short Range Correlations (SRC)	30
1.1.3	Generalized Contact Formalism: Theoretical framework for SRC investigation	32
1.1.4	Consistency of IPM and SRC pictures	34
1.2	State of the art on Short Range Correlations	35
1.2.1	Electron scattering experiments	36
1.2.2	Proton scattering experiments	39
	How to probe SRC	40
	QFS Reaction Mechanism	41
	Test of proton-induced QFS in inverse kinematics	45
1.2.3	SRC and open questions in nuclear physics	47
	EMC effect	47
	Quenching of the spectroscopic factor	50
1.3	Motivations and goals of the experiment	51
<b>2</b>	<b>Experimental Setup</b>	<b>53</b>
2.1	Beam production at GSI	53
2.2	The $R^3B$ Setup	55
2.2.1	Incoming detectors	56
	LOS and ROLU	56
	MWPC (Multi-Wire Proportional Chambers) and MUSic for Light ions (MUSLi)	58
2.2.2	Target recoil detectors	60
	The COCOTIER Liquid Hydrogen Target	61
	FOOT (FragmentatiOn Of Target)	62
	The CALIFA detector	63
2.2.3	Outgoing detectors	66
	Large-acceptance dipole magnet GLAD	66
	Fiber detectors	67
	Time-of-Flight wall detector TOFD	67
	NeuLAND	68
	Resistive Plate Chamber (RPC) detector	70
2.2.4	Data Acquisition System of the $R^3B$ Collaboration	72
	Data Acquisition System (DAQ) and Trigger Logic	72

<b>3</b>	<b>Calibration and alignment</b>	<b>77</b>
3.1	R3BRoot Workflow . . . . .	77
3.2	Detectors calibration and alignment . . . . .	79
3.2.1	Incoming detectors calibration . . . . .	80
	S2 . . . . .	80
	LOS . . . . .	80
	MWPC and MUSLi calibration . . . . .	83
	ToF selection S2-LOS for $^{16}\text{C}$ setting . . . . .	86
3.2.2	Target recoil detectors calibration . . . . .	87
	CALIFA calibration . . . . .	87
	FOOT . . . . .	94
3.2.3	Outgoing detectors calibration . . . . .	101
	TOFD calibration . . . . .	101
	Fiber calibration . . . . .	107
	NeuLAND calibration . . . . .	110
	RPC calibration . . . . .	113
3.3	Detectors Alignment . . . . .	117
<b>4</b>	<b>Data analysis</b>	<b>121</b>
4.1	Simulations . . . . .	124
4.1.1	INCL Event Generator . . . . .	124
4.1.2	The QFS Event Generator . . . . .	126
4.1.3	Generalised Contact Formalism Event Generator . . . . .	127
4.2	Particles identification and tracking . . . . .	128
4.2.1	Beam particles identification . . . . .	129
4.2.2	Fragments tracking . . . . .	133
4.2.3	Proton tracking . . . . .	139
4.2.4	Neutrons tracking . . . . .	140
4.3	$(p,2p)$ reaction investigation . . . . .	145
4.3.1	Protons identification via QPID . . . . .	146
4.3.2	Punch-trough protons energy reconstruction . . . . .	147
4.3.3	Protons momentum and angular distribution . . . . .	153
4.3.4	$^{12/16}\text{C}(p,2p)\text{A-1}$ QFS selection . . . . .	158
4.4	SRC physics investigation . . . . .	167
4.4.1	$^{12/16}\text{C}(p,2p)\text{A-2}$ semi-exclusive investigation . . . . .	169
<b>5</b>	<b>Conclusions and perspectives</b>	<b>177</b>
5.1	Conclusions . . . . .	177
5.2	Future Prospects . . . . .	179
<b>A</b>	<b>Appendix</b>	<b>183</b>
A.1	RPC efficiency . . . . .	183
A.2	NeuLAND efficiency . . . . .	184

# Résumé

Les systèmes à plusieurs corps composés de fermions sont omniprésents dans la nature, se manifestant dans divers phénomènes physiques et domaines d'étude, allant des supraconducteurs à haute température et des liquides de Fermi aux noyaux atomiques, à la matière de quarks et aux étoiles à neutrons. Ces systèmes, régis par les lois de la mécanique quantique, présentent des comportements uniques découlant directement des propriétés fondamentales des fermions. Contrairement aux bosons, les fermions obéissent au principe d'exclusion de Pauli, qui stipule qu'aucun fermion identique ne peut occuper simultanément le même état quantique. Ce principe constitue la base de l'organisation structurée, en "couches", des fermions dans ces systèmes à plusieurs corps, contribuant aux complexités et aux corrélations qui émergent de leurs états quantiques, en particulier dans des conditions de haute densité comme celles que l'on trouve dans les noyaux atomiques ou les étoiles à neutrons.

L'un des défis majeurs dans l'étude des systèmes à plusieurs corps de fermions réside dans la résolution des équations complexes et interdépendantes qui gouvernent leur comportement. Dans de tels systèmes, l'état et le mouvement de chaque particule sont influencés non seulement par des interactions directes avec les particules voisines, mais aussi par les effets cumulatifs de toutes les autres particules au sein du système. Cette interdépendance en mécanique quantique conduit à ce qu'on appelle le "problème à plusieurs corps", où le calcul détaillé du comportement de chaque particule devient rapidement infaisable à mesure que le nombre de particules augmente. Pour rendre ces problèmes complexes plus abordables, des méthodes d'approximation simplifiant le comportement du système sans avoir besoin de prendre en compte chaque interaction individuellement sont souvent employées.

Parmi les approximations les plus largement utilisées pour les systèmes à plusieurs corps figure l'approche du champ moyen, qui modélise chaque particule comme évoluant indépendamment dans un champ de potentiel effectif représentant l'influence moyenne de toutes les autres particules. Ce modèle réduit considérablement la complexité des équations, car il supprime la nécessité de calculer chaque interaction individuellement. Cependant, l'approximation du champ moyen, bien qu'efficace pour capturer les caractéristiques générales d'un système, échoue souvent à décrire certaines interactions résiduelles cruciales qui découlent des corrélations entre nucléons. Ces interactions résiduelles conduisent à des écarts par rapport au modèle de particule indépendante et offrent un aperçu des véritables dynamiques du système, jouant un rôle clé dans la distribution des fermions autour du niveau de Fermi et au-delà.

En mécanique quantique, le niveau de Fermi désigne le niveau d'énergie le plus élevé occupé par des fermions à température nulle. Les états en dessous de ce niveau sont généralement occupés, tandis que ceux au-dessus restent vacants. Dans un système idéalisé sans interaction, les fermions occuperaient ces états jusqu'au niveau de Fermi de manière ordonnée. Cependant, dans les systèmes réels, les interactions résiduelles provoquent des déplacements de fermions vers des états d'énergie plus élevés ou des vides sous le niveau de Fermi. Ces corrélations, souvent dues à des interactions à courte portée, sont particulièrement notables en physique nucléaire, où les nucléons (protons et neutrons) interagissent à courte distance.

Les noyaux atomiques, avec leurs interactions à courte portée, sont particulièrement intéressants. La physique des corrélations à courte portée (SRC) découle des interactions à courte distance et se manifeste par des paires de nucléons. Les paires SRC présentent un moment relatif élevé et un moment de centre de masse faible par rapport au moment de Fermi ( $k_F = 250 \text{ MeV}/c$ ). Ces paires forment des fluctuations de haute densité temporaires, limitées par l'interaction fortement répulsive entre nucléons à des distances inférieures à environ 1 fm. La plupart de nos connaissances sur les SRC proviennent d'expériences de diffusion d'électrons et de protons. Les études indiquent qu'environ 20% des nucléons liés occupent cette région à haut moment. La première preuve expérimentale des SRC a été fournie par la mesure d'une queue à haut moment dans les distributions de moment des protons lors des expériences de diffusion d'électrons. Dans ce cadre expérimental, nous avons étudié les SRC en utilisant des réactions spécifiques, telles que  $^{12}\text{C}(p, 2p\text{N})A-2$  et  $^{16}\text{C}(p, 2p\text{N})A-2$ , où (p, 2pN) représente l'éjection de deux protons et d'un nucléon additionnel N. Ces réactions nous ont permis de mesurer les caractéristiques des SRC, incluant les moments relatifs et de centre de masse des paires de nucléons ainsi que le rapport de paires  $np/pp$ . Nos résultats pour les rapports de paires  $np/pp$  étaient inférieurs à ceux prévus par le *Generalized Contact Formalism* (GCF), qui estime la prévalence des paires  $np$  par rapport aux paires  $pp$  en fonction de la structure nucléaire. Cette divergence suggère que les effets de champ moyen et les interactions d'état final pourraient interférer avec les observations de SRC à ce niveau d'énergie, pointant vers une probabilité réduite de rupture de paires SRC et une nécessité d'approfondir ces effets à différents niveaux d'énergie.

Notre analyse des données a été davantage compliquée par les limitations de la résolution en moment du système de détection, ce qui a nui à notre capacité de distinguer avec précision les événements SRC des canaux concurrents. La résolution en moment est cruciale pour séparer les SRC d'autres processus nucléaires, et les limitations de notre système ont affecté la clarté de nos résultats. Par conséquent, bien que notre étude ait apporté des informations précieuses sur les propriétés des SRC, les limites statistiques et les contraintes d'acceptance nous ont empêchés d'obtenir des mesures exclusives, soulignant des domaines à améliorer pour les futures expériences.

Cette recherche marque une avancée significative dans les études des SRC, en particulier grâce à l'utilisation de la cinématique inverse dans les noyaux riches en neutrons. Bien que des défis tels que la résolution limitée en moment et des rapports  $np/pp$  inférieurs aux prévisions aient mis en évidence la complexité de l'étude des SRC dans de tels environnements, notre méthodologie a posé les bases de recherches futures. Les résultats expérimentaux suggèrent qu'à l'énergie de faisceau de 1.25 GeV par nucléon, la section efficace pour la "rupture" des paires SRC pourrait ne pas être suffisante pour explorer pleinement la physique des SRC, indiquant que l'énergie de faisceau et la résolution de détection sont des facteurs critiques dans les études de SRC.

La compréhension des SRC dans les systèmes riches en neutrons approfondira notre connaissance de la structure nucléaire et de la physique des systèmes à plusieurs corps, avec potentiellement un impact sur notre compréhension des étoiles à neutrons et de la matière nucléaire dense. Cette recherche constitue une étape fondamentale dans l'étude des SRC en utilisant la cinématique inverse. Malgré les difficultés rencontrées, la méthodologie développée fournit des informations importantes pour mieux identifier la physique des SRC. Les expériences futures devraient envisager des énergies de faisceau plus élevées ou de meilleures techniques de détection pour mieux isoler les événements SRC.

# List of Figures

1	Chart of the nuclides representing stable nuclei with black squares, neutron-rich or neutron-deficient nuclei already produced in terrestrial laboratories with light yellow shading, and nuclei not studied yet in light blue. . . . .	17
1.1	Binding energy per nucleon ( $\frac{E_b}{A}$ ) as a function of the mass number ( $A$ ) for stable nuclei. . . . .	22
1.2	Cartoon representing a nucleus at different RG resolutions. . . . .	25
1.3	Schematic illustration of the nuclear shell model. . . . .	27
1.4	Some typical axially symmetric nuclear shapes. . . . .	30
1.5	The Av18 and CDBONN NN potentials in the $^1S_0$ channel are depicted. . . . .	31
1.6	Diagram illustrating the momentum distribution of nuclear single particles at high-resolution scale. . . . .	31
1.7	The left Figure compares the correlated momentum distributions of symmetric nuclear matter. On the right, the Av18 and CDBONN NN potentials in the $^1S_0$ channel are depicted. . . . .	35
1.8	The comparison of the experimental momentum distribution from electron scattering on $^{12}\text{C}$ (markers) to the momentum distribution calculated within the independent particle model (dashed line). . . . .	36
1.9	An artistic representation of the results obtained from the observations of $^{12}\text{C}(e, e'pp)$ and $^{12}\text{C}(e, e'pn)$ reactions. . . . .	37
1.10	The ratios of proton-proton to neutron-proton short-range correlation pairs in stable isotopes are shown as a function of their mass $A$ . . . . .	37
1.11	The ratio of $(e, e'0pp)$ $^{12}\text{C}$ and $(e, e'0p)$ $^{12}\text{C}$ events, as a function of missing momentum. . . . .	38
1.12	Left: double ratio of high-to-low momentum protons (neutrons) in nucleus $A$ with respect to carbon marked with dots (squares). Right: SRC fractions ( $n$ and $p$ ) relative to $^{12}\text{C}$ in low-order correlation operator approximation (LCA). . . . .	38
1.13	Top: direct kinematics (e.g. electron scattering experiments) when the electron beam impinges directly on the nucleon of interest. Bottom: inverse kinematics (e.g. proton scattering experiments), where the nucleus of interest is the beam that impinges on a hadronic target. . . . .	40
1.14	A schematic view of the quasi-free scattering reaction $(p, pN)$ is shown in the rest frame of the target nucleus $A$ . . . . .	41
1.15	Illustration of the $^{12}\text{C}(p, 2pN)$ reaction visualized in direct kinematics. . . . .	43
1.16	Diagrammatic view of the SRC scattering process on nucleus $A$ . . . . .	43
1.17	Visual diagrams representing the physics of the different Mandelstam variables. . . . .	45
1.18	Setup used for the SRC test experiment at the Nuclotron accelerator in Dubna. . . . .	46
1.19	Correlations between missing energy and missing momentum. . . . .	46
1.20	Distribution of the cosine of the angle between the recoil nucleon and missing momentum (left), and $^{10}\text{B}$ fragment and pair relative momentum (right) . . . . .	47
1.21	Ratio of the nucleon structure functions $F_2$ of Iron and deuterium. . . . .	48

1.22	Left plot: ratio of $^{56}\text{Fe}$ deep inelastic cross-section with respect to deuterium in function of the Bjorken factor $x_B$ . Right plot: electron inelastic scattering cross-sections of $^{56}\text{Fe}$ with respect to deuterium at large $x_B$ . . . . .	49
1.23	Per-neutron (left) and per-proton (right) strength of the EMC effect versus the per-neutron and per proton number of SRC pairs. . . . .	50
1.24	Quenching of proton SFs as a function of $(N - Z)/A$ for $(e, e'p)$ and $(p, 2p)$ data compared to a phenomenological calculation including SRC and LRC. . . . .	51
1.25	Double ratio of high-to-low momentum protons (neutrons) in nucleus $A$ with respect to carbon marked with dot (squares), and corresponding calculations with rectangles. . . . .	52
2.1	Layout of the current heavy-ion beam facility (left, blue colour) at GSI is shown together with the future FAIR facility (right, red colour). . . . .	54
2.2	Schematic overview of the FRS at GSI. . . . .	55
2.3	The $R^3B$ setup in Cave C. . . . .	57
2.4	Top Left: LOS Octagonal shaped scintillator. Top right: focus on LOS with the octagonal-shaped scintillator coupled to the 8 PMTs, one for each side. Bottom: the final version of LOS with the octagonal scintillator and the PMTs. . . . .	58
2.5	Photo of ROLU detector. . . . .	59
2.6	Structure of a MWPC and the internal electric field. . . . .	60
2.7	Geometry volume showing the $\text{LH}_2$ target, surrounded by the FOOT detectors and the CALIFA calorimeter. . . . .	60
2.8	Left: technical drawing of the target and cryostat ensemble. Right: photos of three target cells with their support and pipes. . . . .	61
2.9	Strip configuration with a highlight on the bound strip every 2 floating strips. . . . .	63
2.10	Top left: top view of the system $\text{LH}_2 + \text{FOOT}$ . Top right: zoom photo of a single FOOT detector. Bottom: scheme of the configuration of the 12 FOOT detection system around the target. . . . .	64
2.11	Artistic view of the CALIFA calorimeter. . . . .	65
2.12	Different artistic views of CALIFA Barrel crystals geometry. . . . .	66
2.13	Left: View of the cold mass (cryostat + magnetic coils) of $R^3B\text{-GLAD}$ . Right: Magnetic field map of GLAD. . . . .	67
2.14	Left: a sketch of a fiber detector read on both sides by two Hamamatsu multi-anode PMT H13700 with 256 anodes. Right: photo of the 4 fibers detector used in the current experiment. . . . .	68
2.15	Mechanical design of TOFD detector and front view of plane 1 of TOFD with the 44 scintillator. . . . .	69
2.16	Schematic layout of one NeuLAND frame and Photo of the NeuLAND detector located in Cave C. . . . .	70
2.17	Schematic of the internal structure of the of RPC detector. . . . .	71
2.18	Schematic of the positioning of the scintillator behind the RPC. . . . .	71
2.19	Histogram representing the experimental on-spill triggers $T_{\text{pat}}$ from 0 to 4096. . . . .	73
3.1	General calibration scheme for experimental data from raw to hit level. . . . .	78
3.2	LOS multiplicity for $^{12}\text{C}$ (left) and $^{16}\text{C}$ (right) settings. . . . .	81
3.3	Left: Hit level $X - Y$ position correlation plot (in cm) after the calibration procedure for $^{12}\text{C}$ (Top left) and for $^{16}\text{C}$ (Bottom left). Right: Charge $Z$ of $^{12}\text{C}$ after the calibration process (Top right) and for $^{16}\text{C}$ (Bottom right). The $X$ - $Y$ MWPC position are presented without applying alignment offset. The charge $Z$ in LOS is not aligned at the nominal value since we expect only one charge peak in the $Z$ distribution. . . . .	82

3.4	Top left: Correlation between the $X$ position of the beam in MUSLi and $\theta$ angle in the $X - Z$ plane for $^{12}\text{C}$ . Bottom left: Same correlation for $^{16}\text{C}$ . Top right: $X$ position correlated with the charge $Z$ of the beam. Bottom right: Same correlation for $^{16}\text{C}$ . . . . .	84
3.5	Correlation between the charge $Z$ in LOS and charge $Z$ in MUSLi. . . . .	84
3.6	Top left: Correlation between the $X$ position of the beam in MWPC0 for $^{12}\text{C}$ . Bottom left: Same correlation for $^{16}\text{C}$ . Top right: Correlation between the $X$ position of the beam in MWPC1 for $^{12}\text{C}$ . Bottom right: Same correlation for $^{16}\text{C}$ . The $X$ and $Y$ positions are directly taken from the "Hit" level without alignment offsets applied. . . . .	85
3.7	Time-of-flight ( $ToF$ ) between S2 and LOS detectors, showing a clear peak around 1395.4 ns. . . . .	86
3.8	Correlation between the charge $A/Q$ determined by S2-LOS $ToF$ and charge $Z$ in MUSLi. . . . .	87
3.9	Exponential background plus Gaussian fit for $^{22}\text{Na}$ (left) and $^{60}\text{Co}$ (right) source spectra, crystal 4851. . . . .	88
3.10	AmBe Spectrum and fit for crystal 4851. . . . .	89
3.11	Linear relation between channel number and energy in keV for crystal 4851. . . . .	90
3.12	$\text{Log}(wss)$ distribution versus crystal ID for the Gamma-range crystals (left) and the Proton-range crystals (right). . . . .	91
3.13	Example for "good" (left) and "bad" (right) linear fit for different crystals. This justifies the $wss$ threshold at 0.001. . . . .	91
3.14	Distribution of slope versus crystal ID, for both gamma and proton ranged crystals	92
3.15	Distribution of the difference between calibrated energy peaks and expected energy peaks in keV for each crystal at 511 keV. . . . .	93
3.16	Distribution of the difference between calibrated energy peaks and expected energy peaks in keV for each crystal at 1274.5 keV. . . . .	93
3.17	Resolution (sigma) v. crystal ID. . . . .	93
3.18	This Figure represents a summary of the step employed to reach a fine correction of the baseline with pedestal subtraction. From left to right: pedestals plot with a "bad" strip identification, their sigma values before (blue) and after (red) the 3 steps mentioned above, the dispersion of the pedestal values after this correction.	94
3.19	Cluster for $^{12}\text{C}$ visible at the Cal level. . . . .	95
3.20	Position dependence of the cluster sums corresponding to $^{12}\text{C}$ hits. Zoom in the plot showing the energy at the Cal level with respect to the position. The influence of the interstrip impact parameter $\eta$ on the cluster sum results in a regular pattern across the readout gap. This pattern is identified and corrected accordingly. . . . .	96
3.21	Cluster energy with respect to the $\lambda$ value, for 2 different FOOTs. As we can notice here, the shape of the charge component varies significantly from sensor to sensor. . . . .	97
3.22	Corrected cluster after $\lambda$ -energy correction with respect to the $\lambda$ value done with s509 $^{21}\text{N}$ FRS setting. $Z=1/2$ are the particles with $Z=1$ and $Z=2$ that populates a very similar region. . . . .	97
3.23	Energy correlation (energy in ADC channel) between the two In-beam FOOT detectors inside the vacuum chamber for a $^{12}\text{C}$ incoming beam. $Z=1/2$ are the particles with $Z=1$ and $Z=2$ that populates a very similar region. . . . .	98
3.24	Plot showing efficiency against sigma threshold value for the 1 GeV proton beam.	100
3.25	Time-over-Threshold measurement. The time width, while the signal exceeds the pre-defined threshold, is defined by the leading and trailing edge. . . . .	101

3.26	Time measurement with TOFD. The number of cycles of a 200 MHz clock defines the coarse time (red) with a precision of 5 ns. The fine time (green) is defined by the difference of the signal rise to the start of the next clock cycle and is determined with an FPGA-based TDC (lower panel). The signal is propagated through delayed FPGA modules until the next clock cycle stops the sampling process. . . . .	102
3.27	Raw ToFD data, Top left: $ToT$ vs. bar number for data from an $x$ sweep run at $y = \text{center}$ position. Negative bars display the bottom PMT channels, and positive the top PMT channels. Right: Time-of-Flight over bar number. Bottom left: time difference between the average times of the bars and the trigger time for a sweep run. Right: $ToF$ parameter calculation by a Gaussian fit over the maximum. . . . .	104
3.28	$ToT$ vs bar number during a $x$ sweep run at $y = 20$ cm position. The up-located channels (positive bar numbers) measure a higher $ToT$ than the down-located channels. . . . .	105
3.29	$ToT$ distribution along one bar (Top) in the meander run for two example bars (left and right). Although the geometric mean of the $ToT$ is expected to be constant along the bar, edge effects are clearly visible. Below, the same plot with the set granularity (rebinned) is shown. The code is set for a coarse threshold. If, for a given $Y$ -projection, the maximum is below the threshold or outside the range of the bar (here $\pm 40$ cm), that data point is rejected (see red lines). These data points are then fitted by a third-order polynomial. With the fit parameters determined, the procedure is repeated with a lower threshold and refitted (two lower panels). In all the plot the $x$ axis show the position along the bar in $cm$ and on the $y$ axis the ToT information in $ns$ . . . . .	106
3.30	Top: result from the meander run after the smiley correction for two bars. On the left, the results for a bar with a good calibration are displayed. There is almost no position dependency left and in the projection (middle panel) all charge peaks can be easily distinguished and used for fitting (lower panel). On the right, a bar with a "bad" smiley correction is shown. The position dependency is still present, and the exact peak recognition is hindered. Furthermore, it can be seen that different charges need a different correction function/different parameters. In our case, this is still in the acceptable range, as the bands for charge 6,5,4 do not differ significantly. . . . .	106
3.31	Charge in TOFD after the calibration procedure for $^{12}C$ (left) and $^{16}C$ (right). .	107
3.32	Time difference calibration for Fib32 with $^{12}C$ sweep run. (a) $\Delta t$ as a function of the fiber number. For every channel, the maximum is identified (b). (c) Calibrated $\Delta t$ spectrum. . . . .	108
3.33	Top: $Y$ -Fiber detector calibration results with dispersed $^{12}C$ beam. Only fiber numbers 150-400 could be properly calibrated. Therefore, $ToT$ and time synchronization parameters only exist for these channels. Outer channels remain uncalibrated. Bottom: $Y$ -position in Fib30 against $X$ -position in Fib32 for $^{12}C$ production run of S522 campaign. In panel (a), one can observe a slight gap in the noise band at fibers 320. This hints at less efficient channels. As the data band is still sufficiently filled, this will not affect further analysis. . . . .	109
3.34	The time measurement is split into coarse (clock cycle) and fine (channel) time. The coarse counter of VFTX is reset at 2047. Figure from M. Heil's presentation on the calibration of FPGA TDC. . . . .	110
3.35	Left: number of counts with respect to the TDC channel. Right: time calibration of the channel number (from the left figure) using the Eq.3.30. . . . .	111

3.36	Top: Time difference between left (bottom) and right (top) signals of one bar vs the bar number for run 140 (with primary $^{12}\text{C}$ beam and looking at of-spill data). Bottom: Time difference between a muon hit in a bar and a hit in a central bar 625 (top, horizontal plane central bar) and bar 675 (bottom, vertical plane central bar) after synchronization. The structure shown in the bottom figures is related with the different angles that the muon tracks can reach NeuLAND detector. . . . .	112
3.37	Top left: Corrected time of flight spectrum of $^{16}\text{C}$ beam run. The three peaks are $\gamma$ , neutron and beam dump ( i.e. scattering of neutron at the wall located around 3 meters from the last neutron wall), respectively. Top right: Corrected time of flight spectrum of $^{16}\text{C}$ run for $\gamma$ . The timing resolution is 206.8 ps. Bottom left: Corrected time of flight spectrum at $\gamma$ peak versus bar ID for a $^{16}\text{C}$ run. Bottom right: Gamma ToF spectrum after fine correction to align the gamma peak in each bar. The timing resolution improved to 187.4 ps. . . . .	113
3.38	$ToT$ distribution (blue) and the bin by bin derivative (red). . . . .	115
3.39	$ToT$ calculation per strip without applying the $\epsilon_{ToT,i}$ parameters (Left) and when applying (right). . . . .	115
3.40	Top: $X, Y$ map before (Left) and after (right) applying calibration parameter $\epsilon_{X,I}$ . The central spot corresponding to the forward emitted particles (protons) and the geometrical acceptance defined by the GLAD magnet (halo at the periphery of the plot) are clearly visible in the right plot. Bottom: Normalized accumulated histogram of hits in strip 21 of the RPC. . . . .	116
3.41	Left, $T_{sc1} - T$ difference per strip, without calculation of $\epsilon_{T,I}$ parameters and with calculated ones in bottom. . . . .	117
3.42	$z$ position of the in-beam tracking detectors and central positions for all the FOOT detectors derived from the laser scan. . . . .	118
3.43	Laser scan of the FOOT detectors and the $\text{LH}_2$ target. . . . .	119
4.1	Scheme of a process of SRC investigation. With the proton probe we aim to separate the components of the SRC pair and to detect them in the final state. After the $np$ SRC breakup we expect to detect at the final state one neutron, two protons and the related A-2 fragment. . . . .	122
4.2	Scheme of a FSI process. The proton probe interact with a proton inside the nucleus. The proton probed, while going out from the nucleus, can rescattered with a neutron of the medium causing its emission. This process will give in the final state one neutron, two protons and the A-2 fragment as in the case of SRC breakup. . . . .	123
4.3	Left: LOS charge $Z$ for $^{12}\text{C}$ with a green area showing the region selected for a good charge in LOS (between 5.3 and 7.2 charge units). Right: LOS $Z$ for $^{16}\text{C}$ with the red area showing the selection on the charge of LOS (between 5.3 and 6.8 charge units). . . . .	130
4.4	Correlation between the $A/Q$ and $Z$ derived from MUSLi using S2 and $ToF$ and charge information from LOS detector. In red is shown the selection applied to identify $^{16}\text{C}$ . . . . .	131
4.5	Left: MWPC beam trajectory projected onto the center of the target position as the interaction vertex. Correlation between the $XY$ coordinates projection at the center of the target ( $^{12}\text{C}$ ). Left: same plot for $^{16}\text{C}$ beam. . . . .	132
4.6	$Z$ component of the $^{16}\text{C}$ beam momentum. The momentum is calculated at the center of the target after energy loss in the incoming detector and half of the target volume. . . . .	133

4.7	The left plot displays the reaction fragments for the $^{12}\text{C}$ beam, while the right plot shows those for the $^{16}\text{C}$ beam. The main fragments of interest for this analysis are highlighted in the figure. . . . .	137
4.8	Momentum component distribution for $^{11}\text{B}$ and $^{15}\text{B}$ with (p,2p) selection in the beam rest frame. $p_x, p_y$ of $^{11}\text{B}$ and $^{15}\text{B}$ exhibit a small shift of the order to few MeV, with a Gaussian width of approximately 100 MeV/c. $p_z$ shows a shift of around 30 MeV/c for $^{11}\text{B}$ and 40 MeV/c for $^{15}\text{B}$ . . . . .	138
4.9	Momentum component distribution for $^{10}\text{B}$ and $^{14}\text{B}$ with (p,2pn) selection in the beam rest frame. $p_x, p_y$ of $^{10}\text{B}$ and $^{14}\text{B}$ exhibit a small shift of the order to few MeV, with a Gaussian width of approximately 120 MeV/c that is consistent with its physics width. $p_z$ shows a shift of about 10 MeV/c for $^{10}\text{B}$ while for $^{14}\text{B}$ the shift is around 40 MeV/c. . . . .	138
4.10	Momentum component distribution for $^{10}\text{Be}$ and $^{14}\text{Be}$ with (p,3p) selection in the beam rest frame. $p_x, p_y$ of $^{10}\text{Be}$ and $^{14}\text{Be}$ exhibit a small shift of the order to few MeV, with a Gaussian width of approximately 120 MeV/c that is consistent with its physics width. $p_z$ shows a shift of 10 MeV/c for both $^{10}\text{Be}$ and $^{14}\text{Be}$ . . . . .	139
4.11	Momentum component distribution for RPC protons with (p,2p) selection in the beam rest frame. $p_x, p_y$ and $p_z$ exhibit a shift of the order of 50 MeV/c, with a Gaussian width of approximately 100 MeV/c that is consistent with its physics width. . . . .	140
4.12	Top left: corrected $ToF$ spectrum for the first hit in Neuland. Top right: corrected $ToF$ v. deposited energy in Neuland. Bottom left: corrected $ToF$ spectrum for the first hit in Neuland. Bottom right: corrected $ToF$ vs. deposited energy in Neuland. All plots are made with charge veto and a minimum energy deposition cut at 6 MeVee. . . . .	141
4.13	Energy versus bar ID (left) and $ToF$ versus bar ID (right) for all Neuland hits. . . . .	142
4.14	Neuland hit position v. $ToF$ distribution with $^{10}\text{B}$ and (p,2p) tagging. . . . .	143
4.15	Angular and beta alignment of $^{10}\text{B}$ and selected neutrons in Neuland. . . . .	143
4.16	Momentum component distribution for neutrons in NeuLAND with (p,2p) selection in the beam rest frame. $p_x, p_y$ and $p_z$ exhibit a small shift of the order to few MeV/c, with a Gaussian width of approximately 70 MeV/c for $^{12}\text{C}$ and 40 MeV/c for $^{16}\text{C}$ . . . . .	145
4.17	Top left: $N_f + N_s$ vs $\frac{N_f}{N_f+N_s}$ CALIFA particle identification. Distinct lines can be observed, corresponding to neutrons ( $n$ ), punch-through protons ( $p$ ), and gamma rays ( $\gamma$ ). The upper line is associated with stopped protons. Top right and bottom: $N_f + N_s$ vs. $\frac{N_f}{N_f+N_s}$ for different CALIFA angular ranges. As the angle increases, the separation of the lines becomes clearer, and the background is more suppressed. . . . .	146
4.18	Top left: Exponential fit of the $N_f + N_s$ vs $\frac{N_f}{N_f+N_s}$ stopped proton PID line. Top right: $N_f + N_s$ vs $\frac{N_f}{N_f+N_s}$ with PID lines scaled relative to the stopped proton line using the exponential fit. Bottom left: Projection of $\frac{N_f}{N_f+N_s}$ for $N_f + N_s = 125$ MeV, showing the separation of the two CALIFA particle regions. Bottom right: $N_f + N_s$ vs $\frac{N_f}{N_f+N_s}$ with a defined threshold in $\frac{N_f}{N_f+N_s}$ based on the projection, distinguishing the regions of stopped protons from punch-through protons. . . . .	148
4.19	$\theta/\phi$ dependence of simulated proton deposited energy at a fixed generated incident energy of 650 MeV. . . . .	149
4.20	Deposited energy correlation for the two highest-energy protons. Left: data. Right: (p,2p) signal reconstructed from Geant simulation through detectors. . . . .	150

4.21	Full kinetic energy correlation in generated $(p,2p)$ simulation (no detector effects applied). . . . .	150
4.22	Deposited energy [MeV] versus full kinetic energy [MeV] of protons at $\theta = 30^\circ, \phi = 30^\circ$ in proton simulation. . . . .	151
4.23	Top: Multiplicity of high-energy CALIFA clusters with incoming beam charge selection and outgoing fragment associated with $(p,2p)$ reactions, $^{11}\text{B}$ for $^{12}\text{C}$ beam (left) and $^{15}\text{B}$ for $^{16}\text{C}$ beam (right). The more intense blue and red distribution are associated with the selection of the outgoing $(p,2p)$ $A - 1$ fragment. A good $(p,2p)$ signal will result in exactly 2 clusters in CALIFA. Bottom: Correlation between the cluster multiplicity and opening angle (angle between the two scattered protons in the $XZ$ plane) selecting $^{11}\text{B}$ for $^{12}\text{C}$ beam (left) and $^{15}\text{B}$ for $^{16}\text{C}$ beam (right). The selection of multiplicity of CALIFA selects an opening angle region associated with a good $(p,2p)$ reaction around $77^\circ$ . . . . .	152
4.24	Sum of the crystal numbers in the two CALIFA clusters with $^{11}\text{B}$ tagging (red) and with $^{11}\text{C}$ tagging (blue). . . . .	153
4.25	The measured laboratory angles of an outgoing proton pair from the $(p, 2p)$ reaction. A spherical coordinate system is chosen such that the polar direction is associated with the beam axis $Z$ . . . . .	154
4.26	Left: $\theta$ and $\phi$ correlation $^{12}\text{C}$ data without $(p,2p)$ selection. Right: $\theta$ and $\phi$ correlation with $(p,2p)$ and $^{11}\text{B}$ selection. . . . .	156
4.27	Left: $\theta$ and $\phi$ correlation $^{16}\text{C}$ data without $(p,2p)$ selection. Right: $\theta$ and $\phi$ correlation with $(p,2p)$ and $^{15}\text{B}$ selection. . . . .	157
4.28	In gray inclusive opening angle of the $(p,2p)$ without selection on the $^{11}\text{B}$ fragment (left) and $^{15}\text{B}$ fragment (right). In green, the exclusive opening angle is shown with the selection on the $^{11}\text{B}$ fragment (left) and in pink on the right panel for the $^{15}\text{B}$ fragment. It is possible to observe the effect of gating on the $^{11/15}\text{B}$ fragment and only 2 clusters in CALIFA (blue and red distribution). The region at a smaller opening angle associated with FSI and IE component of the reaction is suppressed gating on the fragment. . . . .	157
4.29	In the left plot in grey, the inclusive missing mass of the $(p,2p)$ without selection on the $^{11}\text{B}$ fragment. The exclusive missing mass is shown in blue with the selection on the $^{11}\text{B}$ fragment. Also, here, it is possible to observe the effect of gating on the $^{11}\text{B}$ fragment. The region at smaller missing mass, associated with FSI and IE component of the reaction, is suppressed gating on the fragment. In the right plot, we can observe a similar situation for $^{16}\text{C}$ beam without and with $^{15}\text{B}$ selection. . . . .	158
4.30	Distribution of the $M_{miss}^2$ for IE/FSI events that populate the region below $0.5 \text{ GeV}^2/c^4$ (left plot). In the right plot, the correlation with the missing momentum is displayed. . . . .	159
4.31	The correlation between the measured missing energy ( $E_{miss}$ , calculated in the $^{12}\text{C}$ rest-frame) and the measured lab-frame two-proton in-plane opening angle ( $\theta_1 + \theta_2$ ). Distributions are shown for inclusive $^{12}\text{C}(p,2p)$ events (left) and exclusive $^{12}\text{C}(p,2p)^{11}\text{B}$ events (right). QE events are seen as a peak around low missing energy and opening angles of $\approx 79^\circ$ . IE reactions populate higher missing energy and lower opening angles, while ISI/FSI populate both regions and the ridge between them in the inclusive spectra. The bottom left figure shows the inclusive $^{12}\text{C}(p,2p)$ channel, and the bottom right figure the exclusive channel, i.e., with tagging $^{11}\text{B}$ of the correlation between missing mass squared ( $y$ -axis) and missing momentum ( $x$ -axis). In both cases, the quasi-elastic peak (QE) and inelastic (IE) events are visible, while ISI/FSI are reduced by fragment tagging. . . . .	160

4.32	The correlation between the measured missing energy ( $E_{\text{miss}}$ , calculated in the $^{16}\text{C}$ rest-frame) and the measured lab-frame two-proton in-plane opening angle ( $\theta_1 + \theta_2$ ). Distributions are shown for inclusive $^{16}\text{C}(p,2p)$ events (left) and exclusive $^{16}\text{C}(p,2p)^{15}\text{B}$ events (right). QE events are seen as a peak around low missing energy and opening angles of $\approx 79^\circ$ . IE reactions populate higher missing energy and lower opening angles, while FSI populates both regions and the ridge between them in the inclusive spectra. The left figure shows the inclusive $^{16}\text{C}(p,2p)$ channel, and the right figure the exclusive channel, i.e., with tagging $^{15}\text{B}$ of the correlation between missing mass squared ( $y$ -axis) and missing momentum ( $x$ -axis). In both cases, the quasi-elastic peak (QE) and inelastic (IE) events are visible, while FSIs are reduced by fragment tagging. . . . .	161
4.33	Opening angle (left) and $\Delta\phi$ (right) comparison between data (red) and simulation (black) for $^{11}\text{B}$ tagged events. . . . .	163
4.34	Missing-momentum distribution in $^{12}\text{C}$ rest frame for QE $^{12/16}\text{C}(p, 2p)$ and $^{12/16}\text{C}(p, 2p)^{11/15}\text{B}$ events. . . . .	163
4.35	Schematic representation of the coplanar test between the normal vector to the scattering plane (given by $p_1 \times p_2$ ) and the missing momentum $q = P - Q$ vector. . . . .	164
4.36	Distribution of the $\alpha$ coplanar angle for $^{12/16}\text{C}$ incoming beams before (grey) and after (blue and red) applying the QFS kinematical selection described previously. . . . .	165
4.37	Cosine of the opening angle between the missing- and fragment-momenta. While broadened due to detector resolutions, a clear back-to-back correlation is observed. . . . .	165
4.38	Correlation between the ratios of the simulated and generated angular distribution ( $TX_{n,NeuLAND}, TX_{p,RPC}$ ) and momentum distribution ( $P_{n,NeuLAND}, P_{p,RPC}$ ). In red, we represent the RPC acceptance region that overlaps with the NeuLAND one. . . . .	168
4.39	Fragment efficiency corrected experimental missing momentum distribution for the $^{12/16}\text{C}(p,2p)\text{A-2}$ reaction channels. . . . .	169
4.40	Light-Cone (LC) $\alpha$ distribution comparison between data (red), mean-field simulation (black), and GCF simulation (blue) at different slices of missing momentum. Data agrees well with the GCF simulation, especially at higher missing momentum values. I remain you here that GCF allow us to simulate SRC events, while for other reaction processes QFS and INCL generator are employed. These simulation were performed for $^{12}\text{C}$ nucleus. . . . .	171
4.41	Left: distribution of the cosine of the angle between the recoil nucleon and the missing momentum for $^{12}\text{C}(p, 2p)^{10}\text{B}/\text{Be}$ events with SRC selection. Right: distribution of the cosine of the angle between the recoil nucleon and the missing momentum for $^{16}\text{C}(p, 2p)^{14}\text{B}/\text{Be}$ events with SRC selection. These are raw numbers before the correction with the fragment efficiencies. . . . .	173
4.42	Simulation results comparing different reaction channels and selection conditions. Left: INCL simulation with QFS conditions. Right: $\text{Cos}(\theta_{p_{\text{miss}}, p_n})$ from experimental data without SRC conditions (blue) and with SRC conditions (red). . . . .	174
4.43	The ratios of proton-proton to neutron-proton short-range correlation pairs in stable isotopes are shown as a function of their mass $A$ . . . . .	175
4.44	Ratio of $^{12}\text{C}(p, 2p)^{10}\text{B}/^{12}\text{C}(p, 2p)^{10}\text{Be}$ as function of $p_{\text{miss}}$ . The blue area represents the selection on $p_{\text{miss}} > 0.4 \text{ GeV}/c$ that was performed. . . . .	176
5.1	Rescattering $pp$ and $pn$ total (elastic and inelastic processes) and elastic cross section. . . . .	178

---

5.2	Double ratio of high-to-low momentum protons (neutrons) in nucleus $A$ with respect to carbon marked with dot (squares), and corresponding calculations with rectangles, adapted from. The horizontal yellow and green lines are the region of the new measurement from the letter of intent. . . . .	180
5.3	The conceptual design and a tentative timeline for the $R^3B$ TRT device. . . . .	181
A.1	Estimated efficiency of the RPC as a function of the Hsc longitudinal position placed behind the RPC, showing an average value of around 95%. . . . .	183
A.2	Ratio of reconstructed to input relative energy as a function of reconstructed relative energy, representing the NeuLAND efficiency $\epsilon$ . . . . .	185



# List of Tables

2.1	Nominal specifications of the CALIFA calorimeter. . . . .	64
2.2	Specifications of the CALIFA Barrel. . . . .	65
2.3	Bulk properties of the CALIFA Endcap. . . . .	65
2.4	Overview of characteristic parameters of NeuLAND in the current experimental situation. . . . .	69
2.5	First part of the on-spill trigger and relevant Tpat trigger combination. . . . .	73
2.6	Second part of the on-spill trigger and relevant Tpat trigger combination. . . . .	74
3.1	FOOT Detector Parameters derived from the laser measurement done in August 2022. More details are presented later in the detector alignment section. . . . .	99
3.2	MWPCs position offsets derived with a relative alignment procedure using fixed positions for the FOOT detectors. . . . .	119
4.1	Fiber efficiency relative to TOFD detector. We notice that the efficiency for unreacted beam is slightly higher compared to the one derived with $^{11}\text{B}$ fragment. . . . .	135
4.2	Contributions to the total MDF tracking efficiency. . . . .	136
4.3	Offsets in cm for Fibers positions. . . . .	136
4.4	Offsets in cm for RPC positions. . . . .	140
4.5	In red: $^{12}\text{C}$ SRC $pp$ and $np$ ratio from the ratio of GCF contact terms propagated at the final state. $pp$ and $np$ SRC candidates ratio derived in this analysis. This ratio show a much smaller $np$ dominance. In green: V. Panin $^{12}\text{C}$ $pp$ and $np$ removal ratio and the one obtained in this work considering a low-missing momentum region related to mean field events (MF). . . . .	175



# Introduction

Nuclear physics, despite its long history, continues to reveal new and unexpected properties of the atomic nucleus. Understanding the nucleus's structure and behaviour, especially in terms of interactions between its constituents, remains a fundamental goal. However, such a description remains challenging, even for light nuclei with a small number of nucleons.

Many-body quantum mechanical systems with interacting particles are present in various areas of modern physics, such as condensed matter and atomic and nuclear physics. Typically, obtaining analytical solutions for the equations that describe the dynamics of particles in these quantum systems, based explicitly on the interactions between individual particles, is not feasible. Historically, the nucleus's fundamental properties were explored by simplifying the N-body problem into independent nucleons within a mean field. This approach successfully explained phenomena such as magic numbers associated with stable nucleon configurations and led to the shell model.

However, even if the stable nuclei are the most abundant on Earth, their diversity (nearly 300) represents only a small fraction of the existing nuclei. Today, over 3000 nuclei have been experimentally observed (see Fig. 1), with an expected equal number yet to be discovered. Nuclei beyond the stable region have limited lifetimes and decay primarily via  $\beta$  decay.

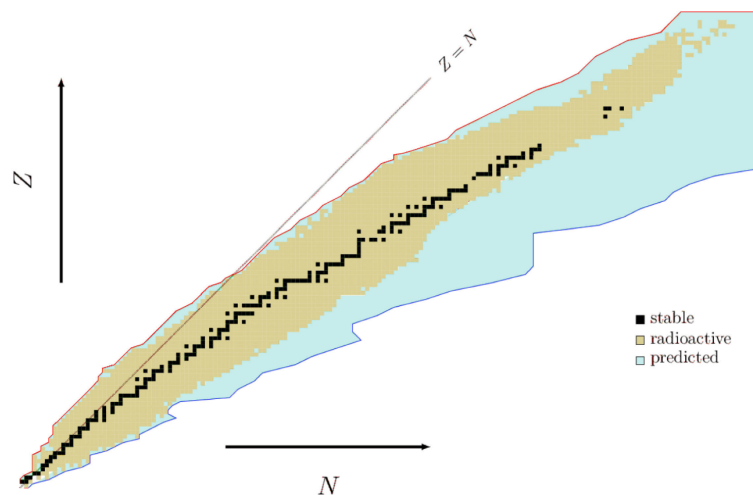


Figure 1: Chart of the nuclides representing stable nuclei with black squares, neutron-rich or neutron-deficient nuclei already produced in terrestrial laboratories with light yellow shading and nuclei not studied yet in light blue. The limits of proton and neutron particle stability (or driplines), predicted by theoretical models, are shown with red and blue lines, respectively [1].

As neutrons deviate from equilibrium values for a given  $Z$ , nuclei become less stable, eventually reaching the neutron (or proton) dripline, beyond which nuclei are unbound and decay rapidly. Research in modern nuclear physics aims to explore regions near these driplines, where extreme neutron-proton imbalances exist, to determine precise dripline positions.

Studying nuclei in these regions provides insights into structural evolution towards the limits of existence. The study of nuclear structure has been a cornerstone of physics for over a century, uncovering the fundamental building blocks and interactions that govern the behaviour of matter at its most fundamental level. Within this realm, exotic nuclei, characterized by extreme neutron-to-proton ratios or unusual proton and neutron configurations, offer a unique window into the underlying principles of nuclear physics. Experimental results refine existing theoretical models and inspire new ones.

It is particularly challenging to study NN interaction at short-range distance. The Short-Range interaction is strong between unlike fermions and weaker between identical fermions. In all these systems, the interaction generates Short-Range Correlated (SRC) pairs with a large relative momentum ( $k_{\text{rel}} > k_F$ ) and a small center of mass (CM) momentum ( $k_{\text{tot}} < k_F$ ), where  $k_F$  represents the Fermi momentum of the system. This interaction drives fermions from low momenta ( $k < k_F$ , where  $k$  is the fermion momentum) to high momenta ( $k > k_F$ ), resulting in the formation of a "high-momentum tail" in the single nucleon momentum distribution.

In nuclear physics, short-range correlations stand as intricate phenomena that are crucial for understanding the internal dynamics of atomic nuclei. These correlations emerge due to the powerful influence of the strong nuclear force, acting at extremely close distances between nucleons (protons and neutrons). Within the nucleus, SRCs manifest as intense interactions occurring at distances comparable to the size of individual nucleons.

Understanding the nature and implications of SRCs in  $n$ -rich nuclei like  $^{16}\text{C}$  is important for several reasons. Firstly, SRCs provide insights into the fundamental forces and dynamics governing nuclear interactions at short distances in neutron-rich environments. Secondly, these correlations have profound implications for nuclear astrophysics, influencing the Equation of State (EoS) [2], affecting neutron star density and protons and neutrons momentum distribution in  $n$ -rich environments [3]. Lastly, SRCs are essential for interpreting experimental data from high-energy and nuclear physics experiments, guiding the development of theoretical models. This thesis presents the first study of SRC in an exotic nucleus employing inverse kinematic reaction with a hadronic probe. The methodology to identify SRC events from competing channels is also presented in this work.

Chapter 1 provides a comprehensive review of the theoretical framework and experimental evidence for short-range correlations in nuclear systems, laying the groundwork for subsequent analysis. Chapter 2 will present the experimental setup used to study QFS reactions in inverse kinematics and an overview of the detectors that allow a kinematically complete study of the reactions. Chapter 3 includes a description of the detector calibration procedure. Chapter 4 presents the analysis method employed in this study, including nuclear models and related event generators used to investigate SRC. It also presents the main results of the thesis, including the characterization of SRCs in  $^{12}\text{C}$  and  $^{16}\text{C}$ . Finally, Chapter 5 summarizes the findings, discusses their implications, and outlines directions for future research in  $n$ -rich nuclei and short-range correlations.

Through this investigation, we aim to deepen our understanding of nuclear structure and dynamics in neutron-rich exotic systems, contributing to the broader quest to unravel the mysteries of the atomic nucleus and its implications in the universe.

# Chapter 1

## The Atomic nucleus

### Contents

---

<b>1.1 Nuclear models</b> . . . . .	<b>24</b>
1.1.1 Independent particle model (IPM) . . . . .	26
1.1.2 The N-N interaction . . . . .	29
1.1.3 Generalized Contact Formalism: Theoretical framework for SRC investigation . . . . .	32
1.1.4 Consistency of IPM and SRC pictures . . . . .	34
<b>1.2 State of the art on Short Range Correlations</b> . . . . .	<b>35</b>
1.2.1 Electron scattering experiments . . . . .	36
1.2.2 Proton scattering experiments . . . . .	39
1.2.3 SRC and open questions in nuclear physics . . . . .	47
<b>1.3 Motivations and goals of the experiment</b> . . . . .	<b>51</b>

---

The atomic nucleus is the central core of an atom, consisting of protons and neutrons, collectively known as nucleons. It plays a crucial role in determining the properties of an atom. Here is a short summary of the most important notions:

#### *Composition*

The nucleus is primarily composed of two types of fermions: protons ( $p$ ) and neutrons ( $n$ ), collectively known as nucleons. The strong nuclear force, one of the four fundamental forces of nature, holds these particles together.

Protons are positively charged subatomic particles with a charge of  $+1e$  (where  $e$  is the elementary charge, approximately  $1.602 \times 10^{-19}$  coulombs) and a rest mass of approximately  $0.938 \text{ GeV}/c^2$ . The proton is composed of three valence quarks (two up quarks and one down quark) held together by the strong force, mediated by gluons. Protons have a spin of  $\frac{1}{2}$ , which is a fundamental property arising from their quantum nature. The proton's properties and its role in defining the atomic number  $Z$  of an element make it a fundamental component of matter.

Neutrons are electrically neutral subatomic particles with no net charge and a rest mass slightly greater than that of the proton, approximately  $0.939 \text{ GeV}/c^2$ . Like protons, neutrons are made up of three valence quarks (one up quark and two down quarks) bound by the strong force. Neutrons also possess a spin of  $\frac{1}{2}$ , contributing to the overall angular momentum of the nucleus. Neutrons play a crucial role in the nucleus by contributing to the nuclear binding energy

and providing stability to the nucleus. The presence of neutrons counteracts the electrostatic repulsion between positively charged protons, allowing nuclei to exist with multiple protons. The number of neutrons, in combination with the number of protons, defines the isotope of an element and significantly influences its nuclear properties, including stability and radioactive decay processes.

The interaction between protons and neutrons within the nucleus is primarily governed by the strong nuclear force, which is attractive at short ranges and much stronger than the electrostatic repulsion between protons. This force ensures the nucleus's cohesion, overcoming the repulsive forces between like-charged protons. The exchange of mesons, particularly pions, mediates this interaction, resulting in the complex binding dynamics observed in nuclear systems.

Despite the strong nuclear force binding nucleons together, variations in the number of protons and neutrons lead to different nuclear binding energies and stability profiles. Stable nuclei exist only within a certain range of neutron-to-proton ratios, with deviations resulting in unstable, radioactive isotopes. Understanding the balance of forces within the nucleus is essential for explaining phenomena such as nuclear fusion, fission, and various modes of radioactive decay.

### *Atomic Number and Mass Number*

The **atomic number** ( $Z$ ) of an element represents the number of protons in the nucleus. Each element is uniquely identified by its atomic number. For example, hydrogen ( $H$ ) has an atomic number of 1, indicating that it has one proton in its nucleus.

The **mass number** ( $A$ ) represents the total number of nucleons (protons and neutrons) in the nucleus. It is the sum of the number of protons ( $Z$ ) and the number of neutrons ( $N$ ). The number of neutrons ( $N$ ) in the nucleus can be calculated using the equation:

$$N = A - Z. \quad (1.1)$$

Isotopes of an element have the same atomic number ( $Z$ ) but different mass numbers ( $A$ ). The ratio of neutrons to protons ( $N/Z$ ) varies among different isotopes, affecting their stability and properties. The  $N/Z$  ratio between their number of neutrons and protons varies slightly, varying around 1.

### *Size*

The nucleus is incredibly small compared to the overall size of an atom. It has a typical diameter of about  $10^{-15}$  meters, (1 Fermi). Despite its small size, the nucleus contains almost all of the atom's mass. The size of the nucleus is determined by the range of the strong nuclear force, which acts over very short distances compared to the electromagnetic force. Their radius can be described by the empirical formula  $R = r_0 A^{1/3}$  [4], where  $r_0$  is the effective radius of a nucleon ( $r_0 \approx 1.2$  fm) and  $A$  is the total number of nucleons. Such a description assumes a homogeneous distribution of the nucleons in the nucleus (independently of their nature).

### *Charge*

Protons have a positive charge, while neutrons are electrically neutral. Therefore, the nucleus as a whole carries a positive charge equal to  $Z \times e$ , where  $e$  is the elementary charge. This positive charge is balanced by the negative charge of the electrons orbiting the nucleus in the electron cloud. The net charge of the nucleus determines the overall charge of the atom. Atoms with an equal number of protons and electrons are electrically neutral.

### ***Binding Energy***

The nuclear binding energy is a fundamental concept in nuclear physics that quantifies the energy required to keep the nucleus of an atom intact. It represents the energy released when nucleons (protons and neutrons) come together to form a nucleus, overcoming the repulsive forces between positively charged protons. Mathematically, the nuclear binding energy ( $E_b$ ) can be calculated using the formula:

$$E_b = [Z \cdot m_p + (A - Z) \cdot m_n - M_c]c^2. \quad (1.2)$$

Where:

- $Z$  is the number of protons in the nucleus.
- $N$  is the number of neutrons in the nucleus.
- $m_p$  is the mass of a proton.
- $m_n$  is the mass of a neutron.
- $M_c$  is the mass of the nucleus.

The mass defect ( $\Delta m$ ) can be expressed as the difference between the total mass of the individual nucleons and the mass of the nucleus:

$$\Delta m = Z \cdot m_p + (A - Z) \cdot m_n - M_c. \quad (1.3)$$

Using Einstein's famous equation  $E = mc^2$ , where  $c$  is the speed of light in a vacuum, we can find the nuclear binding energy ( $E_b$ ) by multiplying the mass defect ( $\Delta m$ ) by  $c^2$ :

$$E_b = \Delta m \cdot c^2. \quad (1.4)$$

The average binding energy per nucleon ( $\frac{E_b}{A}$ ), where  $A$  is the mass number (total number of nucleons), is a crucial parameter for understanding the stability of nuclei. It represents the average energy required to remove one nucleon from the nucleus. The average binding energy per nucleon is typically around 8 MeV for stable nuclei.

Now, let's discuss the plot of the binding energy per nucleon ( $\frac{E_b}{A}$ ) as a function of the mass number ( $A$ ) presented in Fig. 1.1. This plot is a fundamental tool in nuclear physics and provides insights into the stability and structure of atomic nuclei.

The plot typically shows a characteristic curve with a peak around the mass number  $A \approx 60$ . This peak represents the most stable nuclei, where the binding energy per nucleon is highest. Nuclei with mass numbers smaller or larger than this peak value have lower binding energy per nucleon, indicating they are less stable.

For lighter nuclei (smaller  $A$ ), the binding energy per nucleon increases as the nucleus gains more nucleons, leading to a steeper rise in the curve. This is due to the increasing dominance of the attractive nuclear force over the electrostatic repulsion between protons.

For heavier nuclei (larger  $A$ ), the binding energy per nucleon decreases as the nucleus becomes more massive. This decrease is primarily attributed to the increasing influence of the repulsive electrostatic forces between protons, which outweigh the attractive nuclear forces,

causing the nucleus to become less stable.

Overall, the plot of binding energy per nucleon versus mass number provides valuable insights into the stability and structure of atomic nuclei, which is crucial for understanding nuclear phenomena and the behaviour of nuclear matter.

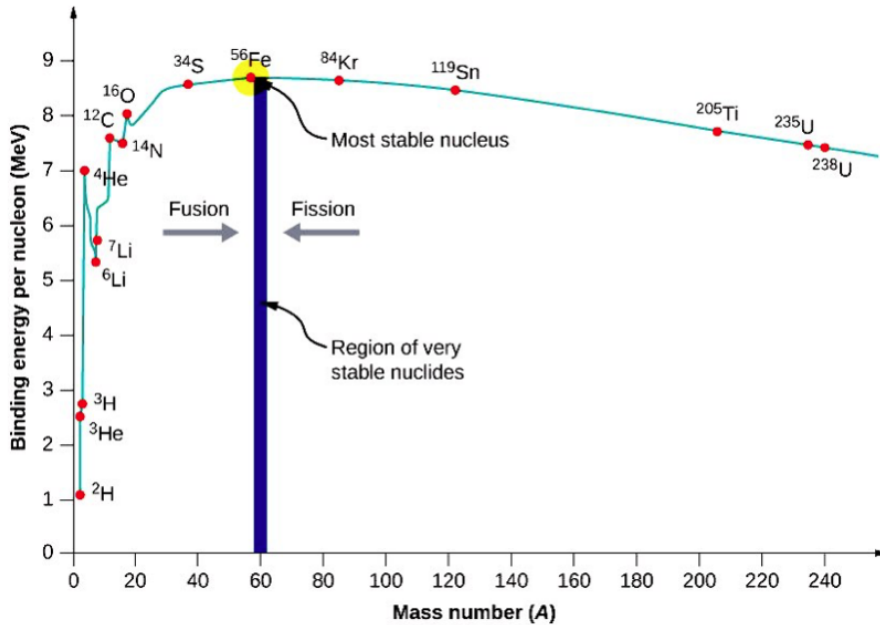


Figure 1.1: Binding energy per nucleon ( $\frac{E_b}{A}$ ) as a function of the mass number ( $A$ ) for stable nuclei. Figure taken from [5].

### *Nuclear Stability*

This stability is influenced by different fundamental forces, primarily the strong nuclear force and the weak interaction. The strong force is the primary force responsible for holding protons and neutrons (nucleons) together within the atomic nucleus. It is a short-range force but extremely powerful, overcoming the electrostatic repulsion between positively charged protons. The strong nuclear force acts attractively between nucleons. The stability of a nucleus depends on the balance between the strong nuclear force, which holds the nucleons together, and the electrostatic repulsion between protons. Nuclei with too many or too few neutrons compared to protons tend to undergo radioactive decay to achieve a more stable configuration.

When the strong force is insufficient to keep the nucleus intact due to its large size and resulting electrostatic repulsion, the nucleus can undergo an  $\alpha$  decay. This is a type of radioactive decay where an unstable nucleus emits an alpha particle, which consists of 2 protons and 2 neutrons (essentially a <sup>4</sup>He nucleus). Alpha decay occurs primarily in heavy nuclei where the strong nuclear force alone cannot overcome the repulsive electrostatic forces between protons. The emission of an alpha particle reduces the atomic number by 2 and the mass number by 4, leading to a new, often more stable, element.

Unlike the strong force, the weak interaction does not bind nucleons together but instead enables their transformation. It operates over a much shorter range and is weaker than the strong nuclear force, but it is crucial for processes that involve changing particles' identities.  $\beta$  decays are mediated by the weak interaction. This involves the transformation of a neutron into a proton (beta-minus decay) or a proton into a neutron (beta-plus decay), with the emission of beta particles (electrons or positrons) and neutrinos.

While moving away from stability, those properties change rapidly, and nuclei become unstable, with shorter and shorter lifetimes. If the lifetime of the nuclei close to stability varies from a few years to a few seconds, the lifetime of the neutron-rich nuclei drops rapidly under the second, and they survive only a few milliseconds approaching the dripline.

### *Isotopes*

Atoms of the same element with different numbers of neutrons in their nuclei are called **isotopes**. Isotopes have the same atomic number ( $Z$ ) but different mass numbers ( $A$ ). Some isotopes are stable, while others are radioactive and undergo decay over time.

Isotopes with unstable nuclei undergo radioactive decay to reach a more stable configuration. This process may involve, for example, the emission of alpha particles, beta particles, gamma rays emission and spontaneous fission.

### *Spin and Isospin*

Spin and isospin are fundamental quantum properties that govern the behavior and interactions of nucleons (protons and neutrons) within atomic nuclei.

**Spin** is an intrinsic form of angular momentum associated with elementary particles like protons and neutrons. Unlike classical angular momentum, spin is a fundamental quantum property that does not arise from physical rotation. The spin of a nucleon is quantized, with a spin quantum number  $s = \frac{1}{2}$ , leading to two possible spin states:

$$m_s = +\frac{1}{2} \quad (\text{spin-up}), \quad m_s = -\frac{1}{2} \quad (\text{spin-down}). \quad (1.5)$$

Spin is mathematically represented by operators corresponding to its components along different axes, denoted by  $S_x$ ,  $S_y$ , and  $S_z$ . The spin state of a particle is often described using spinors. The spin of nucleons plays a critical role in nuclear interactions, particularly through mechanisms like spin-orbit coupling and the tensor force, both of which are sensitive to the relative orientation of the spins of interacting nucleons. The tensor force is particularly important in nucleon pairs where the spins are not aligned, such as in the case of the deuteron (a bound state of a proton and a neutron).

**Isospin** (or isotopic spin) is a quantum number introduced to describe the near-identical behavior of protons and neutrons under the strong nuclear force. Isospin is mathematically analogous to spin but applies to the proton-neutron system. Protons and neutrons are treated as two states of a single particle, the nucleon, with an isospin quantum number  $T = \frac{1}{2}$ . The third component of isospin,  $T_3$ , takes on values of  $+\frac{1}{2}$  for protons and  $-\frac{1}{2}$  for neutrons.

In a system of two nucleons, the possible isospin states include:

- The **isospin triplet** with  $T = 1$ , which includes the proton-proton ( $pp$ ), neutron-neutron ( $nn$ ), and symmetric proton-neutron ( $pn$ ) states.
- The **isospin singlet** with  $T = 0$ , which is an antisymmetric proton-neutron ( $pn$ ) state.

The interplay between spin and isospin is crucial for understanding the structure, stability, and interactions within atomic nuclei. These quantum properties help explain the arrangement of nucleons, the forces that bind them, and the outcomes of nuclear reactions and decays.

## 1.1 Nuclear models

The investigation of the atomic nucleus and its components has been a central area of nuclear physics since the neutron's discovery in 1932 [6]. A primary objective in this field is to comprehend the nucleon-nucleon ( $NN$ ) interaction and its role in determining the characteristics of atomic nuclei. Despite significant progress in Nuclear Physics over the past century, a comprehensive nuclear theory based on fundamental principles remains elusive. The nucleus, a complex quantum system, consists primarily of two types of fermions whose interactions are not fully understood. According to the Standard Model, nucleons themselves are composite systems of quarks and gluons. This intricate many-body problem poses a challenge to quantum chromodynamics, the theory governing strong interactions that underlie nuclear forces.

Nuclear models are theoretical frameworks used to describe the structure and behaviour of atomic nuclei. These models are essential tools in nuclear physics, each offering different perspectives on nuclear structure and behaviour. In 1935, Yukawa proposed a theory of strong interaction to explain the cohesion of the atomic nucleus. He suggested that a virtual particle, later known as a meson, mediated a force between nucleons [7]. This force accounted for the stability of nuclei against Coulomb repulsion and described the attractive strong interaction with a shorter range than the electromagnetic repulsion between protons. Thus, a stable nucleus can be considered a compact, dense assembly of nucleons held together by a strong nuclear force. The motion of nucleons within a nucleus can be described by solving the  $A$ -body Schrodinger equation:

$$H |\Psi\rangle = E |\Psi\rangle; \quad (1.6)$$

where  $|\Psi\rangle$  represents the nuclear wave function and the Hamiltonian is given by:

$$\hat{H} = \hat{T} + \sum_{i \leq j}^A V_{NN}(i, j) + \sum_{i \leq j \leq k}^A V_{3N}(i, j, k) + \dots; \quad (1.7)$$

where  $\hat{T}$  is the kinetic energy, and  $V_{NN}$  and  $V_{3N}$  represent the two-nucleon and three-nucleon potentials, respectively. Solving even the nonrelativistic Schrödinger equation for this Hamiltonian was initially a formidable challenge. Analytical solutions for the dynamics of such systems, starting from individual particle interactions, are generally unattainable. Instead, numerical methods like Quantum Monte Carlo are employed, but they are computationally intensive and limited to a few interacting particles[8; 9; 10]. Therefore, effective models were developed to describe the nucleus and interpret the extensive experimental data. In order to distinguish between the various nuclear models, it is useful to introduce the concept of *resolution scale*, a theoretical concept setting the level of details that characterise a given description<sup>1</sup>. At different resolution scales, different pictures of the nucleus emerge:

1. **High scale resolution:** At high resolution, the system is examined at small length scales (or high energy scales). In this regime, details of the interactions, such as high-momentum components, are significant. The Hamiltonian describing the system includes these fine details. The "hard" Hamiltonian incorporates high-momentum components into low-energy states, reflecting the presence of short-range correlations (SRCs). We link, for example, the high-resolution description with the Generalised Contact Formalism (GCF) model [11];

---

<sup>1</sup>The resolution scale is determined by a limiting wavelength, which is set not by external kinematics but is internal to the theory. This scale dictates the minimum wavelength or maximum momentum available for the wave functions of low energy states (and the nuclear ground states in particular).

2. **Low scale resolution:** At low resolution, the system is examined at large length scales (or low energy scales). In this regime, the description of the system is coarser, and fine details are averaged out or integrated into effective parameters. One thus employs a "soft" Hamiltonian where the ground-state wave function approaches the mean-field limit, with momenta predominantly below the Fermi momentum  $k_F$ . We link, for example, the low-resolution description with the shell model (configuration interaction), whether in its empirical form or as derived from *ab initio* methods such as coupled cluster or in-medium similarity Renormalisation Group [11]. In this scenario, nucleon momentum distributions sharply decrease beyond  $k_F$  [11].

To aid visualization, Fig. 1.2 illustrates conceptual representations of these resolutions. These visualizations provide qualitative insights into interpreting experimental data. Fig. 1.2 shows the potential configurations sampled at varying resolutions, highlighting that high resolution uniquely reveals the presence of high-momentum pairs. Theoretically, the resolution scale can be smoothly varied using Renormalisation Group (RG) techniques<sup>2</sup> [12].

Using the RG approach allows us to pass between these different resolutions to match the appropriate level of detail to the physical phenomena under study, allowing for a more comprehensive understanding of nuclear structure and dynamics. It's important to note that both descriptions, along with a spectrum of intermediate RG resolutions, can be applied to analyze the same experimental data.

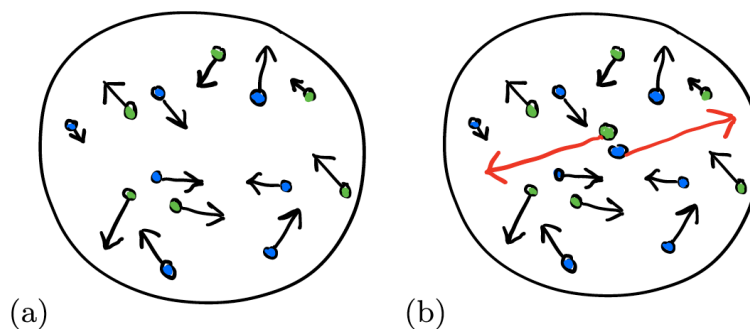


Figure 1.2: Figures (a) and (b) provide cartoon representations of a nucleus at different RG resolutions. At low-RG resolution (a), the nucleus appears in a mean-field configuration. Contrastingly, at high-RG resolution (b), the illustration depicts a pair of nucleons exhibiting short-range correlations characterized by a small center-of-mass momentum. Figure taken from [11].

In the following, I will present the Independent Particle models (IPM) as an example of a low-resolution RG description of the nucleus. Historically, the atomic nucleus is described in terms of these IPM due to the complexity of describing the different interactions inside the nucleons in such a dense quantum system. However, some phenomena escape and are not visible in this low-resolution nucleon picture and manifest only in a higher-resolution picture of the nucleus (like SRC physics). I will show how, with increasing RG resolution, the physics will shift from interaction operators (potential/reactions, described by IPM) to wave functions (structure, high nucleon momentum component) with smooth momentum dependence.

<sup>2</sup>The Renormalization Group (RG) is a mathematical framework used to study the changes in a physical system's behaviour as it is observed at different lengths or energy scales.

### 1.1.1 Independent particle model (IPM)

Mean-field theories are fundamental in nuclear physics. They propose that protons and neutrons independently occupy well-defined quantum orbits within a mean-field potential. These theories have been essential in interpreting extensive experimental data and reliably predicting new observations.

The nuclear system is often modelled as a two-component Fermi gas of weakly interacting protons and neutrons confined within a volume characterized by a constant potential  $V_0$  (a rectangular potential well). Nucleons occupy all available energy levels up to the maximum Fermi energy  $E_F$ , allowing qualitative analysis of nuclear systems. Key parameters such as the maximum kinetic energy  $E_F$  and Fermi momentum  $p_F$  of nucleons at the Fermi surface are calculated as:

$$p_f = p_{f,p} = p_{f,n} = \frac{\hbar}{R_0} \left( \frac{9\pi}{8} \right)^{1/3} \approx 250 \text{ MeV}/c; \quad (1.8)$$

$$E_f = \frac{p_f^2}{2M} \approx 33 \text{ MeV}. \quad (1.9)$$

where  $R_0 = 1.21 \text{ fm}$  is an empirical constant, and  $M$  denotes the nucleon mass, assumed equal for neutrons and protons. Assuming a nearly constant binding energy per nucleon  $B/A \approx 7 - 8 \text{ MeV}$  above the Fermi level  $E_f$ , the average depth  $V_0$  of the potential well is estimated as:

$$V_0 = E_f + \frac{B}{A} \approx 40 \text{ MeV}. \quad (1.10)$$

Refining single-particle states involves solving the Schrödinger equation for  $N$  nucleons within a Spherical Harmonic Oscillator (SHO) potential  $V(r) = \frac{1}{2}M\omega^2r^2$ , where  $\omega$  is the oscillator frequency. The resulting single-particle levels correspond to specific oscillator shells defined by quantum numbers such as orbital angular momentum and parity. Despite its simplicity, the SHO potential remains useful for qualitative estimates, including the calculation of energy gaps between neighbouring oscillator shells, approximating:

$$\hbar\omega \approx 40A^{-\frac{1}{3}} \text{ MeV}. \quad (1.11)$$

Due to the short-range nuclear forces, the mean-field potential's radial dependence mirrors the nuclear density. Initially approximated by a rectangular or harmonic oscillator potential (as in the Fermi gas model [13]), this can later be refined using the Woods-Saxon potential to incorporate nuclear surface effects [13]. In general form, the resulting shell potential  $V_s(r)$  is expressed as:

$$V_s(r) = V(r) + V_{ls}. \quad (1.12)$$

Significant advancements in nuclear shell modelling were achieved by Maria Goeppert-Mayer and J. Hans D. Jensen [14; 15], who introduced a strong spin-orbit interaction  $V_{ls} = U(r)\vec{l} \cdot \vec{s}$  to the spherically symmetric mean-field potential  $V(r)$ . This modification lifts the degeneracy of energy states with different spin projections on orbital momentum  $l$ :  $j = l \pm 1/2$ , naturally accounting for population numbers in primary shells (see Fig. 1.3). Further improvements include nuclear shape deformation and residual interactions, which influence states above the Fermi level.

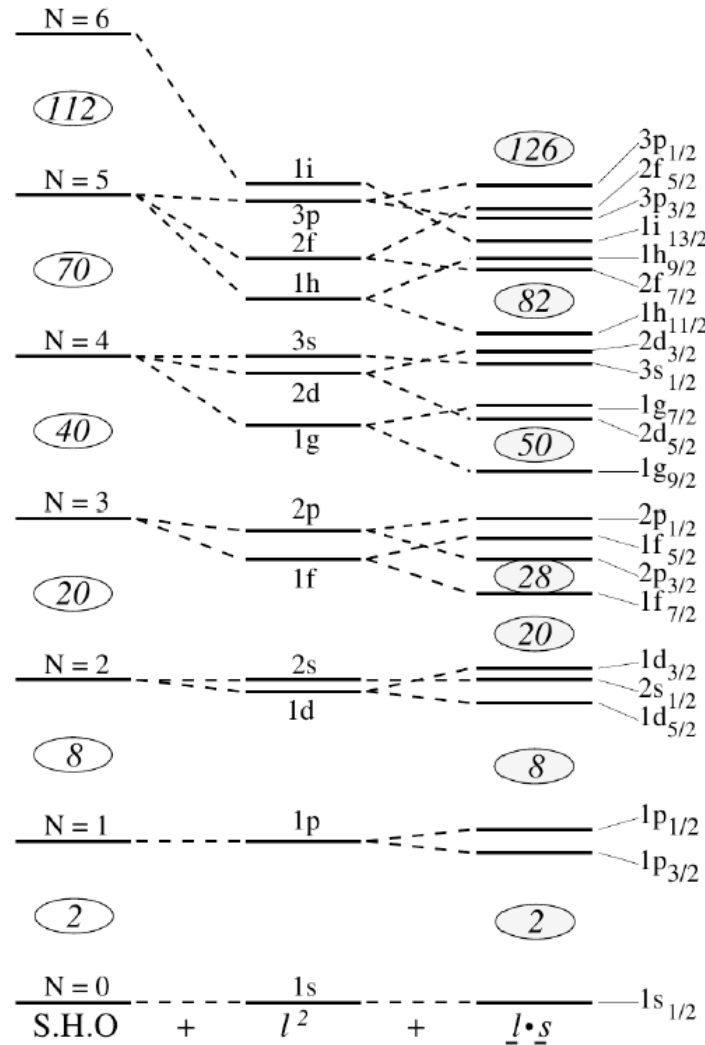


Figure 1.3: Schematic illustration of the nuclear shell model. The left-hand side shows energy levels of the Spherical Harmonic Oscillator with  $N$  indicating the number of oscillating quanta, and the numbers inside ellipses denote the maximum number of nucleons populating all underlying states. On the right, the level scheme represents the shell potential, including an additional spin-orbit interaction. The degeneracy of states with different spin-orbital projections is lifted, resulting in the rearrangement of single-particle states and the appearance of "magic" numbers. Adapted from [16].

Experimental validation of the shell model's accuracy highlights "magic" numbers of neutrons and protons (e.g.,  $N$  or  $Z = 2, 8, 20, 28, 50, 82$ , and  $N = 126$ ), indicative of closed main shells. These nuclei exhibit rigidity against weak excitations and nucleon separation, confirmed by polarization effects in nucleon-nucleus collisions, energy spectra of low-lying excited states in magic nuclei, and internal momentum distributions from quasi-free scattering reactions induced by electrons and protons.

Modern Nuclear Physics explores modifications to nuclear shell structure, especially in neutron- and proton-rich environments where experimental data is limited. Advances in nuclear models have refined and expanded traditional magic numbers. The introduction of the Skyrme-Hartree-Fock model and relativistic mean field models has provided deeper insights into how magic numbers might shift or change with varying nuclear conditions [17].

Research has expanded to investigate magic numbers in neutron-rich and proton-rich nuclei. This includes the study of neutron skins and proton halos, which have led to the identification of new magic numbers and the re-evaluation of the stability of nuclei far from the valley of stability [18; 19]. New collective excitation modes have been identified as researchers probe beyond the traditional shell model. These include modes related to vibrational and rotational properties of nuclei, which can influence or interact with magic numbers [20; 21]. Magic number quenching [22] was also studied in heavy and exotic nuclei. This can affect both neutron-rich and proton-rich regions [23].

Theoretical innovations have extended beyond the simple shell model to include collective models and *ab initio* calculations. These approaches have provided new insights into the nuclear structure and the conditions under which magic numbers can be modified, or new ones can appear [24].

The independent particle model allows us to reduce the nuclear many-body problem from a complicated two-body treatment to a much simpler one-body one. It also relies on the use of single-particle potentials. The independent particle model corresponds to a low-resolution RG description of a nucleus in terms of non-interacting particles in the orbitals of these single-particle potentials, which themselves are produced by all the nucleons. Thus, nucleons move essentially freely in these potentials. In this model, the ground state is formed by filling all the single-particle states located below the Fermi level. The excitation of the particle from an occupied state below this level to an empty one above it leads to an excited state. This process is called a particle-hole excitation.

The single-particle model's success in explaining many aspects of nuclear structure has led to its widespread adoption and application in various areas of nuclear physics, including nuclear spectroscopy, nuclear reactions, and nuclear astrophysics.

### 1.1.2 The N-N interaction

The atomic nucleus consists of strongly interacting nucleons forming a dense quantum system. It is noteworthy that for such a strongly interacting quantum system, the independent-particle model is proven to be a valid approximation and has provided the framework to explain many nuclear properties. This model successfully predicts many bulk properties of nuclei, such as spins, parities, ground-state energies, excitation spectra, and others. From predicting the properties of exotic nuclei to elucidating the mechanisms of nuclear reactions, single-particle models continue to play a central role in advancing our understanding of the atomic nucleus. However, nucleon-nucleon ( $NN$ ) correlations, including long-range (LRC) and short-range correlations (SRC), modify this mean-field approach and modify the pure independent-particle picture [25; 26; 27]. Studies reveal that in stable nuclei, typically only 60% – 70% of states below the Fermi momentum are occupied, with 30% – 40% of nucleons involved in LRC and SRC configurations [28; 29]. Thus, both LRC and SRC significantly reduce the occupation of single-particle states, with LRC primarily affecting states near the nuclear Fermi momentum and SRC populating states well above it.

#### Long Range Correlations (LRC)

Long-range correlations in nuclear physics arise from collective effects and coherent motion of nucleons within the nucleus, leading to spatial correlations that extend beyond the typical range of nuclear forces. Unlike short-range correlations, which are characterized by strong interactions between nucleons confined to small regions within the nucleus, long-range correlations manifest as correlations between nucleons with an interaction distance of the order of several fm, and they often involve many-body collective modes and collective excitations.

One of the most prominent manifestations of long-range correlations in nuclear physics is the phenomenon of nuclear deformation [30]. Nuclei are not static, rigid bodies but rather exhibit dynamic deformations akin to a vibrating or rotating liquid drop. These deformations arise from the collective motion of nucleons, driven by the interplay between the nuclear force and the Coulomb repulsion between protons. The resulting long-range correlations give rise to characteristic shapes and structures in nuclei, such as quadrupole deformations (prolate or oblate) and octupole deformations (pear shape), as it is possible to observe in Fig.1.4.

Another important aspect of long-range correlations is their role in nuclear collective excitations, such as giant resonances and collective nuclear vibrations. These excitations involve the coordinated motion of large numbers of nucleons, leading to oscillations in nuclear density and shape. Examples include the isoscalar giant monopole resonance, which corresponds to compression and expansion of the entire nucleus, and the isovector giant dipole resonance, which involves collective oscillations of protons against neutrons.

Long-range correlations also play a crucial role in nuclear reactions and scattering processes, influencing the cross-sections and angular distributions of scattered particles. For instance, in elastic scattering experiments, long-range correlations can lead to diffraction patterns and angular distributions that deviate from simple geometric predictions, reflecting the underlying nuclear structure and dynamics [31].

Understanding and quantifying long-range correlations in nuclear physics presents significant challenges, both theoretical and experimental. Theoretical models, such as mean-field approaches and collective models, provide valuable insights into the mechanisms driving long-range correlations and their manifestations in nuclear properties.

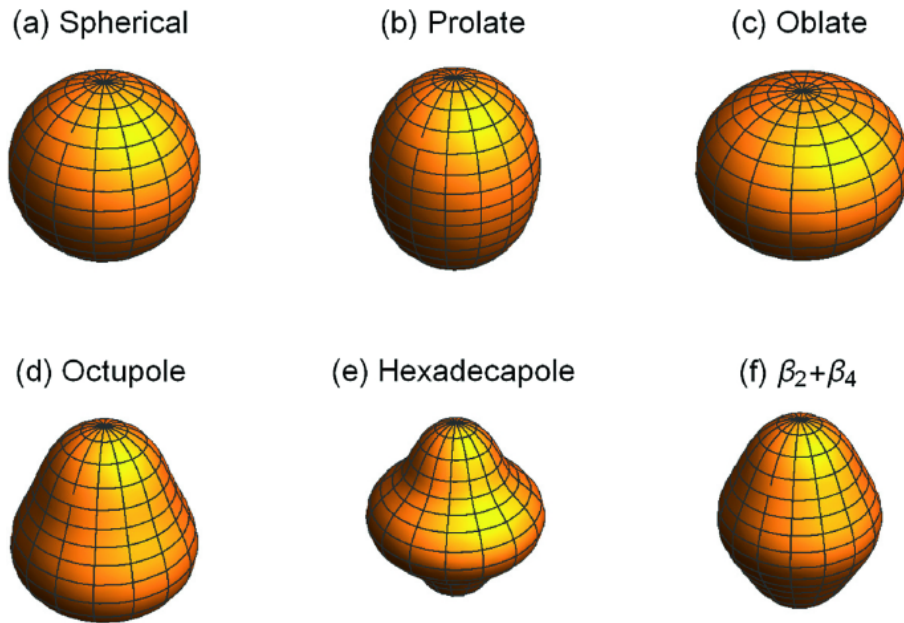


Figure 1.4: Some typical axially symmetric nuclear shapes. The shapes shown are: (a) spherical; (b) prolate spheroid; (c) oblate spheroid; (d) octupole; (e) hexadecapole; (f) quadrupole plus hexadecapole. The Figure is generated using MATHEMATICA.

### Short Range Correlations (SRC)

Since the 1950s, two prominent models of nuclear structure have been developed and applied [32]. The first is the shell model by Goeppert Mayer and Jensen, describing independent particles in a mean-field. This was refined into the collective model by Bohr and Mottelson, which unified single-particle and collective degrees of freedom in nuclei [13; 31]. These low-resolution RG models did not account for high-momentum nucleons. However, in 1995, Brueckner et al. [33], in contrast with the IPM, rejected this low-resolution picture by demonstrating that high-energy reaction cross-sections indicate significant nucleon momentum tails (see Fig. 1.6), leading to the concept of short-range correlations in nuclear physics. They explained that SRCs arise from the strong short-range repulsion in the nucleon-nucleon (NN) interaction, evidenced by the NN S-wave phase shifts turning negative at high energies (see Fig. 1.5). This provided a picture of the nuclear wave function with pairs of nucleons having large relative momentum but a center-of-mass momentum around the Fermi momentum. This is when SRC was born.

SRC physics involves short-distance interactions that manifest at high RG resolution as nucleon pairs with high relative momentum. At low RG resolution, these pairs are suppressed. The SRC regime traditionally begins where the tensor force dominates the nucleon-nucleon (NN) interaction, which occurs around  $2 \text{ fm}^{-1} \approx 400 \text{ MeV}$  or slightly lower. The center-of-mass momentum distributions of SRC pairs have a width comparable to the Fermi momentum. In this context, one can develop a theoretical description exploiting the scale separation of the two regimes [34]. In particular, one can assume a factorization of the nuclear wave-function into a short-range (SR) part, encoding SRC between nucleon pairs, and a long-range (LR) part, describing the mean field properties of the remaining  $A - 2$  nucleons. Starting from this assumption, the Generalised Contact Formalism (GCF) is the model adopted in this analysis to interpret our SRC physics results.

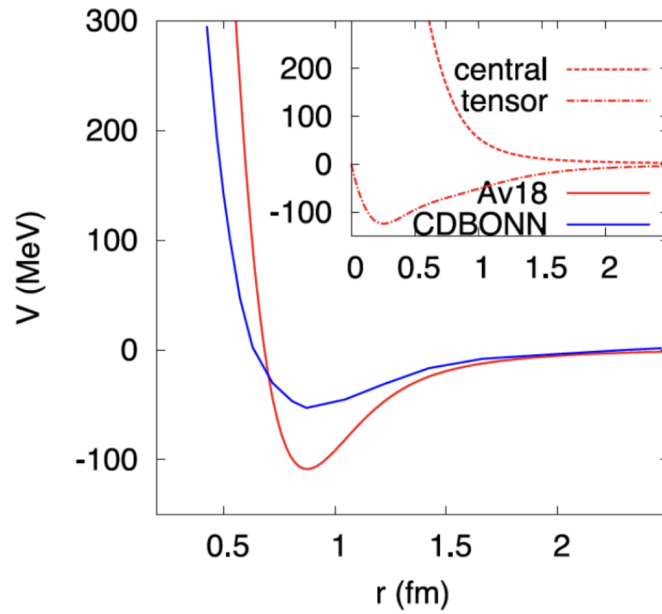


Figure 1.5: The Av18 and CDBONN NN potentials in the  $^1S_0$  channel are depicted. The inset shows the central and tensor parts of the Av18 potential.

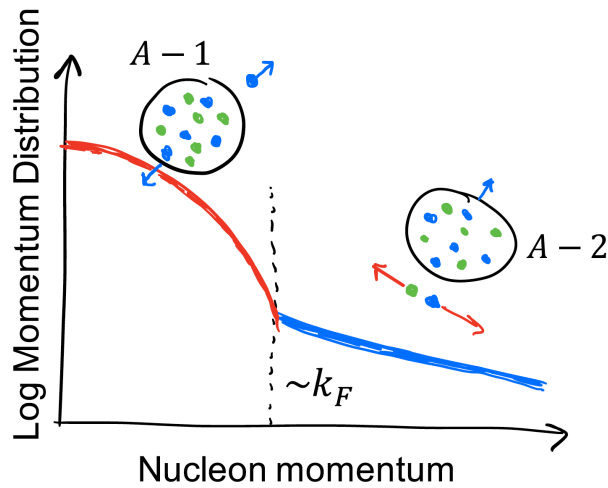


Figure 1.6: Diagram illustrating the momentum distribution of nuclear single particles at high-resolution scale. Below  $k_F$ , there is a Fermi sea of nucleons. Above  $k_F$ , the distribution is primarily influenced by SRC pairs, characterized by center-of-mass momenta approximately equal to  $k_F$ . At lower resolution, the contribution from the upper branch is significantly reduced. Figure taken from [11]

The Generalized Contact Formalism (GCF) model adopts a factorization assumption for the many-body wave function of the nucleus in high-momentum transfer processes [35]. As anticipated before, in this work, we will use the GCF model as a phenomenological theoretical framework to investigate and understand SRC physics. The GCF model represented visually in Fig. 1.2(b), considers the nuclear wave function relevant for SRC events as a product consisting of a short-distance component multiplied by a mean-field component. In the following, I will give an overview of the GCF theoretical framework. In particular, I will focus on the nuclear description of GCF applied to SRC physics.

### 1.1.3 Generalized Contact Formalism: Theoretical framework for SRC investigation

The contact formalism is a relatively recent method for examining short-range correlations in quantum systems. It was shown that if the interaction range  $r_0$  is much shorter than the average interparticle distance  $d$ , and the scattering length  $a_s$ <sup>3</sup> is large, a contact theory can be used to describe the system [37; 38; 39]. A series of relations between different observables and the probability of finding a particle pair in close proximity emerge within this description. The contact theory has been studied in great detail theoretically and validated experimentally for ultra-cold Fermi gases [11; 34; 37; 38; 39]. The original contact theory was formulated for systems with significant scale separation. This concept was initially introduced by Shina Tan [37; 38] to describe non-interacting Fermi gas with a contact interaction between the two components (“spin states”) characterized by a nonzero interaction condition. For non-interacting Fermi gas, assuming a factorization of the nuclear wave-function into a Short Range (SR) part, encoding SRC between nucleon pairs, and a Long Range (LR) part, describing the mean field properties of the remaining  $A-2$  nucleons, it was possible to reach a factorized asymptotic wave-function of the form [40]:

$$\Psi \xrightarrow{r_{ij} \rightarrow 0} \phi(r_{ij})A_{ij}(R_{ij}, \{r_k \mid k \neq ij\}). \quad (1.14)$$

where  $\phi(r_{ij})$  is an asymptotic two-body wave function, and  $A_{ij}$  is a function of the residual  $A-2$  particle system. Scale separation allows for the replacement of short-range interactions with a boundary condition, ignoring all partial waves apart from s-waves. In the momentum space, this factorized wave function leads to a high momentum tail that is given by:  $n(k) \rightarrow \frac{C}{k^4}$ , where  $C = 16\pi^2 \langle \phi_{ij} A_{ij} | A_{ij} \rangle$  is known as the *contact* [34]. This approach connected various properties of the system to a single contact parameter. This formalism has since been adapted and applied to nuclear systems. However, unlike systems that obey the zero-range condition, nuclear systems require modifications, including the consideration of contributions from all partial waves (sum on all nucleon-nucleon channels  $\alpha$ ) [34]. Consequently, new nuclear contact matrices and the effects of different partial waves must be taken into account to accurately describe nuclear systems, giving rise to the Generalised Contact Formalism (GCF) [34].

---

<sup>3</sup>The scattering length is a measure of how the wavefunction of a particle scattering off a potential deviates from a free particle at low energy. In terms of the scattering amplitude  $f(k)$  for low-energy scattering, where  $k$  is the wave number, the scattering length  $a_s$  is defined by the asymptotic form of the scattering amplitude:

$$f(k) \approx -\frac{a_s}{k} + (\text{higher order terms}). \quad (1.13)$$

Here,  $k$  is the momentum of the incoming particle, and  $a_s$  is the scattering length. The scattering length for proton-neutron pairs is generally found to be positive and is approximately 5.4 fm. The scattering length for proton-proton pairs is negative and approximately -7.8 fm [25; 36].

Considering these corrections, the factorized asymptotic wave-function takes the form [41]:

$$\Psi \xrightarrow{r_{ij} \rightarrow 0} \sum_{\alpha} \phi_{\alpha}(r_{ij}) A_{ij}^{\alpha}(R_{ij}, \{r_k \mid k \neq ij\}). \quad (1.15)$$

where the index  $ij$  corresponds to  $pn$ ,  $pp$ , and  $nn$  pairs [34]. In this representation, the nuclear wave function for SRC physics events is represented as a product of a short-distance piece ( $\phi_{\alpha}(r_{ij})$ ) that multiplies a mean-field piece related to the  $A - 2$  particle system ( $A_{ij}^{\alpha}(R_{ij})$ ). Considering only the main channels contributing to Short-Range Correlations (SRCs), namely, the  $pn$ -deuteron channel ( $\ell = 0, 2$  and  $s = 1$  coupled to  $j = 1$ ) and the singlet  $pp$ ,  $pn$ , and  $nn$   $s$ -wave channels ( $\ell = s = j = 0$ ), it is possible to derive the distribution of pair momenta in coordinate and momentum space (meaning the probability to find two nucleons within a distance  $r$  or having a relative momentum  $k$ ). These quantities take the factorized form of [11]:

$$\rho_A^{\text{GCF},\alpha}(r) = C_A^{NN,\alpha} |\varphi_{NN}(r)|^2, \quad (1.16)$$

$$n_A^{\text{GCF},\alpha}(k) = C_A^{NN,\alpha} |\varphi_{NN}(k)|^2; \quad (1.17)$$

where  $A$  is the nucleon number (protons plus neutrons) and  $\alpha$  is a spin index. The common coefficient ( $C_A^{NN,\alpha}$ ) is called a *contact* in analogy to the quantity defined previously related to cold atom physics [40], and it determines the number of pairs in a given two-body channel. The two-body functions are extracted from the short-distance (high-momentum) dependence of the zero-energy solutions to the Schrödinger equation for a given NN ( $nn$ ,  $np$ ,  $nn$ ,  $pp$ ) interaction. Given the probabilities to find two nucleons within a distance  $r$  or having a relative momentum  $k$  displayed in Eq. 1.16 and Eq. 1.17, it is possible to derive a formulation of the GCF cross-section, as shown in [35]. Without entering into details, the nucleon-knockout cross-section for the  $A(e, e'N)$  reaction, which involves high momentum transfer and quasielastic short-range correlation (SRC) breakup, can be modelled using a factorized plane wave impulse approximation (PWIA)<sup>4</sup> [35]:

$$\frac{d^6\sigma}{d\Omega_{k'} dE'_k d\Omega_{p'_1} dE'_1} = p'_1 E'_1 \sigma_{eN} S_A(p_1, E_1). \quad (1.18)$$

where  $(\Omega_{p'}, E'_p)$  is the scattered electron four-momentum,  $\sigma_{eN}$  is the off-shell electron-nucleon cross-section [42], and  $S_A(p_1, E_1)$  is the nuclear spectral function for nucleus  $A$ , which defines the probability of finding a nucleon in the nucleus with momentum  $p_1$  and energy  $E_1$ . Replacing the  $S_A(p_1, E_1)$  nuclear spectral functions with the probabilities in Eq. 1.16 and Eq. 1.17, the  $A(e, e'pN)$  cross-section can be expressed as:

$$\frac{d^8\sigma}{d\Omega_{p'} d^3p_{\text{CM}} dk_{\text{rel}} d\Omega_{\text{rel}}} = \frac{\sigma_{eN}}{32\pi^4} \frac{k_{\text{rel}}^2}{\left|1 - \frac{\vec{k}'_1 \cdot \vec{p}'_1}{E'_1 E'_p}\right|} \sum_{\alpha} C_{NN}^{\alpha} |\tilde{\varphi}_{NN}^{\alpha}(\vec{k}_{\text{rel}})|^2 n_{NN}^{\alpha}(\vec{k}_{\text{CM}}). \quad (1.19)$$

The cross-section requires several input parameters. Their values have been determined by previous electron scattering experiments. To compare with experimental data, the cross-section expression of the Eq. 1.19 is used to produce a weighted Monte Carlo event generator. The generated events are processed analogously to the experimental data and compared with our SRC final data.

We saw that GCF provides a systematic approach to describe these correlations by extending the concept of the nuclear wave function to include two-body correlations beyond mean-field approximations. It incorporates the effects of both short-range and tensor part of the NN interaction, which are crucial for accurately modelling nucleon distributions and momentum

<sup>4</sup>This formulation of the GCF cross-section is called "Instant Form Formulation".

distributions within nuclei.

Utilizing GCF, we can predict and interpret experimental observables related to SRC, such as high-momentum tail distributions in nucleon momentum spectra and SRC pair ratios. The framework allows for a comprehensive understanding of how nucleon-nucleon interactions at short distances impact nuclear structure, dynamics and reaction mechanisms.

We already saw that at high-resolution RG, short-range correlations appear as parts of the nuclear wave function with relative pair momenta exceeding the Fermi momentum. This scale separation allows for wave-function factorization, which can be utilized with phenomenology like the generalized contact formalism presented above. When evolved to lower resolutions, the SRC physics transitions from nuclear structure to reaction operators, keeping the measured observables unchanged. However, low-resolution RG pictures (e.g. mean field) do not feature explicit short-range structure in the nuclear wave function. Nevertheless, it is possible to demonstrate how the characteristics of SRC phenomenology seen at high RG resolution can be recognized at low RG resolution using the RG properties [11].

#### 1.1.4 Consistency of IPM and SRC pictures

Understanding short-range correlations is essential for comprehensively describing nuclear structure and dynamics, as they play a crucial role in shaping the properties of nuclei and their responses to external probes such as electron or hadron scattering experiments. These correlations also have significant implications for our understanding of the nuclear equation of state, nucleon-nucleon interactions, and the structure of neutron-rich nuclei, among other areas of nuclear physics research.

Measured cross sections in a different series of experiments at high energy have long highlighted the need for short-range correlations in the description of the atomic nucleus [33]. Recent experiments have effectively isolated this physics [43; 44; 45; 46; 47], yet integrating SRC phenomenologies with existing nuclear structure models, such as the shell model, remains a challenge due to their differing theoretical frameworks. In fact, mean-field models in their phenomenological form or derived from *ab initio* methods traditionally do not incorporate explicit short-range structures in their wave functions (low-resolution RG).

In [11], Tropiano et al. show that the application of the renormalization group can help resolve this conflict. The RG approach reveals how short-range correlation physics manifests across different resolution scales in nuclei. This framework can effectively connect low- and high-resolution analyses of the same experiments, offering insights into the implications of SRC physics and addressing persistent discrepancies between theoretical predictions and experimental observations.

As mentioned in [11], the apparent success of interpreting SRC pairs by the Generalized Contact Formalism might suggest that the high-resolution RG perspective is definitive. However, these observations can also be explained by an alternative scenario where the Hamiltonian operates at low RG resolution, characterized by a softer interaction. Here, a virtual photon probe interacts not with a single nucleon involved in an SRC pair but rather with two nucleons within the Fermi sea (referred to as a two-body current). All relevant observables can be similarly reproduced in this alternative framework, often with simpler calculations. It looks like different interpretations arise from the same event among different observers. The renormalization group framework elucidates how these interpretations can coexist and transition continuously between each other to describe nuclear phenomena.

Without going into detail, Tropicano et al. showed that SRC physics naturally emerges from a low-resolution perspective from the unitary transformation operator evaluated in a few-body space and that the renormalization group framework explains that both hard and soft descriptions are valid representations of nature, forming a continuum of perspectives. Consistency in treating both nuclear structure and reactions ensures that these descriptions accurately describe nuclear phenomena.[11].

## 1.2 State of the art on Short Range Correlations

We already saw before that SRC pairs can be interpreted as two-body components of the nuclear wave function with high relative momentum and low center of mass (c.m.) momentum with respect to the Fermi momentum  $k_F = 250$  MeV/c [44; 48]. The effect of SRC results in the population of high-momentum states with  $k > k_F$ , beyond what is expected for a free Fermi gas (FFG) as illustrated in Fig.1.7 (left). SRC nucleon-nucleon pairs are formed as temporary high-density fluctuations with 2-5 times the nuclear saturation density, limited by the nucleon-nucleon (NN) interaction that becomes highly repulsive for NN distances smaller than about 1 fm [49] (Fig. 1.7, right). Theory [50; 51; 52] and experiments [53; 54] agree that about 20% of bound nucleons are found in this high-momentum region, corresponding to a significant fraction of the kinetic energy of the nucleus (50% - 60% for symmetric nuclear matter[52]). The momentum distribution of protons in nuclei was first observed to have a high-momentum tail extending beyond  $k_F$  in electron scattering experiments (see Fig.1.8). This provided the first experimental indication of short-range correlations.

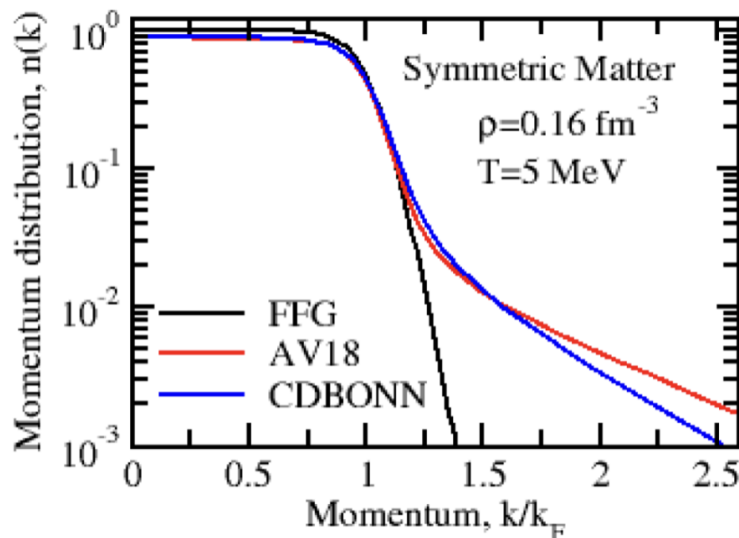


Figure 1.7: The left Figure compares the correlated momentum distributions of symmetric nuclear matter from Av18 [9] and CDBONN<sup>5</sup> [55] interactions to the free Fermi gas (FFG) [56]. It is adapted from [52]. On the right, the Av18 and CDBONN NN potentials in the  $^1S_0$  channel are depicted. The inset shows the central and tensor parts of the Av18 potential.

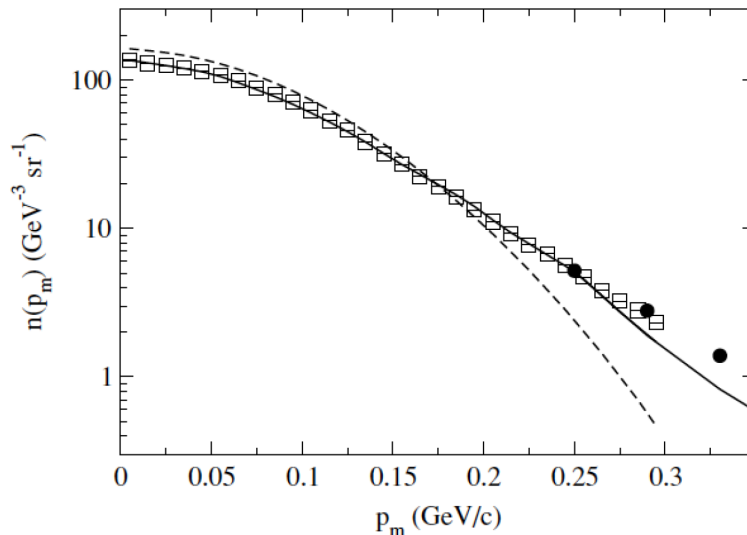


Figure 1.8: The comparison of the experimental momentum distribution from electron scattering on  $^{12}\text{C}$  (markers) to the momentum distribution calculated within the independent particle model (dashed line) and the Correlated Basis Function theory (solid line) [50]. This Figure is adapted from Ref. [57].

### 1.2.1 Electron scattering experiments

Electron scattering, particularly quasi-elastic scattering, is typically described by well-understood electromagnetic interactions. When electrons scatter off nucleons, the primary interaction occurs through the exchange of a virtual photon. One key advantage of electron scattering is that the final-state interactions (FSI) between the scattered electron and the rest of the nucleus are relatively small. The scattered electron interacts only once via the virtual photon, and after the scattering event, the interaction with the rest of the nuclear medium is minimal. This reduces the complexity of interpreting the data and allows for a clearer extraction of the properties of SRC pairs. In electron scattering, the high-momentum tail of the nucleon momentum distribution, which is dominated by SRC pairs, can be measured with relatively little distortion. This makes electron scattering a "clean" probe of SRC, providing direct access to the high-momentum components of nucleons involved in SRC.

Most of the knowledge we have to date about SRC comes from proton and, mainly, electron-induced quasi-free scattering (QFS) experiments in large-momentum transfer kinematics [37; 44; 54]. These measurements showed, for example, that the high-momentum tail of the nuclear momentum distribution is dominated by SRC in the form of  $np$  pairs [43] and that neutron-proton pairs are about 20 times more abundant than isospin-like pairs [43; 53; 54] due to the tensor part of the NN interaction, which is dominant for NN distances of about 1 fm (Fig.1.9). Electron-induced QFS has allowed the probing of the momentum dependence of the isospin composition of the SRC pairs. It was shown that the neutron-proton dominance decreases with increasing momentum, corresponding to the transition from the tensor to the central force-dominated region (see Fig. 1.5) [46; 49]. The study of the isospin composition of pairs in a large variety of stable nuclei, with different masses and therefore different proton/neutron ratios, has allowed to establish that the neutron-proton and proton-proton pair fractions remain unchanged (see Fig. 1.10)[43; 45; 47], with important consequences for asymmetric nuclei. Even in stable heavy nuclei with  $N > Z$ , it implies that the fraction of high-momentum protons, i.e., the minority species in asymmetric nuclei, increases by a factor of 1.6 with respect to  $N = Z$  in  $^{12}\text{C}$  [47; 58]. The dominance of  $T = 0$  isospin content in the high-momentum tail implies that, in  $N/Z$  asymmetric nuclei, the average momentum of the minority species will be higher, and the fraction of high-momentum nucleons of the majority species will saturate.

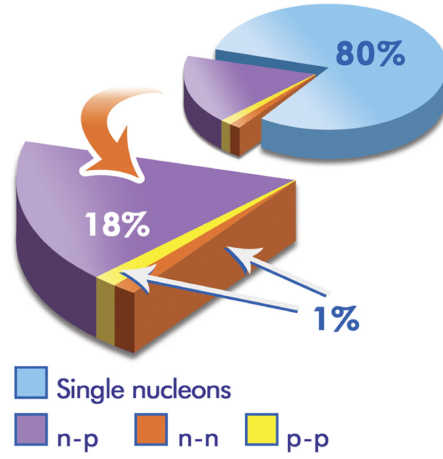


Figure 1.9: An artistic representation of the results obtained from the observations of  $^{12}\text{C}(e, e'pp)$  and  $^{12}\text{C}(e, e'pn)$  reactions (the picture is taken from [53]). It was concluded that about 20% of all nucleons in the ground state of  $^{12}\text{C}$  exist in the form of correlated pairs with a large relative momentum, from which 18% have proton-neutron configuration and only 2% are neutron-neutron and proton-proton pairs.

Since there are the same number of protons and neutrons in the high-momentum part ( $k > k_F$ ) of the momentum distribution, the low-momentum part ( $k < k_F$ ) will be more depleted for the minority species. A study on the momentum dependence of the isospin composition of SRC

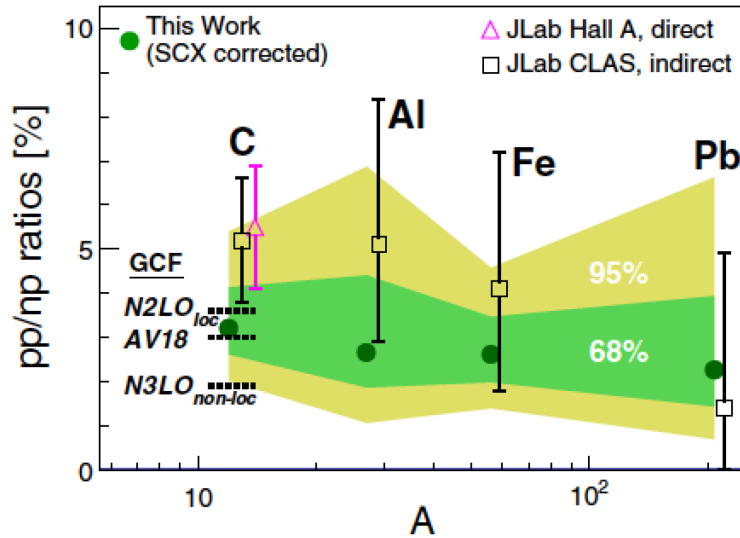


Figure 1.10: The ratios of proton-proton to neutron-proton short-range correlation pairs in stable isotopes are shown as a function of their mass  $A$  [58]. The dashed horizontal lines represent the ratios calculated with the Generalized Contact Formalism for different nucleon-nucleon (NN) potentials.

pairs was reported in Refs. [45; 49] and is shown in Fig. 1.11. An increase in the number of proton-proton pairs for missing momentum greater than 500 MeV/c is observed, which is associated with the transition from a tensor force-dominated regime to a central force-dominated regime.

The Jefferson Lab results from Ref. [47; 59] revealed that in neutron-rich nuclei, the ratio of the fraction of high-to-low-momentum protons increases as a linear function of the ratio of neutron to proton number ( $N/Z$ ), while the equivalent fraction for neutrons is rather constant or possibly decreasing slightly (see Fig. 1.12). This implies that the high-momentum fraction of protons is greater for  $N > Z$  than for  $N = Z$ , so the percentage of protons participating in SRC pairs increases for neutron-rich systems and consequently depletes the proton strength from the region below the Fermi momentum. The SRC interpretation is that excess neutrons correlate with core protons so that protons “speed up” in neutron-rich nuclei. In contrast, the high-momentum fraction of neutrons remains constant.

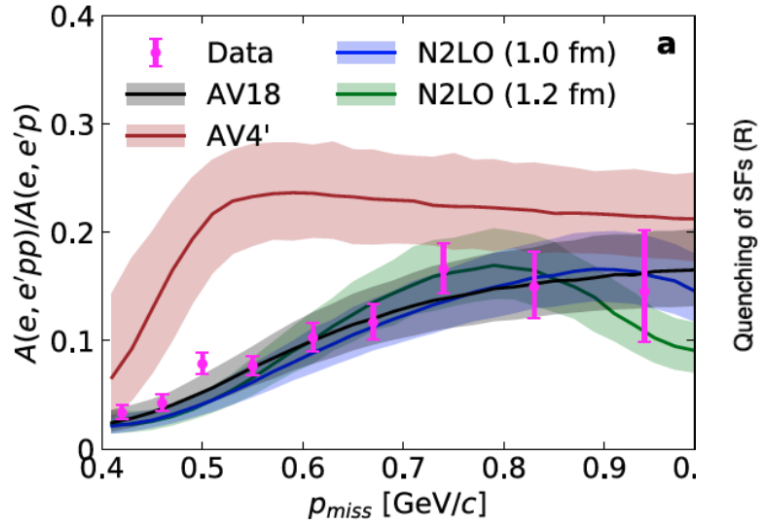


Figure 1.11: The ratio of  $(e, e'0pp)$   $^{12}\text{C}$  and  $(e, e'p)$   $^{12}\text{C}$  events, as a function of missing momentum, is compared with Generalized Contact Formalism calculations using different interactions [49].

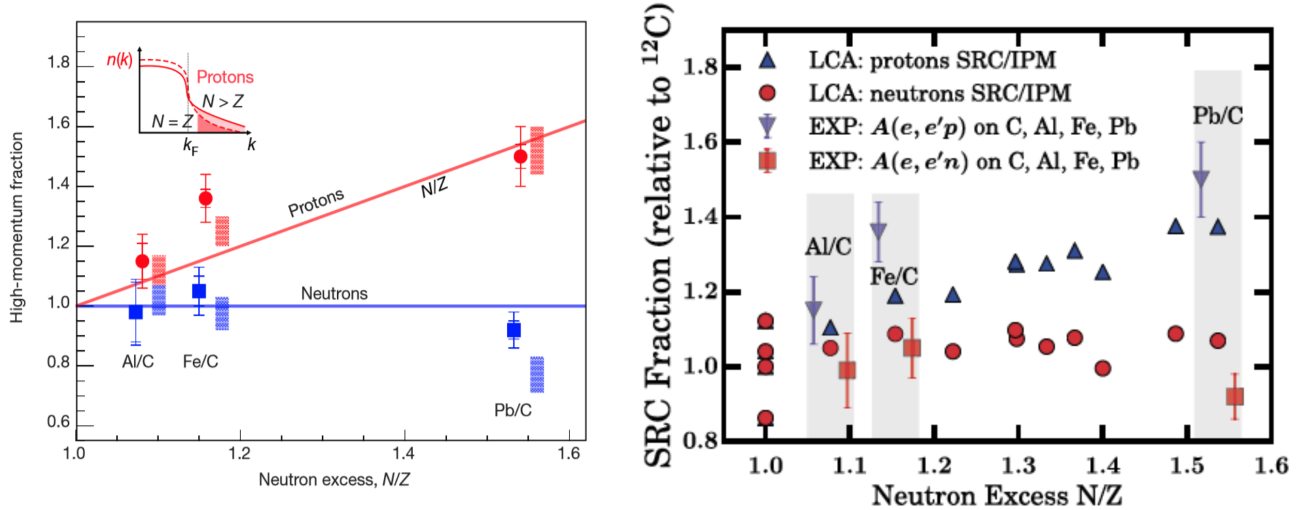


Figure 1.12: Left: double ratio of high-to-low momentum protons (neutrons) in nucleus  $A$  with respect to carbon marked with dots (squares), and corresponding calculations with rectangles [47]. Right: SRC fractions ( $n$  and  $p$ ) relative to  $^{12}\text{C}$  in low-order correlation operator approximation (LCA) [60], compared to data of [47].

The SRC pair itself acts like a mean field nucleon, having low center-of-mass momentum, as shown in an indirect measurement of the pair center-of-mass momentum [61]. The neutron-proton ratio has an important impact on the pair's properties. Previous measurements were conducted only on stable nuclei, although with increasing asymmetry but at the same time with increasing mass going up to Pb. That is not necessarily free of other effects affecting the ratio with  $^{12}\text{C}$ , as increased FSI with nuclear mass  $A$  [62]. Moreover, open/closed-shell effects can arise, having a significant impact on the SRC pair properties [63; 64]. Instead, radioactive nuclei allow more direct and systematic access to SRC properties as a function of the  $N/Z$  ratio. We can study light nuclei along isotopic chains and even in more extreme asymmetry. Such experiments need to be carried out in inverse kinematics, adding the advantage of being kinematically complete and measuring the reaction products exclusively.

### 1.2.2 Proton scattering experiments

For the study of stable nuclei, one might prefer the  $A(e, e'p)$  reaction, as it results in reduced parameter dependence of the extracted observables, such as spectroscopic factors. This preference arises primarily from the electromagnetic nature of the interaction vertex. Additionally, the sensitivity to the modeled nuclear attenuation is greater for the  $A(p, 2p)$  reaction than for the  $A(e, e'p)$  reaction.

Although most of our knowledge about SRC comes from electron scattering experiments, those cannot be performed with radioactive nuclei today. To overcome this limitation and extend the study of SRC to radioactive beams, we employed inverse kinematics scattering off a hadronic probe. Compared to electron scattering, proton scattering is fundamentally different because it involves strong, hadronic interactions. When a proton is used as a probe, the interaction between the incoming proton and the nucleons inside the nucleus is mediated by the strong force. In proton scattering experiments, both the incoming proton and the struck nucleons experience strong final-state interactions (FSI) with the surrounding nuclear medium. These FSIs can significantly alter the momentum and energy of the scattered proton and nucleons, making it more difficult to cleanly extract information about SRC pairs.

Similar to the  $A(e, e'p)$  reaction, the observables from  $A(p, 2p)$  measurements are complicated because nuclear attenuation prevents a direct connection between the properties of the measured ejected nucleons and the physics at the interaction point.

In  $A(p, 2p)$ , one proton experiences initial-state interactions (ISI), while two protons are influenced by final-state interactions (FSI). Therefore, developing a reliable reaction theory is crucial for quantitatively analyzing the  $A(p, 2p)$  data. It is well known that nuclear attenuation reduces the sensitivity of detected signals to the high-density areas of the target nucleus. This raises the question of whether  $A(p, 2p)$  can provide insights into the bulk properties of nuclei. Specifically, we want to know if the information from ejected nucleons reflects the interior of the nucleus or mainly comes from its peripheral regions. In [65], this question was addressed by quantifying which regions of the target nucleus can be explored in  $A(p, 2p)$ . The findings indicate that while nuclear attenuation significantly impacts the signals detected in  $(p, 2p)$  reactions, both  $(p, 2p)$  and  $(e, e'p)$  can probe similar densities in light nuclei, reaching saturation density  $\rho_0$ . However, in heavier nuclei like lead ( $^{208}\text{Pb}$ ), the average densities accessible through  $(p, 2p)$  reactions can be much lower—potentially half those accessible via  $(e, e'p)$ . The study emphasizes that the nuclear interior is less effectively probed in heavier nuclei due to strong attenuation.

Proton-induced QFS in inverse kinematics has been successfully applied in recent years, especially at GSI<sup>6</sup> [66; 67; 68], RIBF<sup>7</sup> at RIKEN<sup>8</sup> [69; 70]. Taking the experience and knowledge from these measurements, we aim to apply proton-induced QFS to the study of Short-Range Correlations.

### How to probe SRC

This section aims to describe how to probe SRC physics via QFS reactions, focusing in particular on proton scattering reactions in inverse kinematics. In Fig. 1.13, we visually illustrate the difference between direct kinematics (e.g. electron scattering experiments) when the electron beam impinges directly on the nucleon of interest and inverse kinematics (e.g. proton scattering experiments) where the nucleus of interest is the beam that impinges on a hadronic target. In the latter case, due to the reaction kinematics, the reaction products are boosted in the forward direction, contrary to the direct kinematics reactions. Quasi-free scattering reactions

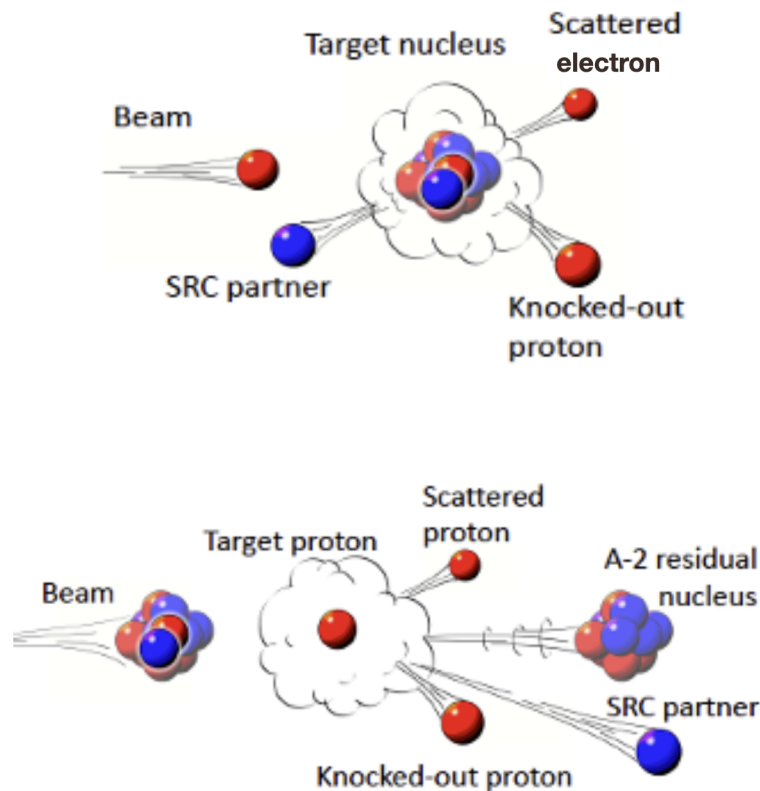


Figure 1.13: Top: direct kinematics (e.g. electron scattering experiments) when the electron beam impinges directly on the nucleon of interest. Bottom: inverse kinematics (e.g. proton scattering experiments), where the nucleus of interest is the beam that impinges on a hadronic target [71].

are a fundamental tool in nuclear physics for probing the internal structure of atomic nuclei, particularly for investigating SRC between nucleons.

In a QFS reaction, a high-energy projectile, such as a proton or electron, is scattered off a target nucleus, resulting in the ejection of one or more nucleons. This process is termed "quasi-free" because the incident particle interacts primarily with a single nucleon within the nucleus while the remaining nucleons act as spectators. This interaction allows for a relatively clean investigation of the nucleon-nucleon interaction without the complexities introduced by the

<sup>6</sup>Gesellschaft für Schwerionenforschung (GSI Helmholtz Centre for Heavy Ion Research), Germany.

<sup>7</sup>Radioactive Ion Beam Facility, Japan.

<sup>8</sup>RIKEN Nishina Center for Accelerator-Based Science in Wako.

entire nuclear medium.

The study of QFS reactions provides valuable insights into the momentum distribution and spatial configuration of nucleon pairs within the nucleus. By analyzing the momentum and angular distributions of the knocked-out nucleons, it is possible to infer the presence and characteristics of SRC pairs.

### QFS Reaction Mechanism

In contrast to many nuclear reactions at low energies, which typically proceed via the mechanism of compound intermediate states involving the entire nucleus, direct QFS reactions involve the incident particle interacting with only a small fraction of the nucleus. For the sudden approximation to be valid, the time interval of the reaction must be shorter or comparable to the characteristic nuclear time ( $\sim 10^{-22}$  s), assuming the nucleons inside the nucleus are "frozen" during the reaction. In this section, only a qualitative description will be given, and more detailed information can be found here [66; 72; 73; 74; 75].

Quasi-free scattering reactions of the type  $(p, pN)$ , where  $N$  denotes a nucleon (or cluster) being knocked out, can be qualitatively described as a direct process. In this process, an incident proton with energy  $E_0$  and momentum  $\vec{k}_0$  is scattered on a bound nucleon as if both particles were free, and the nucleon is subsequently ejected from the nucleus (see Fig. 1.14). The process is considered "quasi-free" when the incident proton energy is sufficiently high and there are no other significant interactions between the spectator nucleons and either the incoming proton or the two outgoing particles. The residual nucleus, denoted as  $(A - 1)$ , contains a

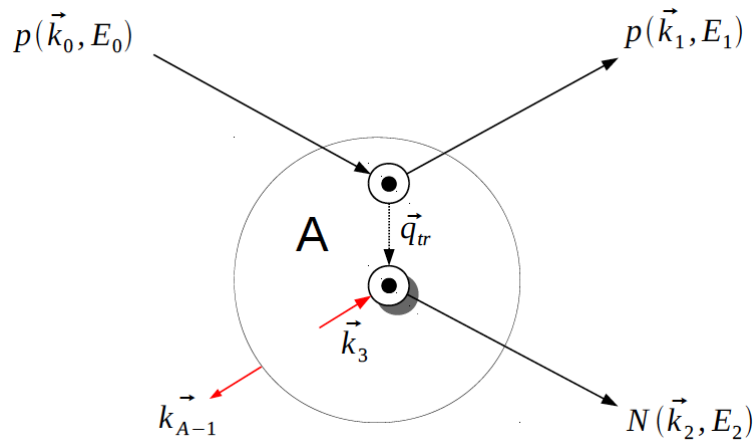


Figure 1.14: A schematic view of the quasi-free scattering reaction  $(p, pN)$  is shown in the rest frame of the target nucleus  $A$ . In this reaction, the incoming proton knocks out a nucleon  $N$  (either a proton or neutron) from the nucleus, creating a hole in the residual  $(A - 1)$  nucleus. The red arrows  $\vec{k}_3$  and  $\vec{k}_{A-1}$  represent the internal momentum of the knocked-out particle and the balancing recoil momentum of the  $(A - 1)$  system, respectively [72].

hole in a specific energy level previously occupied by the knocked-out nucleon. If this hole is produced at a level lying below the Fermi surface, the residual nucleus obtains an additional excitation energy  $E_{A-1}$  corresponding to the energy of this single-particle state relative to the Fermi level.

By applying the energy conservation principle, one can determine the separation energy  $S_N$  of the state assuming the target nucleus to be at rest:

$$S_N = T_0 - (T_1 + T_2 + T_{A-1}) - E_{A-1}. \quad (1.20)$$

$S_N = (M_A - M_{A-1} - m_N)c^2$  is the minimum energy needed to separate the least bound nucleon from nucleus A, where  $M_A$ ,  $M_{A-1}$ , and  $m_N$  are the masses of the target, residual nucleus ( $A - 1$ ), and the removed nucleon  $N$ , respectively.  $T$  denotes kinetic energies of the incoming and outgoing proton (subscripts 0 and 1), the outgoing nucleon (2), and the final state nucleus ( $A - 1$ ).

The energy of the single-particle state can be determined in two ways. The first method, traditionally used in experiments employing direct QFS kinematics, relies on measuring the kinetic energies of the projectile and the outgoing particles. Alternatively, the excitation energy  $E_{A-1}$  can be used. Depending on the magnitude of  $E_{A-1}$ , the final ( $A - 1$ ) system will decay either via emission of  $\gamma$ -rays if  $0 < E_{A-1} < S_{A-1}$  (where  $S_{A-1}$  is the smallest particle separation threshold in the ( $A - 1$ ) nucleus) or via breakup if  $E_{A-1} > S_{A-1}$ .

Not only the binding energy is an important quantity characterizing the individual state of a nucleon, but also its internal momentum inside the nucleus, denoted as  $\vec{k}_3$ . This momentum can be associated with a specific nuclear shell. By applying the momentum conservation law, one can write:

$$\vec{k}_{A-1} = \vec{k}_0 - \vec{k}_1 - \vec{k}_2 = -\vec{k}_3. \quad (1.21)$$

This equation shows that the nucleon's internal momentum is directly related to the recoil momentum of ( $A - 1$ ) taken with a negative sign. The idealized picture of the incoming proton interacting only with one nucleon needs several important modifications to account for secondary interactions in the incoming and outgoing channels. Nevertheless, this simple model contains the essential physics of quasi-free knockout, which motivates the use of these reactions for investigating nuclear single-particle structures.

In this experiment, the QFS kinematical study with the selection of the  $A - 1$  fragment is fundamental as the first step to tackle SRC physics. In proton-induced quasielastic scattering, the pair (with center-of-mass momentum) is broken up. Experimentally, a high-momentum probe can knock a proton out of a nucleus, leaving the rest of the system nearly unaffected. If, on the other hand, the proton being struck is part of an SRC pair, the high relative momentum in the pair would cause the correlated nucleon to recoil and be ejected as well, leaving the  $A - 2$  system unaffected (see Fig. 1.15).

When scattering off an  $np$  pair, such as in  $^{12/16}\text{C}(p,2pn)$ , or a  $pp$  pair, like in  $^{12/16}\text{C}(p,2pp)$ , the heavy  $A - 2$  fragments are  $^{10/14}\text{B}$  and  $^{10/14}\text{Be}$ , respectively. The heavy fragment and recoil nucleon of the pair moves forward in the laboratory system while the scattered particles emerge at large laboratory angles. Fig. 1.16 illustrates a sketch of the process in the nucleus rest frame ( $A$ ).

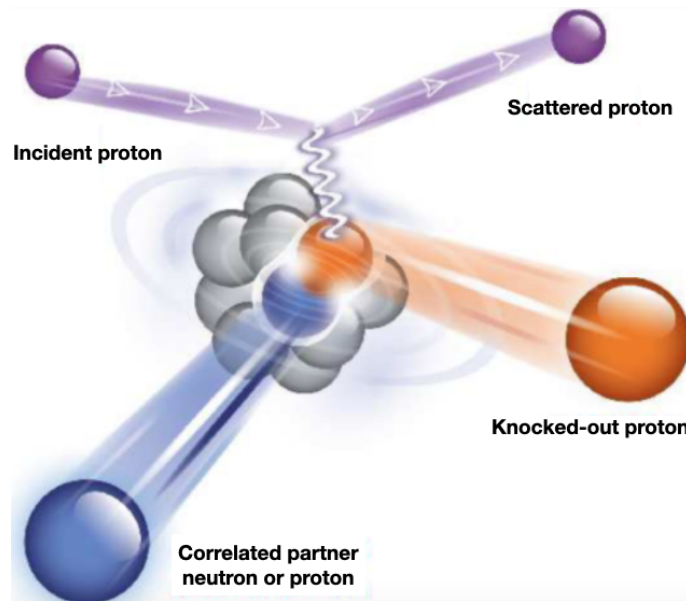


Figure 1.15: Illustration of the  $^{12}\text{C}(p,2pN)$  reaction visualized in direct kinematics. In the final state, the scattered proton is detected along with the two nucleons that are ejected from the nucleus. Adapted from [76].

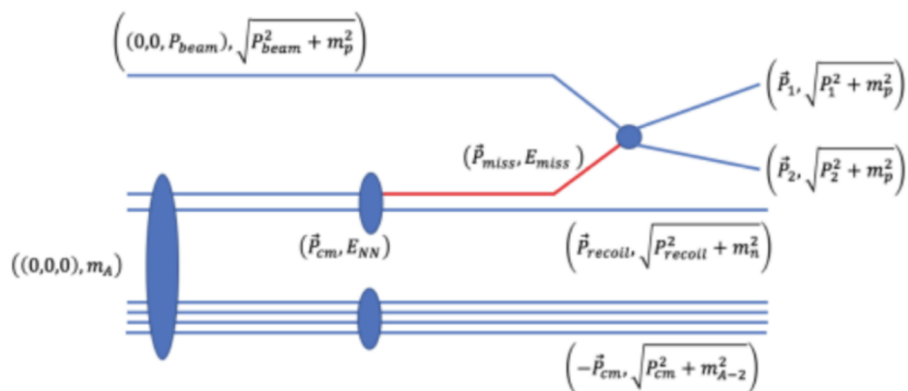


Figure 1.16: Diagrammatic view of the SRC scattering process on nucleus  $A$ . Figure taken from [77].

We utilize scattering off a proton target where the momentum is fully absorbed by one nucleon of the pair, which is highly off-shell. The pair is assumed to be decoupled from the  $A - 2$  system. The knocked-out proton and the recoil nucleon from the broken SRC pair ejected back-to-back in the nucleus rest frame will move forward independently like the  $A - 2$  system. In the laboratory, the particles are strongly boosted forward by the beam momentum. The signature of scattering off an SRC pair is the detection of a  $(p, 2pn)A-2$  or  $(p, 3p)A-2$  reaction, with missing momentum  $p_{\text{miss}} > k_F$ . The straightforward selection of SRC will, therefore, be made based on the detection of a  $(p, 2p)$  reaction, an  $A - 2$  fragment, and a recoil proton or neutron with high relative momentum with respect to the  $A - 2$  fragment. We will call those events "exclusive". If we require only the detection of a  $(p, 2p)$  reaction, an  $A - 2$  fragment, and we do not use the information on the recoil neutron or proton, we will call those events "inclusive".

The missing momentum is reconstructed from the four-momenta  $P_1, P_2$  of the scattered protons (same as Eq. 1.21) after boosting them to the beam center of mass. The missing momentum definition is:

$$P_{\text{miss}} = P_1 + P_2 - P_{\text{target}}. \quad (1.22)$$

with  $P_{\text{target}}$  being the target proton momentum before the reaction, also in the beam c.m. frame. To identify processes with high transferred momentum, we will make use of the Mandelstam variables. These variables play a crucial role in describing the kinematics of particle interactions. In theoretical physics, the Mandelstam variables are numerical quantities that encode the energy, momentum and angles of the particles in a scattering process in a Lorentz-invariant fashion. They are used for scattering processes of two particles to two particles. The Mandelstam variables were first introduced by physicist Stanley Mandelstam in 1958 [78].

If the Minkowski metric is chosen to be represented by a diagonal matrix  $(1, -1, -1, -1)$ , the Mandelstam variables  $s$ ,  $t$ , and  $u$  are then defined by:

$$s = (p_1 + p_2)^2 = (p_3 + p_4)^2. \quad (1.23)$$

$$t = (p_1 - p_3)^2 = (p_4 - p_2)^2. \quad (1.24)$$

$$u = (p_1 - p_4)^2 = (p_3 - p_2)^2. \quad (1.25)$$

Here,  $p_1, p_2, p_3$ , and  $p_4$  are the four-momenta of the particles involved in the scattering process. In our situation,  $p_1$  and  $p_2$  are the initial momentum of the proton in the nucleus that we probe ( $p_{\text{miss}}$ ) and the momentum of the proton of the hadronic probe.  $p_3$  and  $p_4$  are the momentum of the two scattered protons leaving the nucleus. Using these quantities combined with the information of the two scattering protons, we can infer the transfer momentum of the QFS reactions, thus requiring high momentum transfer processes.

- **s-channel:** The two particles "merge" into a virtual intermediate particle that finally splits into the two final particles. Note that since four-momentum is conserved at each vertex, we have for the momentum  $q$  of the intermediate particle  $q^2 = (p_1 + p_2)^2 = s = E^2$ , where  $E$  is the total energy of the virtual particle interchanged (dotted lines in Fig. 1.17).
- **t-channel:** Particle 1 emits a virtual particle and, in doing so, turns into particle 3. The virtual particle is absorbed by particle 2, which, as a consequence of this interaction, turns into particle 4. Since the first particle had momentum  $p_1$  before the emission and particle 3 has momentum  $p_3$ , the difference of these must have gone into the emitted

virtual particle; thus, it has squared momentum  $q^2 = (p_1 - p_3)^2 = t$ . Therefore, we can say that particle 1 has "lost" momentum  $q$ , which has been transferred to particle 2.

- **u-channel:** As depicted in Fig. 1.17, the u-channel is analogous to the t-channel with the roles of  $p_3$  and  $p_4$  interchanged. Therefore, we can interpret  $u$  as the momentum transfer from particle 1 to particle 2.

The measurement of  $(p,2p)$  kinematics also allows for the selection of events in the region where the transferred momentum for both indistinguishable scattered protons is high. This criterion identifies events where sufficient momentum is transferred to break the pair and leave the scattered nucleon with high momentum.

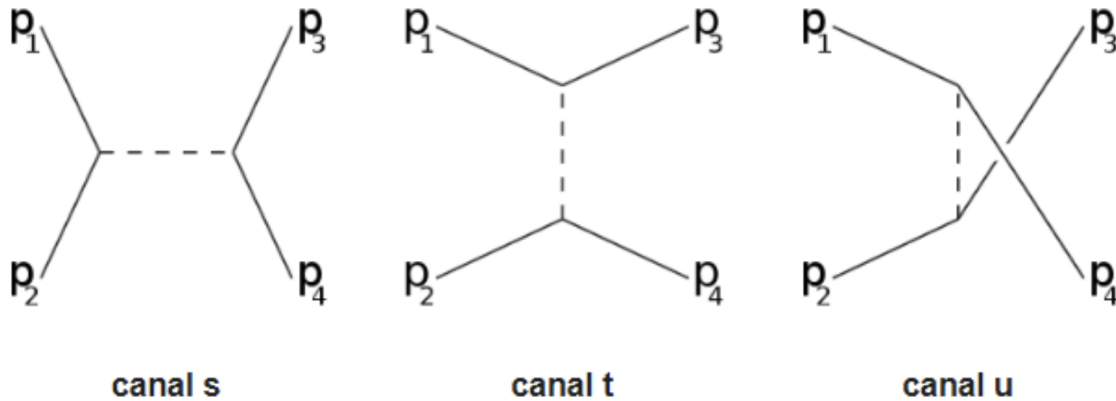


Figure 1.17: Visual diagrams representing the physics of the different Mandelstam variables. Two particles come in with momenta  $p_1$  and  $p_2$ , they interact in some fashion, and then two particles with different momentum ( $p_3$  and  $p_4$ ) leave [79].

### Test of proton-induced QFS in inverse kinematics

In a recent experiment performed in Dubna at the BM@N experimental setup (JINR<sup>9</sup>, Russia) and led by GSI-MIT<sup>10</sup>-CEA<sup>11</sup> and TU Darmstadt<sup>12</sup> collaboration, it was possible to see for the first time that SRC pairs are accessible in inverse kinematics experiments using hadronic probes [71]. A  $^{12}\text{C}$  beam with a momentum of 4 GeV/c/u was scattered off a 30 cm liquid hydrogen target, and the scattered protons and heavy fragments were detected in coincidence.

By measuring the knocked-out proton from pair-breakup in  $^{12}\text{C}$  and the scattered target proton under a large angle, the initial proton momentum  $p_{\text{miss}}$  could be reconstructed. The results of this experiment underline the importance of fragment selection ( $^{10}\text{B}$  in the  $^{12}\text{C}(p,2pn)$  and  $^{10}\text{Be}$  for  $^{12}\text{C}(p,3p)$  case) to significantly reduce the events where initial and final state interactions (ISI and FSI, respectively) may produce signals mimicking the ones of SRC. Methods were developed to identify SRC and reject events coming from mean-field  $^{12}\text{C}(p,2p)$  knockout leading to unbound excited states in  $^{11}\text{B}$  that would finally decay into  $^{10}\text{B}$  or  $^{10}\text{Be}$ . As discussed in [71], neutron decay mostly dominates due to the absence of the Coulomb barrier. The JINR experiment demonstrated that SRC is accessible in inverse kinematics at large momentum transfer, paving the way for the following SRC study at  $R^3B$ .

<sup>9</sup>Joint Institute for Nuclear Research.

<sup>10</sup>Massachusetts Institute of Technology, USA.

<sup>11</sup>Commissariat à l'énergie atomique et aux énergies alternatives, France.

<sup>12</sup>Technische Universität Darmstadt, Germany.

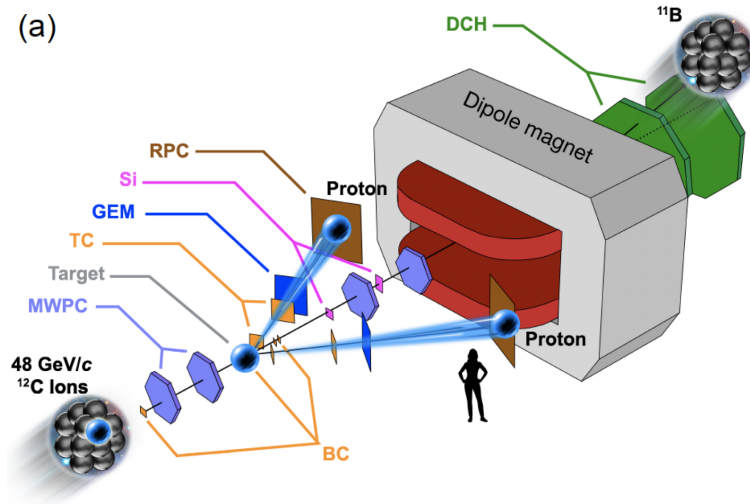


Figure 1.18: Setup used for the SRC test experiment at the Nuclotron accelerator in Dubna [71].

The results of the JINR test experiment suggest that in a significant amount, the SRC breakup leaves the residual nucleus  $A - 2$  with a large excitation energy so it can break into smaller pieces. The coincident measurement of neutrons, protons and light fragments  $A - 2$  that can be carried out at  $R^3B$  will allow us to make use of SRC breakup events for SRC studies. As an example, Fig. 1.19 shows the correlation between missing energy and missing momentum. The SRC events surviving all kinematical selections to isolate SRC physics are superimposed onto GCF-based simulations. The projections in missing energy and momentum show very good agreement with GCF predictions.

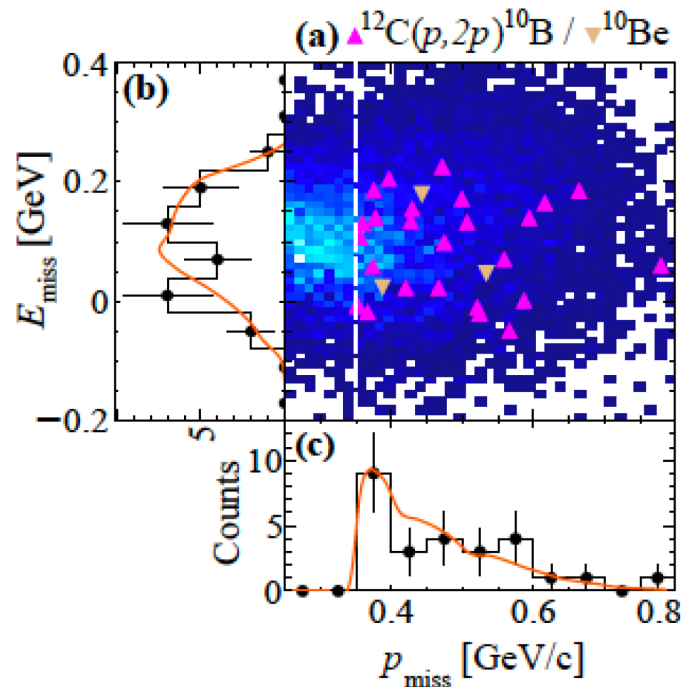


Figure 1.19: Correlations between missing energy and missing momentum for the measured  $^{12}\text{C}(p,2p)^{10}\text{B}$  (upward triangles) and  $^{12}\text{C}(p,2p)^{10}\text{Be}$  (downward triangles) events are shown on top of the GCF simulation.

Even if the statistic was quite limited, one can note that the ratio between SRC  $\frac{np}{pp}$  candidate pairs, from the  $^{12}\text{C}(p,2p)^{10}\text{B}/\text{Be}$  events, is consistent with the  $np$  pairs dominance established by previous experiments and theory [43; 44; 47; 53]. The cosine of the angle between the missing momentum ( $p_{\text{miss}}$ ) and the undetected recoil nucleon momentum shows a clear back-to-back correlation as expected for SRC pairs (Fig. 1.20 left) [43; 44; 71]. The cosine of the angle between  $^{10}\text{B}$  and the relative pair momentum, instead, shows a flat distribution (Fig. 1.20, right), signifying that those variables are uncorrelated. It suggests that the factorization assumption that is at the basis of the theoretical framework used to compare the data is valid.

Taking the steps from the results of the Dubna test experiment, in May 2022, we performed an SRC investigation experiment using the  $R^3B$  setup employing a very similar approach. The breakthrough of the experiment at  $R^3B$  is to extend QFS reactions to study SRC in neutron-rich environment, considering an exotic nucleus ( $^{16}\text{C}$ ) for the first time.

Thanks to the  $R^3B$  setup capabilities, we can perform a fully exclusive kinematics study of SRC pairs with four-fold coincidence  $A(p,2pN)A-2$  measurement [77], where  $N = n, p$ . The motivations of this experiment are detailed in Sec. 1.3.

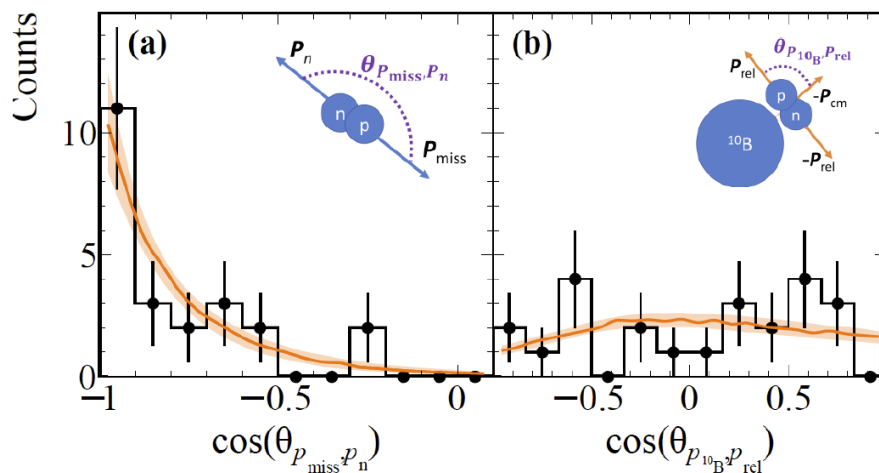


Figure 1.20: Distribution of the cosine of the angle between the recoil nucleon and missing momentum (left), and  $^{10}\text{B}$  fragment and pair relative momentum (right) [71].

### 1.2.3 SRC and open questions in nuclear physics

To illustrate the potential impact of short-range correlations on the understanding of nucleon and nuclear structure, this section will provide two examples at different energy scales.

#### EMC effect

Nucleons are often considered to be the relevant degree of freedom to describe nuclear properties due to the small nuclear binding energy and quark-gluon confinement. The European Muon Collaboration (EMC) at CERN [80] showed for the first time the breakdown of this scale separation, manifested in a decrease of the per-nucleon electron deep inelastic cross-section in nuclei with  $A > 2$  compared to the deuteron. Deep inelastic scattering (DIS) at  $Q^2 > 2 \text{ GeV}^2$ , and  $0.35 \leq x_B \leq 0.7$  ( $x_B = Q^2/2m$ , where  $m$  is the nucleon mass)<sup>13</sup> is sensitive to the nuclear quark distributions.

<sup>13</sup> $Q^2$  is the four-momentum transferred.

The deep inelastic scattering (DIS) energy scale is on the order of several tens of GeV, while nucleons within nuclei are bound by energies of a few MeV. Naively, one might expect that the DIS off a bound nucleon is equivalent to the DIS off a free nucleon.

For the deuteron, the binding energy is approximately 2 MeV, and the average nucleon separation is around 2 fm. Accordingly, we anticipate that the DIS off a deuteron should be similar to the DIS off a free proton-neutron pair. More generally, we expect that the DIS off a bound nucleon in a nucleus can be approximated by the DIS off nucleons in deuterium.

The per-nucleon electron deep inelastic scattering cross sections of nuclei with  $A \geq 3$  are smaller than those of deuterium at  $Q^2 \geq 2 \text{ GeV}^2$ , and moderate  $x_B$ ,  $0.35 \leq x_B \leq 0.7$ . This effect, known as the EMC effect, has been measured for a wide range of nuclei [80; 81]. There is no generally accepted explanation of the EMC effect. The strength of the EMC effect is characterized by the slope of the ratio of the cross-section for a given nucleus with respect to the deuteron as a function of the Bjorken- $x$  ( $x_B$ )<sup>14</sup> variable for  $0.35 < x_B < 0.7$ , as illustrated in Fig. 1.21 and in Fig. 1.22 (left plot).

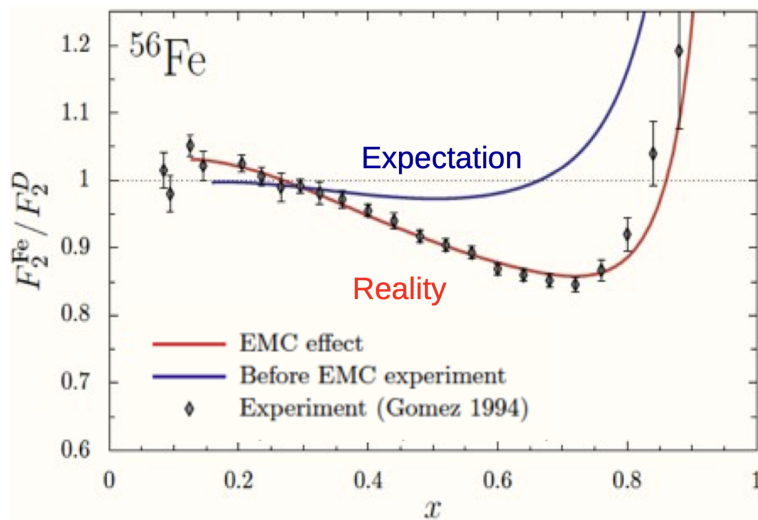


Figure 1.21: Ratio of the nucleon structure functions  $F_2$  of Iron and deuterium. It represents the deviation of the per-nucleon DIS cross section ratio of  $Fe$  relative to deuterium from unity. Figure taken from [81].

Inelastic scattering at  $Q^2 > 1.4 \text{ GeV}^2$  and  $x_B > 1.5$  is sensitive to nucleon-nucleon short-range correlations in the nucleus. The per-nucleon electron inelastic scattering cross sections of nuclei with  $A \geq 3$  exceed those of deuterium for  $Q^2 > 1.4 \text{ GeV}^2$  and large  $x_B$ , where  $1.5 \leq x_B \leq 2$  (see Fig. 1.22, left). The cross-section ratio between two different nuclei (e.g., carbon and helium) exhibits a plateau when plotted against  $x_B$ , indicating independence of  $x_B$ . This plateau region defines the "SRC scale factor"  $a_2$ , which is the ratio of cross sections in this region (see Fig. 1.22, left).

This  $Q^2$  of the deep-inelastic and inelastic scattering measurements independence allows us to compare the EMC slope and the SRC scale factor in their different measured ranges [81; 82]. A clear linear relationship has been observed between the EMC slope and the SRC scale factor  $a_2$  [82] (see Fig. 1.22, right plot). This implies that both stem from the same underlying nuclear physics, such as high local density or large nucleon virtuality ( $v = P^2 - m^2$  where  $P$  is the four-momentum).

<sup>14</sup>In a partonic picture,  $x_B$  is the fraction of the nucleon momentum carried by the struck quark. When  $x_B > 1$ , the struck quark has more momentum than the entire nucleon, which points to nucleon correlation.

This correlation means that we can predict the SRC scale factors for a wide range of nuclei from Be to Au using the linear relationship and the measured EMC slopes. This also suggests that modifications in the quark distributions within nucleons may occur when these nucleons are paired at short distances.

Further analysis indicates that this hypothesis is supported by examining the per-proton and per-neutron EMC and SRC probabilities. These probabilities show linear correlations up to a nuclear mass  $A = 12$  (in  $N/Z$  symmetric nuclei). However, in the neutron sector, these correlations saturate at  $A = 12$ . To restore the linear correlation, especially in the proton sector [83], an  $N/Z$  asymmetry correction is necessary. This study is summarized in Fig. 1.23.

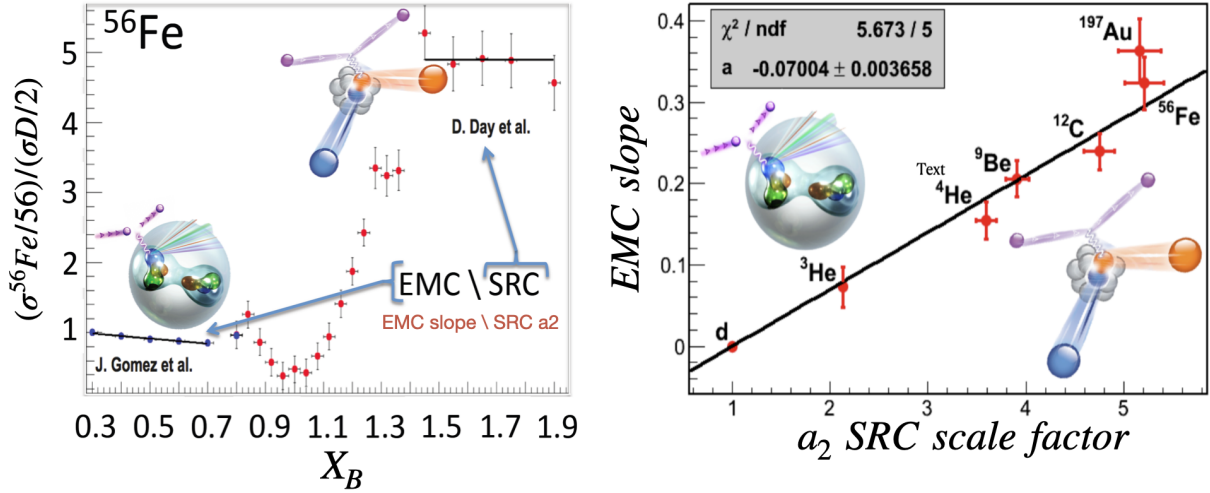


Figure 1.22: Left plot: In the same plot we have measurements from deep inelastic scattering (DIS) experiments which energy scale is on the order of several tens of GeV and  $x_B < 0.7$  and inelastic scattering measurements at  $Q^2 > 1.4 \text{ GeV}^2$  and  $x_B > 1.5$  that are sensitive to nucleon-nucleon short-range correlations in the nucleus. The ratio of  $^{56}\text{Fe}$  deep inelastic and inelastic cross-section with respect to deuterium in function of the Bjorken factor  $x_B$  is shown. The per-nucleon electron deep inelastic scattering cross sections of nuclei with  $A \geq 3$  are smaller than those of deuterium at  $Q^2 \geq 2 \text{ GeV}^2$ , and moderate  $x_B$ ,  $0.35 \leq x_B \leq 0.7$  (EMC effect, left side of the plot). The per-nucleon electron inelastic scattering cross sections of nuclei with  $A \geq 3$  exceed those of deuterium for  $Q^2 > 1.4 \text{ GeV}^2$  and large  $x_B$  (SRC effect, right side of the plot). The region at  $0.7 < x_B < 1.5$  is not taken into account since it is not related with EMC effect and SRC physics. The strength of the EMC effect is characterized by the slope of the ratio of the cross-section (EMC slope) [27; 84]. SRC scale factor  $a_2$  is the ratio of cross sections in the plateau region [81; 82; 85]. Right: The EMC slopes versus the SRC scale factors for different nuclei in the  $0.35 < x_B < 0.7$  region [82].

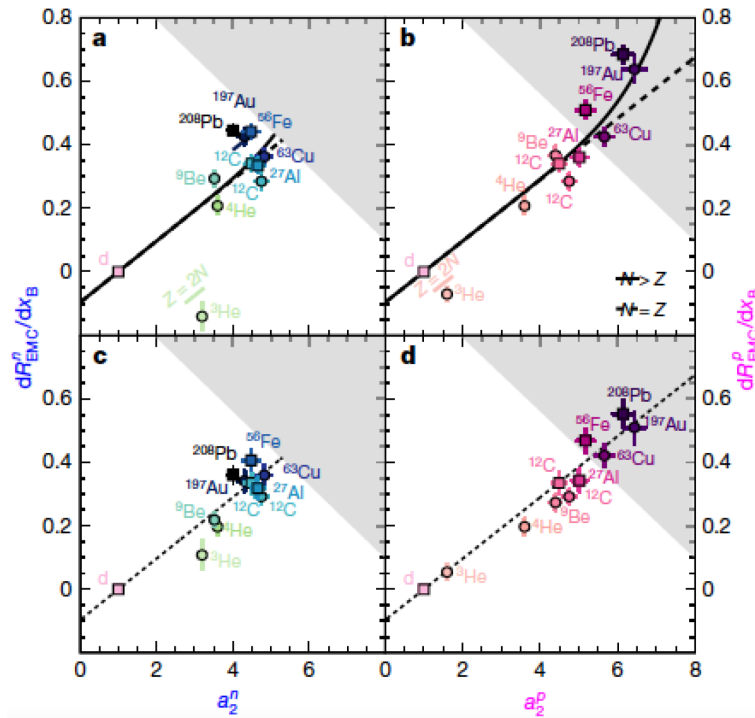


Figure 1.23: Per-neutron (left) and per-proton (right) strength of the EMC effect versus the per-neutron and per proton number of SRC pairs. The bottom panels have an  $N/Z$  asymmetry correction allowing restoration of the linear correlations. Taken from [83].

### Quenching of the spectroscopic factor

Short-range correlations are closely linked to a longstanding question in nuclear physics regarding the reduction of measured knockout cross-sections compared to predictions from mean-field theories, known as the quenching of spectroscopic factors. This reduction is attributed to both long-range correlations (LRC) and short-range correlations (SRC), which deplete the occupancy of single-particle states below the Fermi energy. Studies show that for stable nuclei at any given moment, only 60%–70% of the states below the Fermi momentum are occupied, with 30%–40% of the nucleons participating in LRC and SRC configurations [86; 87]. Therefore, both LRC and SRC deplete the occupancy of single-particle states, with LRC primarily mixing states near the nuclear Fermi momentum and SRC populating states well above it. The quenching has been observed to depend on proton-neutron asymmetry, often characterized by differences in separation energy [88].

It has been argued that this dependence disappears when employing alternative reaction mechanisms, such as nucleon transfer, to extract spectroscopic factors [89]. Additionally, the role of core excitation in depleting the one-nucleon removal channel, especially in cases of deeply bound nucleons, has been discussed [90]. Recent studies using quasi-free scattering on Oxygen isotopes have indicated a reduction factor consistent with weak or no dependence on neutron-proton asymmetry [67]. The increased participation of protons in SRC in neutron-rich systems correlates with a greater depletion of proton strength below the Fermi momentum, as evidenced in  $(p,2p)$  experiments [67].

The weak isospin dependence observed in the data from Ref. [67] has recently been compared to predictions incorporating SRC fractions using a phenomenological approach.

Paschalis et al. [87] developed a phenomenological model linking the reduction of spectroscopic factors to recent studies on SRC at Jefferson Lab. Simple parametric forms were derived to account for the combined impact of LRC and SRC analyzing data from low- $Q^2$  electron scattering and proton-induced QFS experiments. They showed that approximately 20% of the observed missing strength in the  $N = Z$  region can be attributed to SRC, demonstrating good agreement with trends observed in  $(p,2p)$  reactions (see Fig. 1.24, [87]).

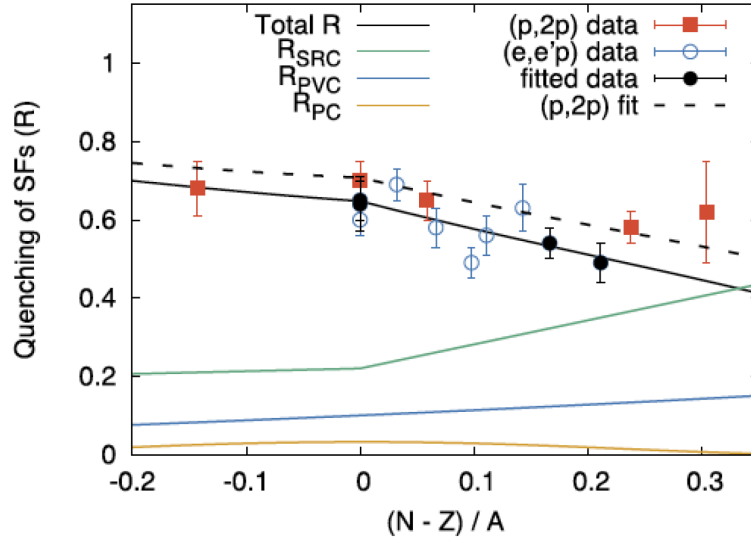


Figure 1.24: Quenching of proton SFs as a function of  $(N - Z)/A$  for  $(e, e'p)$  and  $(p,2p)$  data compared to a phenomenological calculation including SRC and LRC, here decomposed in PVC (particle-vibration coupling) and PC (pairing correlations). The SRC and PC contributions are fixed to  $\gamma = 22\%$  and  $\beta = 3\%$ , respectively.

### 1.3 Motivations and goals of the experiment

In the previous paragraph, two examples were given to illustrate the connection between open puzzles in nuclear and sub-nuclear physics and SRC and its isospin dependence. We aim to study SRC in neutron-rich environment with exotic nuclei to significantly extend the range of isospin values compared to what can be explored using stable nuclei. Nowadays, the only way to access exotic nuclei is by performing experiments in inverse kinematics, i.e., by sending radioactive-ion beams onto a proton target. This approach offers several advantages. Firstly, it provides the possibility to measure (for the first time in an exotic nucleus) the residual system ( $A - 2$  fragment or lighter). Secondly, the measurement of the momentum of the residual system will allow us to directly determine the center-of-mass momentum of SRC pairs. Moreover, due to the kinematical focusing at forward angles, measurements in inverse kinematics will also benefit from increased acceptance for 4-fold coincidences (scattered proton and its partner nucleon, recoil proton, and residual nucleus) compared to 3-fold coincidences in direct kinematics.

The unique facility worldwide for performing QFS measurements with radioactive ion beams in inverse kinematics is the GSI facility, which is undergoing upgrades to become the FAIR facility. This is attributed to the availability of radioactive beams with kinetic energies up to 1 GeV/u (and up to 1.9 GeV/u for  $^{12}\text{C}$ , for example), enabling the study of QFS reactions with sufficiently large momentum transfer.

The collaboration led by MIT and CEA proposed an experiment to the 2020 GSI Program Advisory Committee to investigate short-range correlations in  $^{12}\text{C}$ ,  $^{16}\text{C}$  isotopes, and it was performed in May 2022. This experiment, its analysis, and the interpretation of its results are the subject of this thesis.

The primary objective of our research is to investigate short-range correlations within a neutron-rich environment and define a methodology to infer SRC physics. In particular, we aim to determine SRC properties (pair ratio, relative and pair center-of-mass momentum) in an exotic nucleus for the first time and to perform a fully exclusive SRC study in inverse kinematics with a hadronic probe. In addition to this primary goal, our study also aims to achieve several objectives. It is possible to do a summary of the experiment objectives and have a better understanding of our goals by looking at Fig. 1.25.

The plot [47] shows the double ratio of high-to-low momentum protons (neutrons) in nucleus  $A$  with respect to  $^{12}\text{C}$ . Looking at it, we can make several considerations:

- The existing trend is based on a few points [47; 58].
- The trend behaviour can depend on shell structure (open/closed-shell effects) [63; 64].
- Mass and  $N/Z$  effects cannot be disentangled with stable nuclei.
- We aim to perform a new measurement at  $N/Z = 1.67$ , above the largest available  $N/Z$  and at a much smaller mass.

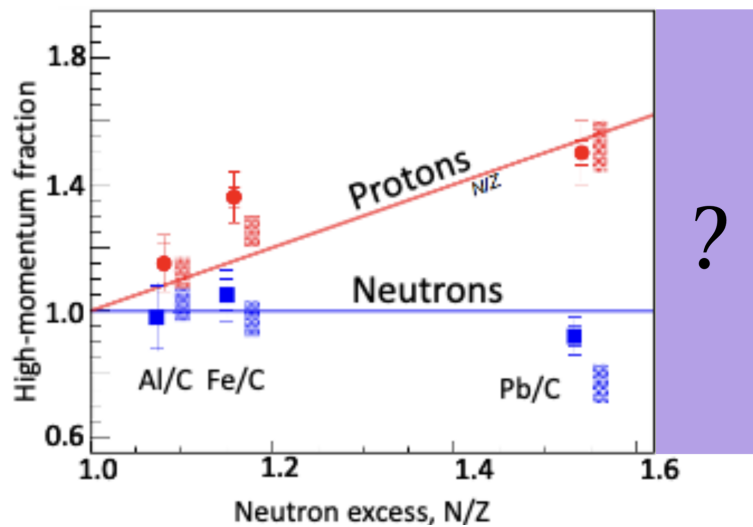


Figure 1.25: Double ratio of high-to-low momentum protons (neutrons) in nucleus  $A$  with respect to carbon marked with dot (squares), and corresponding calculations with rectangles, adapted from [47]. The purple area is the region of the new measurement at  $N/Z = 1.67$ , above the largest available  $N/Z$  and at a much smaller mass.

This experiment is part of a larger experimental program undertaken by the MIT-Tel Aviv-TU Darmstadt-GSI-CEA collaboration. With this experiment, we are proceeding with a coherent program to develop methods and study SRC in neutron-rich matter at FAIR.

# Chapter 2

## Experimental Setup

### Contents

---

<b>2.1</b>	<b>Beam production at GSI</b>	<b>53</b>
<b>2.2</b>	<b>The <math>R^3B</math> Setup</b>	<b>55</b>
2.2.1	Incoming detectors	56
2.2.2	Target recoil detectors	60
2.2.3	Outgoing detectors	66
2.2.4	Data Acquisition System of the $R^3B$ Collaboration	72

---

### 2.1 Beam production at GSI

**G**SI (Gesellschaft für Schwerionenforschung) (Darmstadt, Germany) [91], which translates to the "Society for Heavy Ion Research" in English, is a renowned research facility for nuclear and particle physics located in Germany. It is one of the world's leading centers for studying heavy ions and nuclear physics. In Fig. 2.1, a bird-eye view of the heavy-ion beam facility at GSI is shown.

The first beam acceleration stage consists of the Universal Linear Accelerator (**UNILAC**). A low-energy beam of stable isotopes is extracted from the primary ion source and injected into the UNILAC where it is accelerated up to a maximum energy of 11.4 AMeV [91]. The ejected beam from the UNILAC is transported to a second acceleration stage performed by **SIS 18** [91], a heavy-ion synchrotron. It is possible to produce stable-ions beams in a wide range of atomic masses with energies up to 1 GeV/u and 4.5 GeV/u for U and protons, respectively [91]. The resulting beam from the synchrotron can be used for different purposes. For example, it can impinge on a light nuclear target, such as  $^9\text{Be}$ , to obtain secondary radioactive beams ( $^{16}\text{C}$ ). These beams are typically utilized in experiments involving the Experimental Storage Ring (**ESR**) or the FRagment Separator (**FRS**).

In our experiment, the primary beam, accelerated up to 1.3 GeV/nucleon, is directed toward the production target at the entrance of the Fragment Separator (FRS) as depicted in Fig. 2.2. An  $8\text{ g/cm}^2$  thick  $^9\text{Be}$  production target initiates fragmentation reactions. The primary beam has an intensity of  $10^{10}$  ions per bunch. The composition of the delivered beam to the experimental cave depends uniquely on the FRS settings. In our situation, the beam reaching the cave C experimental area was characterized by a spill length of about 2.5 s.

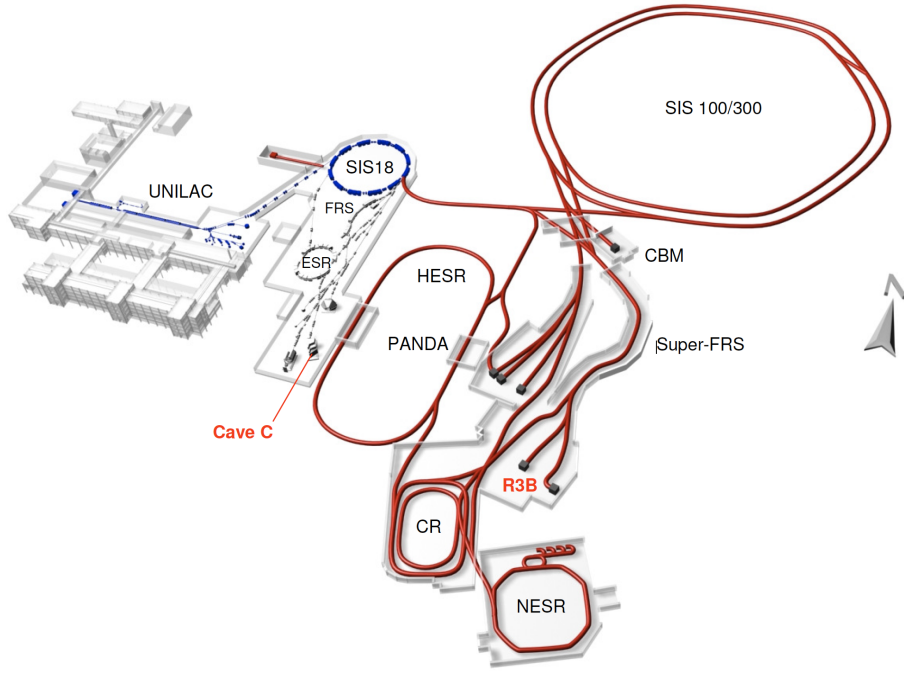


Figure 2.1: Layout of the current heavy-ion beam facility (left, blue colour) at GSI is shown together with the future FAIR facility (right, red colour). The existing  $R^3B$  setup in Cave C is designed as a prototype for the planned  $R^3B$  laboratory, which is also indicated in the figure [91].

For our experiment, the magnetic rigidity  $B\rho$  of the FRS is set to 17.6298 Tm to favour the transmission of nuclei with  $A/Z \approx 2.5$ . The reaction products of the nuclear fragmentation of the incoming  $^{18}\text{O}$  beam striking the  $^9\text{Be}$  target form a cocktail of secondary beams with an energy of approximately 1300 MeV/nucleon. A wide range of elements with masses smaller than that of the primary beam is produced. The beam composition is subsequently selected using the  $B\rho$ , applied within the FRS. These secondary beams are then directed to the  $R^3B$  experimental setup located in Cave C.

The FRS beamline is equipped with two 3 mm thick scintillator paddles. These detectors are essential for conducting time-of-flight ( $ToF$ ) measurements over a considerable distance (from FRS to Cave C) for each ion. One scintillator paddle is positioned at the middle FRS focal plane ( $\mathbf{S2}^1$ ), while the other is located behind the FRS focal plane ( $\mathbf{S8}$ ). In the current experiment, only the scintillator at an intermediate focal plane S2 was used, providing a flight path of nearly 136 m to Cave C.

In summary, in the present experiment, we employed two different settings for the two different beams:

- A primary  $^{12}\text{C}$  beam with an energy of 1.25 GeV/u and an intensity of  $10^5$  pps was transported directly to the experimental setup in Cave C from the UNILAC accelerator.
- The  $^{16}\text{C}$  beam of 1.25 GeV/u (at the entrance of Cave C) is produced in the FRS via fragmentation of  $^{18}\text{O}$  with an  $8045 \text{ mg/cm}^2$   $^9\text{Be}$  target. From the FRS, the radioactive beam was sent to the experimental setup in Cave C.

<sup>1</sup>4 mm thick and 220 mm long scintillator.



The neutrons were detected by the New Large Area Neutron Detector (**NeuLAND**) [93], and the fragments were tracked via four scintillating **Fiber** detectors and the charge determined via a 4-plane time-of-flight wall (**TOFD**). Similar to the fragments, the kinematically focused protons, stemming from the decay of excited reaction fragments or coming from the SRC recoil protons, were measured behind the magnet via an **RPC** detector. In particular, considering an SRC event that can be a  $np$  pair break-up or a  $pp$  pair break-up, with the detectors described below, we want to detect the following particles:

- The first step to identify an SRC break-up event is to detect a  $(p,2p)$  reaction in CALIFA. We expect, as a consequence, to observe the signal of two QF scattered protons at large laboratory angles. One proton will be the scattered proton from the  $\text{LH}_2$  target, and the other proton will be one of the components of the SRC  $np$  or  $pp$  pair.
- If we break up an SRC  $np$  pair, we expect to detect the recoil neutron of the pair in the NeuLAND detector. The detection of the neutron in NeuLAND and the  $(p,2p)$  protons in CALIFA gives us very important information about the SRC  $np$  pair, in particular when we combine this information with TOFD  $A - 2$  fragment identification.
- With Fiber and TOFD detectors, we want to reconstruct the properties of the  $A - 2$  fragments associated with a  $np$  or  $pp$  pair break up, so directly linked with the number of  $np$  and  $pp$  pairs in the nucleus of interest.
- If we break up an SRC  $pp$  pair, we expect the recoil proton to be highly deflected by GLAD and to detect it in the RPC detector. The information on this proton, combined with the information on the two scattered protons in CALIFA and with TOFD fragment information, gives us important information on the SRC  $pp$  pairs properties.

The following sections contain more detailed information on each individual detection system.

### 2.2.1 Incoming detectors

The incoming detectors are designed to provide essential information about the incoming beam properties, including charge, trajectory, and starting time for time-of-flight ( $ToF$ ) measurements. A 3 mm thick octagonal scintillator detector (LOS) was employed to measure the starting time of the beam. The trajectory of the incoming ion was determined using the positions recorded by two MWPCs. The beam charge,  $Z_{\text{beam}}$ , was identified through energy loss measurements obtained from both the LOS and MUSLi detectors.

The following section provides detailed information on these incoming detectors.

#### LOS and ROLU

The LOS detector is used as a starting reference for  $ToF$  measurements and as a trigger for the incoming beam [94]. It is located at a distance of about 2 m upstream with respect to the target. A photo of the design of the detector is shown in Fig. 2.4. The active area of LOS is represented by an octagonal plastic scintillator of dimension 65 mm diameter with a thickness of about 3 mm (Fig. 2.4, top left). The thickness is chosen for each experiment to minimize the material in the beamline (that could induce unwanted reactions) while maintaining sufficient light output and excellent time resolution. When a charged particle hits the scintillator, it produces light which is collected by eight PhotoMultipliers Tubes (PMTs) attached on every side of the octagonal-shaped scintillator (Fig. 2.4, top right). A charge information (from the integrated signal over time that is proportional to the particle energy loss) and arrival time of the particle (obtained by averaging the time signal of the 8 PMT) are recorded and used to

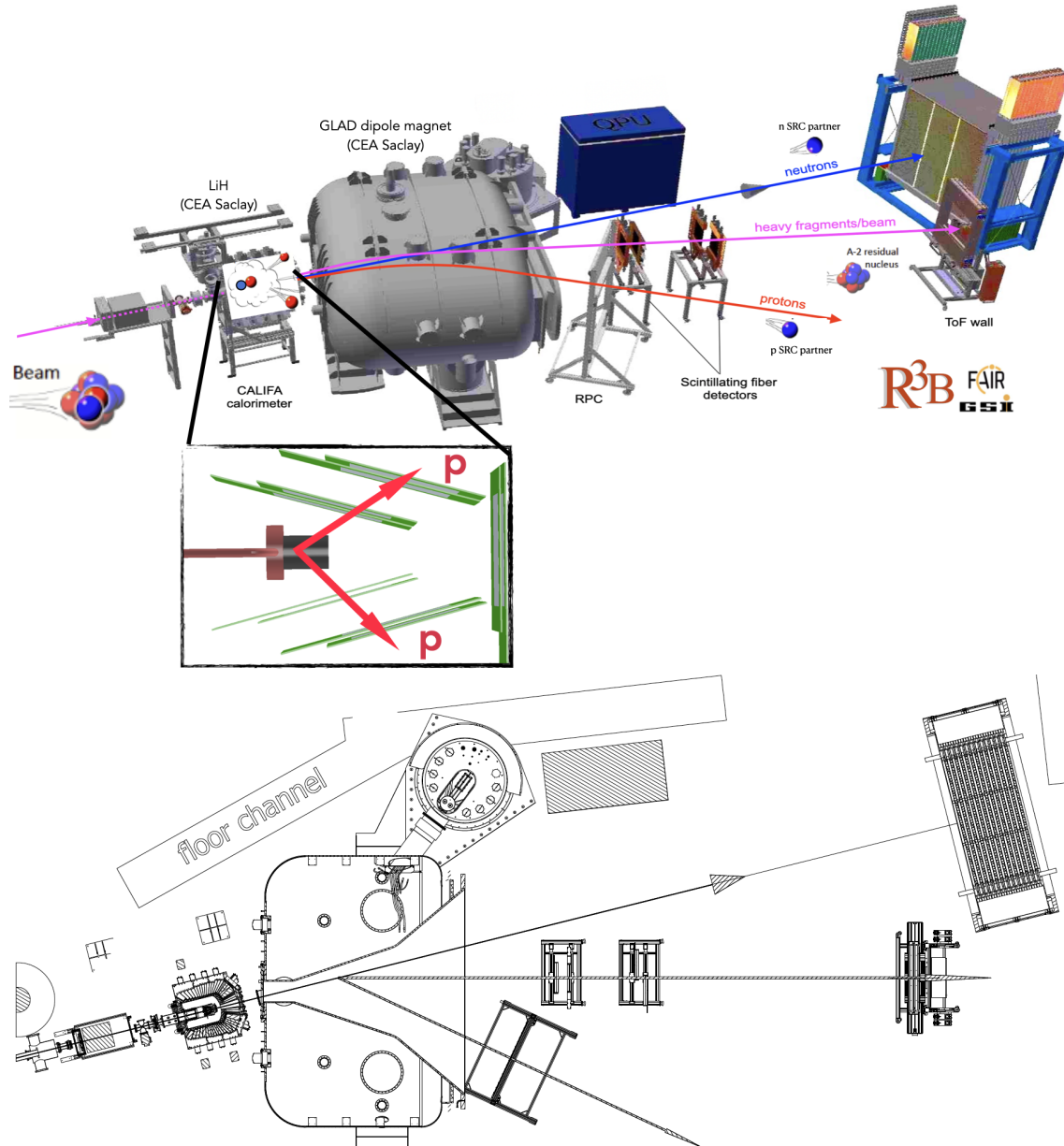


Figure 2.3: The  $R^3B$  setup in Cave C. At the entrance of the experimental hall, the incoming beam is monitored via LOS and collimated via ROLU onto the reaction target. The target and silicon trackers (in the rectangular box) are situated inside the CALIFA detector, which measures protons and  $\gamma$ -rays emerging from the target. The outgoing forward-focused reaction fragments are measured in the corresponding tracking systems (Fiber+TOFD) after the GLAD magnet. The SRC recoil  $n$  and  $p$  are detected by NeuLAND and RPC detectors, respectively.

determine energy loss, time, and position of a particle hit in the scintillator. Fig. 2.4 shows in the bottom panel a photo of the final configuration of LOS after gluing the PMTs at each side of the octagonal scintillator.

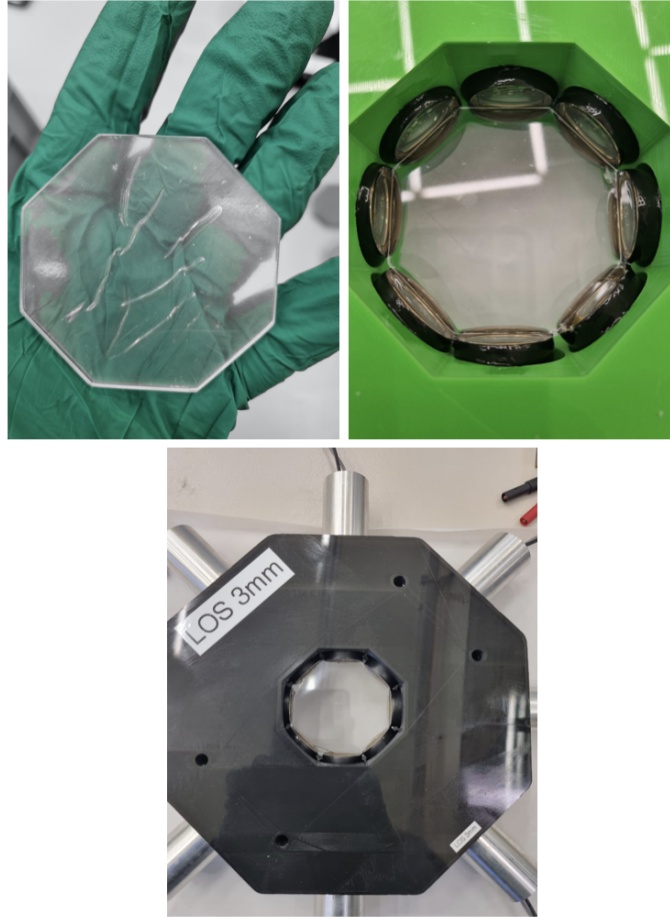


Figure 2.4: Top Left: LOS Octagonal shaped scintillator. Top right: LOS with the octagonal-shaped scintillator coupled to the 8 PMTs, one for each side. Bottom: the final version of LOS with the octagonal scintillator and the PMTs.

The ROLU detector [94] consists of four rectangular scintillators where two of each forming a slit in the vertical and horizontal direction (see Fig. 2.5). The ROLU signal is used as a veto to exclude particles with large offset with respect to the beam-line axis. In the discussed experiment, the ROLU aperture of  $\pm 1\text{cm}$  was employed in both the vertical and horizontal directions. The aperture can be adjusted by closing or opening the vertical and horizontal slits made by the scintillators of ROLU.

### MWPC (Multi-Wire Proportional Chambers) and MUSic for Light ions (MUSLi)

Two MWPCs labeled in our experiment as MWPC0 and MWPC1 are used for the position measurements of the incoming beam [94; 95; 96]. Each MWPC is composed of a plane of wires sandwiched by two foil planes, one segmented horizontally and the other segmented vertically. The wires are placed in parallel and separated by the same distance, on the central plane of two foils perpendicular to the incoming beam. The active dimension of the detectors is  $200 \times 200 \times 5 \text{ mm}^3$ , and the gaseous volume is  $200 \times 200 \times 10 \text{ mm}^3$ .

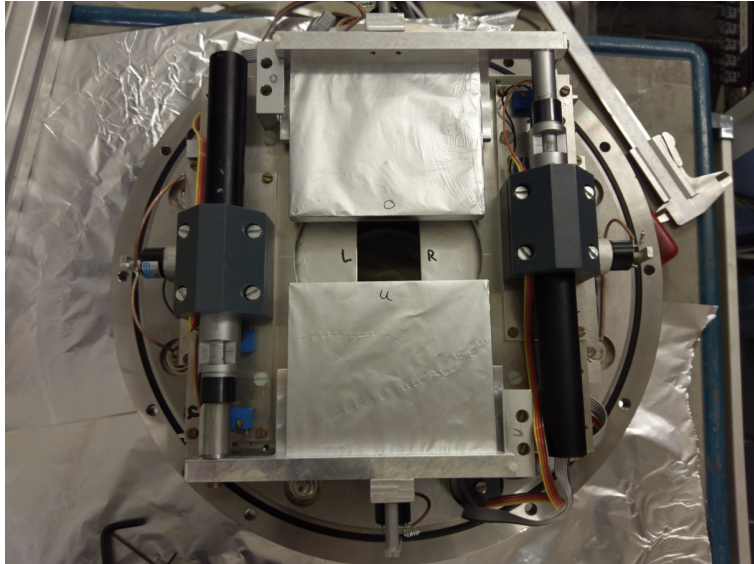


Figure 2.5: Photo of ROLU detector with the 4 scintillators to form a slit [94].

In more detail, the geometrical characteristics of the two MWPCs are:

- **MWPC0** includes input and exit windows made of  $12\ \mu\text{m}$  of Mylar; 64 vertical pads, each with a width of 3.125 mm, where the pads are aluminum ( $Al$ ) evaporated on a  $12\ \mu\text{m}$  foil of Mylar; one plane of horizontal wires, each with a diameter of  $5\ \mu\text{m}$  made of tungsten ( $W$ ); one "cathode" plane made of  $12\ \mu\text{m}$  Mylar; one plane of vertical wires, each with a diameter of  $5\ \mu\text{m}$  made of tungsten ( $W$ ) and 64 horizontal pads, each with a width of 3.125 mm [94].
- **MWPC1** includes one plane of 64 vertical pads segmented into two (up/down), one plane of horizontal wires, and one plane of 40 horizontal pads. The vertical pads have a width of 3.125 mm and are made of aluminum evaporated on a  $12\ \mu\text{m}$  thick Mylar foil. The horizontal pads have a width of 5 mm [94].

A schematic view of the MWPC is presented in Fig. 2.6 (left). The wires are set to a high voltage, acting as anodes, while two foils are led to ground potential and serve as cathodes. A non-uniform electric field is formed between anode wires and cathode planes, as shown in Fig. 2.6 (right). The chamber is filled with a mixture of gas 84% Ar + 16%  $\text{CO}_2$ . When an ion passes through the MWPC, it ionizes the gas into ions and electrons. Both ion and electron signals can be utilized to determine the path of ions. The electric field within the chamber accelerates the electrons towards the anode wires, resulting in an avalanche multiplication of charges. The cathode pads are arranged in two orthogonal planes. As electrons drift towards these anode wires, the ions induce a signal that can be read out by the cathodes to determine the position of the original ionizing event. **MUSLi** is the modified double ionization chamber TWIN MUSIC [94], consisting of a quarter of TWIM MUSIC and serves as the  $\Delta E$  detector for the incoming ions. It consists of a double ionization chamber with a central cathode and is read out by 16 anodes along the length of the detector in the beam direction. Each anode is segmented up/down. The chamber was filled with  $\text{CH}_4$  [79%], Ar [20%] and  $\text{CO}_2$  [1%] gas mixture. The signal from the anodes is fed into a digitization module via 16 dedicated pre-amplifiers [94]. The reading of 16 anode signals allows a horizontal trajectory to be deduced, redundantly with the MWPCs. A dedicated firmware was employed to discriminate small amplitude signals from light ions properly.

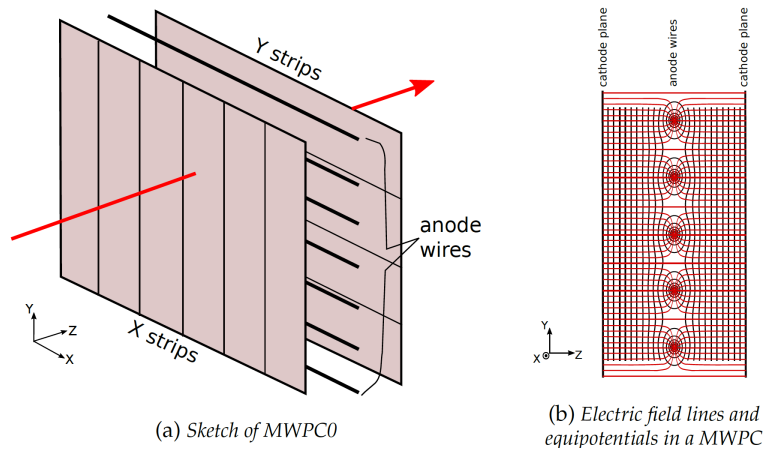


Figure 2.6: Structure of a MWPC and the internal electric field. Left: a sketch of the MWPC0/1 detector. It is composed of a plane of anode wires sandwiched by two cathode foils. The wires are placed horizontally, and two cathodes are segmented vertically and horizontally to measure positions in the directions for the  $X$  and  $Y$  coordinates, respectively. The red arrow represents the flight path of the secondary beam. Right: Schematic view of the electric field between anode wires and cathode planes. Red lines are electric field lines, and black lines represent equipotentials [94].

### 2.2.2 Target recoil detectors

The target recoil detector system, which includes all detectors surrounding the target, is essential for investigating QFS reactions. The 5 cm thick  $LH_2$  target was surrounded by the CALIFA calorimeter (see Fig. 2.7), which detects  $\gamma$  rays and light particles, such as protons, resulting from QFS reactions. To obtain angular information about the reaction products, specifically the two scattered protons, the target area was equipped with an array of eight Single-Sided Silicon Strip Detectors (SSSDs) as part of the FOOT setup.

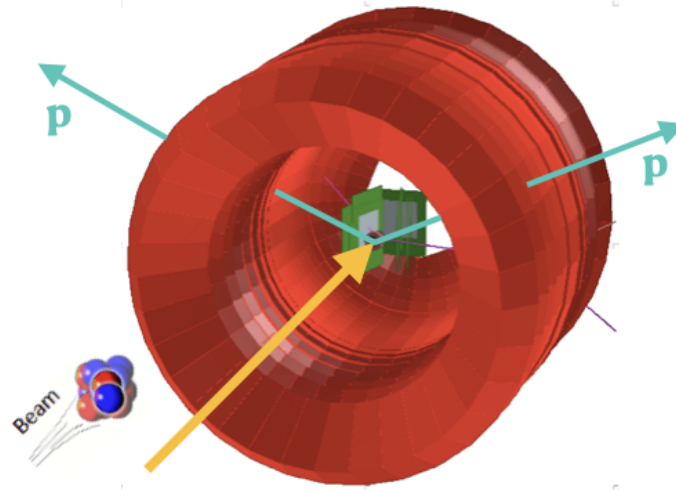


Figure 2.7: Geometry volume showing the  $LH_2$  target, surrounded by the FOOT detectors and the CALIFA calorimeter. The Figure was generated using R3BRoot simulation to reproduce the CALIFA and FOOT geometry.

### The COCOTIER Liquid Hydrogen Target

An important part of the  $R^3B$  Setup is the Liquid Hydrogen target ( $LH_2$ ). It allows us to study QFS reactions in inverse kinematics, and it represents the hadronic probe that breaks up SRC pairs, allowing us to study their properties. The target has been built at IRFU<sup>5</sup> (CEA-Saclay) within the ANR<sup>6</sup> grant COCOTIER<sup>7</sup> [97]. The target is designed to perform quasi-free scattering experiments and, due to its thickness of about 5 cm, is meant to be coupled with a tracking detector to allow vertex reconstruction.

The hydrogen is liquefied in a cryostat equipped with a cryocooler (cold head mounted on the cryostat and compressor in the vicinity of the cryostat) with a temperature of 19 K. The hydrogen is liquefied in the condenser and falls by gravity into the target cell. A turbomolecular pump is used to achieve a good vacuum ( $10^{-7}$  in the cryostat and in the target chamber) to prevent heat flux via convection.

The full system is sketched below in Fig. 2.8. The target cell is made of Mylar and composed of an entrance window and an exit window. The thickness corresponds to  $120\ \mu\text{m}$  for the entrance and  $180\ \mu\text{m}$  for the exit window and the cylindrical body. The target cell is further wrapped in several  $5\ \mu\text{m}$  thick multilayer insulation foils to reduce heat flux via radiation. The target cell diameter is 42 mm, compatible with the beam spot size. After liquefaction, the hydrogen is at 20.3 K and 1041 mbar. A silicon tracker further surrounds the target to reconstruct the reaction vertex position inside the target.

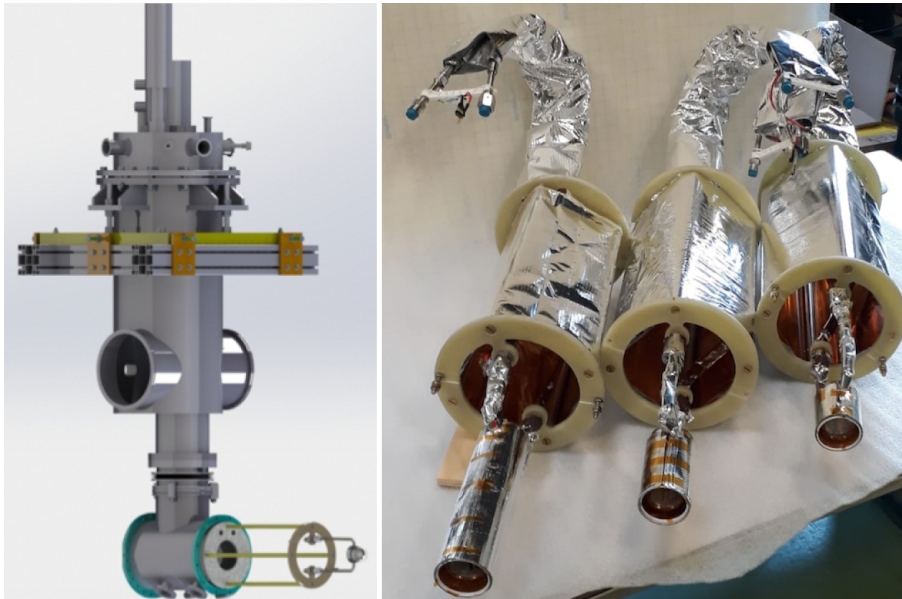


Figure 2.8: Left: technical drawing of the target and cryostat ensemble. Right: photos of the three target cells with their support and pipes, all wrapped in the multilayer insulation foils [97].

<sup>5</sup>Institute for Research on the Fundamental Laws of the Universe (Institut de recherche sur les lois fondamentales de l'univers).

<sup>6</sup>French National Research Agency (Agence Nationale de la Recherche).

<sup>7</sup>COrrélatiOns à COurte porTée et spin Isotopique à  $R^3B$ .

## FOOT (FragmentatiOn Of Target)

The FOOT (Fragmentation Of Target) detectors, as depicted in Fig. 2.10, were utilized in the  $R^3B$  2022 experimental campaign. This experiment marked the first use of twelve silicon microstrip detectors by the  $R^3B$  collaboration.

FOOT's semiconductor track detectors are designed as a series of  $p - n$  junction diodes operated under reverse bias. This configuration creates a sensitive region devoid of mobile charge carriers [98], generating a strong electric field that drives the separated electron-hole pairs toward the electrodes. To balance the need for minimizing acquisition channels with maintaining high spatial resolution, the detectors employ a floating strip readout scheme. In this configuration, connections alternate every three strips (see Fig. 2.9), and the charge collected on non-connected strips is capacitively transferred to neighbouring readout strips [99].

The silicon sensors manufactured by Hamamatsu Photonics are notably thin at  $150 \mu\text{m}$ , which is considerably thinner than typical microstrip sensors. They feature a  $96 \times 96 \text{ mm}^2$  active area segmented into 640 strips, each with a  $50 \mu\text{m}$  implantation pitch [100]. Each IDE1140 ASIC [100] reads out 10 strips, using a floating strip approach with a final pitch of  $150 \mu\text{m}$ , where every readout strip is paired with two floating strips. The electronics' readout time is just under  $100 \mu\text{s}$ , necessitating a carefully defined dead time. This dead time must balance approaching the intrinsic readout time of the ASIC while avoiding interference from consecutive readout cycles due to limitations in the front-end electronics.

The strip signal is initially very weak and is preamplified by the ASICs before being processed by a combination of a 32-bit ADC and an FPGA board. This preamplification process shapes the signal, with the amplitude increasing with the pre-amplification time up to a certain point, after which it begins to decrease. The analog signal from the ASICs is ultimately digitized by a 12-bit ADC.

The recoil system is composed of a total of 12 FOOT detectors (Fig. 2.10, bottom). 4 FOOT planes (oriented along the  $Y - X - X - Y$  coordinates, from closest to furthest relative to the target) form a telescope to track the scattered protons. The two telescopes (one on the Wixhausen side (right side with respect to the beam direction) and one on the Messel side (left side with respect to the beam direction)) cover the polar angle  $\theta$  in the  $X - Z$  plane from  $22^\circ$  to  $64^\circ$ .

The purpose of the two telescopes is to obtain the angle information of the two scattered protons and, after combining this information with the energy, derive the momentum of the protons. Other 4 FOOT detectors (oriented  $Y - X - X - Y$ , from closest to furthest relative to the target along the  $z$  direction) are located in the beamline to obtain a particle identification of the reaction products before the GLAD magnet. A photo of the target surrounded by the FOOT detector system is shown in Fig. 2.10.

Due to several issues with the FOOT detectors, such as baseline fluctuations, high noise levels, and very low efficiency, we decided not to use the angular and positional information from the FOOT detectors for the  $(p, 2p)$  proton hits. Instead, to reconstruct the angle of the two scattered protons, we will rely solely on data from the CALIFA detector. Since reconstructing the FOOT vertex position was not feasible, we will derive the vertex position using the projection of the MWPC tracks at the center of the target,  $V_{\text{mwpc}} = (V_{x,\text{mwpc}}, V_{y,\text{mwpc}}, 0)$ , where the target is considered to be centered at the origin. More information will be given in the FOOT calibration section (Sec. 3.2.2) in chapter 3.

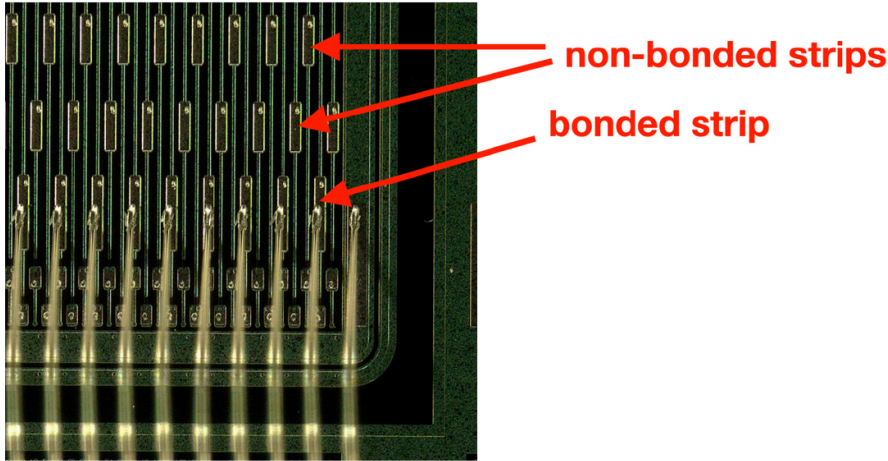


Figure 2.9: Strip configuration with a highlight on the bound strip every 2 floating strips [94].

### The CALIFA detector

One of the key detectors in the  $R^3B$  setup is CALIFA (CALorimeter for the In-Flight detection of  $\gamma$  rays and light-charged particles), which is composed of 2560 CsI(Tl) crystals. It is designed to work both as a high-resolution spectrometer as well as a high-efficiency calorimeter in its full configuration (Barrel + Endcap). The CALIFA calorimeter surrounds the COCOTIER LH<sub>2</sub> reaction target. Its main purpose in the current experiment is to detect and measure the energy of the two scattered protons of the  $(p,2p)$  reactions at large laboratory angles. It is also employed for the detection of  $\gamma$ -rays and light-charged particles. CALIFA detects stopped  $\gamma$ -rays up to 30 MeV and stopped protons up to 300 MeV. For protons exceeding 300 MeV, we can reconstruct the full energy of the protons from their deposited energy in CALIFA. A pulse-shape analysis of the CsI crystal response could differentiate between stopped protons and punch-through protons. For the current experiment, CALIFA consists of two parts, the iPhos (conical shape in the forward direction) and the Barrel (cylinder-like shape around the target) as it is possible to observe in Fig. 2.11 (Tab. 2.2 presents the nominal specifications of CALIFA are reported) [101; 102]. In the current experiment, the CEPA part of the CALIFA Endcap is not used (see Fig. 2.11).

The iPhos and barrel detector units are all CsI(Tl) crystals, wrapped in a reflective foil and glued to an APD<sup>8</sup> readout. The Barrel part showed in Fig. 2.12 covers a polar angular range of  $43^\circ < \theta < 140^\circ$  (see Tab. 2.2 for more details). CALIFA Barrel consists of a total of 1952 crystals arranged in carbon fiber alveoli. These crystals are divided into six types corresponding to six angular sectors. The first five forward angular sections are filled with four crystals each, representing two different geometries that are mirror images of each other. The alveolus covering the most backward angles is filled with a single crystal. More properties of the Barrel can be found in Tab. 2.2. In our experiment, the barrel part is optimized for proton detection. The iPhos part is dual-phased for  $\gamma$ 's and protons detection. The crystals in the iPhos are connected to double-range preamplifiers, which allow the team to collect data with two different gains. Typically, the lower gain is used to measure light-charged particles, and the higher one is used to measure gammas. In the barrel area, this possibility does not exist, and only one mode is possible. In the current experiment, the lower-gain mode was used. The iPhos covers a polar angular range of  $20^\circ < \theta < 43^\circ$  (in Tab. 2.3 the properties of CALIFA Endcap (iPhos+CEPA) are presented).

<sup>8</sup>Avalanche Photodetectors.

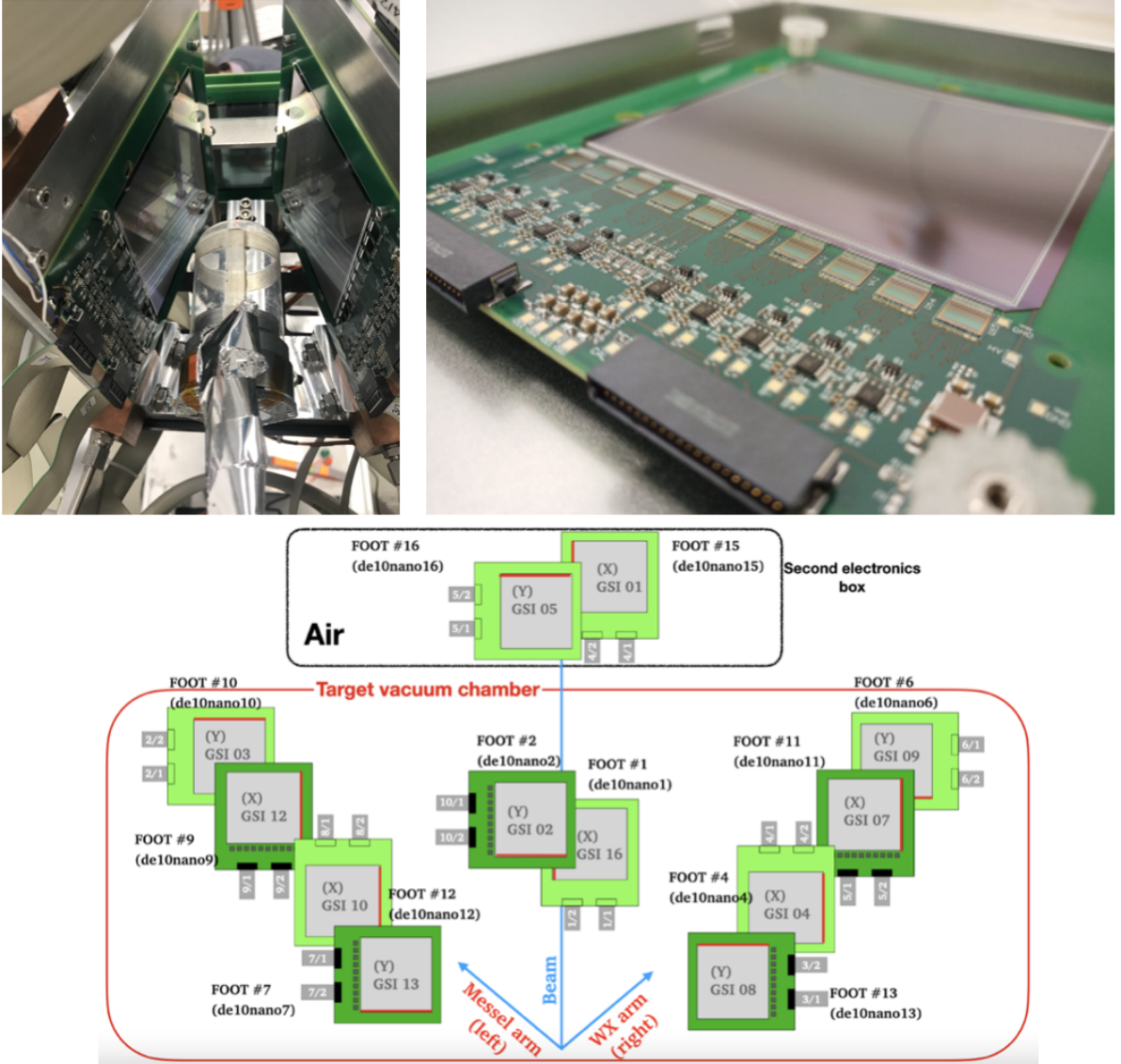


Figure 2.10: Top left: top view of the system  $\text{LH}_2$ +FOOT. The target is surrounded by the two FOOT telescopes to detect the scattered protons and the reaction products. Top right: zoom photo of a single FOOT detector. The silicon buffer and front board are visible, in particular, the 10 ASICs located below the silicon layer. Bottom: scheme of the configuration of the 12 FOOT detection system around the target [94].

<b>Intrinsic photopeak efficiency</b>	40% (at $E_\gamma = 15$ MeV projectile frame)
<b><math>\gamma</math>-ray sum energy resolution <math>\Delta(E_{\text{sum}})/\langle E_{\text{sum}} \rangle</math></b>	$< 10\%$ for 5 $\gamma$ -rays of 3 MeV
<b><math>\gamma</math>-ray Energy resolution</b>	$< 6\% \Delta E/E$ for 1 MeV $\gamma$ -rays
<b>Energy range for protons</b>	Up to 700 MeV in Lab system
<b>Energy resolution, protons stopped</b>	$< 1\% \Delta E_p/E_p$
<b>Energy resolution, protons punch through</b>	$< 7\% \Delta E_p/E_p$
<b>Full energy peak efficiency for protons</b>	$> 50\%$ (for all energies)
<b>Proton-<math>\gamma</math>-ray separation</b>	for 1 to 30 MeV $\sqrt{E}$ (at $E_p = 500$ MeV)

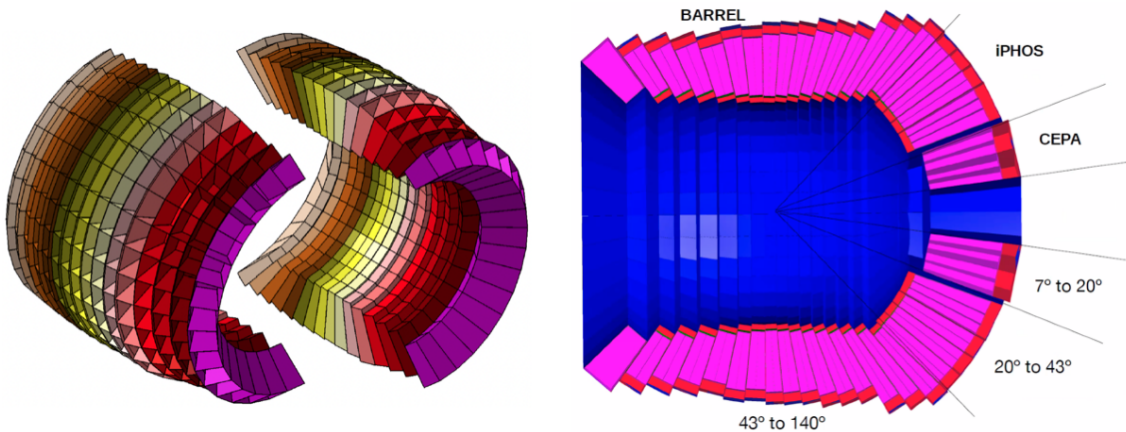
Table 2.1: Nominal specifications of the CALIFA calorimeter (at  $\beta = 0.82$ ). These parameters are defined by the physics program discussed in the  $R^3B$  Technical Proposal [101; 102].

Parameter	Value
Inner radius	30 cm
Number of crystals	1952
Different crystal geometries	11
Average crystal volume (CsI(Tl))	$\approx 285,000 \text{ cm}^3$
Average crystal weight (CsI(Tl))	$\approx 1300 \text{ kg}$
Full operation system weight	$\approx 6100 \text{ kg}$

Table 2.2: Specifications of the CALIFA Barrel [101].

Property	Value
Inner radius	41 cm
Number of crystals	608
Different crystal geometries	18
Crystal volume (CsI(Tl))	$\approx 90.020 \text{ cm}^3$
Crystal weight (CsI(Tl))	$\approx 408 \text{ kg}$
Crystal volume (LaBr <sub>3</sub> /LaCl <sub>3</sub> )	$\approx 10.700 \text{ cm}^3$
Crystal weight (LaBr <sub>3</sub> /LaCl <sub>3</sub> )	$\approx 47 \text{ kg}$
Full operation system weight	$\approx 1100 \text{ kg}$

Table 2.3: Bulk properties of the CALIFA Endcap. I remind the reader that in the current experiment, we only use the IPhos part of the Endcap [102].

Figure 2.11: Left: Artistic view of the CALIFA calorimeter. The inner radius of the Barrel is 30 cm. The main symmetry axis is placed along the beam direction and defines the origin for polar angles [101]. Right: Side view of the different sections of CALIFA with the  $\theta$  angular range. In our experiment, we used CALIFA with Barrel and iPhos, without CEPA [102].

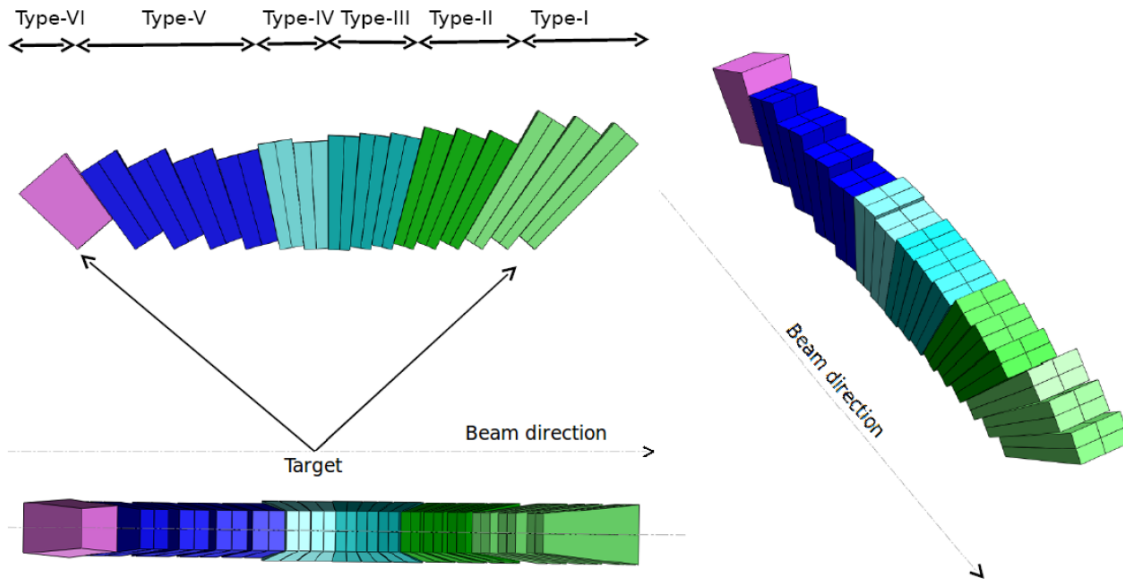


Figure 2.12: Different artistic views of CALIFA Barrel crystals geometry [101]. It is possible to observe the different sections of CALIFA characterized by different crystal lengths. Following the beam direction, the crystal length increases. This is designed to match the forward focusing of the gamma-rays and light-charged particles.

### 2.2.3 Outgoing detectors

The outgoing detectors are designed to reconstruct the properties of various reaction products. Specifically, they measure:

- The recoil SRC pair neutron (after the  $pn$  pair breakup), arriving in NeuLAND, resulting from the  $(p,2pn)$  reaction.
- The recoil SRC pair proton (after the  $pp$  pair breakup), detected in RPC, resulting from the  $(p,3p)$  reaction;
- The residual fragments (after SRC pair removal) of the reaction with mass numbers  $A-2$ , including their positions as detected in the fiber detectors and their charges as measured in ToFD.

The following section provides detailed information on these outgoing detectors.

#### Large-acceptance dipole magnet GLAD

GLAD is a zero-degree superconducting dipole magnet with a large angular acceptance ( $\pm 80$  mrad for neutrons) and an adjustable integrated magnetic field of up to  $5 \text{ Tm}$  [103]. The  $R^3B$ -GLAD magnet features a unique design with four superconducting coils arranged in a “Tigra-Trace” (Tilted GRAded Trapezoidal RACe track) configuration, as illustrated in Fig. 2.13.

The design includes two main racetrack-shaped coils that widen from the entrance to the exit and are tilted vertically. These are complemented by side coils oriented horizontally with respect to the magnetic symmetry axis, which contributes to both the main dipole field and magnetic shielding. This configuration minimizes the stored energy by positioning the coils close to the particle and fragment track envelopes, thereby reducing the useful magnetic volume. The geometry ensures a sufficient angular aperture while maintaining a low fringe field in the target region.

The main coils feature a gradually increasing number of turns from the entrance to the exit, which produces a relatively flat magnetic field plateau of  $2.7 \text{ T}$  within the magnetic volume

while keeping the surface field strength below 6.5 T. The GLAD current, and consequently the magnetic field strength, was individually adjusted for each beam energy to direct  $^{12}\text{C}$  and  $^{16}\text{C}$  isotopes onto the 14-degree line relative to the incoming beam axis. Specifically, for a  $^{12}\text{C}$  beam, the GLAD current was set to approximately 2545 A, while for a  $^{16}\text{C}$  beam, it was set to around 3420 A. The spectrometer is dispersive in the x position, thus having a more precise value in X.

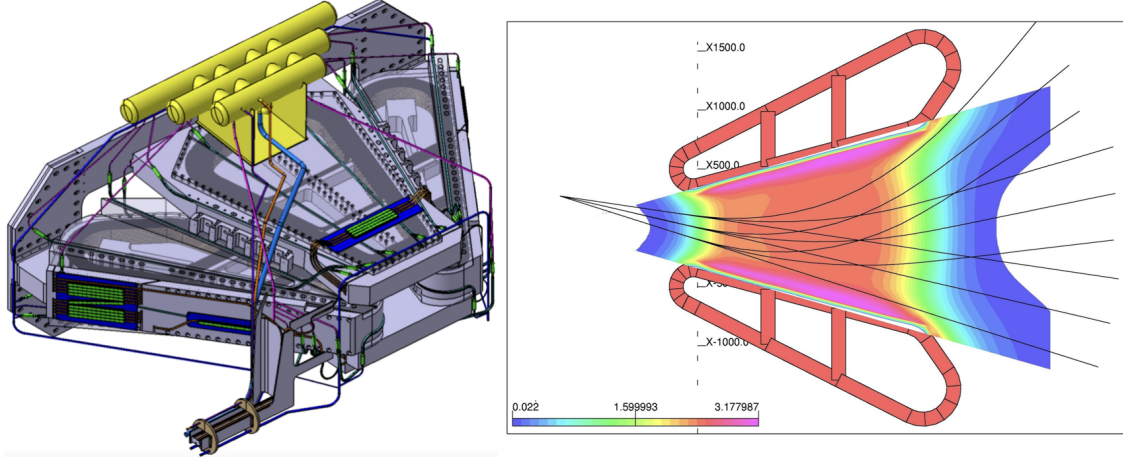


Figure 2.13: Left: View of the cold mass (cryostat + magnetic coils) of  $R^3B$ -GLAD. Right: Magnetic field map of GLAD. The red lines are different tracks of particles in the magnetic field volume [103].

### Fiber detectors

Fiber detectors, in combination with TOFD, are essential for determining the properties of the outgoing fragments (momentum,  $Z$ ,  $A/Z$ ). In the current experiment, four large fiber detectors, positioned at different distances from the GLAD bending point, were employed to determine the  $X$  and  $Y$  position coordinates of the reaction fragments.

A design scheme is presented in Fig. 2.14. Fibers 30, 31, 32, and 33 are detectors with 512 fibers, each with a thickness of 1 mm and a square cross-section. These fibers form an active area of approximately  $50 \times 50 \text{ cm}^2$  and are read out on both sides by two Hamamatsu multi-anode PMT H13700 devices with 256 anodes [94].

The detectors were placed after the GLAD magnet along the  $14^\circ$  line. Specifically, the first fiber encountered after GLAD is Fiber 32, used for  $X$  position measurement, located 4.3 meters from the GLAD bending point. Following this is Fiber 30, used for  $Y$  position measurement, positioned 4.9 meters from the GLAD bending point. At approximately 6 meters, two fibers were located side by side, with Fiber 33 on the NeuLAND side and Fiber 31 on the ToFD side, both used for  $X$  position measurements.

### Time-of-Flight wall detector TOFD

The TOFD detector [94; 104] was located behind the dipole magnet at 11 m from the GLAD bending point. It was positioned to cover the angular range of the fragment from  $11^\circ$  to  $17^\circ$ , with the  $14^\circ$  line centered in the middle of TOFD.

It measures the time-of-flight ( $ToF$ ) and the nuclear charge ( $Z$ ) of the reaction fragments produced after the interaction with the  $\text{LH}_2$  target. The nuclear charge of reaction products is obtained by precise energy-loss measurements of the fragments passing through the scintillator material. The detector working concept is based on the use of plastic scintillators spaces  $120 \times 80 \text{ cm}^2$ . TOFD has four planes of scintillators, and the active part covers an area of  $120 \times 80 \text{ cm}^2$ .

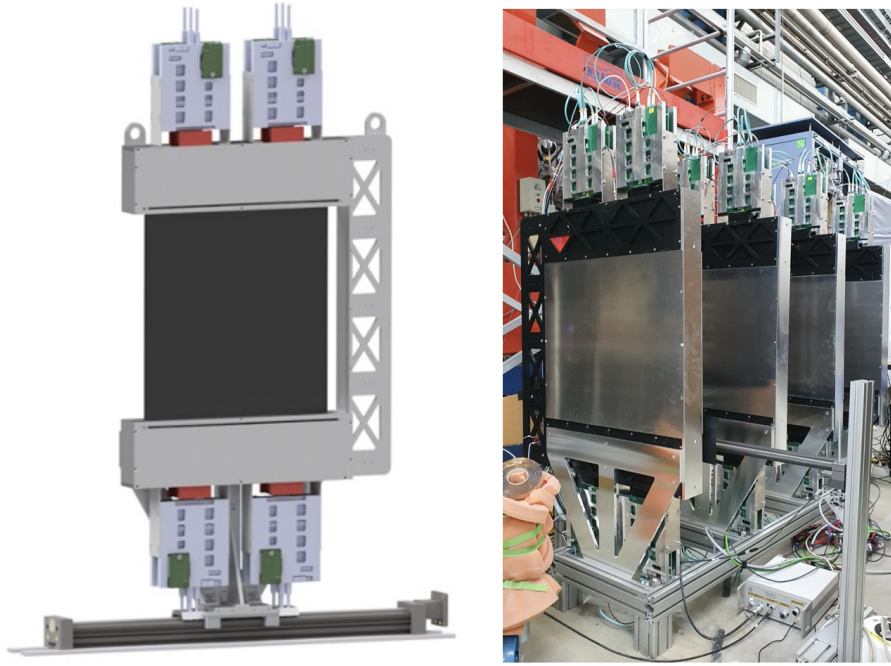


Figure 2.14: Left: a sketch of a fiber detector read on both sides by two Hamamatsu multi-anode PMT H13700 with 256 anodes. Right: photo of the 4 fibers detector used in the current experiment before the positioning in Cave C [94].

The paddles of successive planes are shifted by half a paddle width in order to cover small gaps between two neighboring bars by the previous or next plane. Each plane consists of 44 scintillator paddles spaced  $120 \times 80 \text{ cm}^2$ . The first two planes have scintillators with a thickness of 3 mm, and the last two planes with a thickness of 5 mm. Each scintillator paddle is directly coupled to a PMT on both far ends. The time and energy of a particle can be determined using two Photomultiplier Tubes positioned on either side of the detector. When a charged particle passes through the TOFD detector, it generates scintillation light in the detector medium. This scintillation light is detected by the two PMTs, which convert the light into electrical signals. The arrival times of the signals at both PMTs are recorded. The difference in arrival times ( $\Delta t$ ) between the two PMTs is used to determine the particle's path length and, consequently, its velocity. The total signal amplitude from the PMTs is proportional to the energy deposited by the particle in the detector. By calibrating the PMT response, the energy of the particle can be quantified.

## NeuLAND

NeuLAND (New Large-Area Neutron Detector) is the next-generation neutron detector for the  $R^3B$  experiment at FAIR (Facility for Antiproton and Ion Research [91]). NeuLAND detects neutrons with energies from 100 MeV to 1000 MeV, featuring a high detection efficiency, a high spatial and time resolution and a large multi-neutron reconstruction efficiency. This is achieved by a highly granular design of organic scintillators: 1300 individual submodules with a size of  $5 \times 5 \times 250 \text{ cm}^3$  are arranged in 13 double planes with 100 submodules each, providing an active area of  $250 \times 250 \text{ cm}^2$  and a total depth of 3 m [93] (see Fig. 2.16). The spatial resolution due to the granularity, together with a time resolution of 150 ps, ensures high-resolution capabilities in the measurement of the neutron momentum. It is positioned under zero-degree angles in its available configuration for the detection of forward-emitted partner neutrons and decay neutrons at a distance of about 10 m from the GLAD bending point. The NeuLAND efficiency estimation for the current experiment is presented in App. A. 4

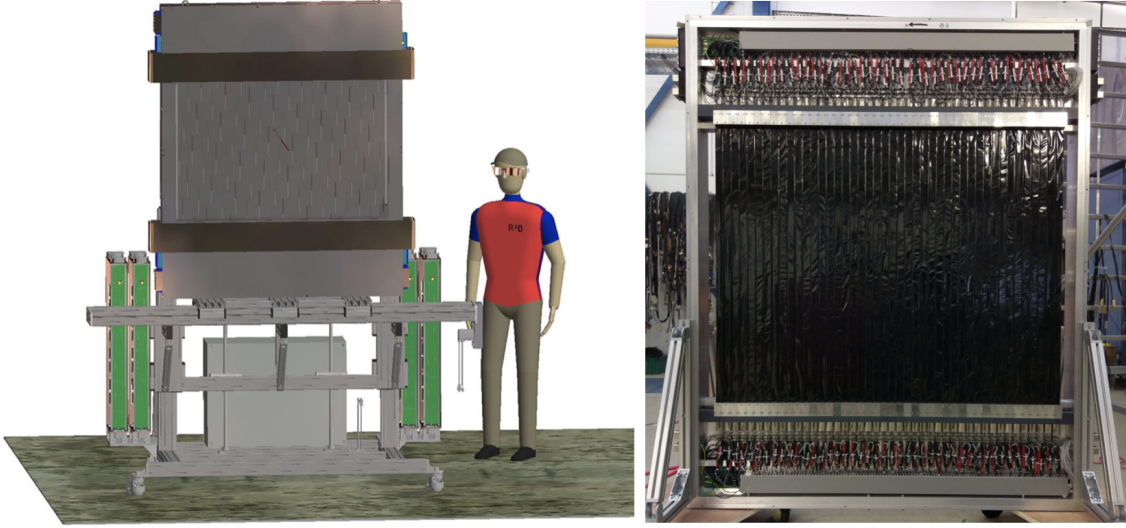


Figure 2.15: Left: Mechanical design of the detector: The detector is mounted on an  $x/y$ -table, which allows to move the detector through the beam. In this way, the position calibration, gain matching, and time-offset determination can be performed. The bands at the top and bottom are made of Mu-metal and can be used for magnetic shielding of the PMTs when the detector is mounted close to the superconducting magnet GLAD. The electronics are mounted on the left and right side (green boxes) [104]. Right: Front view of plane 1 of TOFD with the 44 scintillator bars coupled with a PMT at both ends [94].

More information can be found in Tab. 2.4 and in this reference [93].

Parameter	Value
Modularity	1300 scintillator bars in 13 double-planes
Detector Dimensions	$250 \times 250 \times 300 \text{ cm}^3$
Bar Dimensions	$5 \times 5 \times 250 \text{ cm}^3$
Light Readout	2600 PMTs
Electronics Readout	TAMEX3+FQT
Angular Acceptance	80 mrad at 15 m
Time Resolution	$\sigma < 150 \text{ ps}$
Spatial Resolution	$\sigma \approx 1.5 \text{ cm}$
Excitation Energy Resolution	$\Delta E < 20 \text{ keV}$ at 100 keV
In Efficiency	$\approx 95\%$ at 400 MeV
Multi-Neutron Recognition	$\approx 50\% - 70\%$ for 4n

Table 2.4: Overview of characteristic parameters of NeuLAND in the current experimental situation [93].



Figure 2.16: Left: Schematic layout of one NeuLAND frame supporting 15 double planes in total, here equipped with 13 double planes. A maintenance platform on top of the double planes allows for easy access to the readout electronics hosted in the boxes on both sides above the double plane, the high voltage supply boards are located in the lower left and right corners of each double-plane [93]. Right: Photo of the NeuLAND detector located in Cave C [94].

### Resistive Plate Chamber (RPC) detector

The RPC detector [105] consists of two multigap RPC modules, each of them confined in a permanently sealed plastic<sup>9</sup> gas-tight box equipped with feed-throughs for gas and High Voltage (HV) connections.

Each RPC module has six gas gaps defined by seven 1 mm thick float glass<sup>10</sup> electrodes of about  $1550 \times 1250 \text{ mm}^2$  separated by 0.3 mm nylon mono-filaments. The HV electrodes are made up of a semi-conductive layer<sup>11</sup> applied to the outer surface of the outermost glasses with airbrush techniques. The two modules are read out in parallel by a readout strip plane<sup>12</sup> equipped, in one side, with 41 copper strips (29 mm width, 30 mm pitch, and 1600 mm long) located in between the two modules. Two ground planes, located on top and bottom of the two-module stack, complete the readout planes. The complete structure is enclosed in an aluminium box that provides electromagnetic insulation and mechanical rigidity. The RPC detector operates based on the principle of gas ionization and avalanche multiplication. When a charged particle passes through the RPC, it ionizes the gas, creating electron-ion pairs. This initial ionization occurs due to the energy deposited by the particle. The electric field in the gas gap accelerates the free electrons towards one of the resistive glass. The collected ions charge (at the readout plane) creates a voltage pulse that is read out by an external electronics system. The timing and amplitude of this pulse provide information about the position and energy of the incident particle. In Fig. 2.17, a schematic of the inner structure of the module is shown. The RPC was operated in an open gas loop with a mixture of 98%  $\text{C}_2\text{H}_2\text{F}_4$  and 2%  $\text{SF}_6$  at a pressure of a few millibars below atmospheric pressure. The detector working point was measured to be about 3000 kV/gap.

<sup>9</sup>Poly(methyl methacrylate) (PMMA) for the frame and Polycarbonate (PC) for the covers.

<sup>10</sup>Bulk resistivity of  $\approx 4 \cdot 10^{12} \Omega\text{cm}$  at 25 °C

<sup>11</sup>Based on artistic acrylic paint with around  $100 \text{ M}\Omega^2$  of sheet resistivity.

<sup>12</sup>Made of 1.6 mm Flame Retardant 4 (FR4) Printed Circuit Board (PCB).

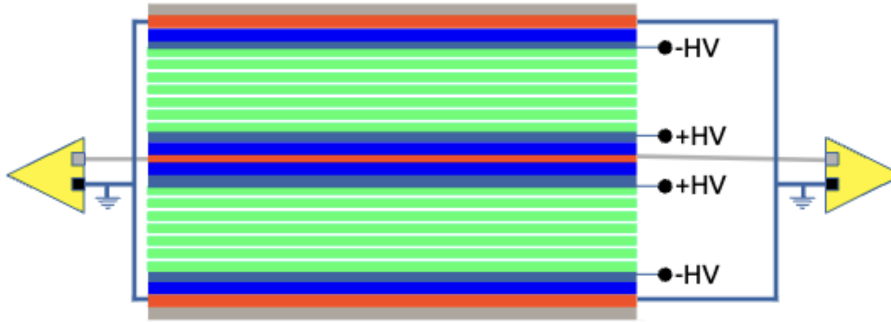


Figure 2.17: Schematic of the internal structure of the of RPC detector (not to scale). Grey - Aluminum box. Red - Readout electrodes. Blue - Plastic tight box. Black - HV electrodes. Green-Glass Electrodes. Yellow triangles - FEE. The beam comes perpendicular to the RPC structure [105].

Three scintillation bars, two verticals,  $V_{sc1}$  and  $V_{sc2}$  and one horizontal,  $H_{sc}$  together with a small, 80 mm long, scintillator,  $D_{sc}$ , were placed behind and parallel to the surface of the RPC, as shown in Fig. 2.18, for calibration purposes (see Chapt. 3). The scintillators are read out on both sides by photomultiplier tubes, the output signals of which are connected to the same FEE that reads the RPC but without the amplification stage. The RPC efficiency estimation for the current experiment is presented in App. A.

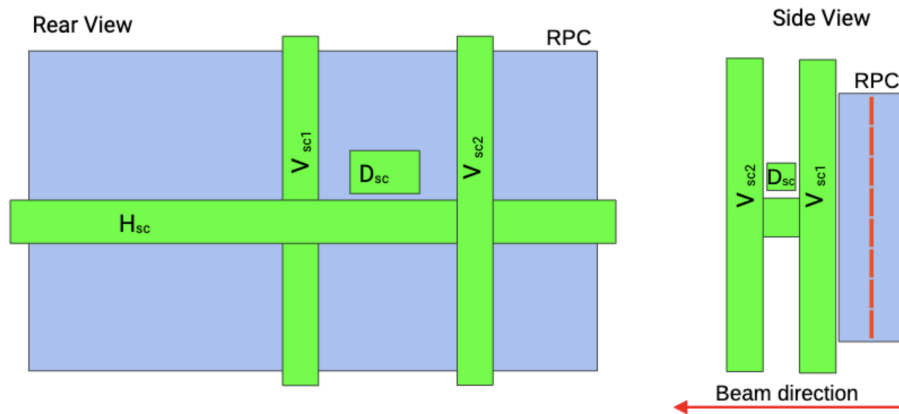


Figure 2.18: Schematic of the positioning of the scintillator behind the RPC, rear view on the left and side view on the right [105].

### 2.2.4 Data Acquisition System of the $R^3B$ Collaboration

The data acquisition (DAQ) system for the  $R^3B$  collaboration is a sophisticated setup designed to handle the high data rates and complex event structures generated during experiments at FAIR [91; 94].

#### Data Acquisition System (DAQ) and Trigger Logic

The primary objective of the  $R^3B$  data acquisition system (DAQ) is to synchronize and correlate the data obtained from various detector systems and their respective DAQ sub-systems. The DAQ system employs three different software: Drasi for most detectors [106], the multi-branch system MBS for CALIFA [101; 107], and DABC<sup>13</sup> for the RPC detector [108]. The event data layouts produced by these software are made compatible with the main  $R^3B$  DAQ, enabling uniform processing by subsequent data handling tools.

Data are acquired on an event-by-event basis using a global readout trigger. To minimize the recording of background noise unrelated to beam ion reactions, careful decisions are made on which events to save. Various detectors in the setup provide logic signals, indicating that data above their specific thresholds have been recorded. These signals serve as trigger conditions. A combination of such triggers within a given time window generates a Trigger PATtern (Tpat), of which there are sixteen, each individually configurable. The Tpats collected within the acceptance window are saved as a 16-bit bit-pattern, where each Tpat value is  $2^n$  (with  $n$  ranging from 0-15). The Tpat with the highest value is selected, and the corresponding trigger number is fired by the trigger logic module in the main DAQ.

One trigger condition is derived from the SIS18 extraction, correlating with the delivery of beam spills to the  $R^3B$  setup. This condition, termed "on-spill," is required for all Tpats related to beam ions. The anti-coincidence with the SIS18 extraction trigger signal is termed "off-spill" and is used for the calibration of detectors using cosmic muons (e.g., NeuLAND, CALIFA, TOFD, and RPC). "Off-spill" is recorded between spills or during dedicated calibration runs before and after beam time. When the "on-spill" signal from the accelerator system coincides with a signal from LOS and no signal from ROLU, it indicates a likely incoming ion that hit the target, termed the "Good Beam" Tpat. Adding the trigger condition from TOFD yields the "Fragment" Tpat, indicating that the incoming particle has an outgoing heavy fragment. Although this Tpat mostly represents unreacted beam, it can also signify reaction events.

Several trigger conditions, when combined with "on-spill" and "LOS!ROLU" (hit in LOS and veto from ROLU), form the reaction Tpats. For example, the "Neutron" Tpat requires a trigger condition from NeuLAND, indicating at least one neutron released during the reaction. Another reaction Tpat, "CALIFA OR," is triggered when at least one CALIFA crystal records a signal above a threshold, typically used as a  $\gamma$ -ray trigger. The primary reaction Tpat for this experiment is "p2p," triggered by at least two signals on opposite sides of CALIFA above a certain threshold, indicative of a QFS reaction.

Adding the condition that the crystals must be in the shadow of the FOOT detectors surrounding the target yields two additional Tpats: "CALIFA OR VETO" and "p2p VETO." Due to the long dead time of the FOOT detectors, the trigger logic differentiates triggers with and without FOOT, depending on whether FOOT's dead-time window is open. The rest of the DAQ does not accept an event when FOOT is about to release its dead time (does not accept a new event if FOOT is still treating signal). For instance, if FOOT has a dead-time of 400

<sup>13</sup>Data Acquisition System Based on a General Purpose Real-Time Data Acquisition and Control Framework.

$\mu\text{s}$  and the other detectors less than  $50 \mu\text{s}$ , the main DAQ will not accept new events between  $350 \mu\text{s}$  to  $400 \mu\text{s}$  after FOOT's dead-time end up. We planned to use the CALIFA signal in coincidence with FOOT but it was a problem due to the long dead time of the FOOT, as well as their low efficiency and small angular coverage. Fig. 2.19 shows the lists of the on-spill Tpat for the current experiment.

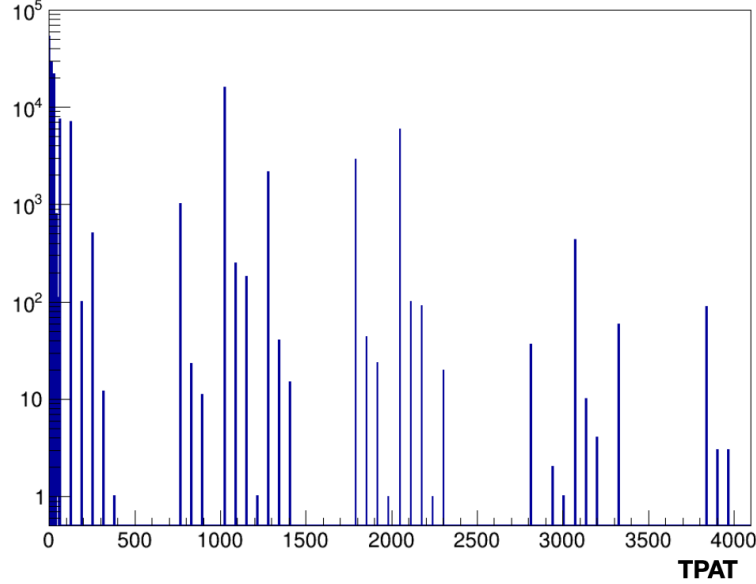


Figure 2.19: Histogram representing the experimental on-spill triggers Tpat from 0 to 4096. Tpat values larger than 4096 are off-spill triggers.

Tab. 2.5 lists the on-spill triggers for the experiment, including off-spill triggers for Tpat values greater than 4096. Two tables are presented due to space problem to show all the information in a single table.

Tpat Value	Tpat name	LOS!ROLU	TOFD	p2p
1	Good Beam	X		
2	Fragment	X	X	
4	p2p	X		X
32	Neutron	X		
64	Good Beam	X		
128	Fragment	X	X	
256	p2p	X		X
2048	Neutron	X		
4096	CALIFA OR			
8192	NeuLand			
16384	TOFD		X	
32768	RPC			

Table 2.5: First part of the on-spill trigger and relevant Tpat trigger combination. An event can have multiple Tpat bit patterns, so the Tpat value is a combination of all valid trigger combinations for that event. For instance, the "p2p" and "Fragment" Tpats might be set for an event, making the Tpat value 6 or 384, depending on FOOT dead time.

Tpat Value	NeuLAND	CALIFA OR	RPC	!FOOT
1				
2				
4				
32	X			
64			X	
128			X	
256			X	
2048	X		X	
4096		X		
8192	X			
16384				
32768			X	

Table 2.6: Second part of the on-spill trigger and relevant Tpat trigger combination.

Even for a valid pattern, an event will be accepted and treated only if the DAQ is not in deadtime, busy triggering a previous event. The DAQ takes approximately  $50 \mu\text{s}$  to gather data from all detectors and save it to memory. During this period, the DAQ cannot process new events. Events arriving within this dead time are not recorded but are counted to recover statistics of lost events. This trigger (or deadtime) locking mechanism is enforced by a combination of the TRLO II firmware [109] and GSI trigger modules, TRIVIA<sup>14</sup> [110], TRIXOR<sup>15</sup> [111], and TRB3<sup>16</sup> [112].

Not all events with a valid Tpat that pass the dead-time veto are recorded, as Tpats can be individually downscaled. This balances common baseline events with interesting reaction events, subjecting interesting events to less dead-time veto and reducing storage space. Each Tpat is assigned a downscaling factor  $n$ , where only every  $n$ th Tpat that passes the dead-time veto is recorded. Multiple Tpats for an event must pass the downscaling process individually, and as long as one passes, the event is registered. A downscale factor of 1 means every event is recorded.

In this experiment, the "p2p" Tpat was not downscaled to ensure most target reactions are measured, while "Good Beam" and "Fragment" Tpats, which occur more frequently, are downscaled to free up the DAQ. The correct numbers of these Tpats can be recovered by multiplying by the downscaling factor. Downscaling factors are determined during the preparation phase to optimize data rate and can vary between settings or runs. An event is saved only if at least one Tpat passes its downscaling veto, global dead-time locking, Tpat construction, and all original trigger conditions.

The data collection process involves multiple steps, including an event builder that collects data within one dead-time domain and delivers one sub-event from each detector per event. The time-sorter gathers events from all event builders and sorts them by a time-stamp from each dead-time domain. Sorted events are saved to disk and copied to tape quickly, with an online stream for online analysis.

The time-stitcher aligns signals from different detectors corresponding to the same physical event. This is done after the save to disk, involving rewriting events after creating the orig-

<sup>14</sup>Trigger Interface for VMEbus In Automated systems.

<sup>15</sup>Trigger Interface and Data Multiplexer for Online Readout.

<sup>16</sup>Trigger and Readout Board 3.

inal copies. A White-Rabbit<sup>17</sup> [113] timestamp is distributed to each dead-time domain for time-sorting and creating a single stream of detector data.

---

<sup>17</sup>The White Rabbit timestamp refers to a highly precise time-stamping system based on the White Rabbit protocol, which is an extension of Ethernet providing sub-nanosecond accuracy and synchronization.



# Chapter 3

## Calibration and alignment

### Contents

---

<b>3.1 R3BRoot Workflow</b> . . . . .	<b>77</b>
<b>3.2 Detectors calibration and alignment</b> . . . . .	<b>79</b>
3.2.1 Incoming detectors calibration . . . . .	80
3.2.2 Target recoil detectors calibration . . . . .	87
3.2.3 Outgoing detectors calibration . . . . .	101
<b>3.3 Detectors Alignment</b> . . . . .	<b>117</b>

---

### 3.1 R3BRoot Workflow

The primary experimental information is provided by digitized analog signals (e.g., from an ADC<sup>1</sup> or TDC<sup>2</sup>) coming from individual detector channels. These observables are collected from all detectors during the experiment, processed, and recorded by the Data Acquisition system (DAQ) on the basis of some trigger decisions. Before using the accumulated data for the actual analysis, the detectors must be calibrated so that their signals can be interpreted in terms of physical quantities such as times, distances, energy losses, etc.

The digitized experimental data of the various detector systems mainly consist of timing and amplitude information and are stored in the so-called LMD (List-Mode-Data) file format. To extract the physics information on the involved particles, the data have to be unpacked, synchronized, and calibrated. The first step is to assign all signals to the corresponding physical detector channels. After matching the signals of all independent detector systems within a global timestamp domain, the data is organized in an event-by-event structure. For this unpacking procedure, the UCESB (Unpack Check Every Single Bit) software tool, developed by Håkan T. Johansson [114], is used. The output file is stored in ROOT format, which is compatible with the analysis software package R3BRoot [94], used in the present work.

The unpacked file contains accumulated electronic signals of the individual detectors mapped on the corresponding physical channels ("Mapped" level). A set of parameters must be produced for synchronization and calibration of the respective channels ("Cal" level). Depending on the required detector information, the calibrated signals can be translated into physical quantities

---

<sup>1</sup>Analog to Digital Converter.

<sup>2</sup>Time to Digital Converter.

such as positions, energy loss, or nuclear charge ("Hit" level). This translation can require a dedicated measurement (e.g., a sweep run along the detector's active area) and the detector geometry. The calibration scheme, which is shown in the figure, can be slightly different for some detectors, but the general concept remains the same for almost all detectors.

Fig. 3.1 illustrates the calibration scheme for a general R<sup>3</sup>B detector from the "Raw" to the "Hit" level.

This section provides an overview of the general calibration procedure for the R<sup>3</sup>B detectors. All calibration steps used in the present work are subroutines of the R3BRoot package [115].

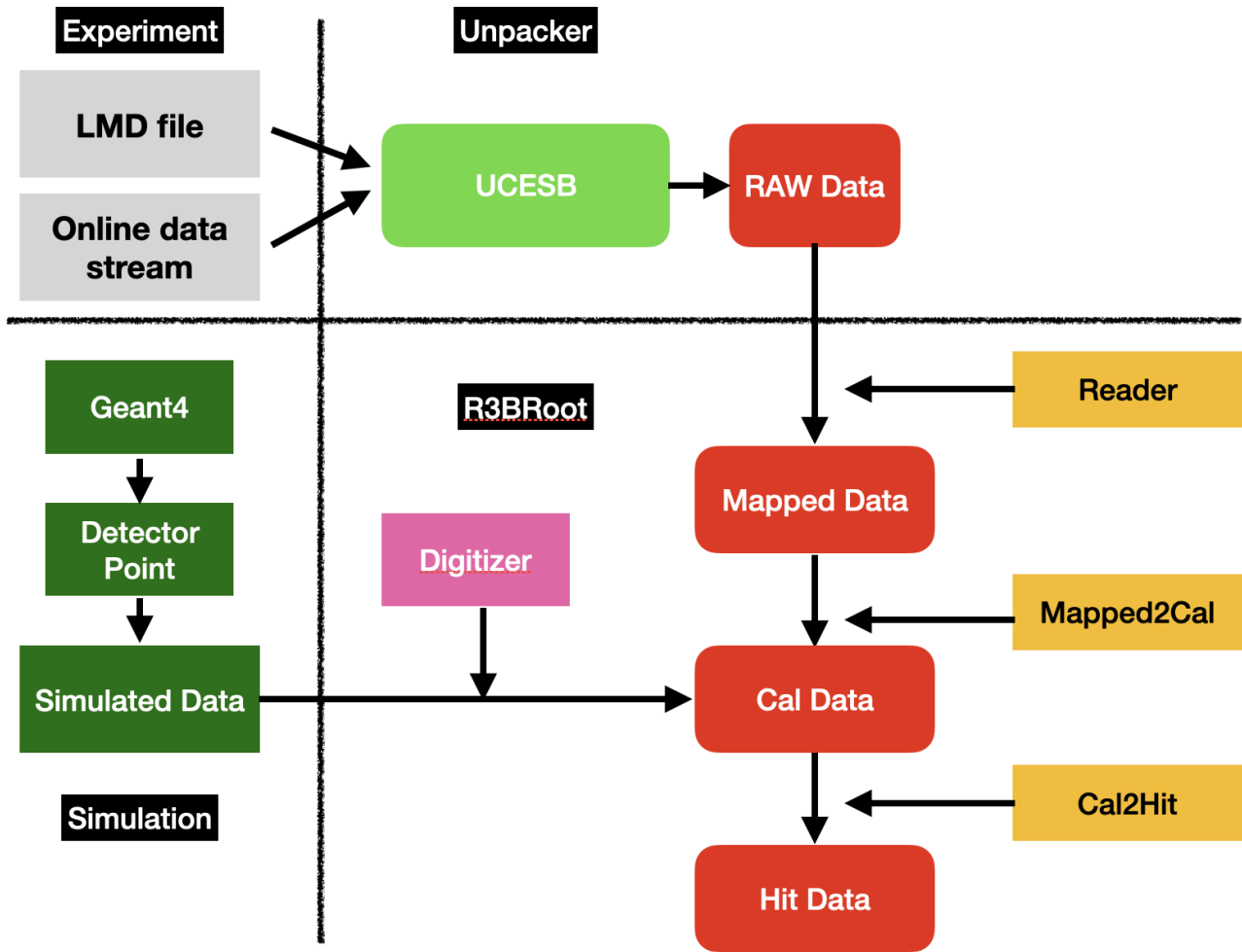


Figure 3.1: General calibration scheme for experimental data from raw to hit level (red boxes). At each calibration step, different parameter files are produced, allowing the final "Hit" level to be reached. The yellow squares illustrate the required parameter sets for the different calibration steps. The output data, in the form of an LMD file produced by the experiment, are unpacked via UCESB and converted into the "Raw" data.

## 3.2 Detectors calibration and alignment

In this section, I will discuss the calibration procedures of the  $R^3B$  setup detectors used in the current experiment. Specifically, I will focus on the detailed calibration process applied to the detectors with which I had direct involvement and experience. While I provide comprehensive details regarding the calibration of these specific detectors, I will also present a general overview of the calibration methodologies employed for the remaining detectors. Before looking in detail at the calibration procedure for several detectors, I present below some brief electronic module descriptions, useful to understand better the procedure and the calibration steps:

- A **VFTX** (Very Fast Time eXtension) is a VME FPGA-based TDC module with a 7 ps time resolution. This electronic module is a device employed for acquiring and processing signals from timing detectors such as scintillators or Photomultiplier Tubes (PMTs). These modules are designed to provide accurate and fast measurements of signal arrival times, requiring high-time precision. They can be used for applications such as measuring particle time-of-flight or synchronizing events in complex detection systems [116; 117].
- A **FQT** (Fast Quadratic TDC) board is an electronic module used to measure the arrival time of fast signals from detectors such as scintillators or photomultiplier tubes (PMTs). These boards are designed to provide a fast and accurate response. FQT has the main role of discriminating and collecting triggers. Generally provides good timing resolution but may not be as precise as VFTX in high-rate environments [117].
- A **VULOM**(Versatile Universal Logic Module) is a hardware component used in data acquisition systems to interface timing and trigger logic, providing event synchronization and signal processing functionalities. VULOM can act as a logic unit with clock generators that can produce OR and AND signals from several inputs and clock signals by the internal clock of the FPGA. The delay and gate generator part of VULOM can produce delay and width of output signals, and it can also act as a scaler [117; 118].
- A **TAMEX** (TAnk Module for the EXperiment with Multi-detector System) module is an electronic device used for high-resolution time and charge measurements. However, unlike FQT boards, TAMEX modules are designed to be used in systems with multiple detectors and offer additional features, such as the ability to handle signals from multiple channels and synchronize data from different detectors. Additionally, they can be equipped with integrated data acquisition capabilities.

For the charge measurement, the leading and trailing edge information of the time signal pulse from the detector is used. The leading edge refers to the rising edge of a signal pulse, indicating the start of an event or the arrival of a particle. The trailing edge, on the other hand, corresponds to the falling edge of the signal pulse, marking the end of the event or particle interaction.

These edges are crucial for precisely measuring the timing information of events, allowing for accurate reconstruction of particle trajectories and properties. The TAMEX module processes these leading and trailing edges to determine the precise timing information of particle interactions with detectors in a multi-detector system. The charge  $Q$  can be determined from the TAMEX time information using the Time-over-Threshold ( $ToT$ ) method [117].

### 3.2.1 Incoming detectors calibration

In this section, I will provide a general overview of the calibration procedures for the incoming detectors, specifically **S2**, **LOS**, **MWPC**, and **MUSLi**. Proper calibration of these detectors is essential for accurately extracting key quantities necessary for beam particle identification (PID). This process includes determining the arrival time using LOS, tracking the trajectory with MWPCs, and measuring the charge with LOS and MUSLi.

#### S2

The scintillator at S2 [94] in the FRS setup provides the start time for the time-of-flight (*ToF*) measurement of incoming ions. This scintillator is equipped with two photomultiplier tubes (PMTs) positioned on the left and right sides of the detector. In the current configuration, the PMT signals are routed to the VFTX<sup>3</sup> board, which also receives a master start trigger signal from the VULOM<sup>4</sup> module. The calibration procedure follows the standard procedure of R3BRoot [115].

The calibration process begins with fine-time TDC calibration, a critical step for FPGA-based timing systems. This calibration, known as "TCal" calibration, is standardized in R3BRoot [115] and follows a specific procedure as described in the previous section. Additional details about TDC calibration can be found in the TOFD calibration procedure.

Subsequent to TDC calibration, we proceed with the *ToF* and position calibration, which were conducted prior to the experiment. For position calibration, we employed two FRS Time Projection Chambers (TPCs) to track the beam. The *x*-position was then extrapolated to the scintillator at S2. The time difference measured between the two PMTs at S2 was linearly related to the extrapolated TPC position.

The *ToF* calibration involves using a known beam with fixed values of  $B\rho$  and  $A/Q$  values to determine the beam velocity and *ToF*, as measured between S2 and LOS (Cave C). This calibration was repeated for various  $B\rho$  values, and a linear fit of the velocity ( $\beta$ ) versus *ToF* was used to derive the flight path parameters.

Additionally, to ensure accurate hit selection in S2, we analyzed the time difference distribution between the left and right PMTs for events with multiplicity 1. Combinations of left and right PMTs within this distribution are assigned as a single hit in the S2 scintillator for all events.

#### LOS

LOS is the start detector for Cave C. It features an octagonal plastic scintillator with a thickness of 3 mm. Eight photomultiplier tubes arranged around its sides read it out. Two independent systems process the raw signals from the PMTs: the VFTX Module and an FQT board in conjunction with the TAMEX3. These systems enable a precise determination of the hit time by averaging the signals from all eight PMTs. As with the S2 detector, the initial calibration step for LOS involves fine-time TDC calibration ("TCal"). This calibration is performed for both systems and all PMTs. Given the high beam intensity and the associated high multiplicity in the detectors (see Fig. 3.2), a procedure was implemented to match the signals from each PMT accurately. This procedure helps minimize multi-hit events and provides clearer beam time information.

---

<sup>3</sup>Very Fast Time eXtension

<sup>4</sup>Versatile Universal Logic Module

The working principle for defining accurate hits is as follows:

1. Match the signals from the eight PMTs using the VFTX system to produce a single hit within a coincidence window. This window is determined by the maximum time difference among the signals from the eight PMTs for events with multiplicity 1.
2. Align the VFTX hits with the TAMEX leading edge (LE) signal for each PMT within a correlation window defined by:

$$\langle VFTX \text{ time} \rangle - (TAMEX \text{ LE time}). \quad (3.1)$$

where  $\langle VFTX \text{ time} \rangle$  is the average VFTX time of the eight PMTs, specifically for multiplicity 1 events.

3. Match the TAMEX trailing edges (TE) to the corresponding leading edges using a window defined by:

$$\langle TAMEX \text{ LE time} \rangle - (TAMEX \text{ TE time}). \quad (3.2)$$

for multiplicity 1 events.

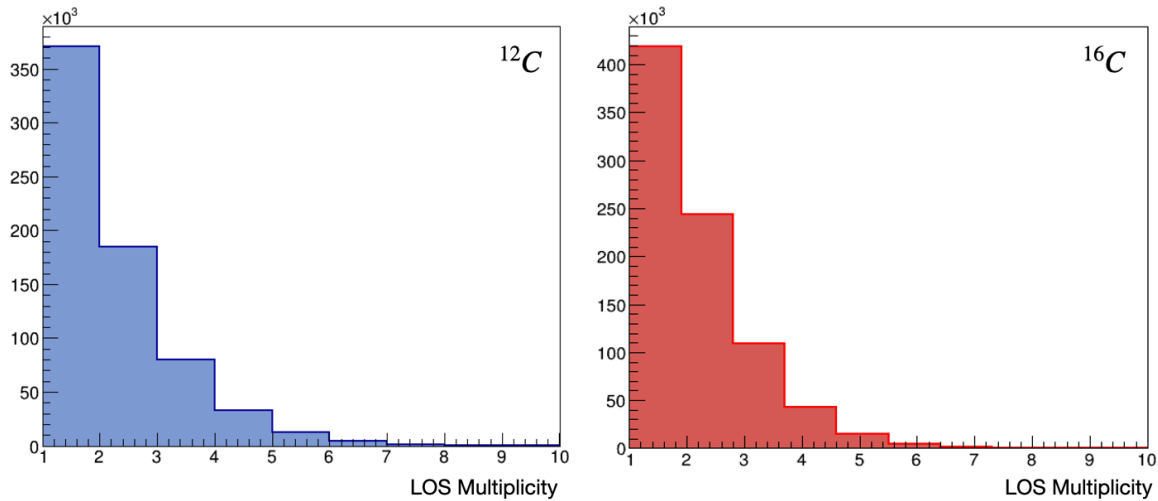


Figure 3.2: LOS multiplicity for  $^{12}\text{C}$  (left) and  $^{16}\text{C}$  (right) settings.

After completing the calibration process, the "Hit" level information derived from the LOS detector includes:

- The  $X$  and  $Y$  positions of the beam in centimeters.
- The start time information for  $ToF$  measurements.
- The charge  $Z$  of the beam, specifically for  $^{12}\text{C}$  and  $^{16}\text{C}$  in this case.

Fig. 3.3 illustrates the  $X$ - $Y$  position correlation at the "hit" level calibration step (top left and bottom left), as well as the charge  $Z$  for  $^{12}\text{C}$  and  $^{16}\text{C}$  (top right and bottom right). This information will be used for beam particle identification in the next chapter (Chapt. 4).

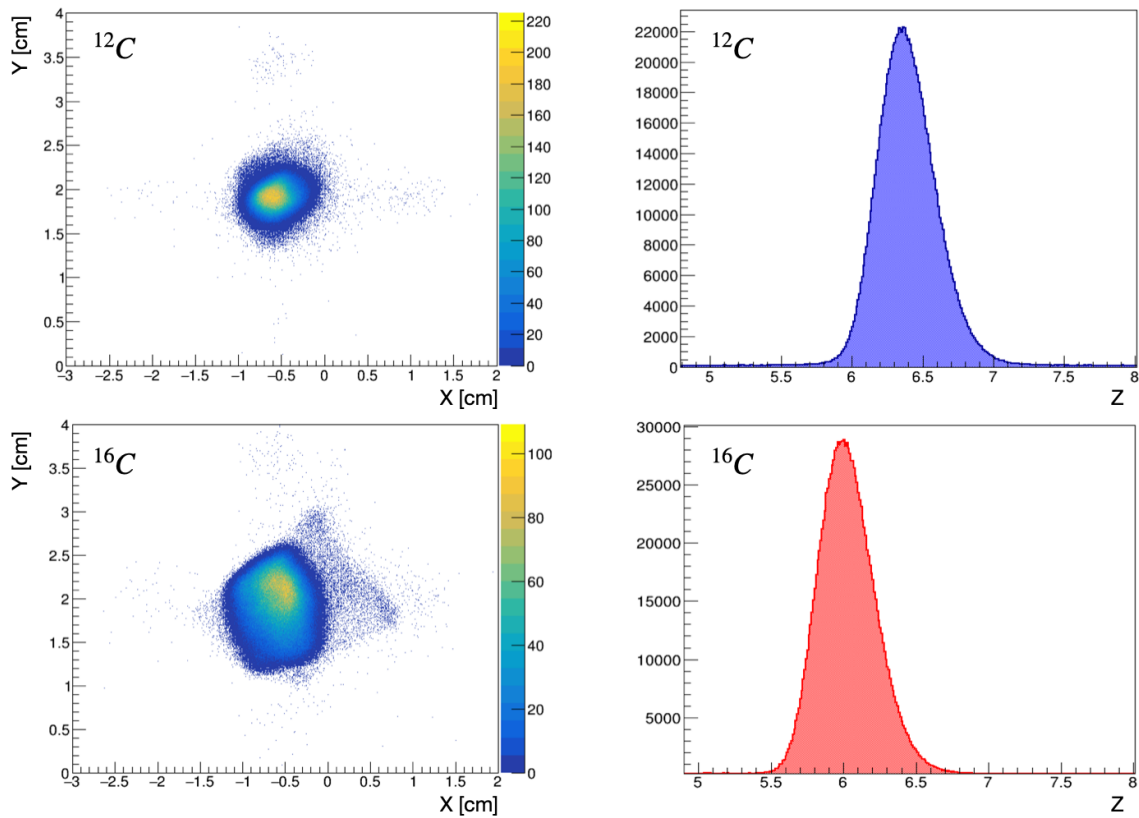


Figure 3.3: Left: Hit level  $X - Y$  position correlation plot (in cm) after the calibration procedure for  $^{12}\text{C}$  (Top left) and for  $^{16}\text{C}$  (Bottom left). Right: Charge  $Z$  of  $^{12}\text{C}$  after the calibration process (Top right) and for  $^{16}\text{C}$  (Bottom right). The  $X$ - $Y$  MWPC position are presented without applying alignment offset. The charge  $Z$  in LOS is not aligned at the nominal value since we expect only one charge peak in the  $Z$  distribution.

### MWPCs and MusLi calibration

The calibration of MWPCs and MUSLi follows the standard R3BRoot procedure for transitioning from "Map" to "Hit" data, employing specific R3BRoot tasks and parameters [115]. For **MUSLi**, the raw output data from the detector includes:

- Anode ID.
- Time: The time information derived directly from the anode signals, not yet calibrated.
- Energy: The uncalibrated energy loss information of the beam particles.

The primary goal of the R3BRoot calibration procedure is to refine these parameters to produce calibrated values for subsequent data analysis. Before the experiment, a MUSLi charge velocity ( $\beta$ ) correction was performed, as detailed in [119]. This involved measuring the energy loss in MUSLi for an incoming beam at multiple known energies and velocities. The resulting distribution was fitted with an appropriate function to obtain the correction parameters  $\beta$ .

The charge calibration of the detector involved two main steps:

1. **Alignment of Charges:** The charges of different anodes were aligned, improving the resolution by approximately 10%.
2. **Energy-to-Charge Calibration:** The energy loss was calibrated to charge by fitting the distribution with a Gaussian function, achieving a final charge resolution of  $1\sigma = 0.12$  Z units.

In previous experiments with TWIN MUSIC, no drift time (position) dependence of the charge was observed. However, in the current experiment, pile-up events in the MUSLi charge were observed due to the high rate, as shown in Fig. 3.4 (right figures). It was found that the pile-up originated from multi-hit events. Applying a condition based on the time difference between consecutive hits reduced the contribution of the pile-up tail, though it still led to a further 10% loss of events in MUSLi.

At the end of the calibration process, the output information for R3BRoot calibration from MUSLi includes:

- Anode ID.
- Position in mm in  $X$  and  $Y$  coordinates, derived from time calibration and the  $\theta$  angle of the beam in the  $X - Z$  plane.
- Charge  $Z$  of the beam, derived from the energy loss calibration procedure.

In the current experiment, the charge  $Z$  is used for beam charge identification and correlation with the charge measured by the LOS detector (see Fig. 3.5). Fig. 3.4 shows the quantities derived after calibration at the "Hit" level. The top left panel shows the correlation between the  $X$  position of the beam in MUSLi and the  $\theta$  angle information in the  $X - Z$  coordinates plane for  $^{12}\text{C}$ . I mention again that in the current experiment and subsequent data analysis MUSLi was not considered (due to pile-up reducing statistics). To obtain the angular information of the incoming beam track as the positions information only the MWPCs detector were used. The bottom left panel shows the same correlation for  $^{16}\text{C}$ . The top right panel displays the  $X$  position correlated with the charge  $Z$  of the beam, with the same correlation shown in the bottom right panel for  $^{16}\text{C}$ . Notably, pile-up in the beam energy loss can be observed at  $Z > 6.5$ .

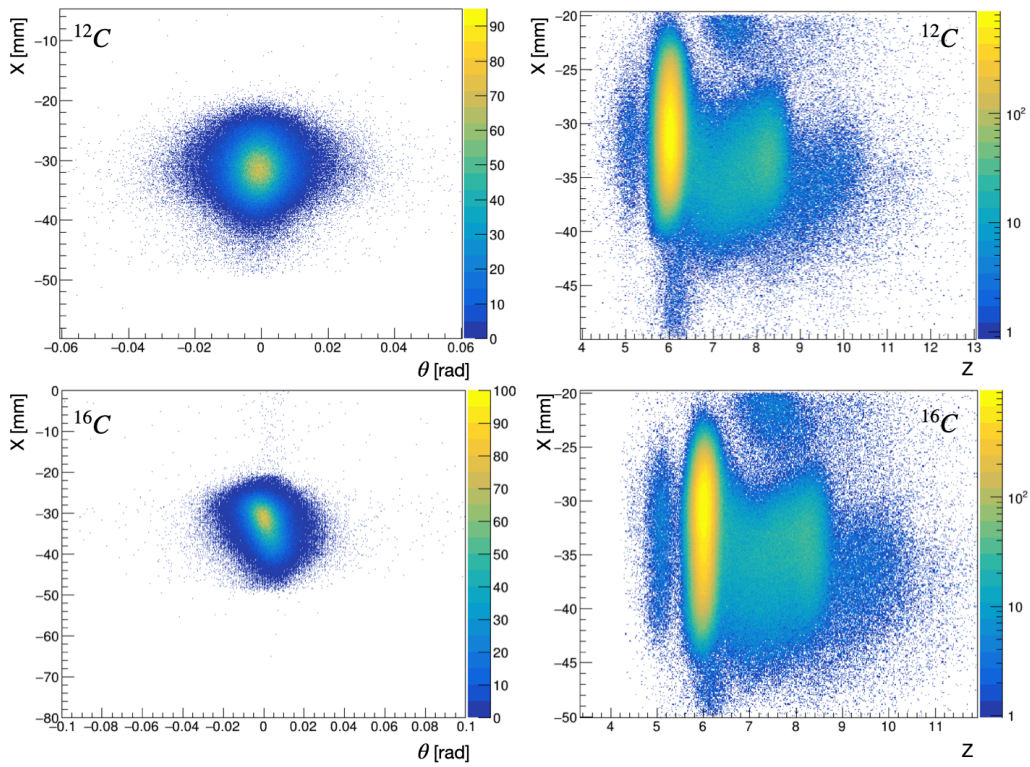


Figure 3.4: Top left: Correlation between the  $X$  position of the beam in MUSLi and  $\theta$  angle in the  $X - Z$  plane for  $^{12}\text{C}$ . Bottom left: Same correlation for  $^{16}\text{C}$ . Top right:  $X$  position correlated with the charge  $Z$  of the beam. Bottom right: Same correlation for  $^{16}\text{C}$ .

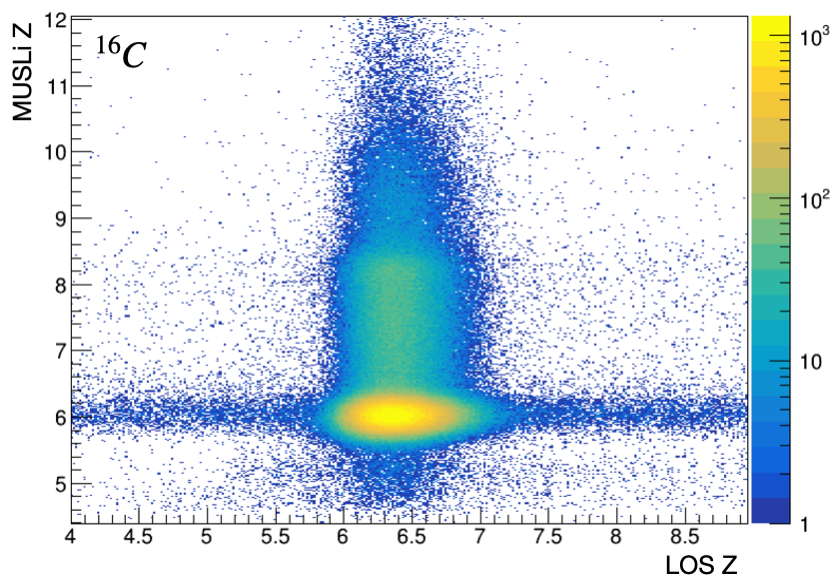


Figure 3.5: Correlation between the charge  $Z$  in LOS and charge  $Z$  in MUSLi.

The calibration procedure for MWPCs using R3BRoot is similar to that of MUSLi. It involves reading every plane and pad of the detector to assess the charge deposited by the beam. The raw output data from MWPCs include:

- PAD number.
- Plane number.
- Charge  $Q$  of each plane.

Post-calibration, the output information from R3BRoot includes:

- Position  $X$  [mm].
- Position  $Y$  [mm].

Fig. 3.6 shows the  $X$  and  $Y$  position correlations of MWPC0 and MWPC1 for  $^{12}\text{C}$  and  $^{16}\text{C}$ . These correlations reveal the beam's footprint as it passes through the detectors. Distinct horizontal lines observed in MWPC1 are associated with the wider and more spaced horizontal cathodes of MWPC1 compared to MWPC0.

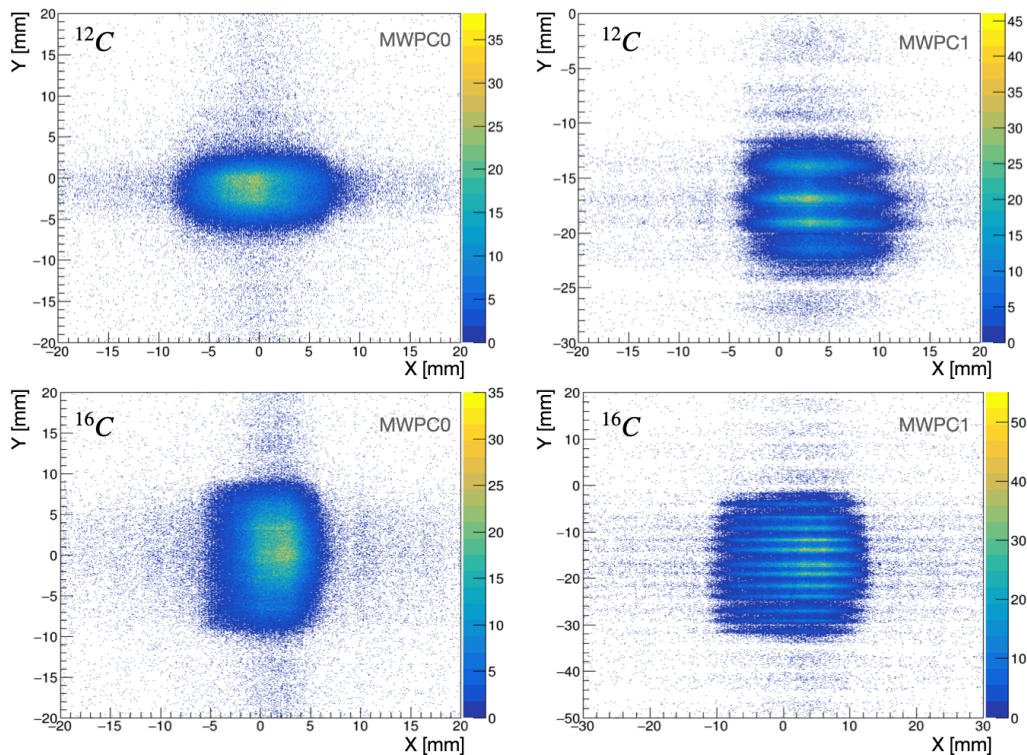


Figure 3.6: Top left: Correlation between the  $X$  position of the beam in MWPC0 for  $^{12}\text{C}$ . Bottom left: Same correlation for  $^{16}\text{C}$ . Top right: Correlation between the  $X$  position of the beam in MWPC1 for  $^{12}\text{C}$ . Bottom right: Same correlation for  $^{16}\text{C}$ . The  $X$  and  $Y$  positions are directly taken from the "Hit" level without alignment offsets applied.

Positions are determined using a reconstruction algorithm that identifies the highest energy hit and derives the hit position by weighting the energy of adjacent pads. The  $X$  and  $Y$  positions from two MWPC detectors are used for beam tracking. The combination of data from MWPCs ( $X$  and  $Y$  beam positions) with LOS and MUSLi charge allows the complete identification of the incoming beam.

### ToF selection S2-LOS for $^{16}\text{C}$ setting

After calibrating the detectors and selecting appropriate hits, the next step is to identify valid candidates  $ToF$  between S2 and LOS for the incoming analysis. This is achieved by applying a  $ToF$  ( $\beta$ ) selection window, which was determined by examining the  $ToF$  distribution between S2 and LOS for multiplicity 1 events in both detectors, as illustrated in Fig. 3.7. Initially, the

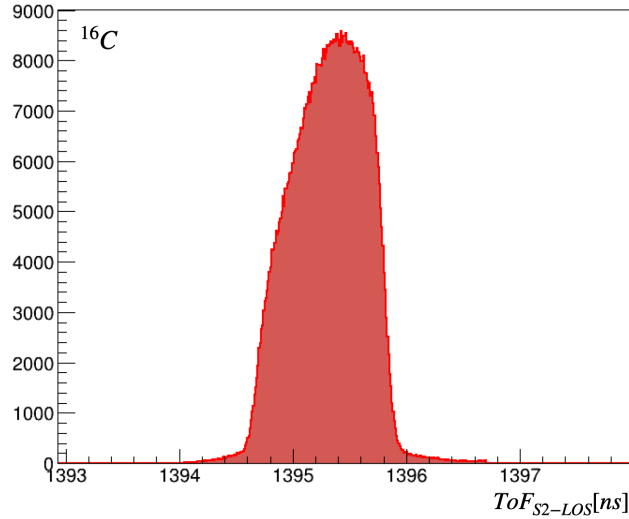


Figure 3.7: Time-of-flight ( $ToF$ ) between S2 and LOS detectors, showing a clear peak around 1395.4 ns.

times recorded by the individual detectors were corrected based on the trigger times from the master clock at the respective VFTX readout modules. For the  $^{16}\text{C}$  settings, a clean single peak corresponding to the pure  $^{16}\text{C}$  beam was observed, resulting in an overall time-of-flight resolution ( $\sigma$ ) of approximately 75 ps.

Next, the time-of-flight is converted to velocity ( $\beta$ ) using the known distance between S2 and LOS. To determine the  $A/Q$  value, the nominal  $B\rho_0$  value is derived from the FRS settings, and the track information is obtained from the position data in S2. The  $A/Q$  values are calculated using the formula:

$$\frac{A}{Q} = \frac{B\rho_0 \cdot (1 - \text{PosS2}/D_{S2-CC})}{3.10716 \cdot \beta \cdot \gamma}; \quad (3.3)$$

where  $\text{PosS2}$  is the  $x$ -position at S2,  $\beta$  is the calculated velocity, and  $D_{S2-CC}$  is the dispersion parameter between S2 and Cave C.

Finally, using the calculated  $A/Q$  from the S2-LOS  $ToF$  and the charge  $Z_{MUSLi}$  information from MUSLi, we can generate the incoming particle identification (PID) plot, as shown in Fig. 3.8.

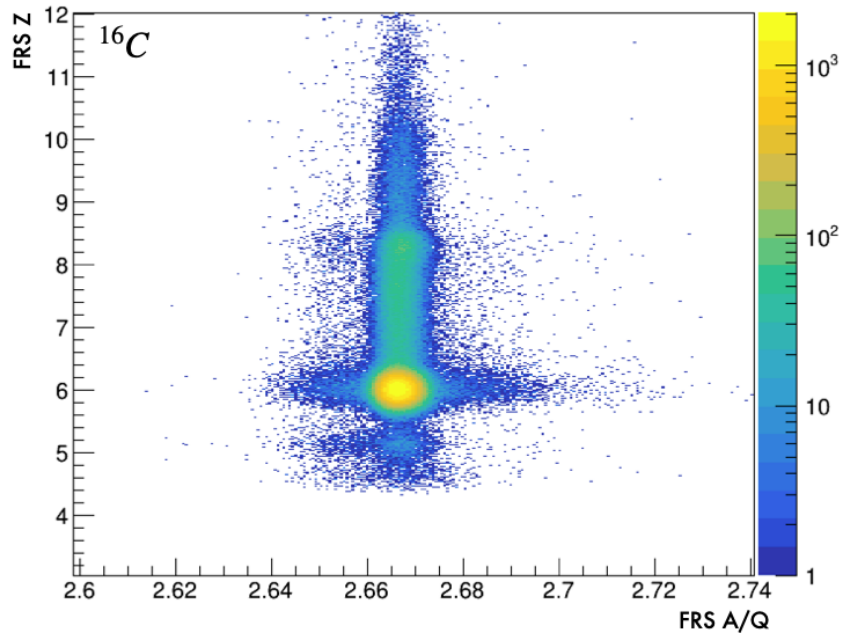


Figure 3.8: Correlation between the charge  $A/Q$  determined by S2-LOS *ToF* and charge  $Z$  in MUSLi.

### 3.2.2 Target recoil detectors calibration

I will now describe the calibration process for the detectors surrounding the  $\text{LH}_2$  target, specifically FOOT and CALIFA. Proper calibration of these detectors is essential for accurately measuring the energy and angle of the scattered protons.

Once calibrated, the energy and angle measurements obtained from these detectors are used to compute the momentum of the two protons scattered in the  $(p, 2p)$  reaction. From this, we can derive the missing momentum  $P_{miss}$ , which is a crucial step for investigating Short-Range Correlation physics.

#### CALIFA calibration

The CALIFA electromagnetic calorimeter is strategically positioned around the target to detect  $\gamma$ -rays and light-charged particles. It effectively detects stopped  $\gamma$ -rays up to 30 MeV and stopped protons up to 300 MeV. For protons exceeding 300 MeV, the full energy of the protons can be reconstructed from their deposited energy in CALIFA, as discussed in the next chapter. A pulse-shape analysis of the CsI crystal response allows differentiation between stopped protons and punch-through protons. In the current experiment, CALIFA comprises two parts: the iPhos and the Barrel. The Barrel part covers a polar angular range of  $43^\circ < \theta < 88^\circ$  and is optimized for proton detection, while the iPhos part, being dual-phased, covers a polar angular range of  $19^\circ < \theta < 43^\circ$ .

The CALIFA calibration procedure involves mapping channel numbers to energy deposition (in keV) using a linear function for each crystal. Seven calibration points from three gamma sources ( $^{22}\text{Na}$ ,  $^{60}\text{Co}$ , and AmBe) are utilized to establish the linear relationship between channel number and energy in keV. The automatic calibration procedure has been updated in R3BRoot.

The calibration procedure comprises several steps described in detail below:

- Read and store the channel number spectrum for each crystal and calibration source, applying spectrum range limits to exclude significant background contribution at low

energy.

- Determine the channel number of each source peak with  $^{22}\text{Na}$  or  $^{60}\text{Co}$  sources, using an exponential background plus Gaussian distribution fit within an energy-dependent range around the peak.
- Find approximate positions for the three peaks in the AmBe spectrum using linear extrapolation from lower energy calibration sources. Next, select valid peaks based on the significance of the peak ( $S/\sqrt{B} > 3.0$ , where  $S$  is the signal and  $B$  is the background).
- Extrapolate the linear relation for 1984 crystals between channel number and corresponding energy peaks, considering both the mean and uncertainty of the Gaussian fits on the channel number spectrum.
- Exclude non-linear crystals (44 such crystals) based on the weighted sum of squares (WSS) test (excluding points with  $\text{WSS} > 0.001$ ).
- Exclude crystals with gains higher than 16 or lower than 10 in the proton range or with gains higher than 1.6 or lower than 1.0 in the gamma range.

The subsequent subsections present step-by-step intermediate and final calibration results.

### ***Fit for Low-Energy Calibration Sources***

First, the automatic peak searching function, with appropriate input thresholds and expected numbers of peaks, identifies the approximate positions of peaks in channel number and extracts the approximate background histogram. To determine the precise mean value in channel number ( $ch$ ) of each source peak, a fit  $f_{\text{fit}}$  of the raw spectrum, using a combined exponential function to describe the background and a Gaussian function in the region of the identified peak, was performed (with a specified energy-dependent range).

$$f_{\text{fit}}(ch) = \exp(A + B \cdot ch) + C \exp\left(-\frac{(ch - D)^2}{E^2}\right). \quad (3.4)$$

The procedures above give the parameters A to E an approximate initial value. Fig. 3.9 illustrates an example of the final fit for both low-energy sources for a single crystal.

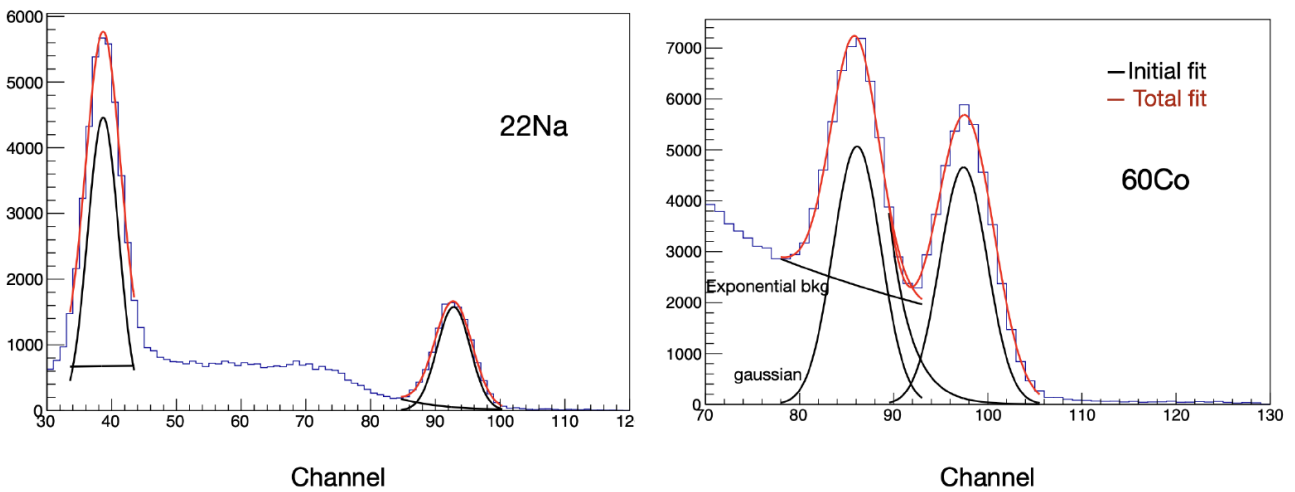


Figure 3.9: Exponential background plus Gaussian fit for  $^{22}\text{Na}$  (left) and  $^{60}\text{Co}$  (right) source spectra, crystal 4851.

### *AmBe source*

Calibration data from an AmBe source are included to include higher energy points (approximately 4 MeV). However, due to limited statistics in some regions of CALIFA, a modified procedure is being employed, as described below.

Initially, a linear fit was derived from the four calibration points provided by the low-energy sources. Using this fit and the known energy peaks in the AmBe spectrum, an extrapolation to the approximate channel peak position on the mapping level in the AmBe spectrum is performed. Subsequently, each identified peak channel is fitted using the same approach as described above, based on Eq. 3.4 (with a fit range of 30 channels in AmBe). Calibration points are only considered when their significance exceeds 3.0.

An example of the fit of the AmBe spectrum is depicted in Fig. 3.10.

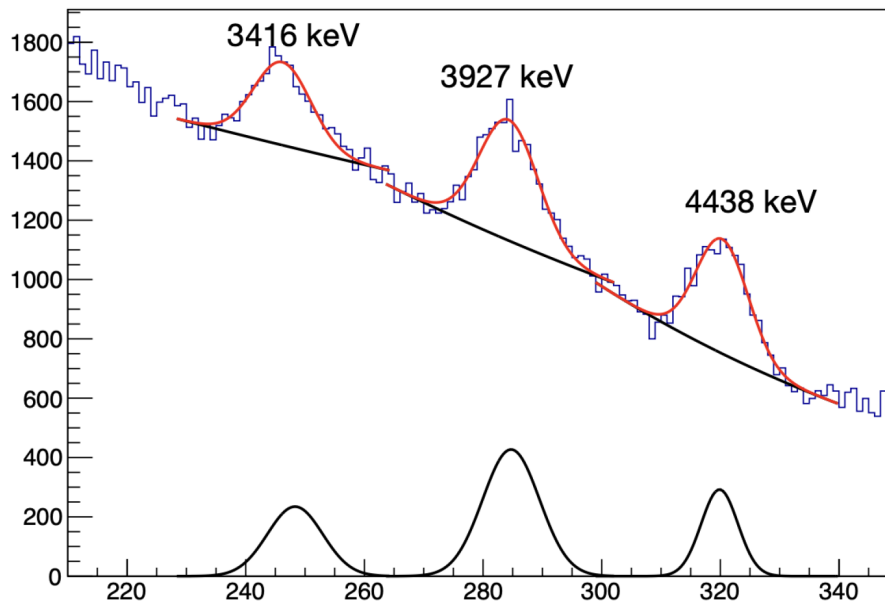


Figure 3.10: AmBe Spectrum and fit for crystal 4851.

### *Linear mapping between channel number and energy*

Upon identification of all available calibration points, the linear relationship between channel number and energy (in keV) for each crystal was refitted while considering the uncertainty of the center of the Gaussian for each calibration point.

An example of the linear relationship between channel number and energy, incorporating all 7 calibration points, is illustrated in Fig. 3.11.

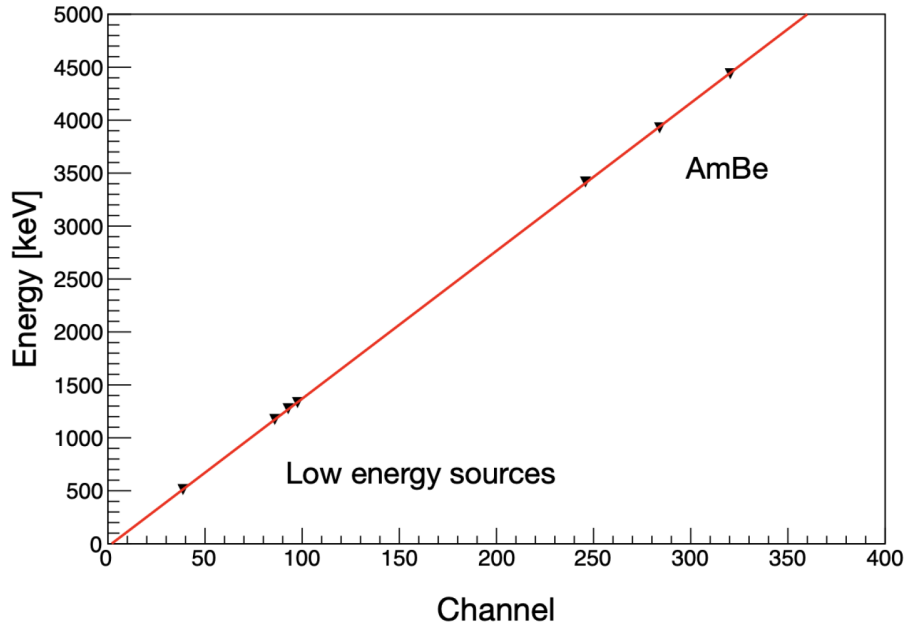


Figure 3.11: Linear relation between channel number and energy in keV for crystal 4851.

### *Crystal quality check*

In some cases, because of background contributions or low statistics, the fitting procedure described in the previous sections may incorrectly identify peaks, resulting in an erroneous linear relationship between channel number and energy for a small subset of crystals. To address this issue, a selection criterion based on the weighted-sum-of-squares ( $wss$ ) in the linear fit to exclude such crystals was employed. The  $wss$  is defined as:

$$wss = \frac{1}{N} \sum_i w_i \frac{(f(x_i) - y_i)^2}{y_i^2} \quad (3.5)$$

where:

- $x_i$  is the peak channel number.
- $f(x)$  is the linear calibration function.
- $y_i$  is the source energy in keV.
- $w_i = \exp(-\Delta x_i^2)$  is the weight assigned to peak channel  $x_i$  with uncertainty  $\Delta x_i$ .
- $N$  is the number of degrees of freedom.

Fig. 3.12 presents the distribution of  $\log_{10} wss$  versus crystal ID. The red line denotes the cutoff between crystals with a satisfactory linear relationship and those with a poor linear relationship. Additionally, Fig. 3.13 provides an illustrative example of a "good" crystal and a "bad" crystal, supporting the chosen cutoff threshold at  $wss = 0.001$ . In the case of a "bad" crystal, the calibration is performed considering only the calibration points that match the linear relationship. In the following, with "Proton Crystal" I will indicate the iPhos crystals in proton gain mode, while with "Gamma Crystals" I will mean the iPhos crystals in gamma gain mode.

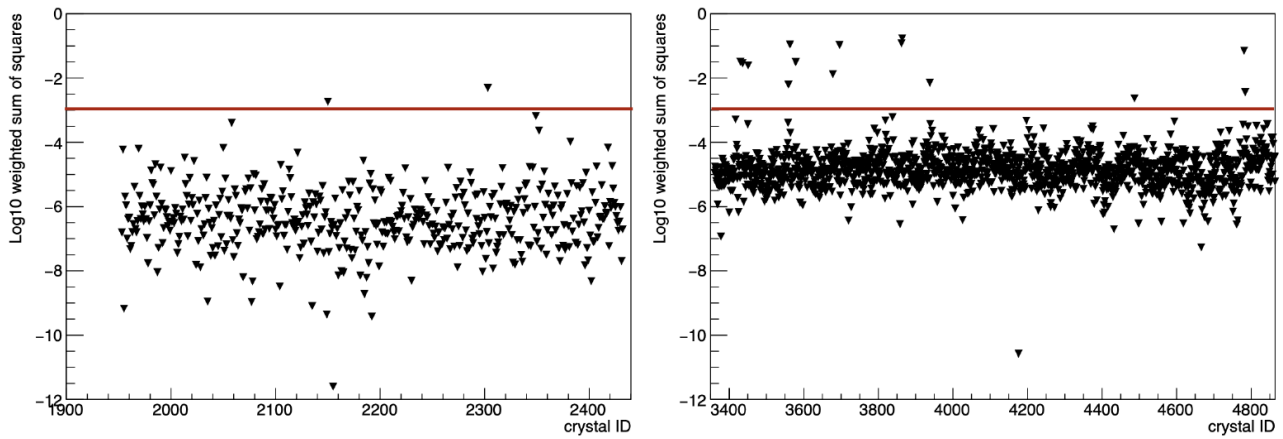


Figure 3.12:  $\text{Log}(wss)$  distribution versus crystal ID for the Gamma-range crystals (left) and the Proton-range crystals (right).

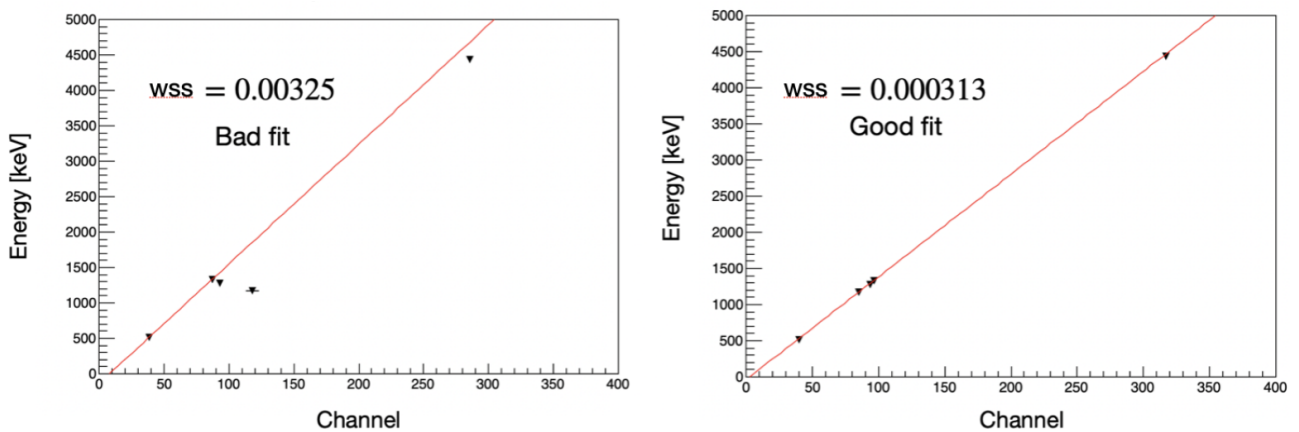


Figure 3.13: Example for "good" (left) and "bad" (right) linear fit for different crystals. This justifies the  $wss$  threshold at 0.001.

### Calibration results

In this part, the calibration results are analyzed. Fig. 3.14 illustrates the slope of the linear raw-to-energy relation versus crystal ID for crystals across all ranges utilized in the current experiment. To ensure the validity of the linear fits, a threshold between 1.2 and 1.4 is applied for gamma-range crystals and between 12.5 and 15 for proton-range crystals, excluding those outside the specified range.

Fig. 3.15 and Fig. 3.16 depict the difference in keV of calibrated energy peaks, identified through the same fitting method applied to the calibrated energy spectrum of  $^{22}\text{Na}$  using the calibration parameters derived earlier, and the expected peak energy for  $^{22}\text{Na}$  at 511 KeV and 1274.5 keV, respectively. Notably, we observe two prominent issues, particularly in proton-range crystals:

- An energy shift of approximately 10 keV at the 1274.5 keV calibration point.
- A periodic energy difference based on crystal ID, suggesting position-dependence of the results.

To address these issues, we conducted two tests:

- Excluding the calibration point at 511 keV, as different interaction lengths in the crystal may result in a non-linear relation between channel number and energy.
- Excluding the Cobalt source due to potential issues with background fitting.

None of these tests was successful in explaining the nature of this shift. However, since the shift appears not to be significant for the subsequent analysis, it was decided to rely on the calibration parameters derived previously.

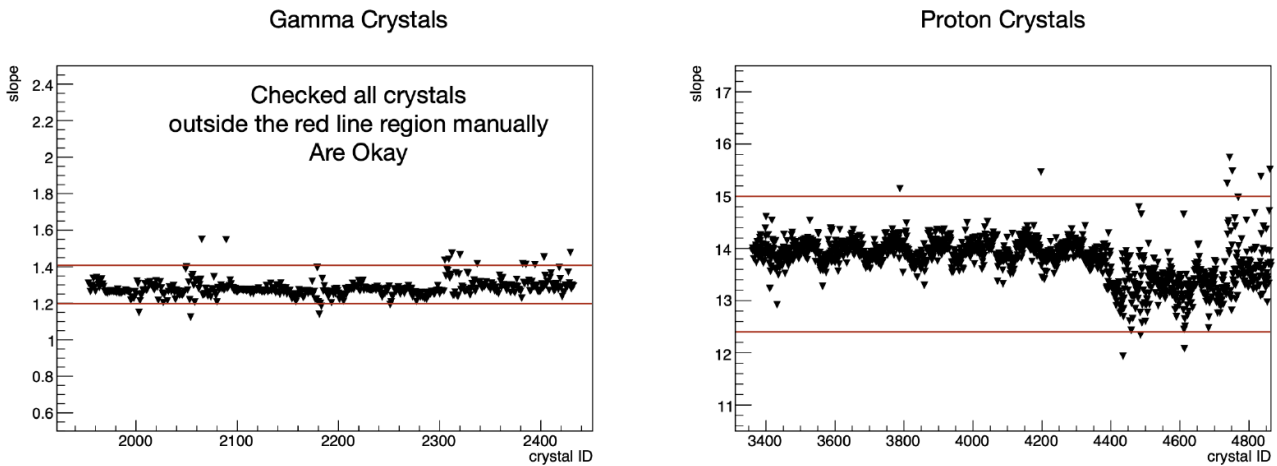


Figure 3.14: Distribution of slope versus crystal ID, for both gamma and proton ranged crystals

### Crystal resolution

The resolution (sigma) of each crystal at 1173 keV is presented in Fig. 3.17. Crystals with a resolution exceeding 10% are excluded from the final calibration parameters, totalling 44 crystals. These crystals also fail the *wss* test exclusion. Interestingly, proton crystals with higher IDs (i.e., those in the endcap) tend to exhibit worse resolution but still remain within specification.

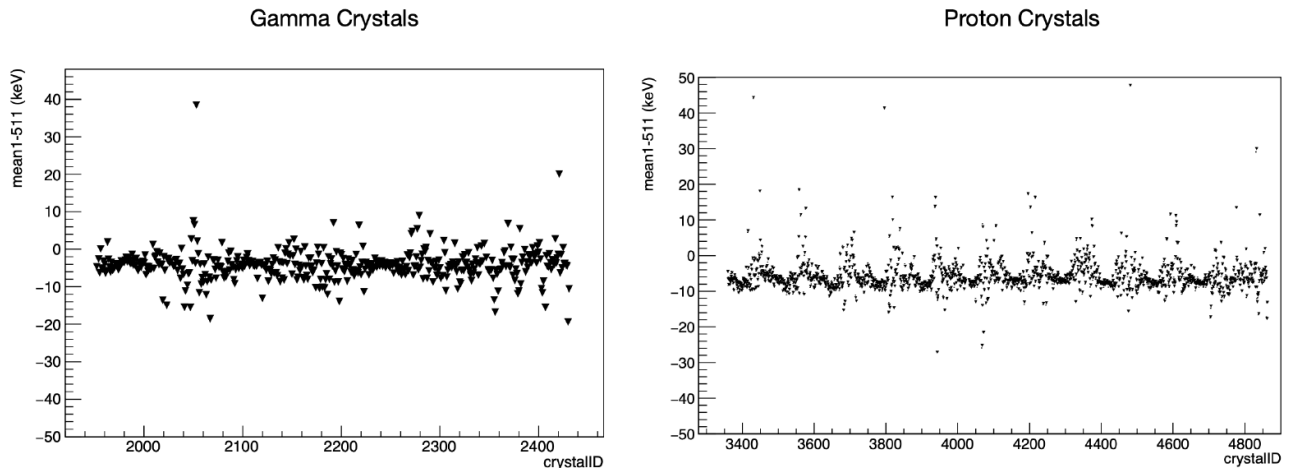


Figure 3.15: Distribution of the difference between calibrated energy peaks and expected energy peaks in keV for each crystal at 511 keV.

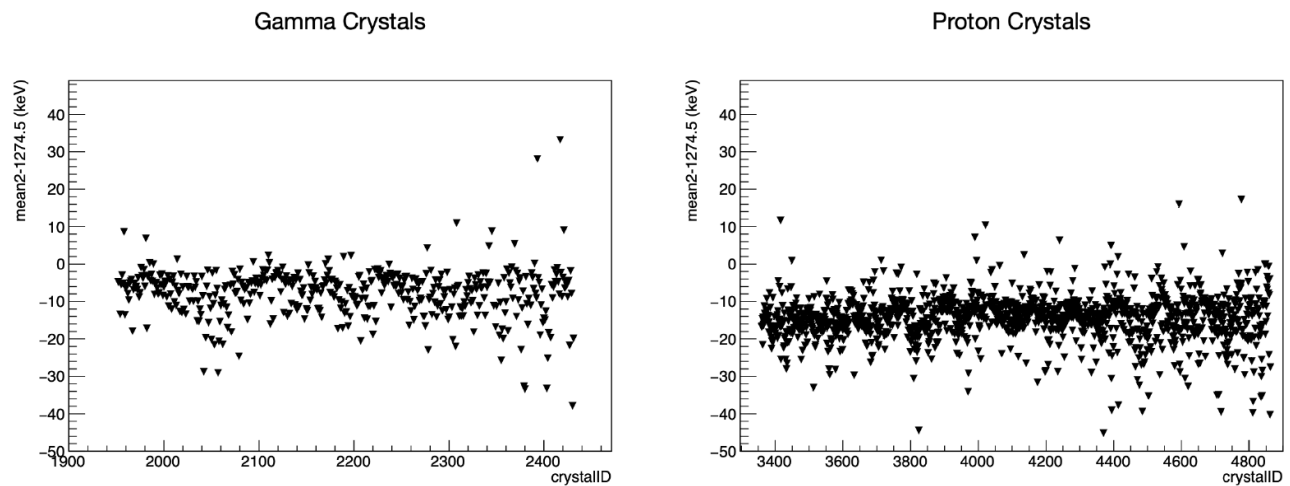


Figure 3.16: Distribution of the difference between calibrated energy peaks and expected energy peaks in keV for each crystal at 1274.5 keV.

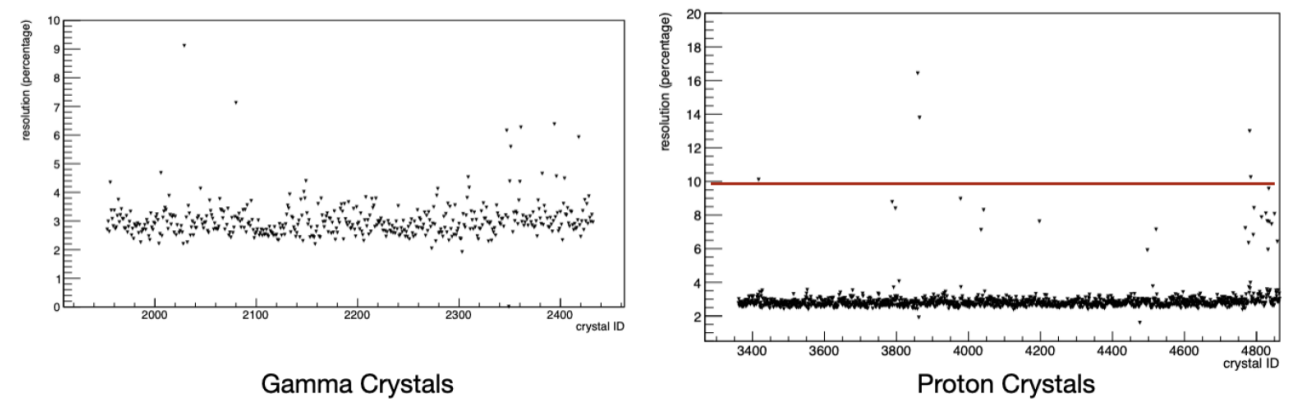


Figure 3.17: Resolution (sigma) v. crystal ID.

## FOOT calibration

The calibration procedure for the FOOT detector is different for the In-Beam FOOT (beam and light fragments identification) and Arm FOOT (QFS protons identification). In the following part, both calibrations are reported, including some consideration regarding the capability and efficiency of the Arm FOOT to detect QFS protons.

### *In-Beam FOOT calibration*

The calibration procedure presented, which aims to improve the energy and position resolution of the detectors, has been adopted from the original AMS work [72; 115]. The calibration procedure consists of a few sequential steps. After each step, the detector response is modified and used for the following manipulations.

In the first calibration stage, the pedestals in individual strips are determined together with the corresponding standard deviations  $\sigma$  using the off-spill data. In the present measurements, the average strip noise was around 3 ADC channels. A strip which does not deliver any signal (as seen after pedestal/noise subtraction) or whose signal is systematically too low or too high is defined as a "dead" strip. A reason for that might be a broken bonding to the VA-chip [100] or some other physical damage. In any case, the presence of dead strips has to be taken into account when searching for clusters of strips because such defects can be falsely interpreted by the reconstruction algorithm as the cluster edges, resulting in splitting into two or more separate clusters. To avoid this problem, dead strips are marked and excluded from the cluster-finding algorithm.

After the pedestal subtraction, a coherent noise of a particular ASIC chip is determined on an event-by-event basis as a mean ADC value over all 64 strips associated with this chip. Only those strips are accepted into the common noise determination, which has signals within  $3\sigma$  (in energy ADC channels) to discriminate the presence of noisy strips and the strips fired by the ionizing particle. A summary of the pedestal subtraction and the fine correction of the baseline event-by-event is shown in Fig. 3.18.

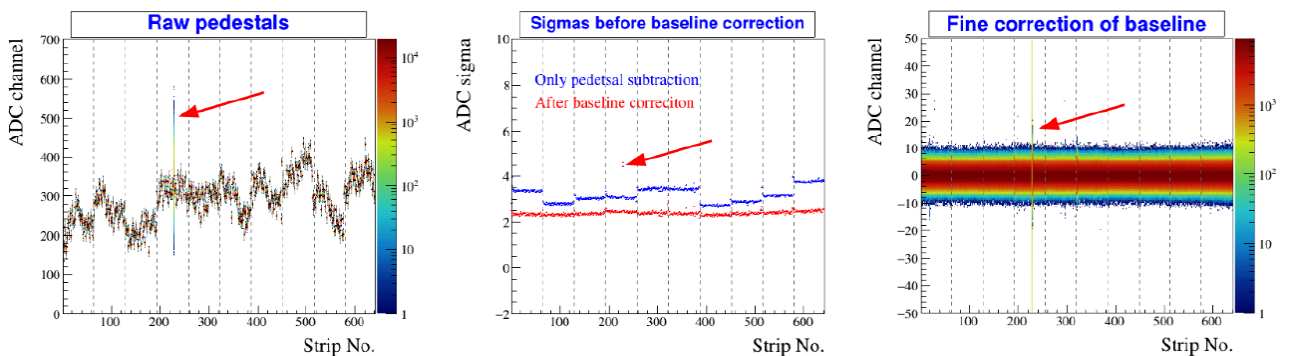


Figure 3.18: This Figure represents a summary of the step employed to reach a fine correction of the baseline with pedestal subtraction. From left to right: pedestals plot with a "bad" strip identification, their sigma values before (blue) and after (red) the 3 steps mentioned above, the dispersion of the pedestal values after this correction.

Depending on the charge of the particle, its overall energy signal (i.e. the total collected charge) is distributed over a group of neighbouring strips. The number of strips in one cluster (the so-called "cluster base width") is not larger than three for a minimum ionizing particle like a proton, while for  $Z = 6$  particles, it is on average 5 strips. A typical cluster from a single  $^{12}\text{C}$  hit is shown in figure 3.19. Adjacent strips which have signals above  $3\sigma$  are combined and

stored in a preliminary cluster structure (SYNC level), which is used later for the energy and position reconstruction of the particle hit. The position information can be obtained from the signal-weighted center-of-gravity (CoG) of the cluster:

$$\text{CoG} = \frac{\sum_{i=a}^b S_i N_i}{\sum_{i=a}^b S_i}. \quad (3.6)$$

where  $a$  and  $b$  denote the first and the last strip of the cluster,  $S_i$  is a signal in individual  $i$ -th strip (after pedestal and noise correction) and  $N_i$  is the corresponding strip number. In this definition, the CoG is expressed in terms of strip numbers, and the summation is done over all strips contributing to the cluster. The hit position is then calculated as:

$$X_{\text{CoG}} = p \cdot \text{CoG}. \quad (3.7)$$

where  $p$  is the readout pitch size.

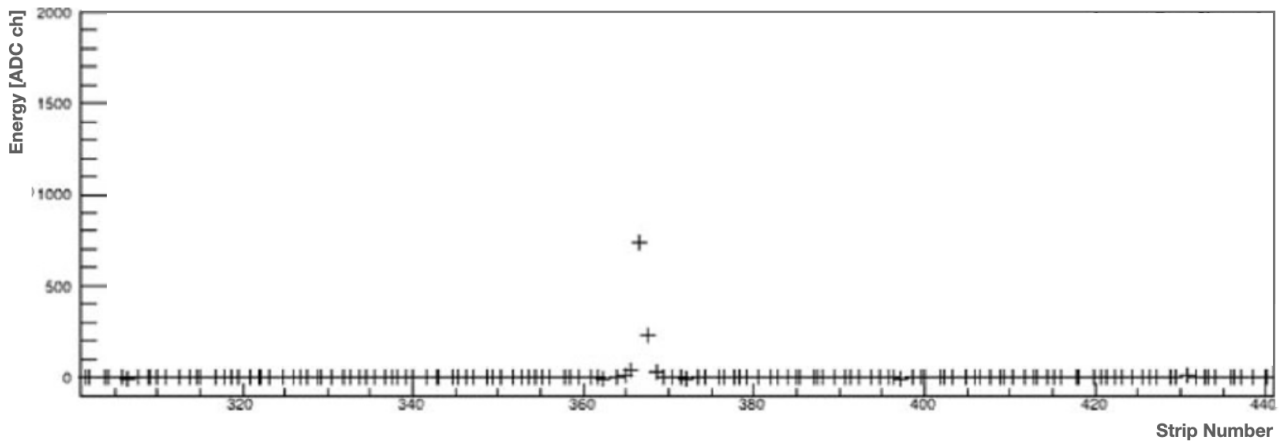


Figure 3.19: Cluster for  $^{12}\text{C}$  visible at the Cal level.

The total energy loss of a penetrating ion is reconstructed via summation of the signals in all strips forming a cluster ("cluster sum" or "cluster area"):

$$E = \sum_{i=a}^b S_i. \quad (3.8)$$

Due to the presence of floating strips in the readout gap and the spacing between the strips (see Fig. 2.9), the reconstructed cluster sum is influenced by the relative position of the hit with respect to the nearest readout strip. This dependence can be expressed through the impact parameter  $\lambda$ , which characterizes the interstrip position of the hit:

$$\lambda = \{\text{CoG} - \text{int}(\text{CoG})\} \in [0, 1]; \quad (3.9)$$

where  $\text{int}(\text{CoG})$  is an integer part of the  $\text{CoG}$ , essentially the number of the central strip of the cluster. When  $\lambda = 0$ , it means that the hit is exactly in the center of the readout strip, and  $\lambda = 1$  means the hit is in the center of the next readout strip (similarly,  $\lambda = 0.5$  stands for the hit which is exactly in between two readout strips).

Fig. 3.20 shows how the cluster area depends on the reconstructed hit position. Such behaviour decreases the overall energy resolution and must be corrected. The  $\lambda$ -effect is also sensitive to the energy loss (i.e. charge) of the passing ion. However, if the charges do not differ too much, i.e. by one or two units, their  $\lambda$ -effects are quite similar.

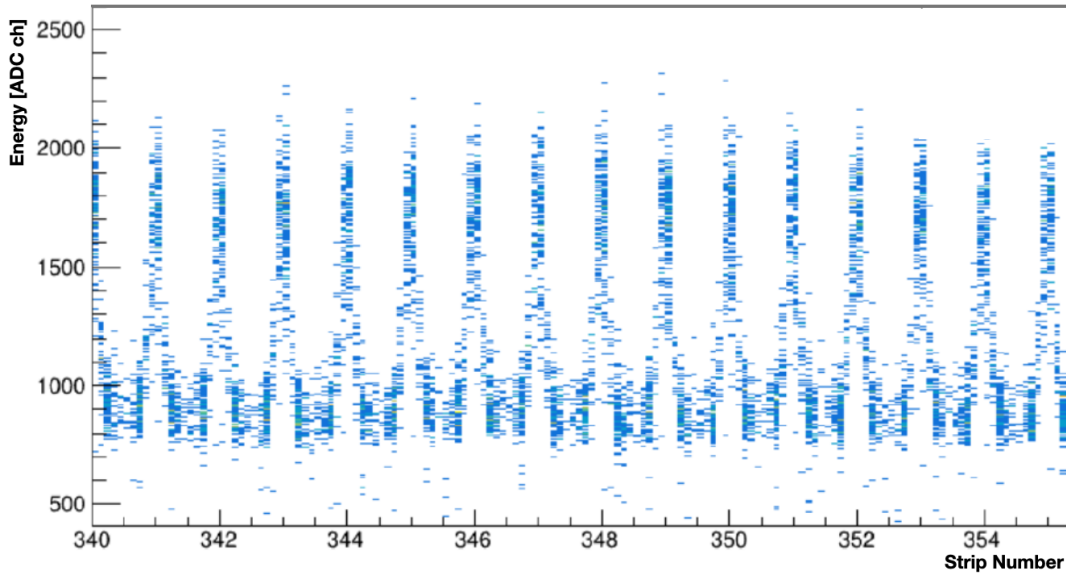


Figure 3.20: Position dependence of the cluster sums corresponding to  $^{12}\text{C}$  hits. Zoom in the plot showing the energy at the Cal level with respect to the position. The influence of the interstrip impact parameter  $\eta$  on the cluster sum results in a regular pattern across the readout gap. This pattern is identified and corrected accordingly.

To ensure uniform energy distribution across the entire  $\lambda$  range, each charge component undergoes correction by fitting it following isolation aided by a cut based on energy deposition in the Time-of-Flight Detector (ToFD), which scales proportionally with  $Z^2$ . In the present experiment, the substantial energy deposition in the FOOTs leads to significant charge variation per cluster based on their  $\lambda$  values (see Fig. 3.21).

In the following section, I will describe the *lambda* correction in the context of a  $^{21}\text{N}$  FRS secondary beam setting, based on data from experiment s509<sup>5</sup> conducted one week after our experiment. The beam in experiment s509 had a lower intensity, which resulted in reduced noise in the FOOT detectors and facilitated a cleaner calibration process.

A polynomial function of either 6th or 8th order is selected to correct this distribution, depending on the detector and specific component. Fewer corrections are applied to lower charges, while components corresponding to  $Z = 2$  and  $Z = 1$  are exempted due to their proximity to background levels. The alignment value for each component is determined by the offset of the function post-fitting.

Upon  $\lambda$ -energy correction for the clusters, the resulting Figure (see Fig. 3.22) reveals the corrected energy distribution across the  $\lambda$  range for a FOOT detector. Fig. 3.23 shows the energy correlation (energy in ADC channel) between the two In-beam FOOT detectors inside the vacuum chamber for a  $^{12}\text{C}$  incoming beam.

It is convenient to correct this  $\lambda$  dependency for all charges (except  $Z = 1$  and  $Z = 2$ ) simultaneously. Charge  $Z = 1$  and  $Z = 2$  don't strongly depend on the  $\lambda$  value. However, the region at low  $Z$  is heavily populated by noisy events and the definition of a proper polynomial function to apply the  $\lambda$ -correction is challenging. The results of the  $\lambda$ -correction are shown in Fig. 3.22.

<sup>5</sup>Study of drip-line phenomena in neutron-rich nuclei, by O. Sorlin et al. [120].

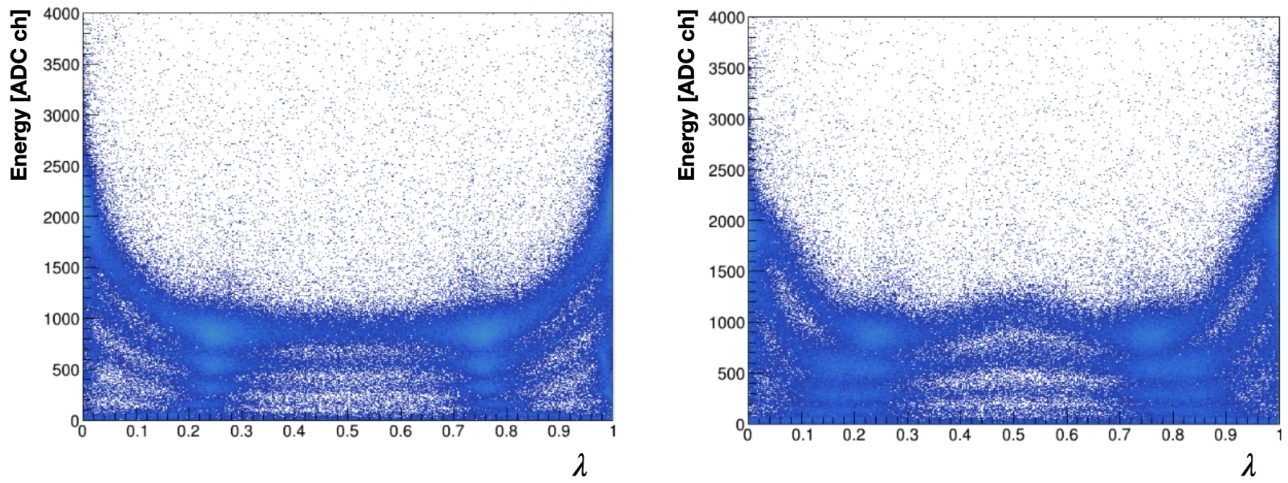


Figure 3.21: Cluster energy with respect to the  $\lambda$  value, for 2 different FOOTs. As we can notice here, the shape of the charge component varies significantly from sensor to sensor.

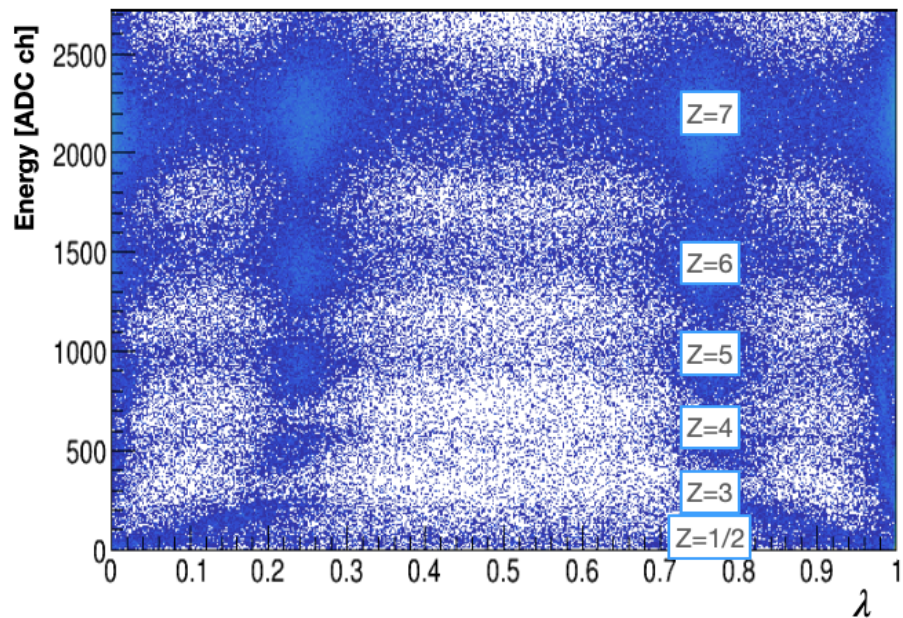


Figure 3.22: Corrected cluster after  $\lambda$ -energy correction with respect to the  $\lambda$  value done with s509  $^{21}\text{N}$  FRS setting.  $Z=1/2$  are the particles with  $Z=1$  and  $Z=2$  that populates a very similar region.

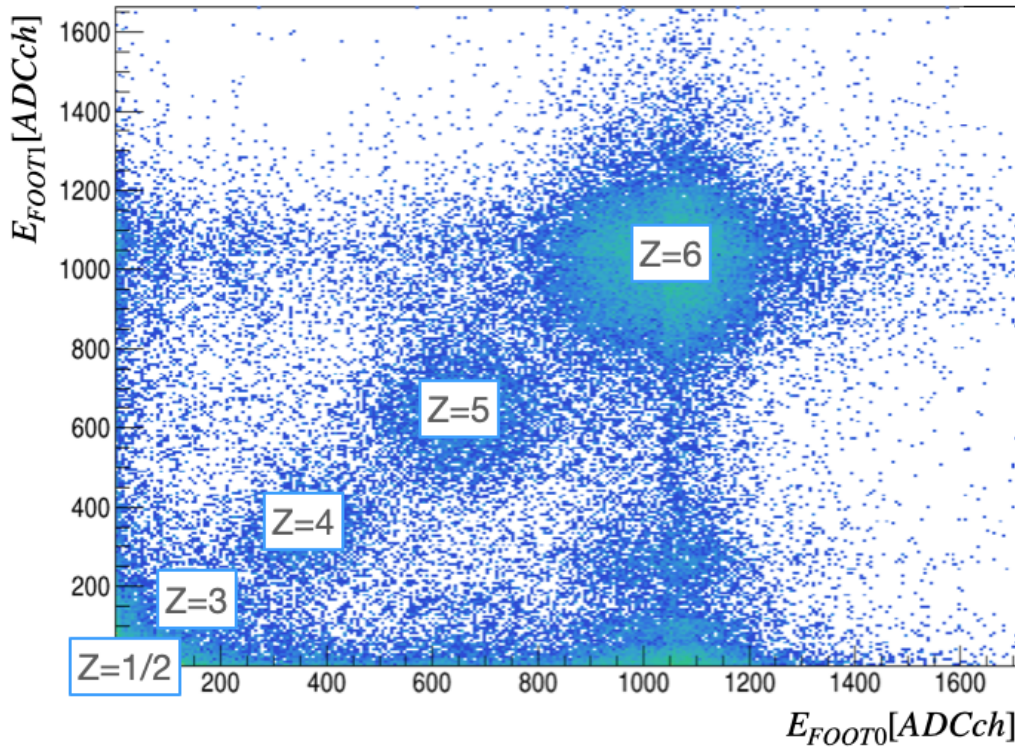


Figure 3.23: Energy correlation (energy in ADC channel) between the two In-beam FOOT detectors inside the vacuum chamber for a  $^{12}\text{C}$  incoming beam.  $Z=1/2$  are the particles with  $Z=1$  and  $Z=2$  that populates a very similar region.

The calibration process for the Arm FOOT detector is straightforward, consisting of a single step that involves pedestal subtraction and fine baseline correction. Additionally, the same clustering algorithm used for the In-Beam FOOT is employed here. However, for the Arm FOOT, the  $\lambda$ -energy correction is not applied. The primary function of the Arm FOOT is to detect scattered protons, specifically identifying particles with charge  $Z = 1$ . As previously mentioned, the identification of charge  $Z = 1$  is not strongly influenced by the  $\lambda$  value. It is important to note that the low  $Z$  region is heavily populated with noisy events, which affects the resolution of cluster position and energy values.

At the conclusion of the calibration process for the FOOT detectors, we achieve the "Hit" level. At this stage, significant quantities are accessible following the clustering algorithm and  $\lambda$ -correction. The position of the hit on the detectors is determined using geometrical information relative to the central  $X$  and  $Y$  positions of the detectors, along with the angular rotation values  $\theta$  and  $\phi$ . Tab. 3.1 displays these values for all the detectors. The central positions of the detectors are given in millimeters, while the angles are in degrees. The position  $z$  indicates the distance of the FOOT from the flange of the vacuum chamber.

FOOT	1	2	4	6	7	9
foot Z [mm]	658.256	642.052	499.979	527.848	490.413	517.386
foot $\theta$ [deg]	-	-	-74.752107	-74.769678	75.25259	75.038226
foot $\phi$ [deg]	-	90	180	90	90	180
foot X [mm]	-1.034	-0.484	45.007	63.395	-39.354	-58.460
foot Y [mm]	2.564	2.262	1.247	2.105	1.782	1.661

FOOT	10	11	12	13	15	16
foot Z [mm]	527.136	518.193	499.755	490.752	1191.645	1156.636
foot $\theta$ [deg]	75.038226	-74.769678	75.252529	-75.752107	-	-
foot $\phi$ [deg]	270	180	180	270	-	270
foot X [mm]	-63.935	57.956	-45.533	38.323	5.636	5.847
foot Y [mm]	1.993	2.258	0.934	1.332	-5.72	-5.796

Table 3.1: FOOT Detector Parameters derived from the laser measurement done in August 2022. More details are presented later in the detector alignment section.

If  $\phi = 0^\circ$  ( $X$ -Foot, StripId numbered from left to right, see Fig. 2.10):

$$\begin{aligned}x &= -(\text{pos} \times \cos(\theta \times \pi/180) + X), \\y &= Y, \\z &= \text{pos} \times \sin(\theta \times \pi/180) + Z.\end{aligned}\tag{3.10}$$

If  $\phi = 90^\circ$  ( $Y$ -Foot, StripId numbered from bottom to top, see Fig. 2.10):

$$\begin{aligned}x &= X, \\y &= \text{pos} + Y, \\z &= Z.\end{aligned}\tag{3.11}$$

If  $\phi = 180^\circ$  ( $X$ -Foot, StripId numbered from right to left, see Fig. 2.10):

$$\begin{aligned}x &= -(-\text{pos} \times \cos(\theta \times \pi/180) + X), \\y &= Y, \\z &= -\text{pos} \times \sin(\theta \times \pi/180) + Z.\end{aligned}\tag{3.12}$$

If  $\phi = 270^\circ$  ( $Y$ -Foot, StripId numbered from top to bottom, see Fig. 2.10):

$$\begin{aligned}x &= X, \\y &= -\text{pos} + Y, \\z &= Z.\end{aligned}\tag{3.13}$$

After these steps, we have access to the position information of the particle hit and its deposited energy. In the following data analysis of Chapt. 4, as previously anticipated, the FOOT detector information was not considered. Since the calibration process and the initial stages of our data analysis, our goal was to obtain clear proton tracks to enable accurate reaction vertex reconstruction. However, we encountered several issues:

- **Low Efficiency:** We observed that requiring a high-quality track in all incoming, outgoing, FOOT, and CALIFA detectors significantly reduced the statistics compared to analyses without the FOOT detectors. In July 2023, V. Panin and summer student W. Stafford investigated the performance of the FOOT detectors, culminating in a report [121]. The report analyzed data from two FOOT detectors exposed to proton beams of various energies to determine detector efficiencies under different thresholds, dead times, and beam positions. Of particular interest is the efficiency estimation for a 1 GeV proton beam (see Fig. 3.24). This estimation indicated that, at a  $4\sigma$  energy threshold (the same threshold was applied in our analysis), a single FOOT detector's efficiency was approximately 60%. Increasing the energy threshold further reduced the efficiency. To track a single proton in one arm, we needed the information of 4 successive detectors, thus leading to an efficiency

of  $0.6 \times 4 = 12\%$  only. Considering that to detect a  $(p, 2p)$  reaction we need also a second telescope, the statistics reduces drastically.

- **High Noise Level:** While attempting to obtain a reaction vertex from the Arm FOOT detectors, we found that the hit multiplicity was extremely high ( $\delta$  electrons, baseline fluctuations and noisy ASICs), ranging from 1 to  $10^3$  hits per detector per event. Vertex reconstruction required all 8 Arm FOOT detectors, and the process involved combining multiple tracks to find pairs of tracks (one from each arm) that were close in space. This resulted in an average of  $10^4$  possible combinations, complicating the reconstruction. We considered increasing the energy threshold to mitigate this issue, but it further reduced the statistics.
- **Baseline Fluctuation:** Following the May 2022 experiment at GSI, an investigation was conducted on FOOT detectors to understand baseline fluctuations occurring at high trigger rates ( $> 8$  kHz). This investigation revealed issues with the FOOT Front End board, particularly in the current rails supplying power to the ASICs, making the detector unable to sustain high trigger rates. More details can be found in [94].

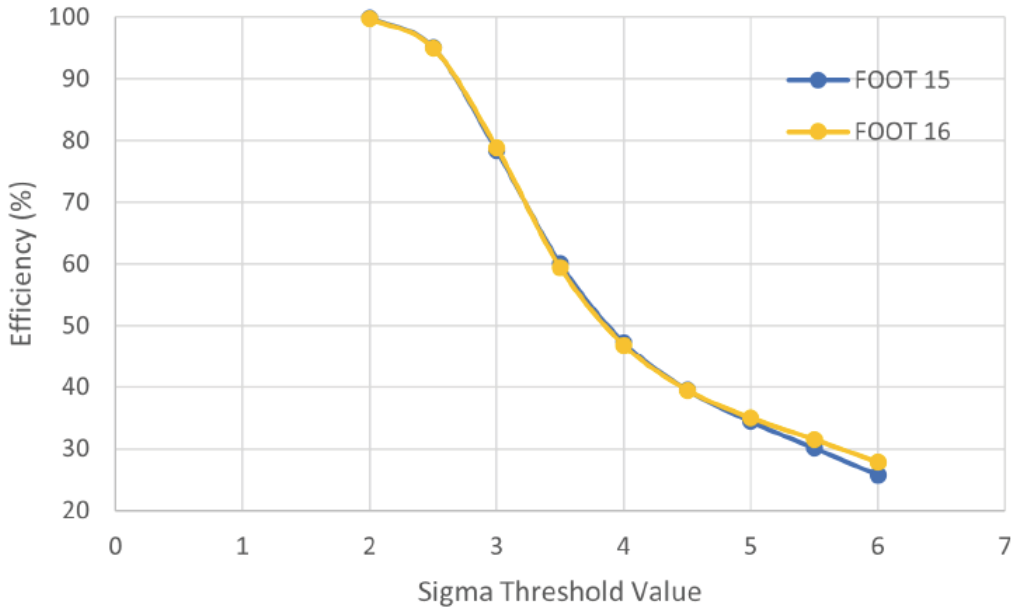


Figure 3.24: Plot showing efficiency against sigma threshold value for the 1 GeV proton beam. Figure taken from [121].

After evaluating the issues with the FOOT detectors, we decided to proceed with the data analysis without utilizing their information. Consequently, the angles of the  $(p, 2p)$  protons were reconstructed using the CALIFA detectors. The reaction vertex was determined by projecting the MWPCs tracks to the center of the target, resulting in the following:

$$V_{\text{MWPCs}} = (V_{x,\text{MWPC}}, V_{y,\text{MWPC}}, 0). \quad (3.14)$$

### 3.2.3 Outgoing detectors calibration

In this section, we discuss the calibration of the downstream detector, with a particular emphasis on the Time-of-Flight Detector (ToFD) calibration. This calibration process is crucial for accurately determining the momentum of the recoil neutron or proton associated with a short-range correlation (SRC) pair. Additionally, it is important to identify the resulting fragment and measure its momentum. Proper calibration of these detectors is essential to ensure precise measurements and reliable experimental results.

#### TOFD calibration

The main purpose of TOFD is to provide  $ToF$  and charge  $Z$  information for the different fragments produced after the reaction and, in particular, after the SRC breakup. This latter measurement poses a significant challenge to the stability performance of the detector, as the electronics must adeptly handle high beam rates with multi-hit capability. Identification of the nuclear charge relies on assessing the energy loss of particles within the scintillator material, achieved through a Time-Over-Threshold ( $ToT$ ) method [93; 104]. Fig. 3.25 illustrates this approach schematically. The time width, expressed by the leading and trailing edge, while the PMT signal exceeds a pre-defined threshold, can be converted to the energy loss in the detector material and, thus, to the nuclear charge of the projectile. To overcome the non-linearity of the amount of charge produced or signal height to the time width in standard  $ToT$  measurements, TOFD uses the filtered and integrated signal to measure the energy loss and identify the nuclear charge [104].

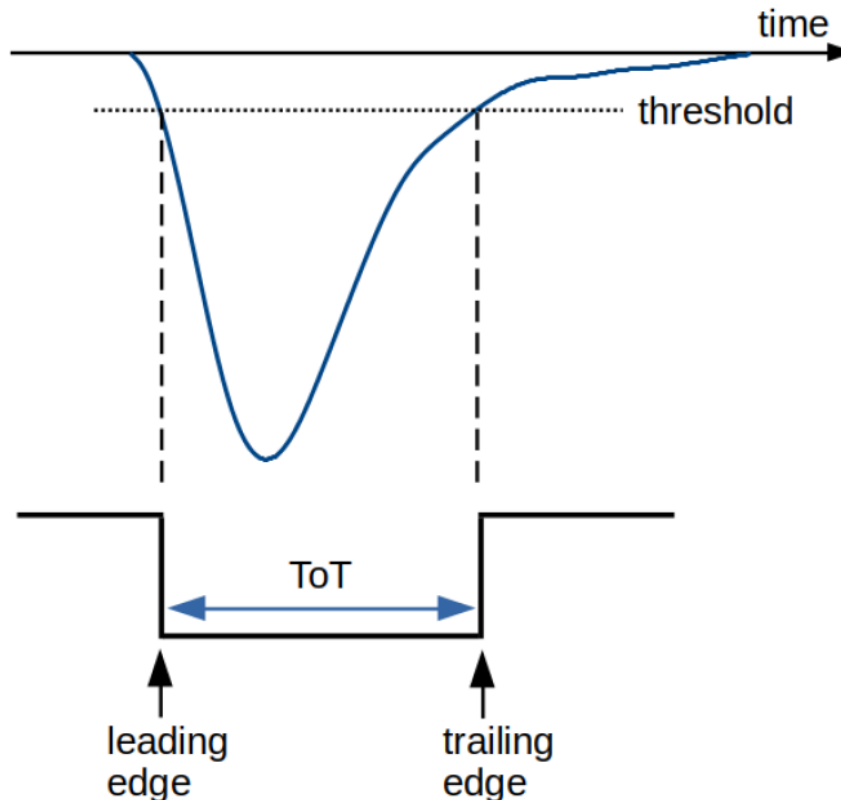


Figure 3.25: Time-over-Threshold measurement. The time width, while the signal exceeds the pre-defined threshold, is defined by the leading and trailing edge.

Time measurements for the leading and trailing edge information of the integrated and digitized signals are divided into coarse and fine time measurements. The coarse time is determined by counting the cycles of a 200 MHz readout clock with a binning of 5 ns. Within each clock cycle, the exact position of the signal rise relative to the next cycle is derived using an FPGA-based Time-to-Digital Converter (TDC). In a so-called tapped delay line (TDL), the incoming signal propagates through the delayed logic modules of the FPGA until the next clock cycle stops the sampling process.

The number of modules can be converted into a time difference from the signal start to the end of the clock cycle, known as fine time. This technique achieves picosecond-level precision in time measurement. Fig. 3.26 illustrates the relationship between coarse and fine time, along with a schematic view of an FPGA-based TDC measurement. Coarse and fine time values are expressed in channel units. Due to the sensitivity of the fine time counter to temperature shifts in the electronics, a calibration must be performed individually for each run. Additionally, since the FPGA delay units are not constant, each channel requires its own calibration parameter set. By estimating the deviation of the measured data from a uniform distribution, a calibration function can be formulated as:

$$\text{Time} = \frac{\sum_{i=0}^{\text{bin}} \text{counts}(i)}{\sum_{i=0}^{\text{max}} \text{counts}(i)} \times \text{ClockTime}. \quad (3.15)$$

This calibration process requires sufficient statistics for each TDC channel to generate an accurate calibration function, which is stored in a lookup table. The leading and trailing edge time information is derived from the difference between corresponding coarse and fine times:

$$\text{Time}_{\text{leading/trailing}} = \text{ClockCycle} \times \text{ClockTime} - \text{FineTime}. \quad (3.16)$$

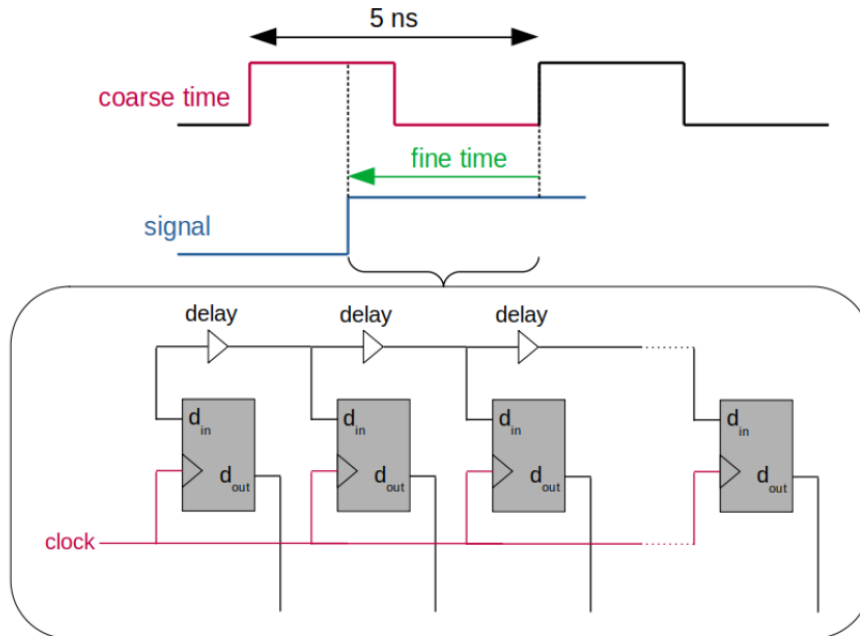


Figure 3.26: Time measurement with TOFD. The number of cycles of a 200 MHz clock defines the coarse time (red) with a precision of 5 ns. The fine time (green) is defined by the difference of the signal rise to the start of the next clock cycle and is determined with an FPGA-based TDC (lower panel). The signal is propagated through delayed FPGA modules until the next clock cycle stops the sampling process.

### *Gain matching and time calibration*

The measured Time-over-Threshold ( $ToT$ ) values are proportional to the collected charges from the corresponding PMTs at each end of the scintillator bar. The PMT signal depends on the position where the particle hits the detector. The measured energy ( $E_{\text{PMT}}$ ) is related to the deposited energy ( $E_0$ ) and can be expressed as:

$$E_{\text{PMT}} = E_0 \cdot \exp(-\lambda \cdot Y_{\text{PMT}}); \quad (3.17)$$

where  $\lambda$  is the attenuation parameter and  $y_{\text{PMT}}$  is the distance between the particle impact position and the PMT. Using this definition, the actual particle position on the bar can be calculated as:

$$y_{\text{TOFD}} = \lambda \cdot \log \left( \frac{\text{ToT}_{\text{PMT1}}}{\text{ToT}_{\text{PMT2}}} \right). \quad (3.18)$$

The first calibration step involves gain- matching the  $ToT$  values for PMT1 and PMT2. This is achieved by conducting a horizontal sweep run in the middle of the detector's active area ( $y = 0$ ). A Gaussian fit is performed around the maximum of the  $ToT$  value for each bar. After deriving the effective ( $y_{\text{eff}}$ ) using the equation before, we can calculate the position offset value as  $y_{\text{off}} = y_{\text{eff}} - 0$ . This offset is then applied to both the up and down channels:

$$\Rightarrow E_{\text{up}} = E_{\text{up},0} \cdot \frac{1}{\sqrt{\exp(y_{\text{off}})}}, \quad (3.19)$$

$$E_{\text{down}} = E_{\text{down},0} \cdot \sqrt{\exp(y_{\text{off}})}. \quad (3.20)$$

These offsets are calculated simultaneously and applied for the subsequent calibration step. In Fig. 3.27, the raw spectrum of the sweep run at  $y = 0$  is displayed. Peaks along the  $ToT$  axis in the top left panel correspond to different charges of incoming particles. As no empty target runs were conducted, the calibration runs also included fragments. Peaks along the bar axis correspond to moments when the Time-of-Flight Detector (ToFD) was stationary for an extended period during the sweep. Consequently, these areas have been illuminated for a longer duration, resulting in higher counts ( $Z$ -axis) being observed.

In order to perform the calibration of time offsets and sync parameters, one performs a sweep run with the  $xy$ -table at the center of the bars ( $y = 0$ ). With this run, one can determine the offsets of the PMTs at the top and bottom of one bar. The offset compensates for the time difference, for example, in cable length. After it is applied, the times of the PMTs are equal if one hits the bar in the middle. Since one does not want to change the average time of the bar, we add half of the offset to one PMT and subtract half of the offset of the other PMT time.

With the same sweep run at  $y = 0$ , the sync parameters can also be determined. For this, we plot the time difference between the average times of the bars and the trigger time (LOS time is also possible) (see Fig. 3.27, bottom figures).

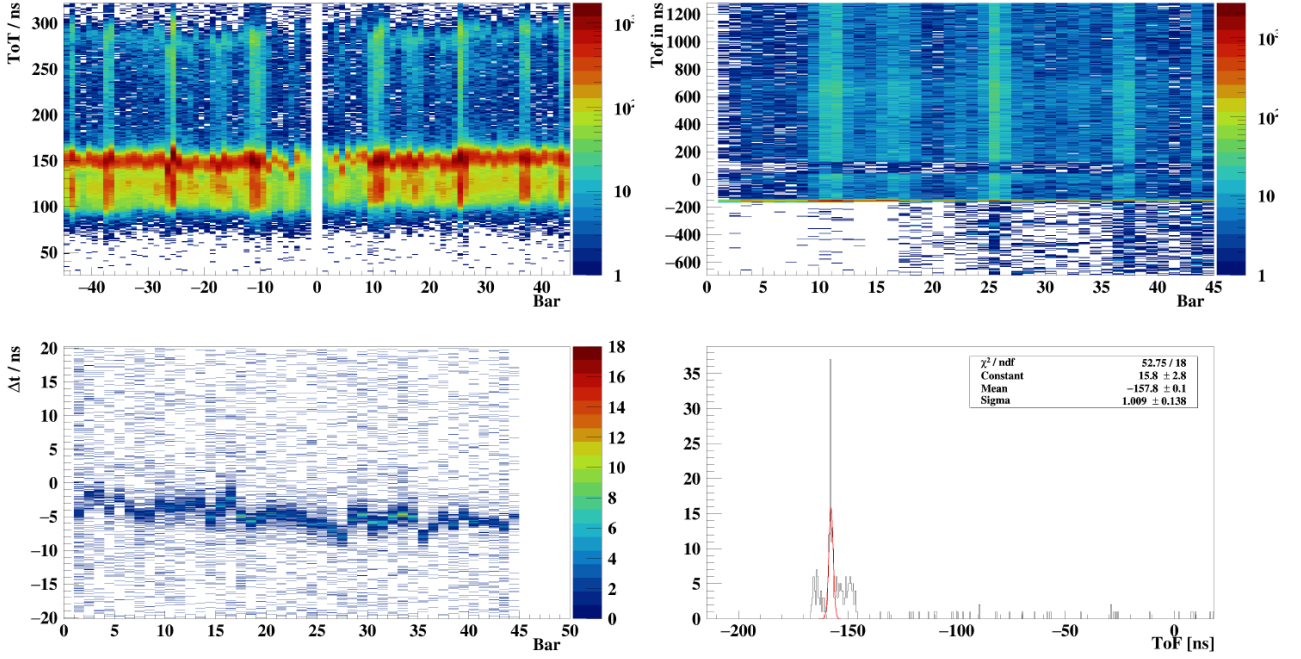


Figure 3.27: Raw ToFD data, Top left:  $ToT$  vs. bar number for data from an  $x$  sweep run at  $y =$  center position. Negative bars display the bottom PMT channels, and positive the top PMT channels. Right: Time-of-Flight over bar number. Bottom left: time difference between the average times of the bars and the trigger time for a sweep run. Right:  $ToF$  parameter calculation by a Gaussian fit over the maximum.

### *Attenuation $\lambda$ and $v_{eff}$*

The second calibration step is performed using a procedure similar to the one before. In order to obtain a  $y$ -position along the bar, the time difference between the PMTs has to be multiplied by the effective speed of light ( $v_{eff}$ ). The effective speed of light takes into account the reduced speed of light in a medium and the longer paths to the end of the bar due to light reflections inside the bar.

$v_{eff}$  determination is accomplished through a second sweep run, initiated at +20 cm from the center, causing the Time-of-Flight Detector (ToFD) to move downwards (see Fig. 3.28). The experimental conditions remain consistent with the previous step. This approach allows for the determination of two key parameters: the effective speed of light ( $v_{eff}$ ) and the light attenuation factor ( $\lambda$ ). For a hit at position  $y$ , the signals reaching the up and down Photomultiplier Tubes undergo attenuation as follows:

$$E_{up} = E_0 \cdot \exp\left(-\lambda \left(\frac{L}{2} - y\right)\right), \quad (3.21)$$

$$E_{down} = E_0 \cdot \exp\left(-\lambda \left(\frac{L}{2} + y\right)\right); \quad (3.22)$$

where  $L$  represents the length of the scintillator bar. Utilizing Eq. (3.12), this can be expressed as:

$$y = \frac{1}{2\lambda} \log\left(\frac{E_{up}}{E_{down}}\right) \cdot v_{eff}. \quad (3.23)$$

Similar to the previous step, a Gaussian fit around the  $ToT$  maximum for each bar is used to

determine the offset. The parameter  $\Lambda$  is then defined as:

$$\Lambda = 20 \text{ cm} \cdot \text{offset}. \quad (3.24)$$

$\Lambda$  is directly utilized as the calibration parameter:

$$y_{\text{calib}} = \Lambda \cdot \log \left( \frac{E_{\text{up}}}{E_{\text{down}}} \right) \cdot v_{\text{eff}}. \quad (3.25)$$

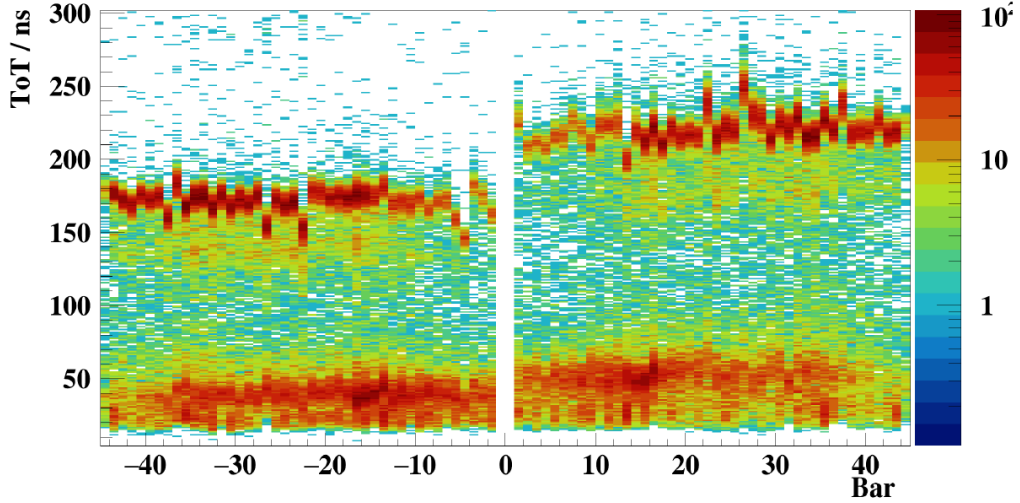


Figure 3.28:  $ToT$  vs bar number during a  $x$  sweep run at  $y = 20$  cm position. The up-located channels (positive bar numbers) measure a higher  $ToT$  than the down-located channels.

### Charge calibration

As already mentioned, the measured energy depends strongly on the distance of the impact position of the particle on the PMT. According to theory, one expects a position-independent  $\Delta E$  measurement if one plots  $\sqrt{ToT_1 \cdot ToT_2}$  and the position along the scintillator bar. However, in reality, we observe a dependence of the measurement on the position along the bar (see Fig. 3.29). This dependency turns out to become non-linear at the edges of the bar. To identify this non-linear behaviour, a meander run is used. This involves conducting a sweep under consistent beam conditions, fully illuminating the bars, as depicted in Fig. 3.29.

Fig. 3.29 shows the deposited energy versus the vertical position for a single bar. The prominent band indicates that the beam scanned the bar over a range of around 100 cm. The smiley effect, observed in Fig. 3.29 for one bar, represents a dependence of the  $ToT$  on the position along the bar length. This happens when edge effects arise, causing deviations of the  $ToT$  near the bar edges. Using a polynomial fit function of the third degree, the position-dependent charge identification can be corrected as:

$$Q_{\text{TOFD}} = \frac{\sqrt{ToT_{\text{PMT1}} \cdot ToT_{\text{PMT2}}}}{(p_0 + p_1 \cdot y + p_2 \cdot y^2 + p_3 \cdot y^3)} \quad (3.26)$$

where  $p_0$  to  $p_3$  are the fitting parameters.

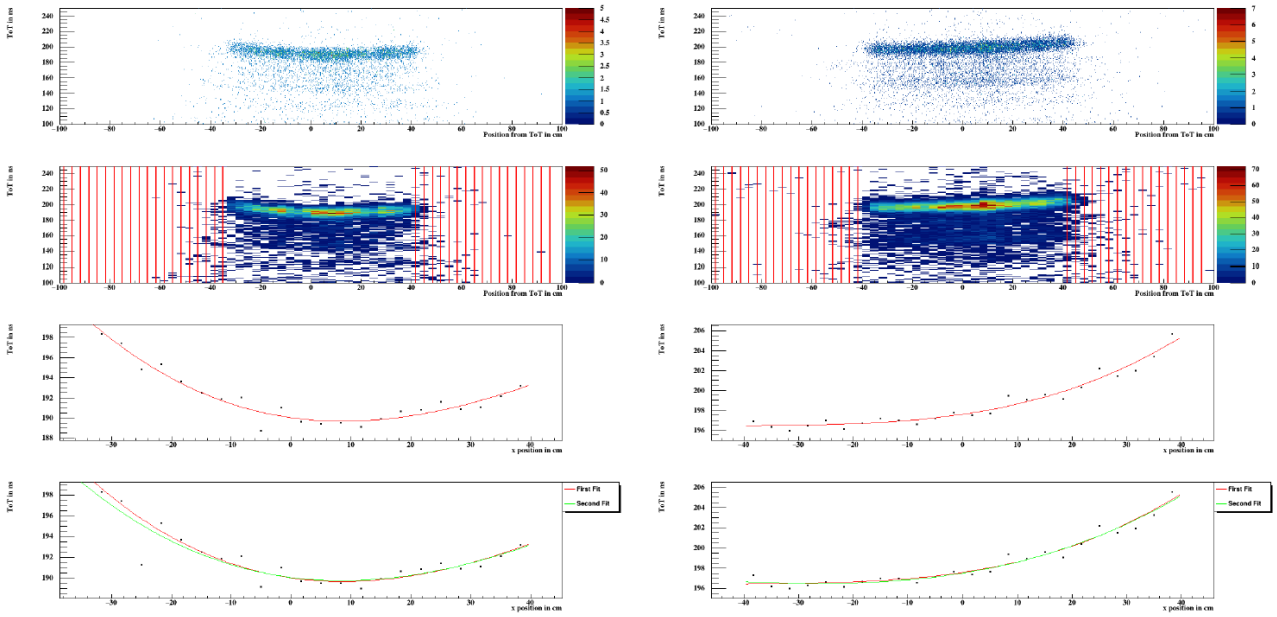


Figure 3.29:  $ToT$  distribution along one bar (Top) in the meander run for two example bars (left and right). Although the geometric mean of the  $ToT$  is expected to be constant along the bar, edge effects are clearly visible. Below, the same plot with the set granularity (rebinned) is shown. The code is set for a coarse threshold. If, for a given  $Y$ -projection, the maximum is below the threshold or outside the range of the bar (here  $\pm 40$  cm), that data point is rejected (see red lines). These data points are then fitted by a third-order polynomial. With the fit parameters determined, the procedure is repeated with a lower threshold and refitted (two lower panels). In all the plot the  $x$  axis show the position along the bar in  $cm$  and on the  $y$  axis the  $ToT$  information in  $ns$ .

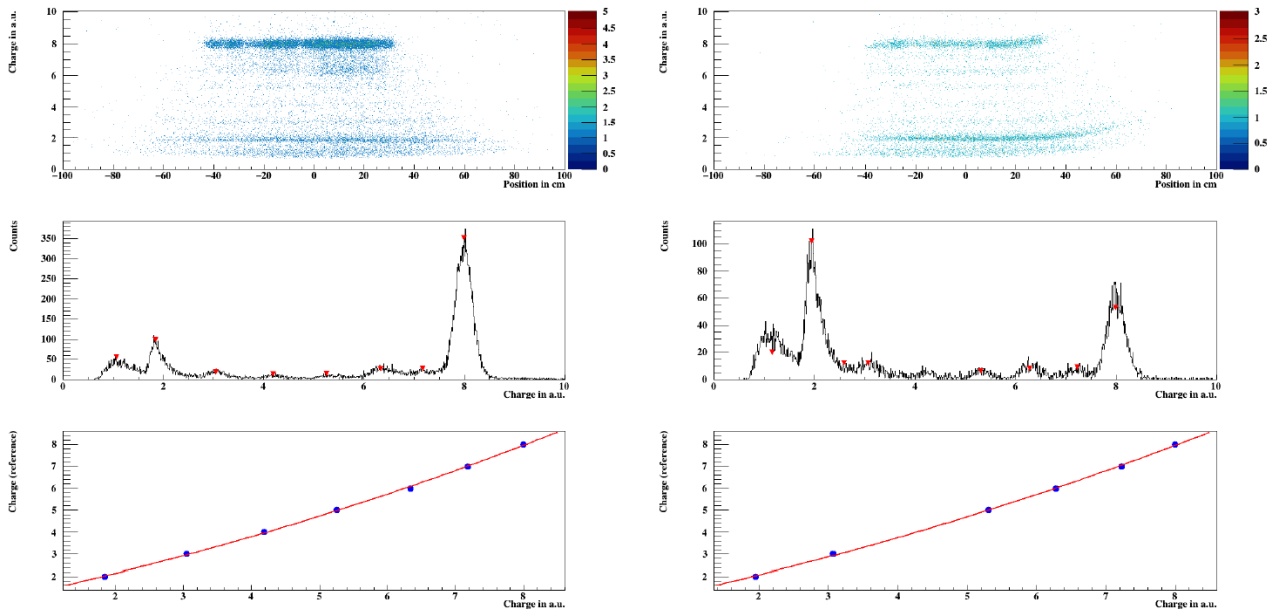


Figure 3.30: Top: result from the meander run after the smiley correction for two bars. On the left, the results for a bar with a good calibration are displayed. There is almost no position dependency left and in the projection (middle panel) all charge peaks can be easily distinguished and used for fitting (lower panel). On the right, a bar with a "bad" smiley correction is shown. The position dependency is still present, and the exact peak recognition is hindered. Furthermore, it can be seen that different charges need a different correction function/different parameters. In our case, this is still in the acceptable range, as the bands for charge 6,5,4 do not differ significantly.

In the final step, a parameter set is derived in an iterative way for each bar to shift the charge  $Q_{tofd}$  peak position to the nominal nuclear charge value. Fig. 3.30 shows the  $ToT$  distribution along one bar (Top) in the meander run after polynomial fit function correction (Top plots). In the central and bottom plots, it is possible to observe this iterative procedure to shift the charge  $Q_{tofd}$  of every bar to the nominal value. The final calibrated charge of TOFD for plane 1 for a horizontal sweep run is shown in Fig. 3.31.

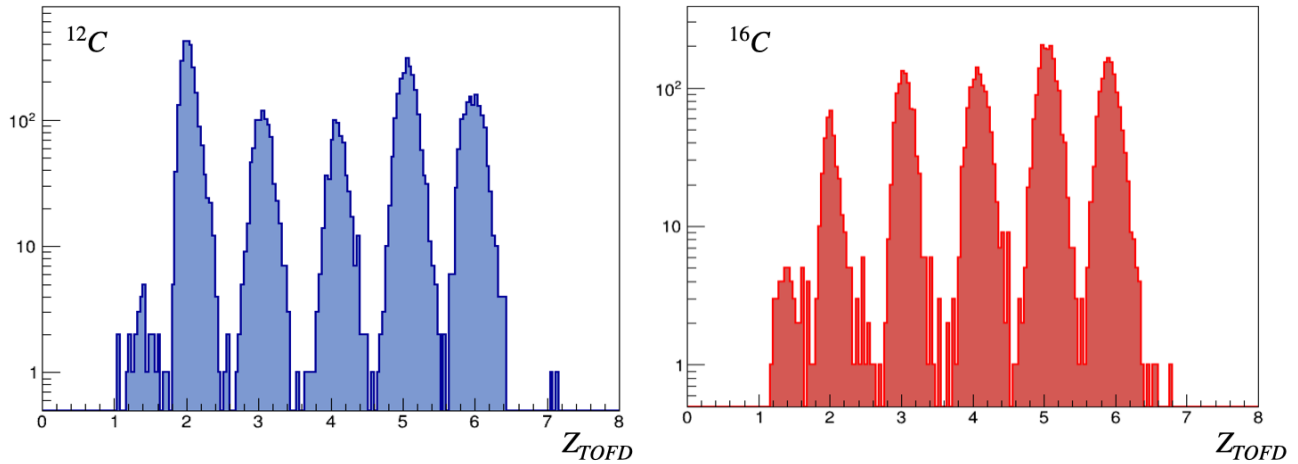


Figure 3.31: Charge in TOFD after the calibration procedure for  $^{12}\text{C}$  (left) and  $^{16}\text{C}$  (right).

### Fiber calibration

This section presents the Fiber time and energy calibration procedure, following a similar approach to the TOFD calibration discussed earlier. The first calibration step exactly resembles the TDC time calibration performed for TOFD using the same procedure. In this section, I will focus on the following steps of fiber calibration.

The calibration procedure of fiber includes:

- Energy-loss calibration.
- Time calibration.
- Time offset.
- Time-of-flight synchronization.

Sweep runs with  $^{12}\text{C}$  at an energy of 1.25 GeV/u were conducted for every Fiber detector. The fiber detectors were movable in the  $x$ -direction while keeping  $y$  constant to illuminate all fibers. For the  $y$ -direction detector (Fib30), a thick lead target was placed before the entrance of GLAD to illuminate as much of the detector as possible.

The calibration procedure is performed individually for each fiber detector with respective datasets. It involves two main steps:

- Conversion of FPGA channel numbers into times.
- Conversion of the signal time information into energy-loss via the Time over Threshold (ToT).

The "Hit" level calibration task ensures time coincidence between up and down channels.  $ToT$  values are calculated as the difference between leading and trailing edges for each up and down channel. A maximum finder algorithm is used for calibration. The extracted gain parameters are then applied to each hit, setting  $ToT$  in relation to a global maximum. After gain correction and geometric mean calculation, the final  $ToT$  values per fiber channel exhibit a clear separation between noise and data bands.

Time offsets between up and down channels are determined by a Gaussian fitting of the  $\Delta t$  spectrum for each channel, with the mean representing the offset parameter  $t_{\text{off}}$ . This ensures the correlation of signals from up/down PMTs to real particle interactions.

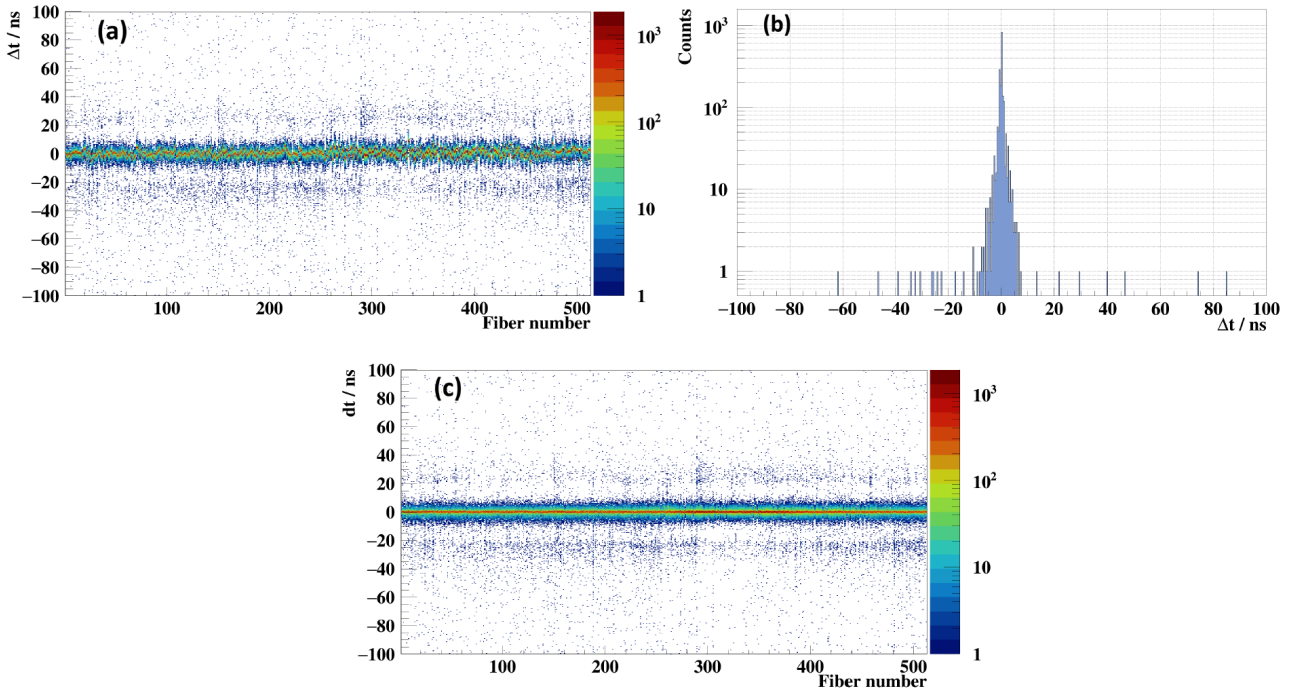


Figure 3.32: Time difference calibration for Fib32 with  $^{12}\text{C}$  sweep run. (a)  $\Delta t$  as a function of the fiber number. For every channel, the maximum is identified (b). (c) Calibrated  $\Delta t$  spectrum.

The calculated time offset is subtracted from  $\Delta t$ :  $t_{\text{up}} - t_{\text{off}}/2$  and  $t_{\text{down}} + t_{\text{off}}/2$ . The results are illustrated in Fig. 3.32. The Figure shows the time difference calibration for Fib32 with a  $^{12}\text{C}$  sweep run. In Figure (a), the time difference as a function of the fiber number is displayed. For every channel, the maximum is identified, as shown in Figure (b). In Figure (c), the calibrated time difference spectrum is presented. The calibrated time differences of each up and down channel now form a sharp band around 0. Time synchronization is performed relative to the event trigger provided by the LOS-detector. By including the triggers in the Cal-level calibration, all times are set relative to the trigger time, which is related to the start signal. Clock cycle jumps within the KILOM2 boards are adjusted, where the trigger-adjusted leading (or trailing) edge is checked to fall within the readout window. The trigger-adjusted time for a given signal in the fiber detectors is calculated as:

$$t_{\text{mean,TrAdj}} = \frac{t_{\text{up,TrAdj}} + t_{\text{down,TrAdj}}}{2}. \quad (3.27)$$

To calculate the  $ToF$ , one subtracts the time of the start signal from the trigger-adjusted times:

$$\text{ToF} = t_{\text{mean,TrAdj}} - t_{\text{start}}. \quad (3.28)$$

The resulting  $ToF$  values are synchronized and aligned to 0 within the DAQ readout window. Cross-talk or noise effects may lead to apparent matches between up/down channels. Gating on the  $ToF$  eliminates the wrong reconstructed hit, while a time difference cut directly removes uncorrelated signals. An acceptance window of 11 ns is estimated, considering the maximum time difference within the same fiber. This compromise ensures sufficient data while cutting out most mishits. Further cuts on  $ToF$  within the readout window can be applied. However, for this campaign, a cut on  $\Delta t$  is deemed sufficient.

Calibrating the  $Y$ -Fiber detector posed challenges, as it was rotated by  $90^\circ$  to measure the  $Y$  position. Illuminating every channel was not feasible, so a 2.5 cm lead brick at the entrance of GLAD dispersed the beam, illuminating roughly 50% of the detectors. Outside channels remain uncalibrated. The calibrated  $ToT$  and synchronized time spectra for the  $Y$ -Fiber detector are shown in 3.33, with visible data bands from fibers 150 to 400. Outside channels exhibit a systematic drift in  $ToT$  values, while the time synchronization appears less affected by lower statistics.

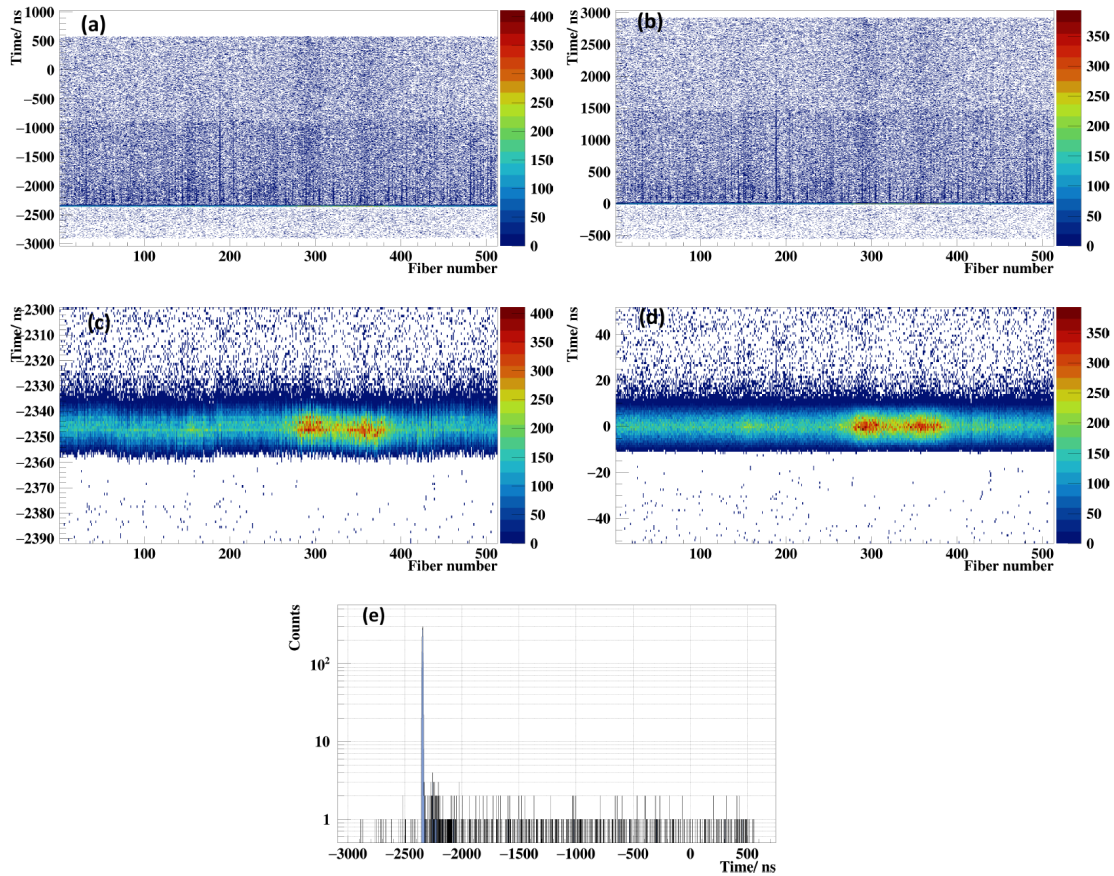


Figure 3.33: Top:  $Y$ -Fiber detector calibration results with dispersed  $^{12}\text{C}$  beam. Only fiber numbers 150-400 could be properly calibrated. Therefore,  $ToT$  and time synchronization parameters only exist for these channels. Outer channels remain uncalibrated. Bottom:  $Y$ -position in Fib30 against  $X$ -position in Fib32 for  $^{12}\text{C}$  production run of S522 campaign. In panel (a), one can observe a slight gap in the noise band at fibers 320. This hints at less efficient channels. As the data band is still sufficiently filled, this will not affect further analysis.

### NeuLAND calibration

A portion of the neutrons emitted during the neutron removal reaction ( $p,pn$ ) and during the decay of the unbound states populated by all reactions occurring around and within the target reach the NeuLAND detector. Obtaining the time of flight and the position of the first interaction of each neutron in NeuLAND is crucial for reconstructing relevant features for various studies related to the presented experiments, such as missing mass for ( $p,pn$ ) reactions, invariant mass for unbound states, and neutron correlations.

The following section describes the method applied from the "Mapped" level to the "Hit" level to obtain calibrated values for these two physical quantities: Time of Flight ( $ToF$ ) and position. At the Mapped level, the following quantities are available:

- PlanId (1-26), BarId (1-50), and the PMT side.
- CoarseTime (0-2047)  $\times$  5 ns, for the leading and trailing edge.
- FineTime (TDC channel), which needs to be calibrated to ns, for the leading and trailing edge (good accuracy:  $\sigma(\Delta t) = 7$  ps).

A good precision can be achieved even for the measurement of long-time differences by dividing the time into coarse and fine measurements, as illustrated in Fig. 3.34. To obtain the Time over the Threshold of each hit, the trailing time is subtracted from the leading time.

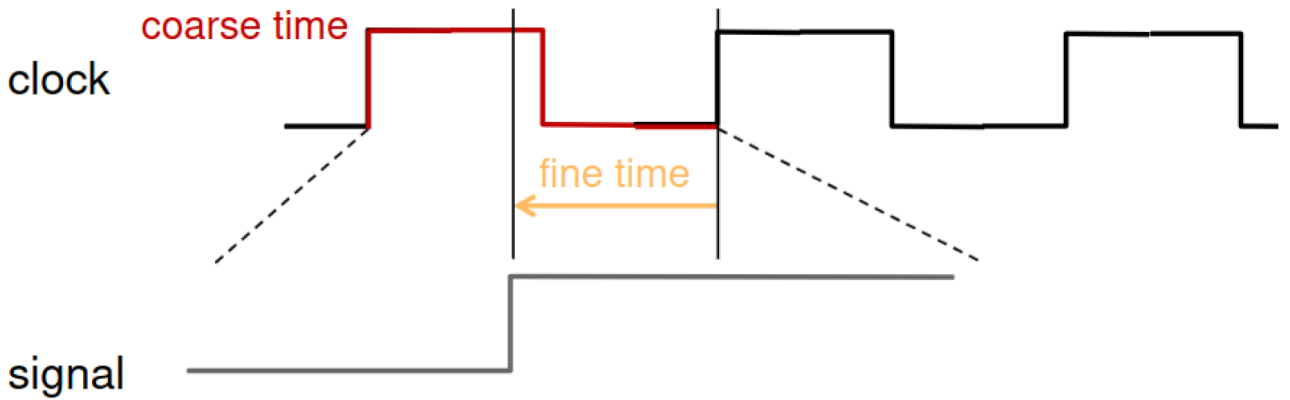


Figure 3.34: The time measurement is split into coarse (clock cycle) and fine (channel) time. The coarse counter of VFTX is reset at 2047. Figure from M. Heil's presentation on the calibration of FPGA TDC.

During this campaign, NeuLAND comprised 13 double-planes, each containing 50 bars, resulting in a total of 2600 PMTs. In the first calibration step, to calibrate the FineTime of each PMT, the following formula is used:

$$\text{Calibrated FineTime} = \text{Raw FineTime} \times \text{Calibration Factor}. \quad (3.29)$$

where the calibration factor is determined on the basis of the physics data collected during the experiment.

$$\text{FineTime}(bin) = \frac{\sum_{i=0}^{i=bin} \text{counts}(i)}{\sum_{i=0}^{i=max} \text{counts}(i)} \times \text{ClockTime}(VFTX). \quad (3.30)$$

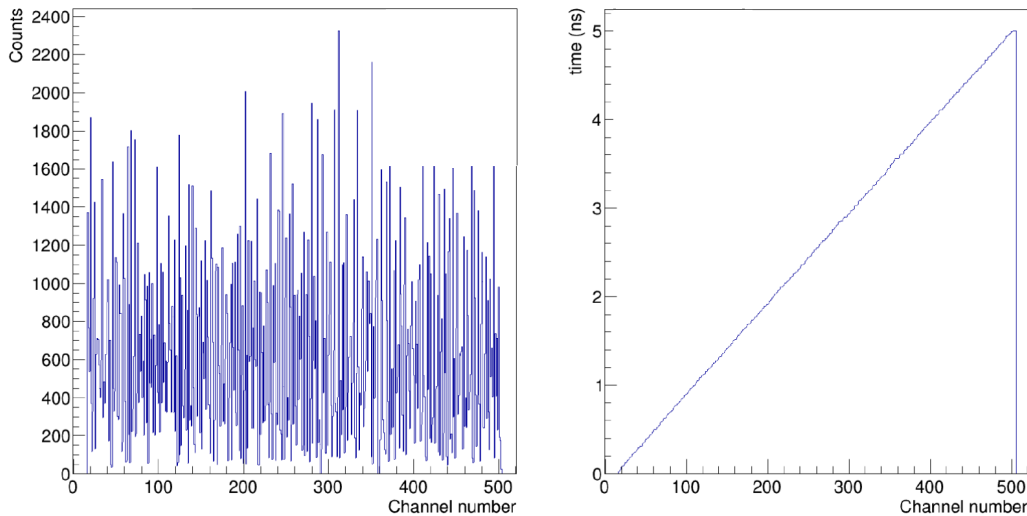


Figure 3.35: Left: number of counts with respect to the TDC channel. Right: time calibration of the channel number (from the left figure) using the Eq.3.30.

Parameter files corresponding to all the runs used for offline analysis are generated to prevent the loss of events that would otherwise fall out of range (due to time jumps or DAQ restarts). The calculation of the time for the leading and trailing edges, as depicted in Fig. 3.35, is performed as follows:

$$\text{Time} = \text{CoarseTime} \times (\text{ClockTime}(\text{VFTX}) + 1) - \text{FineTime}. \quad (3.31)$$

The second calibration step involves adjusting the time difference between the PMTs of the same bar using a  $T_{DIFF}$  offset to center the distribution on interactions occurring in the center of the bars (along their length). Subsequently, by utilizing off-spill events of NeuLAND (primarily cosmic rays,  $T_{pat}=8192$ ), the time signal of one bar is synchronized with respect to the others. Tracks of muons from cosmic rays, travelling (almost) at the speed of light, yield multiple hits in NeuLAND as references, which should align on straight lines with known relative time differences between the bars. Their initial positions are derived from the time difference or the position of the bars based on their orientation (horizontal or vertical). A minimization procedure is then applied to a large number of events to reconstruct individual muon tracks in each of them by applying a set of TSYNC offsets within this detector, leveraging our initial knowledge of the time difference and distance between each pair of hits, and the expected speed of muons (nearly) at the speed of light.

Fig. 3.36 (Top plot) illustrates the time difference between the two timing signals of one bar versus bar ID for a  $^{12}\text{C}$  primary beam (impinging on the  $\text{LH}_2$  target) experimental data run (we looked at off-spill data) after this first calibration step. The first 100 bars belong to two new panels with worse resolution than the rest. Fig. 3.36 (bottom plot) shows the synchronization of the time signal in different bars across all modules for the same run. The time difference between hits in one bar and that in a central bar versus bar ID is depicted. Since most cosmic muons enter NeuLAND from the top at an angle with the vertical line, different behaviours for horizontal and vertical planes time differences are expected. Additionally, a closing of the timing difference gap is observed as the bars studied approach the central reference bar.

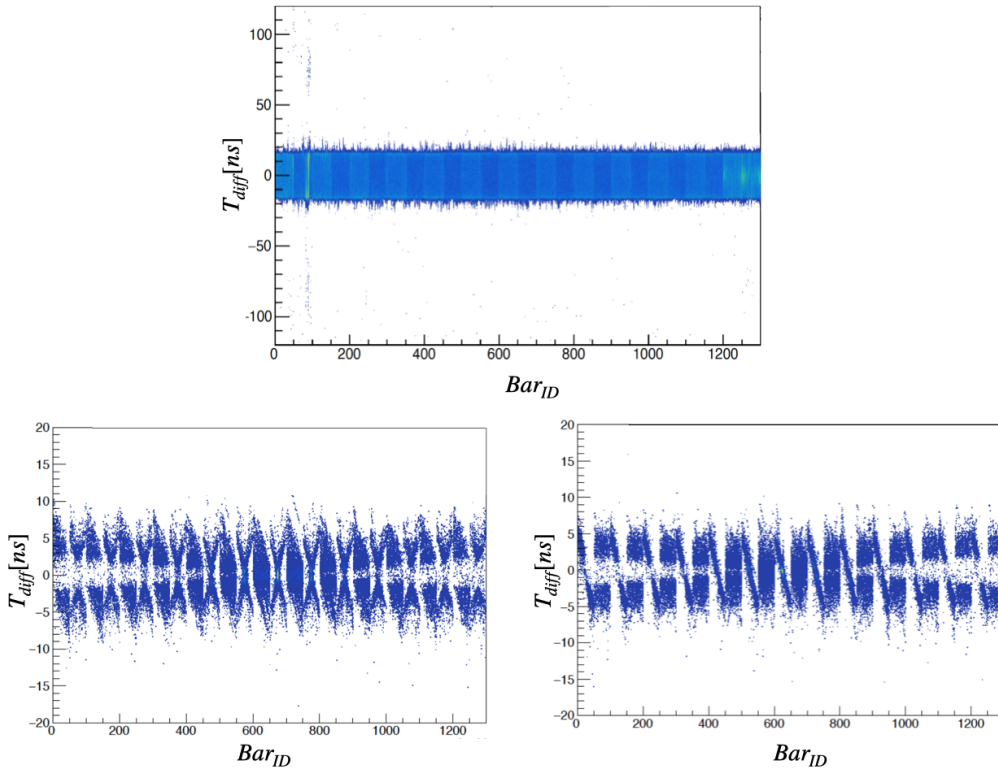


Figure 3.36: Top: Time difference between left (bottom) and right (top) signals of one bar vs the bar number for run 140 (with primary  $^{12}\text{C}$  beam and looking at of-spill data). Bottom: Time difference between a muon hit in a bar and a hit in a central bar 625 (top, horizontal plane central bar) and bar 675 (bottom, vertical plane central bar) after synchronization. The structure shown in the bottom figures is related with the different angles that the muon tracks can reach NeuLAND detector.

The synchronization parameters used in the figures above are derived from the AmBe calibration run for CALIFA. However, due to configuration changes between runs, this set of parameters may not be applicable to every run. Consequently, the synchronization results need to be checked for each run and generate a new set of parameters for runs where the bars are not synchronized.

An absolute alignment of these time differences across the entire detector is achieved by using the  $\gamma$ -ray peak as a reference based on the bar distance from the target.

To compensate for the time difference of a photon hit among different bars due to their positions, the corrected time spectrum was examined, and it is given by:

$$t_{\text{corr}} = t_{\text{hit}} - \frac{\text{dist}}{c}. \quad (3.32)$$

where  $t_{\text{hit}}$  is the time difference between the calibrated NeuLAND hit time and trigger time,  $\text{dist}$  is the difference in distance between the nominal NeuLAND position to target (1520 cm) and the actual hit position to target, and  $c$  is the speed of light. Fig. 3.37 (Top left) displays the corrected time spectrum, where the three peaks correspond to  $\gamma$ , neutron, and beam dump, respectively. Note that the corrected timing solely applies to the photon peak as a timing resolution check. Neutron speed will be computed using position and time of flight information.

Fig. 3.37 (top right) shows the Gaussian-fitted time-of-flight spectrum of the  $\gamma$  peak in a  $^{16}\text{C}$  run. The timing resolution is 206.8 ps, with the peak  $\gamma$  time of flight at 43.33 ns. To align the photon peak to  $\beta = 1$ , the  $\gamma$  peak should occur at 50.7 ns, assuming the distance between NeuLAND and the nominal target is 1520 cm. Consequently, a global shift of 7.37 ns needs to be applied to the time-of-flight spectrum.

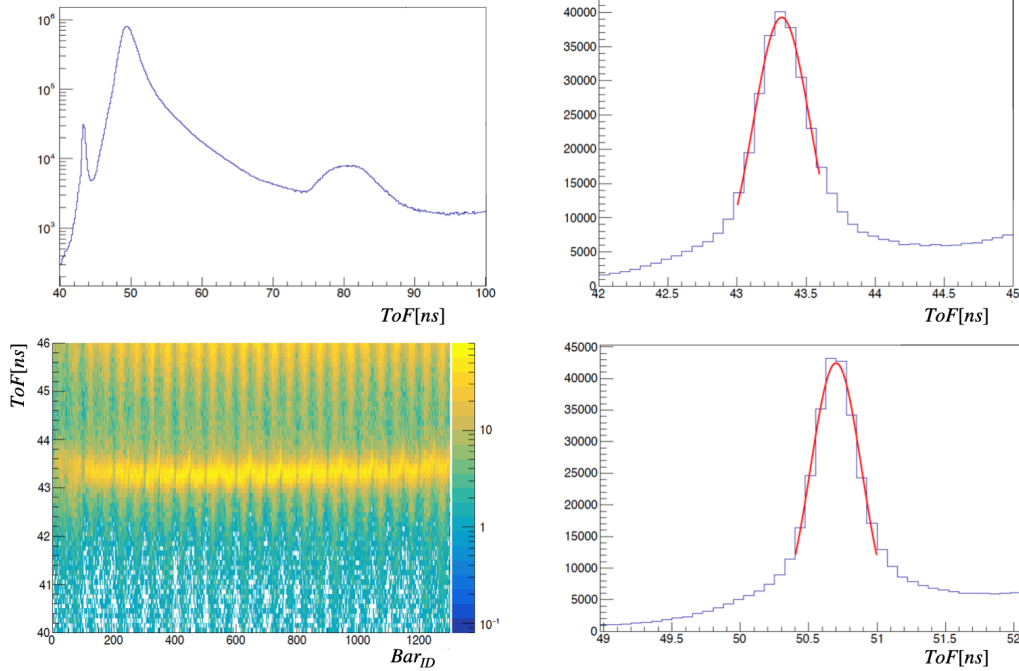


Figure 3.37: Top left: Corrected time of flight spectrum of  $^{16}\text{C}$  beam run. The three peaks are  $\gamma$ , neutron and beam dump (i.e. scattering of neutron at the wall located around 3 meters from the last neutron wall), respectively. Top right: Corrected time of flight spectrum of  $^{16}\text{C}$  run for  $\gamma$ . The timing resolution is 206.8 ps. Bottom left: Corrected time of flight spectrum at  $\gamma$  peak versus bar ID for a  $^{16}\text{C}$  run. Bottom right: Gamma ToF spectrum after fine correction to align the gamma peak in each bar. The timing resolution improved to 187.4 ps.

In addition to aligning the  $\gamma$  peak for all bars, we can further refine the time-of-flight ( $ToF$ ) spectrum by aligning the  $\gamma$  peak in the corrected  $ToF$  spectrum of each bar.

Fig. 3.37 (bottom left) illustrates that the  $\gamma$  peak occurs at slightly different corrected  $ToF$  values for each bar. To determine the peak, a Gaussian fit was performed twice around the local maximum bin in the  $\gamma$  peak region. Subsequently, each bar was adjusted so that the  $\gamma$  peaks aligned across all bars. Fig. 3.37 (Bottom right) demonstrates that the fine correction for the  $\gamma$  peak in each bar reduces the timing resolution from a sigma of 206.8 ps to 187.4 ps.

## RPC calibration

The RPC calibration procedure involves three main steps [105]:

- Time over Threshold calibration.
- Longitudinal strip position calibration.
- Strip time calibration.

Since the RPC detector is a new system used for the first time by the R3B collaboration, I recall that the RPC detector functions on the principles of gas ionization and avalanche multiplication. When a charged particle traverses the RPC, it ionizes the gas, producing electron-ion

pairs as a result of the energy deposited by the particle. An electric field within the gas gap accelerates the free electrons toward the resistive glass plates. The charge collected at the readout plane generates a voltage pulse, which is processed by an external electronics system. The timing and amplitude of this pulse yield information about both the position and energy of the incident particle.

The calibration procedure was performed using off-spill data (Cosmic Rays) from the  $^{16}\text{C}$  run. The main purpose of this calibration is to derive a set of parameters to obtain a precise ToF and position information of the SRC recoil proton to reconstruct its momentum. The results of the calibration procedure for time, ToT, and position are presented in the following.

### ***Time over Threshold calibration***

For each RPC strip,  $i$ , with signals on both sides, the ToT measured on the right and left sides,  $\text{ToT}_{r,i}$  and  $\text{ToT}_{l,i}$  are corrected with a calculated offset associated with each of the FEE and TDC involved,  $\epsilon_{\text{ToT},r,i}$  and  $\epsilon_{\text{ToT},l,i}$ . Computing in this way, the calibrated ToT of each channel is:

$$\begin{aligned}\text{ToT}_{c,r,i} &= \text{ToT}_{r,i} + \epsilon_{\text{ToT},r,i}, \\ \text{ToT}_{c,l,i} &= \text{ToT}_{l,i} + \epsilon_{\text{ToT},l,i}.\end{aligned}\tag{3.33}$$

Furthermore, the strip  $I$ , with maximum  $\text{ToT}_{r,i}$  and  $\text{ToT}_{l,i}$ , will be the assigned strip of the event, and the mean ToT can be calculated from  $\text{ToT}_{r,I}$  and  $\text{ToT}_{l,I}$  as follows.

$$ToT = \frac{\text{ToT}_{c,r,I} + \text{ToT}_{c,l,I}}{2}\tag{3.34}$$

Having assigned a strip to the event, the transversal position (across the strips),  $Y$ , can be computed using the number of the strip  $I$  and the pitch of the strip,  $w$ ,

$$Y = (I - 1) \times w.\tag{3.35}$$

For both the time  $T$  and the longitudinal position (along the strip)  $X$ , the measured times on the right and left sides of the selected strip will be used,  $T_{r,I}$  and  $T_{l,I}$  respectively, being that for each of these variables, an offset must be calculated,  $\epsilon_{T,I}$  and  $\epsilon_{X,I}$ .

To calculate the longitudinal position,  $X$ , equation 3.36 is used, where  $V_{\text{strip}}$  is the propagation velocity of the signals on the strips equal to 165.7 mm/ns.

$$X = \left[ \frac{(T_{r,I} - T_{l,I})}{2} \times V_{\text{strip}} \right] + \epsilon_{X,I}.\tag{3.36}$$

For time  $T$  the equation 3.37 is used.

$$T = \frac{(T_{r,I} + T_{l,I})}{2} + \epsilon_{T,I}.\tag{3.37}$$

The calibration of the Time-over-Threshold ( $ToT$ ) is achieved by determining the  $\epsilon_{\text{ToT},r,i}$  and  $\epsilon_{\text{ToT},l,i}$  parameters, which originate from the different response of each Front-End Electronics (FEE) and Time-to-Digital Converter (TDC) channel. These parameters align the minimum values of  $\text{ToT}_{r,i}$  and  $\text{ToT}_{l,i}$  across all channels. This calibration is essential to accurately determine  $\text{ToT}_{c,r,I}$  and  $\text{ToT}_{c,l,I}$ , subsequently enabling correct calculations of Time ( $T$ ),  $Y$ -coordinate ( $Y$ ), and  $X$ -coordinate ( $X$ ). The point-by-point derivative of the  $ToT$  distribution was used to calculate these parameters. The maximum of this derivative corresponds to the inflexion point of the  $ToT$  distribution. The derivative is computed bin by bin of the  $ToT$  distribution.

The resulting derivative plot is illustrated in Fig. 3.38. With these parameters, all the inflexion points of the  $ToT$  distribution for all channels can be aligned.

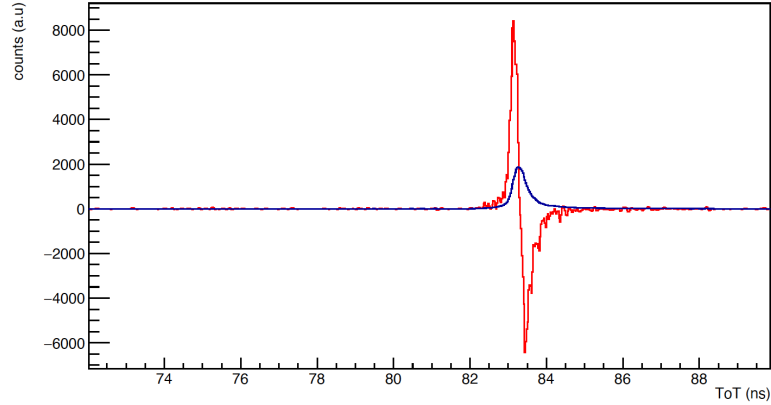


Figure 3.38:  $ToT$  distribution (blue) and the bin by bin derivative (red).

If calibration is not performed accurately,  $ToT_{r,I}$  and  $ToT_{l,I}$  may be assigned to different channels on the left and right sides. In such cases, the event would either be discarded or incorrectly attributed to the wrong strip. This discrepancy is evident in Fig. 3.39 (left), where the uncalibrated  $ToT$  is plotted for each strip. Due to the lack of calibration, approximately 10% of the events will be discarded. However, following a correct calibration, as depicted in Fig. 3.39 (right), the proportion of events with incorrect  $ToT$  values decreases significantly to only 2%.

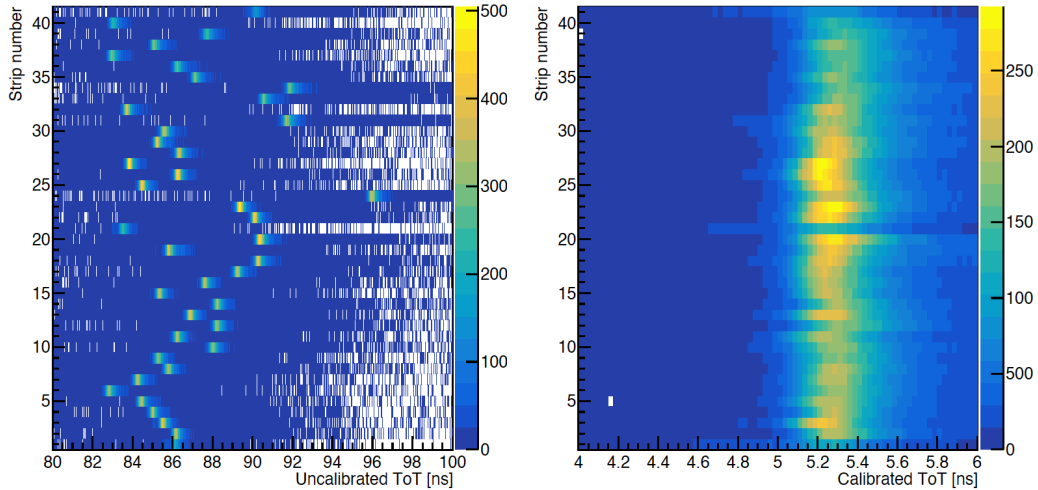


Figure 3.39:  $ToT$  calculation per strip without applying the  $\epsilon_{ToT,l,i}$  parameters (Left) and when applying (right).

### *Longitudinal strip position calibration*

Following the correct calibration of the Time-over-Threshold ( $ToT$ ), the transverse ( $Y$ ) and longitudinal ( $X$ ) positions are computed. To determine the  $X$ -positions, it is essential to ascertain the parameters  $\epsilon_{X,I}$ , which originate from the distinct time offsets associated with the Front-End Electronics (FEE) and Time-to-Digital Converter (TDC) channels of each strip.

The effect of this time offset parameter is illustrated in Fig. 3.40 (top left), which displays a

two-dimensional histogram of  $(X,Y)$  without the calibration parameters. In contrast, Fig. 3.40 (top right) exhibits the same histogram with the calculated calibration parameters, clearly depicting the central spot corresponding to forward-emitted particles (protons) and the geometric acceptance defined by the GLAD magnet (halo at the periphery of the plot).

To determine the calibration parameters  $\epsilon_{X,I}$ , an algorithm was developed to compute the cumulative histograms of hits for all channels  $I$ . Subsequently, these histograms are normalized to their integral, with the parameter defined as the first channel above a predetermined threshold. An example of one of these histograms is shown in Fig. 3.40 (bottom panel).

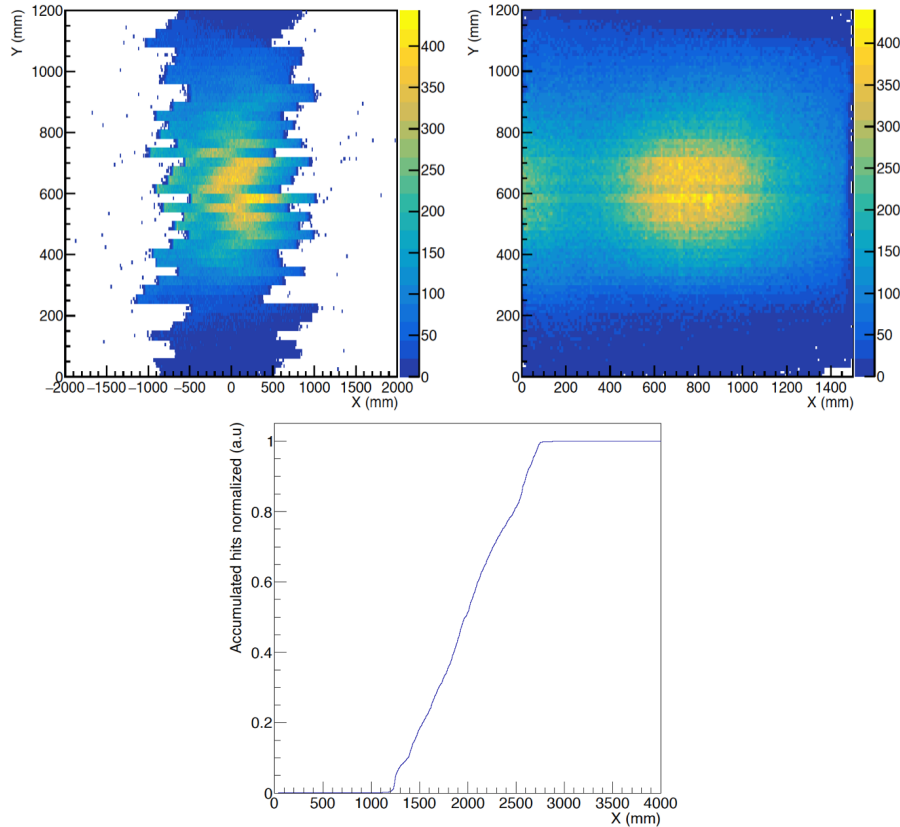


Figure 3.40: Top:  $X, Y$  map before (Left) and after (right) applying calibration parameter  $\epsilon_{X,I}$ . The central spot corresponding to the forward emitted particles (protons) and the geometrical acceptance defined by the GLAD magnet (halo at the periphery of the plot) are clearly visible in the right plot. Bottom: Normalized accumulated histogram of hits in strip 21 of the RPC.

### *Strip time calibration*

To complete the calibration process, the time  $T$  must be determined, which requires the calculation of the parameters  $\epsilon_{T,I}$ . These parameters stem from the distinct time offsets associated with the Front-End Electronics (FEE) and Time-to-Digital Converter (TDC) channels of each strip. Vertical scintillators are utilized to derive these parameters.

For each strip, the differences between the scintillator time and the RPC time,  $T_{sc1} - T$  (in the case of scintillator  $V_{sc1}$ ), are computed. Assuming perfect parallelism between the scintillators and the RPC surface, the time of flight of particles between the two detectors should, on average, remain consistent, regardless of the RPC strip generating the signal. Consequently, the parameters  $\epsilon_{T,I}$  are determined to ensure that the average of  $T_{sc1} - T$  remains constant.

The outcome is depicted in Fig. 3.41, where  $T_{sc1} - T$  is plotted for each strip before (left) and after (right) applying the calculated calibration parameters. This calibration procedure guarantees consistent timing from the RPC surface, irrespective of the strip producing the signal.

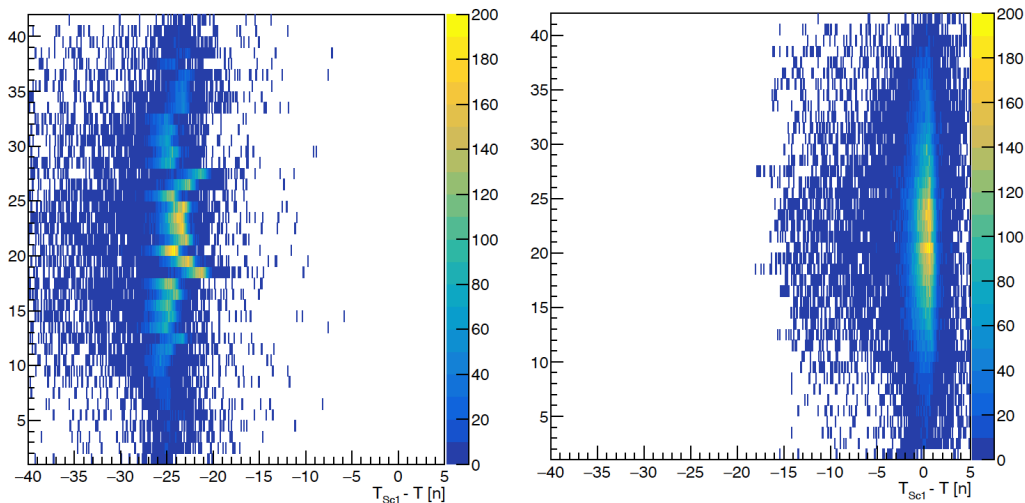


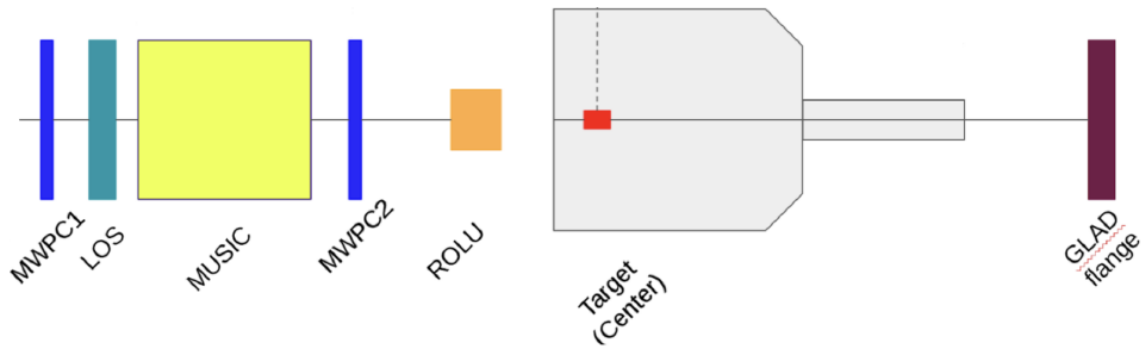
Figure 3.41: Left,  $T_{sc1} - T$  difference per strip, without calculation of  $\epsilon_{T,I}$  parameters and with calculated ones in bottom.

### 3.3 Detectors Alignment

In August 2022, 3D Sigma [122], a private company, conducted a comprehensive laser scan of the upstream detectors (LOS, MWPC, ROLU, MUSIC) and the target tracking system (CALIFA+FOOT), as shown in Fig. 3.43. Leveraging this laser data along with CAD models provided by D. Koerper, we aligned the detectors and obtained crucial position measurements. The alignment process involved adjusting the CAD models (e.g., FOOT detectors) to match the laser scan using AutoDesk software.

Following this alignment, we determined the central geometric position of all FOOT detectors, which was used to calculate the "Hit" level positions. Since the MWPC lacked a CAD model, laser images were directly employed for measurements.

Fig. 3.42 shows the positions derived after the alignment procedure for various detectors. Subsequently, a relative alignment of MWPC and In-Beam FOOT was performed using experimental data. For this purpose, we considered the positions of all FOOT detectors as fixed parameters based on laser measurements and aligned the MWPC positions relative to this reference system. Specifically, we derived  $^{12}\text{C}$  tracks of in-beam FOOT in the  $(X, Z)$  and  $(Y, Z)$  planes, deriving slope parameters  $(a_x, a_y)$  and offset parameters  $(b_x, b_y)$  for the lines  $x = a_x \cdot z + b_x$  and  $y = a_y \cdot z + b_y$ . These tracks were then projected onto the  $z$  positions of MWPC0 and MWPC1. The projected positions found were  $x_{mwpc0}$ ,  $x_{mwpc1}$ ,  $y_{mwpc0}$ , and  $y_{mwpc1}$ . The differences between these values and the  $x_{mwpc}$  and  $y_{mwpc}$   $^{12}\text{C}$  hit positions from the MWPC "Hit" level were computed as  $(x_{mwpc0} - x_0)$ ,  $(x_{mwpc1} - x_1)$ ,  $(y_{mwpc0} - y_0)$ , and  $(y_{mwpc1} - y_1)$ , where  $x_0$ ,  $x_1$ ,  $y_0$ ,  $y_1$  are the MWPC  $^{12}\text{C}$  "Hit" positions. Gaussian fit of these plots enabled us to determine the centroid value of the position differences, serving as the offset applied to the  $(x_0, y_0, x_1, y_1)$  positions of the MWPCs.



taken from the front	MWPC1	LOS	MUSLI	MWPC0
z	-2238.584	-2137.5	-1484.467	-1047.107

Center Position for all foots in mm!

Inbeam	x	y	z
Foot 2	0.484	2.262	642.052
Foot 1	1.034	2.564	658.256

Outside	x	y	z
Foot 16	-5.847	-5.796	1156.636
Foot 15	-5.637	-5.72	1191.645

Arm MS	x	y	z
Foot 7	39.354	1.782	490.413
Foot 12	45.533	0.934	499.755
Foot 9	58.46	1.661	517.386
Foot 10	63.935	1.993	527.136

Arm WX	x	y	z
Foot 13	-38.323	1.332	490.752
Foot 4	-45.007	1.247	499.979
Foot 11	-57.956	2.258	518.193
Foot 6	-63.395	2.105	527.848

Figure 3.42:  $z$  position of the in-beam tracking detectors and central positions for all the FOOT detectors derived from the laser scan.

Tab. 3.2 presents the offsets obtained using the previously mentioned method.

Detector	X offset [cm]	Y offset [cm]
MWPC0	0.0946	0.5337
MWPC1	-0.6996	2.6318

Table 3.2: MWPCs position offsets derived with a relative alignment procedure using fixed positions for the FOOT detectors.

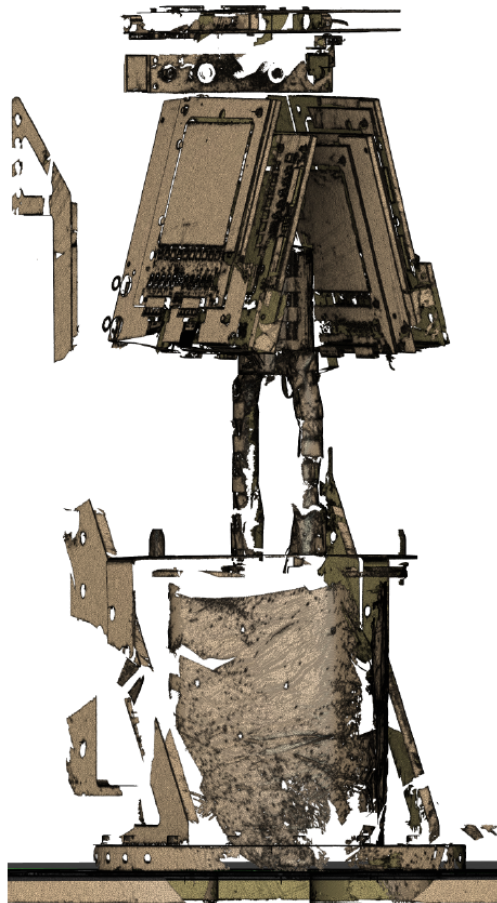


Figure 3.43: Laser scan of the FOOT detectors and the  $\text{LH}_2$  target conducted by the 3D Sigma company [122].



# Chapter 4

## Data analysis

### Contents

---

<b>4.1</b>	<b>Simulations</b>	<b>124</b>
4.1.1	INCL Event Generator	124
4.1.2	The QFS Event Generator	126
4.1.3	Generalised Contact Formalism Event Generator	127
<b>4.2</b>	<b>Particles identification and tracking</b>	<b>128</b>
4.2.1	Beam particles identification	129
4.2.2	Fragments tracking	133
4.2.3	Proton tracking	139
4.2.4	Neutrons tracking	140
<b>4.3</b>	<b><math>(p,2p)</math> reaction investigation</b>	<b>145</b>
4.3.1	Protons identification via QPID	146
4.3.2	Punch-trough protons energy reconstruction	147
4.3.3	Protons momentum and angular distribution	153
4.3.4	$^{12/16}\text{C}(p,2p)\text{A-1}$ QFS selection	158
<b>4.4</b>	<b>SRC physics investigation</b>	<b>167</b>
4.4.1	$^{12/16}\text{C}(p,2p)\text{A-2}$ semi-exclusive investigation	169

---

In this chapter, we outline the analysis method used to identify SRC physics and distinguish SRC pairs from competing reaction channels. By utilizing simulations and applying appropriate kinematic conditions, we aim to pinpoint a specific kinematic region where SRC physics is separated from other processes, such as FSI and mean field channels, which can produce similar signals of SRC pair breakup, leading to incorrect interpretations of the data.

In the analysis of short-range correlations (SRCs), it is crucial to reject final state interaction (FSI) and inelastic events (IE) and to separate secondary processes from SRC events. These reactions can significantly affect the observed properties of the particles involved, creating a background that complicates the investigation of SRCs. In SRC studies using high-energy scattering experiments, we aim to probe the short-distance, high-momentum components of nuclear wavefunctions. However, FSIs and IE processes can distort the signals from these interactions.

Going more into detail, for SRC studies the reaction channel we are interested in is represented in Fig.4.1. We aim to look at the process in which we remove from the nucleus of

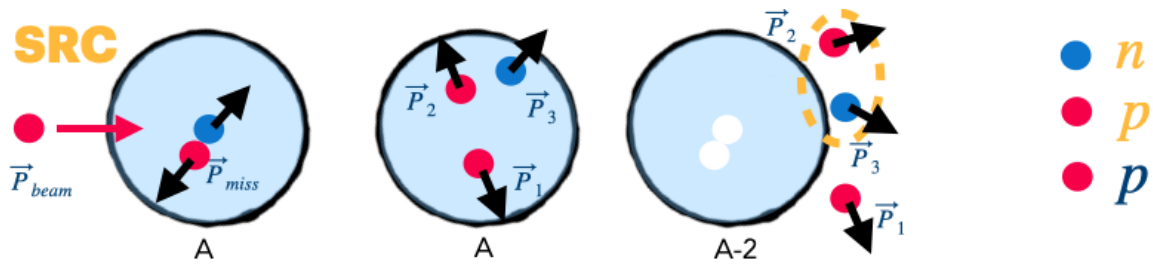


Figure 4.1: Scheme of a process of SRC investigation. With the proton probe we aim to separate the components of the SRC pair and to detect them in the final state. After the  $np$  SRC breakup we expect to detect at the final state one neutron, two protons and the related  $A-2$  fragment.

interest ( $^{12/16}\text{C}$ ) a proton involved in an SRC pair. Due to the high relative momentum of the pair, the SRC partner nucleus will be emitted as well. In the case of a  $np$  pair, we expect to have 2 protons, a neutron and the  $A-2$  fragment in the final state. As already mentioned, there are competing reaction channels that can mimic the same final state of an SRC breakup, but in this case, the reaction process is not related at all to SRC probing. The reaction processes that hide the SRC signals and that need to be identified and separated in the current experiment are classified as **IE** processes and **FSI**. In this thesis, to better understand the steps we carried on to select SRC events, I will maintain this distinction between IE reactions and FSI. Still, we should keep in mind that there are several overlaps in the definition and categorization of IE processes and FSI that will not be treated in this thesis. In the current work, I present and categorize IE processes and FSI as:

**Final-state interactions (FSI)** occur after the probe interacts with a nucleon inside the nucleus. In this case, after the initial scattering event (e.g., a nucleon is ejected by a proton probe), the struck nucleon or its partners may undergo further interactions with the residual nuclear system on their way out of the nucleus. This can alter the detected final-state properties, such as energy and momentum, in ways that can mimic SRC signatures.

- **Rescattering:** After the initial interaction, the struck nucleon may rescatter off other nucleons in the nucleus, leading to a redistribution of momentum and energy with a modification of the nucleon trajectory (emission angle modification) or energy loss during the secondary interactions. This can create a signal that resembles that of nucleon pairs with large relative momentum, a signature of SRC events. Fig.?? presents a scheme of a rescattering of a proton within a neutron in the medium. This process produces the same final state as an SRC breakup event.
- **Single Charge Exchange (SCX):** During final-state interactions, a nucleon may undergo a process called *single charge exchange*, in which a proton is converted into a neutron, or vice versa, as a result of an interaction with other nucleons or mesons in the nuclear medium. This occurs because of the strong nuclear force, which allows for the exchange of charged mesons (like pions) between nucleons. For example, a proton can exchange a positively charged pion ( $\pi^+$ ) with a neutron, turning the proton into a neutron. The SCX process does not significantly affect the nucleon's momentum, but it alters the nucleon's charge. As a result, a particle that was originally detected as a proton might exit the nucleus as a neutron, or vice versa. This charge exchange can complicate the interpretation of experimental results because the final-state particle no longer matches the charge of the nucleon that initially interacted with the probe.

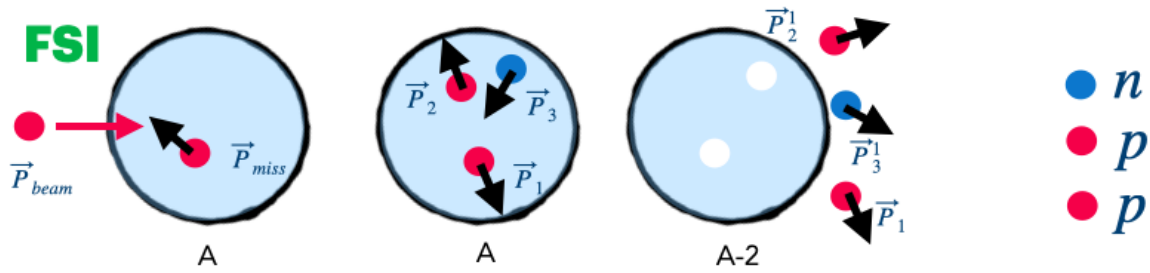


Figure 4.2: Scheme of a FSI process. The proton probe interact with a proton inside the nucleus. The proton probed, while going out from the nucleus, can rescattered with a neutron of the medium causing its emission. This process will give in the final state one neutron, two protons and the A-2 fragment as in the case of SRC breakup.

This mismatch can mimic SRC signatures, particularly when trying to identify correlated nucleon pairs or reconstruct the initial interaction dynamics.

**Inelastic processes**, where energy is absorbed by nucleons or the nucleus, can produce signals similar to Short-Range Correlations (SRCs), making it hard to differentiate between them. Inelastic scattering transfers energy to nucleons, sometimes knocking them out with high momentum—much like what happens in SRC events. This energy absorption can excite the nucleons or the entire nucleus, leading to the release of high-energy particles similar to those from SRC nucleon ejections.

- **Excited Nuclear States:** When nucleons absorb energy, they can enter excited states and be released with high momentum, resembling SRC nucleons. Sometimes, nucleons are excited to higher-energy states, like the  $\Delta$  resonance, which decays and emits high-energy nucleons, further mimicking SRC behavior.
- **Multi-Particle emission and nuclear fragmentation:** Inelastic processes can also cause the emission of multiple nucleons or even the breakup of the nucleus (nuclear fragmentation). This results in several high-momentum nucleons, making it difficult to distinguish these events from SRC ejections of tightly correlated nucleon pairs.

The first steps of the analysis will be focused on distinguish and select the **Quasi-Elastic (QE)** part of the reaction, where we expect to find clear SRC events. QE refers to interactions where a nucleon is ejected from the nucleus with minimal interaction with the remaining nucleons, approximating free nucleon-nucleon scattering. A QE event occurs when a proton is knocked out with minimal interaction with the residual nucleus, allowing the study of the momentum distribution of nucleons inside the nucleus. By effectively rejecting FSI and IE events, we ensure that the observed particle momenta and energies reflect the primary reaction, providing a clearer picture of the SRC. To mitigate the impact of FSI/IE backgrounds, a combination of simulation and experimental techniques is employed. Simulations and data analysis techniques are used to disentangle the effects of IE/FSI processes from the true SRC signals, allowing for a clearer understanding of the underlying nuclear dynamics.

## 4.1 Simulations

As mentioned previously, suppression of FSI and identification of QE and high-momentum transfer processes are essential for investigating SRC physics. Simulations play a crucial role in helping us understand the conditions and methods to apply in our steps to better separate and identify SRC pairs. In our analysis, several event generators were used to study several aspects of SRC physics. A general description and overview of these event generators are presented.

### 4.1.1 INCL Event Generator

The INCL (Isospin-dependent Intranuclear Cascade with Liège) generator [123] is a sophisticated model used to describe the interactions of high-energy particles with atomic nuclei. Introduced by the Liège Intranuclear Cascade group and now developed by CEA-Saclay, the INCL model is particularly effective for simulating intermediate-energy nuclear reactions, typically in the range of a few tens of MeV to several GeV. The INCL generator is useful to simulate the kinematical properties of rescattering, evaporation, and fragmentation events that represent our FSI background source. Here I present the key features of the INCL event Generator:

1. **Intranuclear Cascade Model:** The INCL simulation's core is the intranuclear cascade model, which describes the sequence of binary collisions between the incident particle and nucleons within the target nucleus. The model tracks the trajectories and interactions of all involved particles, including protons, neutrons, pions, and other resonances.
2. **Isospin Dependence:** INCL incorporates isospin-dependent interactions, allowing it to accurately simulate reactions involving different isotopes and account for the effects of neutron-proton asymmetry in the target nucleus. This is crucial for understanding reactions in both stable and exotic nuclei.
3. **Detailed Interaction Dynamics:** The model includes detailed descriptions of various interaction processes, such as elastic and inelastic scattering, charge exchange, and pion production. The interactions are governed by cross-sections derived from experimental data and theoretical calculations.
4. **Nuclear Medium Effects:** INCL takes into account the influence of the nuclear medium on particle interactions. This includes the Pauli exclusion principle, which prevents nucleons from occupying the same quantum state, and the nuclear potential, which affects the propagation of particles within the nucleus.
5. **Fragmentation and Evaporation:** After the intranuclear cascade phase, the excited residual nucleus can undergo fragmentation and evaporation processes. INCL is often coupled with statistical models like ABLA (Advanced Breakup of Light A) to describe these de-excitation mechanisms, leading to the emission of light particles and fragments.
6. **Short-Range Correlations:** A modified version was developed to simulate short-range correlations [124], which are high-momentum interactions between pairs of nucleons within the nucleus. These correlations are essential for understanding the high-momentum tail of the nucleon momentum distribution and play a crucial role in various nuclear reactions. Since the INCL version with SRC implementation can only simulate  $np$  pairs, we will not consider this for our analysis of SRC.

The workflow of INCL is the following:

1. **Initialization:** The simulation starts by initializing the properties of the incident particle and the target nucleus, including their momenta, positions, and internal configurations.
2. **Cascade Phase:** The intranuclear cascade phase begins with the incident particle entering the nucleus. This phase involves multiple binary collisions between the incident particle and the nucleons, as well as among the nucleons themselves. Each interaction is governed by the respective cross-sections and takes into account isospin-dependent effects. The total cross section  $\sigma_{\text{tot}}$  for a given interaction can be expressed as:

$$\sigma_{\text{tot}} = \sigma_{\text{elastic}} + \sigma_{\text{inelastic}} + \sigma_{\text{charge exchange}} + \sigma_{\text{pion production}}. \quad (4.1)$$

3. **Propagation and Interaction:** During the cascade, the particles propagate through the nuclear medium, with their trajectories influenced by the nuclear mean field. The Pauli exclusion principle is applied to ensure that no two nucleons occupy the same quantum state. The nuclear mean field can be approximated by a potential  $U(r)$ , which affects the particle's motion via the equation of motion:

$$\frac{d\vec{p}}{dt} = -\nabla U(r). \quad (4.2)$$

4. **Simulation of Short-Range Correlations:** To simulate SRCs, INCL identifies when nucleons are very close to each other in space, indicating a high probability of short-range interactions. When such conditions are met, the model boosts the momentum of these nucleon pairs to simulate the high-momentum tail characteristic of SRCs. The momentum distribution of nucleons is modified to include a high-momentum tail, described by:

$$n(k) \propto \frac{1}{k^4} \quad \text{for } k > k_F; \quad (4.3)$$

where  $k$  is the nucleon momentum and  $k_F$  is the Fermi momentum.

5. **Cascade Termination:** The cascade phase ends when the energies of the interacting particles drop below a certain threshold or when they escape the nucleus.
6. **De-excitation:** The excited residual nucleus then undergoes de-excitation through fragmentation and evaporation processes leading to the emission of light particles and fragments.

The evaporation process can be described by the Weisskopf-Ewing model, where the emission probability of a particle with energy  $E$  is given by:

$$P(E) \propto \rho(E)E \exp(-E/T). \quad (4.4)$$

Here,  $\rho(E)$  is the level density of the residual nucleus, and  $T$  is the nuclear temperature.

7. **Final State Output:** The simulation outputs the final state of all particles involved, including their momenta, energies, and types. This information can be used to analyze the reaction dynamics and compare it with experimental data.

### 4.1.2 The QFS Event Generator

The present simulation is based on the FairRoot simulation and analysis platform [115]. The kinematical code for QFS reactions was developed by Leonid Chulkov and Valerii Panin at GSI [72]. This code utilizes the Feynman diagram representation to describe the QFS reaction. Consider a projectile-like nucleus with four-momentum  $P = (\vec{P}, E_P)$  and a target proton with four-momentum  $p_0 = (\vec{p}_0, E_0)$ . In the final state, the four-momenta of the particles are:

- Residual nucleus:  $Q = (\vec{Q}, E_Q)$ .
- Scattered proton:  $q_0 = (\vec{q}_0, E'_0)$ .
- Knocked-out nucleon:  $q_1 = (\vec{q}_1, E_1)$ .

The reaction is governed by the conservation of four-momentum:

$$P + p_0 = Q + q_0 + q_1. \quad (4.5)$$

To determine the internal momentum  $\vec{p}_e$  of the knocked-out particle, the Goldhaber model can be employed [125]. According to this model, the internal momentum width  $\sigma_g$  is calculated as follows:

$$\sigma_g^2 = \sigma_0^2 \frac{A_f A_r}{A}; \quad (4.6)$$

where  $A_f$  and  $A_r$  are the masses of the fragment and the residual nucleus, respectively, and  $A$  is the mass of the initial system (e.g.,  $^{12}\text{C}$ ). The quantity  $\sigma_0$  is related to the reaction Q-value  $Q_f = (A_f + A_r - A)$  and to the  $pN$  scattering cross section  $\frac{d\sigma}{dt}$ . The scattering process is chosen to be non-isotropic ( $E_{lab} > 500$  MeV). In this case, a parameterization of  $pN$  scattering cross-section from experimental data is performed.

The  $\sigma_{pN}$  cross-section parametrization implemented was done in function of  $(s, t)$  and  $(s, u)$  Mandelstam variable for  $s > 3 \text{ GeV}^2$ :

- For the  $(s, t)$  Mandelstam variables, the parameterizations are:

$$\begin{aligned} A &= 553.776 \cdot \exp(-1.3121 \cdot s), \\ B &= 234325 \cdot \exp(-2.0952 \cdot s), \\ C &= 0.5 \cdot s - 0.880354, \\ \sigma_{pN} &= A + B \cdot (t + C)^4. \end{aligned} \quad (4.7)$$

- For the  $(s, u)$  Mandelstam variables, the parameterizations are:

$$\begin{aligned} A &= 1779.65 \cdot \exp(-1.61925 \cdot s), \\ B &= 234324 \cdot \exp(-2.0952 \cdot s), \\ C &= 0.5 \cdot s - 0.880354, \\ \sigma_{pN} &= A + B \cdot (u + C)^4. \end{aligned} \quad (4.8)$$

Hence, using the experimental beam energy and the intrinsic momentum of the removed nucleon in the projectile, the proton-nucleon scattering kinematics in the laboratory system is calculated.

The Mean-field Event Generator allows us to study relevant quantities of  $(p, 2p)$  reactions, such as the missing momentum, energy, and mass in the case of a QFS reaction. By looking at these quantities, we can deduce the kinematical region where we expect to have QFS events,

and we can also look at these kinematical regions in the experimental data. In our simulation, we utilize well-established  $pN$  cross-sections extracted from past data to simulate the  $(p,2p)$  reaction using a  $^{12}\text{C}$  beam and a bound  $A - 1$  system. This simulation assists in establishing a good kinematic region with minimal distortion from mis-reconstruction and helps in identifying good quasi-elastic mean-field events.

### 4.1.3 Generalised Contact Formalism Event Generator

As presented in Chapt. 1, the GCF is a theoretical framework that extends the concept of nuclear contacts to include nucleon-nucleon pairs with significant relative momentum but low center-of-mass momentum. This formalism allows for the characterization and prediction of SRC pair properties in various nuclear reactions. We saw that for processes like  $A(p, p'pN)$  reactions, the cross-section can be expressed as:

$$\frac{d^8\sigma}{d\Omega_{p'}d^3p_{\text{CM}}dk_{\text{rel}}d\Omega_{\text{rel}}} = \frac{\sigma_{pp}}{32\pi^4} \frac{k_{\text{rel}}^2}{\left|1 - \frac{\vec{k}'_i \cdot \vec{p}}{E'_i E'_p}\right|} \sum_{\alpha} C_{NN}^{\alpha} |\tilde{\phi}_{NN}^{\alpha}(\vec{k}_{\text{rel}})|^2 n_{NN}^{\alpha}(\vec{k}_{\text{CM}}). \quad (4.9)$$

The cross-section requires several input parameters. Their values have been determined by previous SRC electron scattering experiments. To compare with experimental data, the cross-section expression of the Eq. 4.9 is used to produce a weighted Monte Carlo event generator. Going more in detail, the GCF relies on a few key parameters and concepts:

- **Nuclear Contacts:** These parameters quantify the likelihood of finding a nucleon-nucleon pair at short distances.
- **Relative and Center-of-Mass Momentum:** The relative momentum  $\vec{k}_{\text{rel}}$  and center-of-mass momentum  $\vec{k}_{\text{c.m.}}$  are crucial for identifying SRC pairs.
- **Parametrization of the  $\sigma_{pN}$  cross-section:** The  $\sigma_{pp}$  cross-section parametrization implementation was done in function of  $(s,t)$  and  $(s,u)$  Mandelstam variable for  $s > 3 \text{ GeV}^2$  and the parameters are the same as previously mentioned for the QFS event generator. The parametrization of the cross-section was implemented as weight factors. A suppression of the unphysically high weight given to very off-shell events was performed.

The setup of the GCF simulation follows several steps.

The input parameters for the GCF generator include:

- **Nucleus:** The type of nucleus (e.g.,  $^{12}\text{C}$ ,  $^{16}\text{C}$ ).
- **Beam Energy and Kinematics:** Details of the proton beam energy and scattering angles.
- **Nuclear Contacts:** Pre-determined contact values specific to the nucleus under study.

The GCF generator produces events based on the input parameters. Each event includes:

- **Initial Nucleon Pair:** Selection of a nucleon pair with high relative momentum and low center-of-mass momentum.
- **Scattering Process:** Simulation of the proton-nucleon scattering process using the GCF framework. For each event, a weight value that contains cross-section information is produced.

- **Final State:** Calculation of the final state momenta and energies of the ejected nucleons.

The generated events are processed analogously to the experimental data and compared with our SRC final results.

## 4.2 Particles identification and tracking

In this section, our focus is directed towards the precise identification and tracking of particles crucial for the investigation of Quasi-Free Scattering reactions and Short-Range Correlation physics. This comprehensive procedure is designed to provide a thorough understanding of the particle characteristics, including charge and momentum, which is essential to study various reactions of interest.

Specifically, our efforts are directed towards accurately tracking the following particles:

1. **Beam Tracking:** Utilizing Multi-Wire Proportional Chambers (MWPC) and Multi-Sampling detector for Light Ions (MusLi), we aim to track the trajectory and properties of the incident beam as it interacts with the target. The incoming beam angles are derived using MWPC detectors and the beam momentum of  $^{12}\text{C}$  is determined using the nominal energy value from UNILAC. While for  $^{16}\text{C}$ , the FRS information is used to derive its energy.
2. **Fragment Identification:** The properties of fragments resulting from QFS reactions are essential for understanding the dynamics of the process. Time-of-Flight Detectors (TOFD) and the fiber detectors play a crucial role in accurately identifying and characterizing these fragments.
3. **Neutron and Proton Detection:** The identification of clear and clean  $(p,2p)$  events in CALIFA is the starting point for studying SRC physics. To investigate more in detail SRC physics, precise identification of the recoil neutrons and protons of the pairs is essential. Neutron detectors NeuLAND and proton detector RPC are employed for this purpose.

In summary, these are the quantities of interest we want to derive from the beam identification and tracking procedure in order to separate and identify QE reactions and SRC events:

- **Beam momentum and angles:** The incoming angles allow us to rotate and project the momentum of the fragments, neutrons, and protons along the incoming beam vectors defined by the beam angles. The energy losses through the different setup materials were also considered. The beam momentum is used to boost the particles' momentum in the beam center-of-mass reference system.
- **$(p,2p)$  Reaction identification:** After reconstructing the protons' energy and angles, we can compute their momentum and access important quantities that will help us select SRC physics and suppress FSI. Quantities such as the reaction's missing momentum, missing mass, and missing energy will be crucial in studying the QE part of the reaction and investigating SRC. A detailed description is presented in the dedicated section.
- **Fragment momentum:** The fragment momentum is derived using the Multidimensional Fit tracking method. This procedure provides important quantities such as fragment momentum, charge, mass, and  $A/Z$  ratio. With these quantities, we can select the fragment of interest, clean background contaminations, and identify other reaction channels that might mimic an SRC signal. The detailed procedure for deriving these quantities is presented later.

- **Neutron and Proton momentum:** The momentum of neutrons and protons, derived with NeuLAND and RPC, respectively, are crucially important for a fully exclusive study of SRC. To perform a fully kinematical study of an SRC breakup, we need to detect all reaction products. By detecting the neutron in NeuLAND, an  $A - 2$  fragment ( $^{10/14}\text{Be}$  for  $^{12/16}\text{C}$  incoming beam) in ToFD, and a  $(p,2p)$  reaction in CALIFA, we can reconstruct the properties and kinematics of  $np$  pairs in a fully exclusive way. Alternatively, if we detect a proton in RPC instead of a neutron in NeuLAND and the related  $A - 2$  fragment in TOFD ( $^{10/14}\text{Be}$  for  $^{12/16}\text{C}$ ), we can reconstruct the properties and kinematics of  $pp$  pairs. This procedure is detailed in the dedicated section of the analysis.

For all the particles, we also consider the energy loss through several detectors and beamline components using the classical Bethe-Bloch formula which describes the energy loss per unit path length ( $-\frac{dE}{dx}$ ) of a charged particle travelling through a medium. It is given by:

$$-\frac{dE}{dx} = K z^2 \frac{Z}{A} \frac{1}{\beta^2} \left[ \frac{1}{2} \ln \frac{2m_e c^2 \beta^2 \gamma^2 T_{\max}}{I^2} - \beta^2 - \frac{\delta(\beta\gamma)}{2} \right]; \quad (4.10)$$

where:

- $K$  is a constant ( $K = \frac{4\pi e^4}{m_e c^2} \approx 0.307 \text{ MeV cm}^2 \text{ mol}^{-1}$ ),
- $z$  is the charge of the incident particle (in units of elementary charge  $e$ ),
- $Z$  is the atomic number of the medium,
- $A$  is the atomic mass of the medium (in g/mol),
- $\beta$  is the velocity of the particle relative to the speed of light  $c$ ,
- $\gamma$  is the Lorentz factor ( $\gamma = \frac{1}{\sqrt{1-\beta^2}}$ ),
- $m_e$  is the electron rest mass,
- $c$  is the speed of light in vacuum,
- $T_{\max}$  is the maximum kinetic energy that can be transferred to a single electron in a single collision (in electron volts),
- $I$  is the mean excitation potential of the medium (in eV), and
- $\delta(\beta\gamma)$  is the density correction term.

In the subsequent sections, we provide a detailed overview of the identification and tracking methodologies employed for each of these particles.

### 4.2.1 Beam particles identification

As discussed in the previous chapter, it is crucial to identify and characterize the incoming nuclei event by event. This involves deriving the velocity of the beam  $\beta_b$ , its charge number  $Z_b$ , and its trajectory for each event. To identify incoming ions, the mass-to-charge ratio  $A_b/Z_b$  and the charge number  $Z_b$  need to be known. We can derive these quantities as:

$$\frac{A_b}{Z_b} = \frac{B\rho}{c} \frac{1}{\beta_b \gamma_b}. \quad (4.11)$$

Hence,  $\beta_b$  and  $B\rho$  are required. Considering that  $^{12}\text{C}$  was a primary beam directly going from the UNILAC accelerator to Cave C, the  $\beta_b$  and  $B\rho$  cannot be derived. As a consequence, beam and charge identification is possible only by looking at the charge value in LOS and MUSLi detectors. The charge detected in LOS for  $^{12/16}\text{C}$  beam is shown in Fig. 4.3. A good incoming carbon fragment is selected as an event that reads between LOS charge 5.5 to 7.2 for  $^{12}\text{C}$  and between 5.3 and 6.8 for  $^{16}\text{C}$ . In summary, to select a good incoming  $^{12}\text{C}$ , we require to have multiplicity one in LOS and MWPC, and we make a selection in LOS charge.

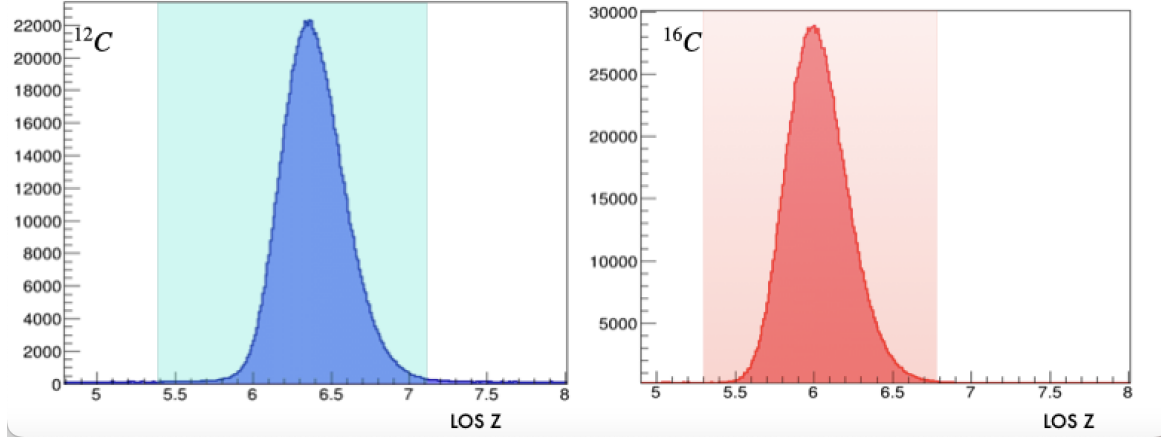


Figure 4.3: Left: LOS charge  $Z$  for  $^{12}\text{C}$  with a green area showing the region selected for a good charge in LOS (between 5.3 and 7.2 charge units). Right: LOS  $Z$  for  $^{16}\text{C}$  with the red area showing the selection on the charge of LOS (between 5.3 and 6.8 charge units).

In the case of  $^{16}\text{C}$  beam, the value of  $B\rho$  is known from the FRS setting. As a consequence, to identify the beam and derive its energy, we only need to determine the velocity of the incoming ion  $\beta_b$ . This is achieved using a time-of-flight (*ToF*) method with two detectors (start and stop) to measure the time needed for a particle to travel a certain distance. In our setup, we use a plastic scintillator paddle at S2 as the start detector, read out with two photo-multiplier tubes (PMTs). LOS detector at the entrance of Cave C serves as a stop detector. These two detectors allow us to measure the times  $t_{\text{start}}$  and  $t_{\text{stop}}$ , from which we can deduce the velocity of the incoming ion  $\beta_b$  using the *ToF* method:

$$\beta_b = \frac{d}{(t_{\text{stop}} - t_{\text{start}})c}; \quad (4.12)$$

where  $c$  is the speed of light, and  $d$  is the distance between the detectors, about 55 m, resulting in very good velocity resolution. To complete the identification of the incoming ion, we need access to its charge number  $Z_b$ . An ion passing through matter loses energy following the Bethe-Block formula:

$$E \propto \frac{Z_b^2}{\beta_b^2}. \quad (4.13)$$

Rearranging this formula:

$$Z_b \propto \beta_b \sqrt{E}. \quad (4.14)$$

The charge number  $Z_b$  can thus be derived from the energy  $E$  measurement using MUSLi detector. With access to  $Z_b$  and  $A_b/Z_b$ , we can select the ions of interest using two-dimensional cuts, as shown in Fig.4.4.

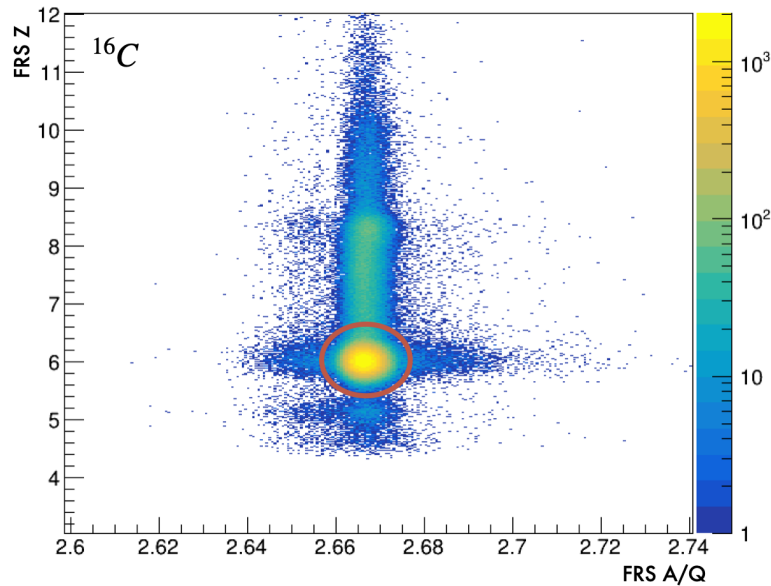


Figure 4.4: Correlation between the  $A/Q$  and  $Z$  derived from MUSLi using S2 and  $ToF$  and charge information from LOS detector. In red is shown the selection applied to identify  $^{16}\text{C}$ .

The identification of the incoming ions is now completed, but we still need information on their trajectories. This information can be obtained using two MWPCs.

We can obtain precise information on the incoming beam profile. It is important to note that due to the multi-hit issues in Arm FOOT detectors, we could not reconstruct the precise vertex of interaction from the scattered  $(p,2p)$  protons. Hence, we used the MWPC beam trajectory projected onto the center of the target position as the interaction vertex. The coordinate system used here labels the  $z$ -axis as pointing in the beam direction, the  $x$ -axis pointing to the left looking from the beam, and the  $y$ -axis pointing upward. Each in-beam MWPC provides measurements in the  $x$ - and  $y$ -directions. With these positions and the distance between the two MWPCs, we can deduce the trajectories of the incoming ions and extrapolate the position of the interaction between the ion and the reaction target (see Fig. 4.5). The figure shows the  $X - Y$  position correlation at the center of the target for  $^{12}\text{C}$  and  $^{16}\text{C}$ . To remind the reader, the target active area in the  $X - Y$  plane is a circumference centred at  $(x = 0, y = 0)$  with a radius of 2 cm. Looking at  $^{12}\text{C}$  vertex (Left plot), we can observe that the beam footprint in the target is well inside the active area of the target. However, for  $^{16}\text{C}$ , the  $X$  component of the vertex is shifted to the right, which means that the beam is very close and, in part, hits the ring around the active area of the target. We expect these events, corresponding to hits in the target ring, to represent a background source that needs to be removed from our analysis and they can be removed event by event as we determine their trajectories.

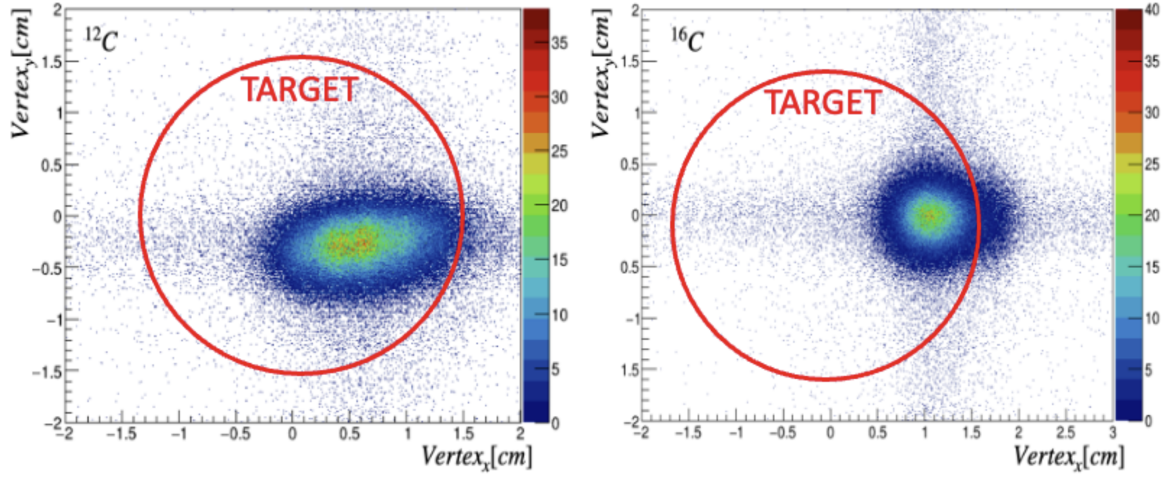


Figure 4.5: Left: MWPC beam trajectory projected onto the center of the target position as the interaction vertex. Correlation between the  $XY$  coordinates projection at the center of the target ( $^{12}\text{C}$ ). Left: same plot for  $^{16}\text{C}$  beam.

### Beam momentum

Given the beam angles in the  $XZ$  and  $YZ$  planes of the laboratory reference system and their energy, we can compute the beam momentum using the following formulas. Let  $E$  be the energy of the beam,  $\theta_x$  be the angle in the  $XZ$  plane, and  $\theta_y$  be the angle in the  $YZ$  plane ( $\theta_{x,y}$  are derived from MWPC beam tracking). The momentum components in the  $X$ ,  $Y$ , and  $Z$  directions can be calculated as follows:

$$\begin{aligned} p_x &= p \cdot \sin(\theta_x), \\ p_y &= p \cdot \sin(\theta_y), \\ p_z &= \sqrt{p^2 - p_x^2 - p_y^2}; \end{aligned} \quad (4.15)$$

where  $p$  is the magnitude of the momentum, given by  $p = \sqrt{E^2 - m^2}$  and  $m_{beam}$  is the rest mass of the beam particle.

### Boost and beam versors

We can define the beam reference frame introducing the beam versors  $\hat{x}'$ ,  $\hat{y}'$ , and  $\hat{z}'$  using the standard rotation matrices:

$$\hat{x}' = (\cos \theta \cos \phi, \sin \theta \cos \phi, -\sin \phi), \quad (4.16)$$

$$\hat{y}' = (-\sin \theta, \cos \theta, 0), \quad (4.17)$$

$$\hat{z}' = (\cos \theta \sin \phi, \sin \theta \sin \phi, \cos \phi); \quad (4.18)$$

where  $\theta$  and  $\phi$  are the polar and azimuthal beam angles, respectively.

Finally, we can define the final beam momentum in its reference frame  $\vec{p}_{beam}$  as:

$$\vec{p}_{beam,rot} = (0, 0, 0, m_{beam}). \quad (4.19)$$

In the following analysis, to compute the momentum of the other particles, we will consider first the beam versor to rotate the momentum of their momentum and then the  $\vec{p}_{beam}$  to perform a boost in the beam c.m. frame. In the case of primary  $^{12}\text{C}$ , the energy and so the momentum is given directly from the UNILAC accelerator, and we will consider a constant energy of 1.25

GeV/u (constant momentum of 23.7 GeV/c). For  $^{16}\text{C}$ , the situation is different.  $^{16}\text{C}$  is a secondary beam provided by FRS. As explained before, thanks to the information of  $ToF$  and  $B\rho$ , we can obtain the information of the velocity  $\beta$  of the beam. Using this information, we can derive the effective energy of the  $^{16}\text{C}$  beam event-by-event. In Fig. 4.6, we can observe the  $Z$  component of the beam momentum at the center of the target after the projection along the  $z$  versor and the correction for energy loss in the upstream detectors. The momentum is centered around 31.6 GeV/c.

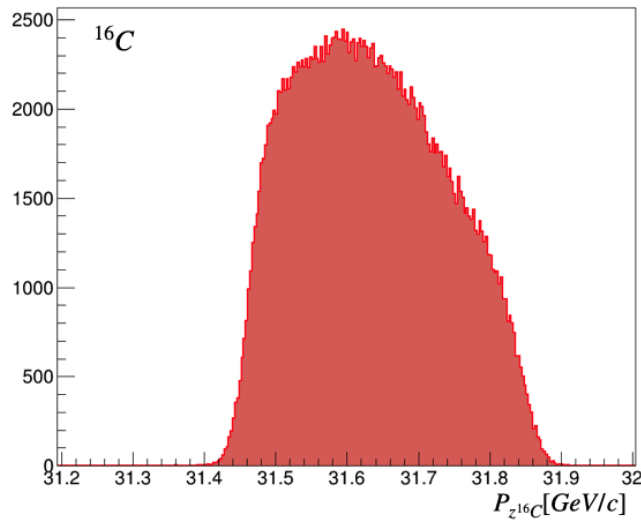


Figure 4.6:  $Z$  component of the  $^{16}\text{C}$  beam momentum. The momentum is calculated at the center of the target after energy loss in the incoming detector and half of the target volume.

Once having defined a beam reference through the definition of beam versors that related to the angular information of the beam in the  $X - Z$  and  $Y - Z$  plane, we derived the beam momentum for  $^{12}\text{C}$  and  $^{16}\text{C}$  in this rotated reference system. The next step of our analysis is to derive information about the fragments' momentum.

### 4.2.2 Fragments tracking

Charged particles travelling with velocity  $\vec{\beta}$  inside a magnetic field with strength  $B$  experience the Lorentz force. Balancing the centrifugal and Lorentz forces along the curved trajectory of the particle yields the following equation:

$$B\rho = \frac{m_u c}{e} \frac{A}{Z} \beta \gamma; \quad (4.20)$$

where  $m_u$  is the unit mass,  $c$  is the speed of light,  $e$  is the charge unit,  $A$  and  $Z$  are the charge and mass numbers of the particle,  $\vec{\beta}$  and  $\gamma$  are the speed and Lorentz factor,  $\rho$  is the curvature radius of the trajectory and  $B$  the magnetic field. For a fixed velocity  $\vec{\beta}$ , the product  $B\rho$  is proportional to the mass-to-charge ( $A/Z$ ) ratio of the particle. This principle forms the basis for the identification of reaction fragments behind the GLAD magnet.

### MDF Tracking Algorithm

The trajectory of charged particles is bent in GLAD according to their magnetic rigidity  $B\rho$ , i.e., momentum-over-charge ratio  $B = A/Z$  with charge  $Z$ . This allows us to determine the fragment's total momentum. For this purpose, simulations of the fragments propagating in the magnetic field were carried out using the field map of the magnet. The corresponding materials of the beamline detectors were also implemented in the simulation. The simulated fragments were chosen to have the maximum possible position, angular range and momentum spread to cover the entire geometrical acceptance of the magnet and detectors. The simulation output is then used as a training sample for the multidimensional fit (MDF) algorithm [126] in the form of n-tuples which hold the positions and angles of the fragment trajectory upstream and downstream of the magnet:  $(x_0, y_0, z_0, \theta_x, \theta_y)$  and  $(x_1, y_1, z_1, \theta_{x1}, \theta_{y1})$  respectively. Performing MDF over the training sample produces an analytical fit function  $P/Z_{\text{mdf}} = f(x_0, y_0, z_0, \theta_x, \theta_y, x_1, y_1, z_1, \theta_{x1}, \theta_{y1})$ , which can be applied to the positions and angles measured in the experiment. Similarly, other MDF functions were generated. An MDF function for  $\theta_x$  angle was derived as  $\theta_{\text{mdf}}^x = g(x_0, y_0, z_0, \theta_x, \theta_y, x_1, y_1, z_1, \theta_{x1}, \theta_{y1})$  and one  $\theta_{\text{mdf}}^y = g(x_0, y_0, z_0, \theta_x, \theta_y, x_1, y_1, z_1, \theta_{x1}, \theta_{y1})$  for the  $\theta_y$ . These functions gave us the reaction products' angular information. In combination with  $P/Z_{\text{mdf}}$ , they are used to derive the fragment momentum in the laboratory frame as:

$$\begin{aligned} P_{\text{frag}} &= (\theta_{\text{mdf}}^x, \theta_{\text{mdf}}^y, 1), \\ P_{\text{frag}, \text{magnitude}} &= P/Z_{\text{mdf}}. \end{aligned} \quad (4.21)$$

Another MDF function is  $FlightPath_{\text{mdf}}$ . This function gives the value of the Flight Path of the fragment from a point before GLAD magnet to the TOFD detector. With the Flight Path, we can derive the velocity  $\beta_{\text{mdf}}$  of the different fragments. Having determined these functions,  $\theta_{\text{mdf}}^{x,y}$ ,  $P/Z_{\text{mdf}}$  and  $FlightPath_{\text{mdf}}$ , experimental data for the reference trajectory of unreacted  $^{12}\text{C}$  is used to adjust the input variables' offsets, which reflect the alignment of the real detectors in the experimental setup with respect to the magnetic field. This is achieved by variation of the offsets in the experimental input variables simultaneously for  $\theta_{\text{mdf}}^x$  and  $P/Z_{\text{mdf}}$  until the residual between  $P/Z_{\text{mdf}}$  and its reference value is minimal. The reference value is chosen to be the  $P/Z$  of the unreacted  $^{12}\text{C}$  at the exit of the liquid-hydrogen target.

In the current analysis, only events with one good global track, which combines the up and downstream detectors, are considered. To ensure that real detected single-track events are selected, we required that all the incoming detectors, the fibers detectors, and ToFD saw at least one good track.

Before deriving the total MDF tracking efficiency, I will briefly illustrate the efficiency value for the fiber detectors with respect to TOFD. This calculation is performed considering TOFD efficiency 100%. We define the tracking efficiency for individual fibers as the ratio of events in a single fiber detector with a good ToF value and charge  $Z_{\text{TOFD}} = 6$  in TOFD, to the total number of events with  $Z_{\text{TOFD}} = 6$  in TOFD. In both cases, a good ToF value was selected for TOFD:

$$\epsilon_{\text{Fib}} = \frac{\#^{12}\text{C}_{\text{Fib}}}{\#^{12}\text{C}_{\text{TOFD}}}. \quad (4.22)$$

Since Fiber33 was not illuminated by the  $^{12}\text{C}$  unreacted beam, we estimate the efficiency using the  $^{11}\text{B}$  fragment. The efficiency values for each individual fiber are reported in Tab. 4.1:

Contributing Factor	Efficiency (%)
Fib32	93.1
Fib30	93.9
Fib31	94.2
Fib33	87.6 ( $^{11}\text{B}$ )
TOFD	100
Fib32 + Fib30 + Fib31	83.7
Fib32 + Fib30 + Fib33	78.9

Table 4.1: Fiber efficiency relative to TOFD detector. We notice that the efficiency for unreacted beam is slightly higher compared to the one derived with  $^{11}\text{B}$  fragment.

On average, the fiber detectors have an efficiency of 93.3% for unreacted beam, while for  $^{11}\text{B}$ , the efficiency is around 87%. The overall tracking efficiency (Fiber + TOFD) is around 80% for the unreacted  $^{12}\text{C}$  beam, while for the reacted beam, the tracking efficiency is around 64%. This tracking efficiency is not the total tracking efficiency but only one of the factors contributing to the total MDF fragment tracking efficiency.

After estimating the fiber efficiencies, we verified that all reaction products of interest ( $A - 1$  and  $A - 2$  fragments) were within the acceptance range of TOFD. Upon examining the fragment  $x$ -position distribution in TOFD, we found that 2% of  $^{10}\text{Be}$  was outside the TOFD geometrical acceptance. However, for the  $^{16}\text{C}$  incoming beam, we observed that 56% of  $^{14}\text{Be}$  was outside the TOFD acceptance. This significant acceptance loss has a substantial impact on the data analysis of the  $^{16}\text{C}$  data presented in this chapter.

A "good track" for MDF tracking is defined by the following criteria:

- Tracks present in one of the upstream MWPC detector systems;
- A good vertex position of the projected track from MWPC that falls inside the real target geometrical dimensions;
- A good ToF between LOS-Fibers and LOS-TOFD;
- Exactly one reconstructed matched global track based on the combined information from upstream detectors and fibers and TOFD detectors;
- A "good"  $P/Z$  value; for  $^{12}\text{C}_{\text{out}}$ , the  $P/Z$  value is expected to be centered around 2 GeV/c (for a beam momentum of 23.7 GeV/c).

Tab. 4.2 presents the different contributions to the total MDF tracking efficiency. Indeed, the total efficiency will be a sum of different contributions:

$$\varepsilon_{\text{mdf}} = \varepsilon_{\text{detectors}} + \varepsilon_{\text{Mul}=1} + \varepsilon_{\text{Good}P/Z}. \quad (4.23)$$

In all the analysis and efficiency estimation, I consider "On Spill" events with a proper TPAT selection. We have already estimated the efficiency of the tracking system (LOS + MUSLi + MWPC + Fibers + TOFD) for the unreacted beam. The CALIFA ( $p, 2p$ ) efficiency will not be considered in this fragment analysis section. Now, the percentages for each contributing factor to the total MDF tracking efficiency (for the reaction products) are presented: The total MDF tracking efficiency is reduced from 100% to 35%, mainly due to the detector efficiency in the tracking procedure and the requirement for a reconstructed single global track.

Contributing Factor	Efficiency (%)
Upstream track	100
Downstream track	64
Global track	64
Good $P/Z$	60
Good $P/Z$ Mult 1	35

Table 4.2: Contributions to the total MDF tracking efficiency.

### MDF alignment

The next step involves aligning the detectors using an iterative procedure that shifts the positions of the downstream detectors (Fiber detectors) until the  $P/Q$  value, derived using the MDF functions, aligns with the reference value (for  $^{16}\text{C}$ ). This alignment process utilized an unreacted  $^{16}\text{C}$  beam from the s509 experiment, which illuminated both fiber 31 and fiber 33.

In greater detail, the experimental data used for alignment were selected with stringent conditions: multiplicity of 1 in all tracking detectors, a precise cut on the  $P/Q$  value that required alignment, and a  $ToF$  cut with the fibers and TOFD detectors. Once this dataset was obtained, it was input into the alignment function. Essentially, the alignment function generates a starting random offset (one for each position to align) within a uniform distribution. This offset is applied to the detector, and the new detector position is input into the MDF functions to calculate a new  $P/Q$  value. This new  $P/Q$  is compared with the reference value, and a minimization error based on the residue between these two quantities is determined. This procedure is repeated for a number of iterations until the minimization error reaches a global minimum.

Once the minimum is reached, the alignment procedure stops, and we can derive the offset relative to the aligned positions that provide the best agreement with the reference  $P/Q$ . In our case, after studying the sensitivity of the alignment procedure to different coordinate offsets, we aligned the  $x$  positions for fibers 32, 31, and 33 and the  $y$  position for fiber 30. This approach significantly reduced the number of offset parameters, resulting in a precise alignment with narrow peaks associated with the position offsets and a good minimization residual value.

In the Tab. 4.3, the offsets associated with the  $x$  position of fibers 32 and 31 and the  $y$  position of fiber 30 are displayed.

Fiber	Offset
Fib32 x	0.7581 cm
Fib30 y	2.725 cm
Fib31 x	-0.8647 cm
Fib33 x	-0.126 cm

Table 4.3: Offsets in cm for Fibers positions.

After the alignment procedure, we can use the MDF tracking to derive the quantities of interest for fragment PID and momentum calculation ( $A/Z$ ,  $Z$ ,  $p_x$ ,  $p_y$ ,  $p_z$ ). In Fig. 4.7, the fragment PID is shown with the correlation between  $A/Z$  and  $Z$ . The left plot displays the reaction fragments for the  $^{12}\text{C}$  beam, while the right plot shows those for the  $^{16}\text{C}$  beam. The main fragments of interest for this analysis are highlighted in the figure. The  $^{11}\text{B}$  and  $^{15}\text{B}$  fragments

are associated with proton removal reactions  $^{12}\text{C}(p,2p)^{11}\text{B}$  and  $^{16}\text{C}(p,2p)^{15}\text{B}$ , respectively. The  $^{10}\text{B}$  and  $^{14}\text{B}$  fragments are associated with neutron-proton removal reactions  $^{12}\text{C}(p,2pn)^{10}\text{B}$  and  $^{16}\text{C}(p,2pn)^{14}\text{B}$ , respectively. We expect to find our  $np$  SRC pairs after proper kinematical selection in these reactions. The  $^{10}\text{Be}$  and  $^{14}\text{Be}$  fragments are associated with two-proton removal reactions  $^{12}\text{C}(p,2pn)^{10}\text{Be}$  and  $^{16}\text{C}(p,2pn)^{14}\text{Be}$ , respectively. We expect to find our  $pp$  SRC pairs after proper kinematical selection in these reactions.

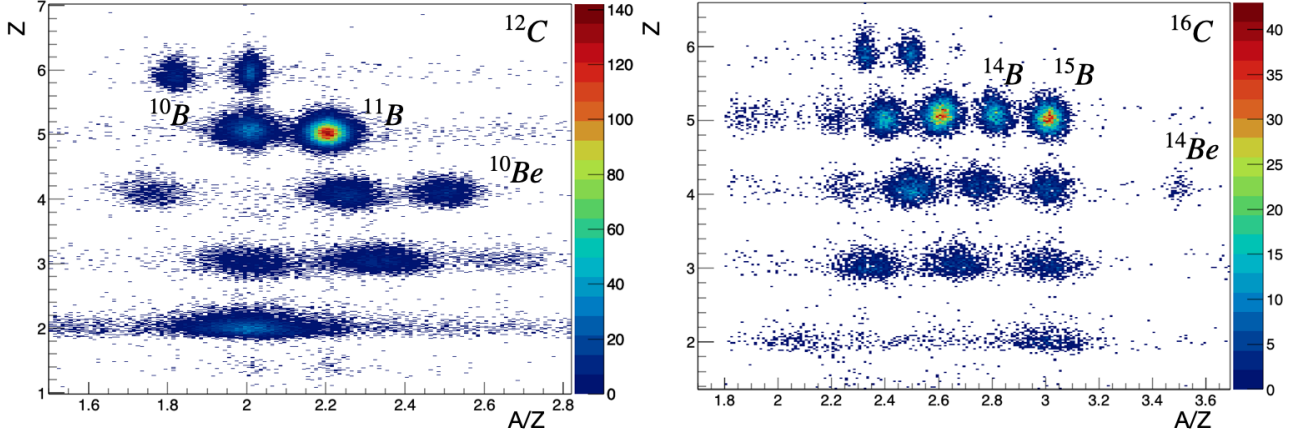


Figure 4.7: The left plot displays the reaction fragments for the  $^{12}\text{C}$  beam, while the right plot shows those for the  $^{16}\text{C}$  beam. The main fragments of interest for this analysis are highlighted in the figure.

After obtaining the Multi-Detector Function (MDF) for the charged fragments, we can calculate their momentum in the laboratory frame using the three components  $(p_x, p_y, p_z)$  obtained from the MDF. The total momentum of the fragments  $\vec{p}_{\text{frag}}$  is given by:

$$\vec{p}_{\text{frag}} = p_x \hat{x}_{\text{lab}} + p_y \hat{y}_{\text{lab}} + p_z \hat{z}_{\text{lab}}; \quad (4.24)$$

where  $\hat{x}_{\text{lab}}$ ,  $\hat{y}_{\text{lab}}$ , and  $\hat{z}_{\text{lab}}$  are the unit vectors along the laboratory coordinate axes. Next, to align the momentum of the fragments with respect to the beam direction, we rotate the total fragment momentum  $\vec{p}_{\text{frag}}$  using the beam versors  $\hat{x}'$ ,  $\hat{y}'$ , and  $\hat{z}'$ . The rotated momentum  $\vec{p}_{\text{rot}}$  is given by:

$$\vec{p}_{\text{rot}} = p'_x \hat{x}' + p'_y \hat{y}' + p'_z \hat{z}'; \quad (4.25)$$

where  $p'_x$ ,  $p'_y$ , and  $p'_z$  are the components of  $\vec{p}_{\text{frag}}$  along the rotated coordinate axes. Finally, to boost the fragment momentum into the center-of-mass (CM) frame of the beam reference system, we apply a Lorentz boost along the beam direction with the Lorentz factor  $\gamma$ . The boosted momentum  $\vec{p}_{\text{CM}}$  is given by:

$$\vec{p}_{\text{Frag}_{cm}} = \gamma \left( \vec{p}_{\text{rot}} + \frac{E_{\text{beam}}}{c^2} \hat{z} \right); \quad (4.26)$$

where  $E_{\text{beam}}$  is the energy of the beam and  $\hat{z}$  is the unit vector along the beam direction. Fig.4.8, Fig.4.9 and Fig.4.10 show the  $(x,y,z)$  components of the different fragments momentum distribution in the beam c.m. reference system.

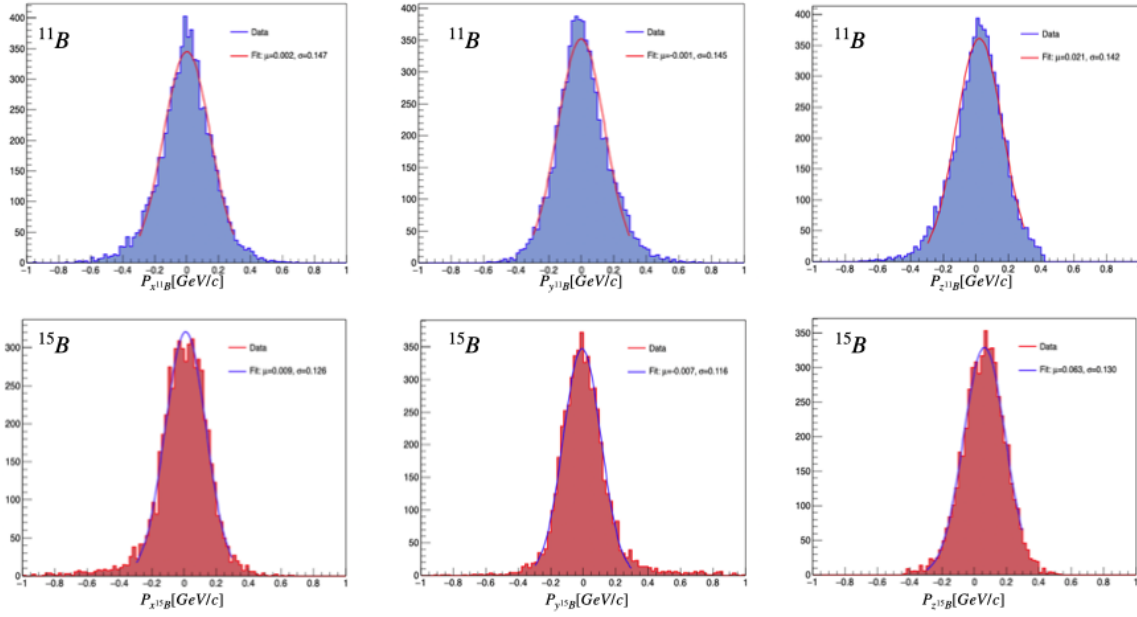


Figure 4.8: Momentum component distribution for  $^{11}\text{B}$  and  $^{15}\text{B}$  with (p,2p) selection in the beam rest frame.  $p_x$ ,  $p_y$  of  $^{11}\text{B}$  and  $^{15}\text{B}$  exhibit a small shift of the order to few MeV, with a Gaussian width of approximately 100 MeV/c.  $p_z$  shows a shift of around 30 MeV/c for  $^{11}\text{B}$  and 40 MeV/c for  $^{15}\text{B}$ .

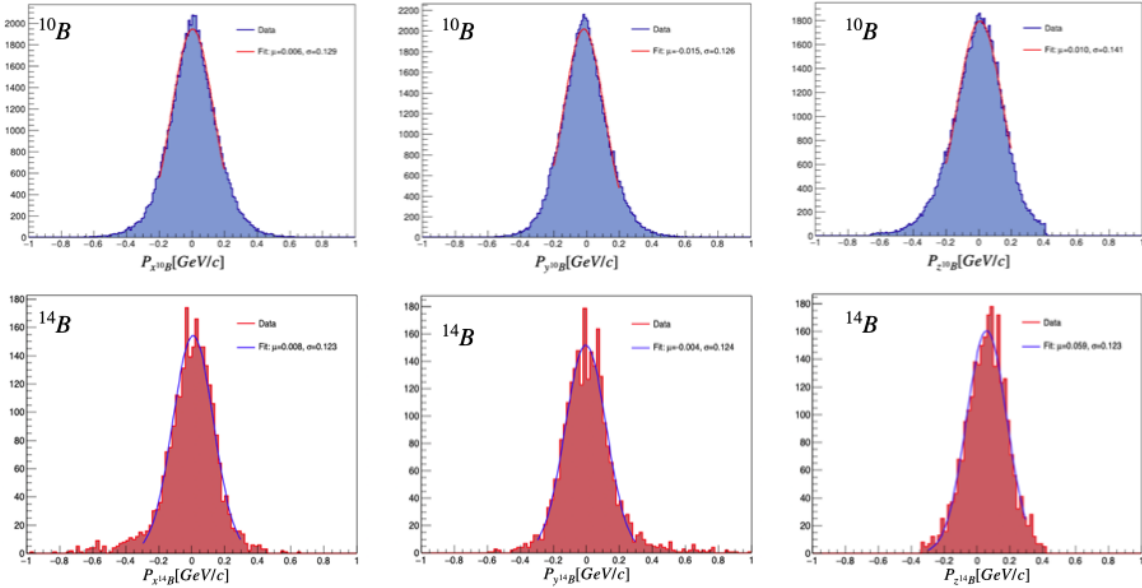


Figure 4.9: Momentum component distribution for  $^{10}\text{B}$  and  $^{14}\text{B}$  with (p,2pn) selection in the beam rest frame.  $p_x$ ,  $p_y$  of  $^{10}\text{B}$  and  $^{14}\text{B}$  exhibit a small shift of the order to few MeV, with a Gaussian width of approximately 120 MeV/c that is consistent with its physics width.  $p_z$  shows a shift of about 10 MeV/c for  $^{10}\text{B}$  while for  $^{14}\text{B}$  the shift is around 40 MeV/c.

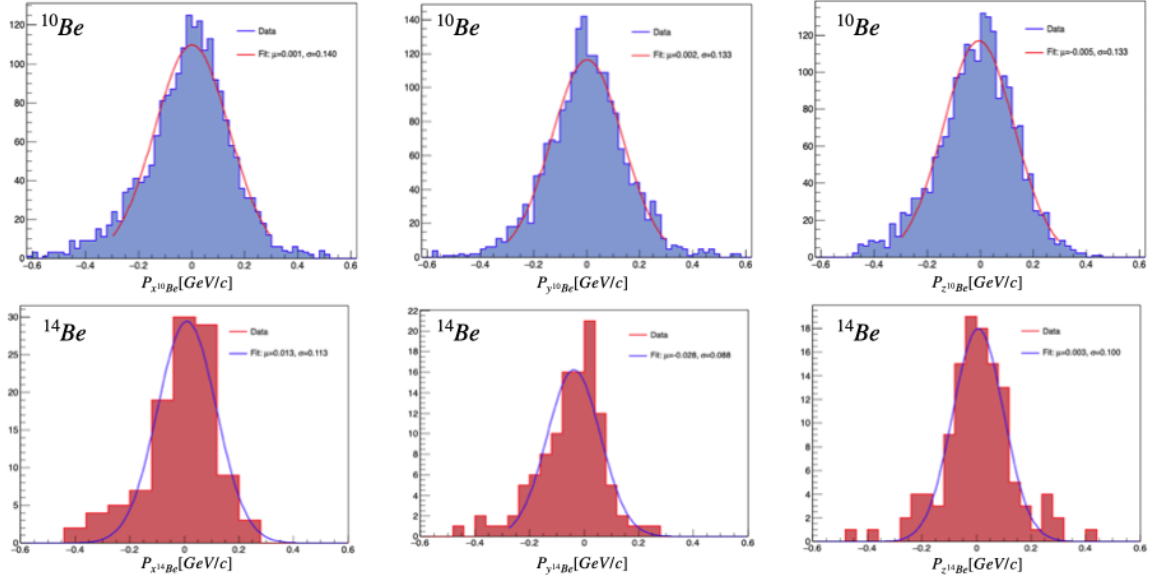


Figure 4.10: Momentum component distribution for  $^{10}\text{Be}$  and  $^{14}\text{Be}$  with (p,3p) selection in the beam rest frame.  $p_x$ ,  $p_y$  of  $^{10}\text{Be}$  and  $^{14}\text{Be}$  exhibit a small shift of the order to few MeV, with a Gaussian width of approximately 120 MeV/c that is consistent with its physics width.  $p_z$  shows a shift of 10 MeV/c for both  $^{10}\text{Be}$  and  $^{14}\text{Be}$ .

### 4.2.3 Proton tracking

Similarly to the fragment, the momentum of protons in RPC detector is calculated using MDF functions. As for the fragments, the trajectory of protons is heavily bent in GLAD according to their magnetic rigidity. This property allows us to determine the protons' total momenta. To achieve this, simulations of protons propagating in the magnetic field were conducted using the field map of the GLAD magnet. The simulation results serve as a training sample for the multidimensional fit (MDF) algorithm. Compared to the fragments, the MDF functions n-tuples we use for protons containing the positions and Times of Flight of the proton trajectory both upstream and downstream of the magnet:  $(x_0, y_0, z_0, \text{ToF}_0)$  and  $(x_1, y_1, z_1, \text{ToF}_1)$ , respectively.

The MDF applied to the training sample generates an analytical fit function  $P/Z_{\text{mdf}} = f(x_0, y_0, z_0, \text{ToF}_0, x_1, y_1, z_1, \text{ToF}_1)$ , which can be used on the positions measured in the experiment in combination with a second MDF function for  $\text{ToF}_{\text{mdf}} = g(x_0, y_0, z_0, \text{ToF}_0, x_1, y_1, z_1, \text{ToF}_1)$ . With these two functions,  $\text{ToF}_{\text{mdf}}$  and  $P/Z_{\text{mdf}}$ , experimental data for the reference trajectory of  $^{40}\text{Ar}$  beam ( $^{40}\text{Ar}$  is an RPC empty target calibration run from the test beam of March 2022) is used to adjust the offsets of the input variables. This adjustment reflects the alignment of the real detectors in the experimental setup relative to the magnetic field. The offsets in the experimental input variables are varied simultaneously for  $\text{ToF}_{\text{mdf}}$  and  $P/Z_{\text{mdf}}$  until the residual between  $P/Z_{\text{mdf}}$  and its reference value is minimized. The reference value is chosen to be the  $P/Z$  of unreacted  $^{40}\text{Ar}$  at the entrance of GLAD magnet. Following a similar procedure as the one described for the fragments, we obtained the following offset for the RPC  $\text{ToF}$ ,  $x$ ,  $y$  and  $z$  positions: To determine the momentum of protons after MDF tracking, we begin by calculating their momentum components  $(p_x, p_y, p_z)$  in the laboratory frame using the MDF data. The total proton momentum  $\vec{p}_{\text{prot}}$  is then expressed as:

$$\vec{p}_{\text{prot}} = p_x \hat{x}_{\text{lab}} + p_y \hat{y}_{\text{lab}} + p_z \hat{z}_{\text{lab}}; \quad (4.27)$$

where  $\hat{x}_{\text{lab}}$ ,  $\hat{y}_{\text{lab}}$ , and  $\hat{z}_{\text{lab}}$  are unit vectors along the laboratory coordinate axes.

RPC pos	Offset [cm]
x	-3.44
y	1.849
z	-1.11
ToF [ns]	0.1596

Table 4.4: Offsets in cm for RPC positions.

Subsequently, to align the proton momentum with respect to the beam direction, we rotate  $\vec{p}_{\text{prot}}$  using the beam versors  $\hat{x}'$ ,  $\hat{y}'$ , and  $\hat{z}'$ . This results in the rotated momentum  $\vec{p}_{\text{rot}}$ , expressed as:

$$\vec{p}_{\text{rot}} = p'_x \hat{x}' + p'_y \hat{y}' + p'_z \hat{z}'; \quad (4.28)$$

where  $p'_x$ ,  $p'_y$ , and  $p'_z$  are the components of  $\vec{p}_{\text{prot}}$  along the rotated coordinate axes. Finally, to boost the proton momentum into the center-of-mass frame of the beam reference system, we apply a Lorentz boost along the beam direction with the Lorentz factor  $\gamma$ . The boosted momentum  $\vec{p}_{\text{CM}}$  is given by:

$$\vec{p}_{\text{P}_{cm}} = \gamma(\vec{p}_{\text{rot}} + \frac{E_{\text{beam}}}{c^2} \hat{z}); \quad (4.29)$$

where  $E_{\text{beam}}$  represents the energy of the beam and  $\hat{z}$  is the unit vector along the beam direction. Fig.4.11 shows the  $(x,y,z)$  components of the proton momentum distribution in the beam c.m. reference system.

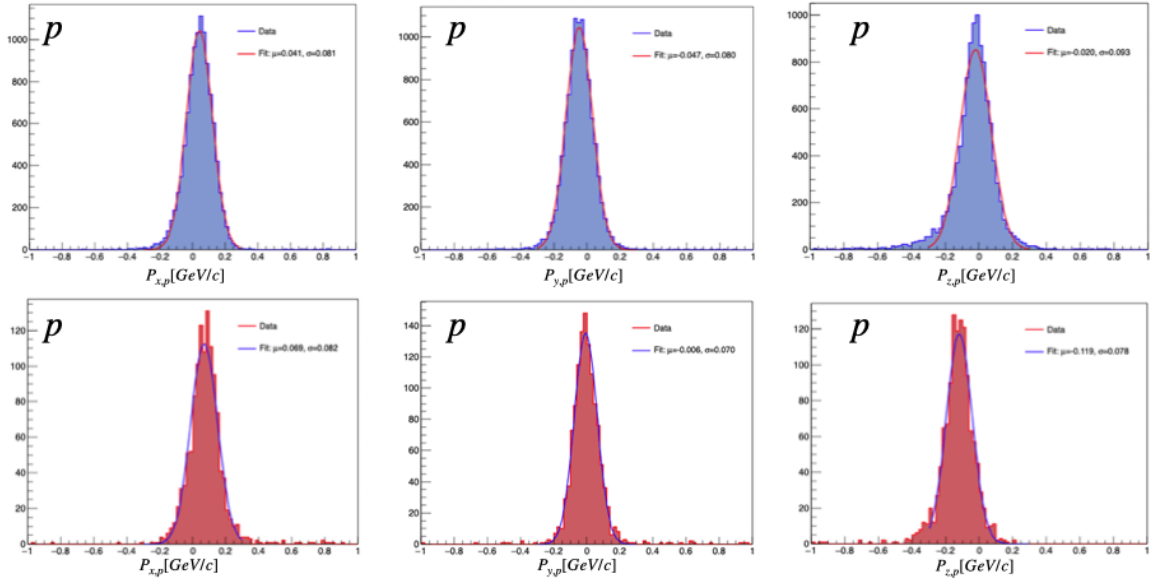


Figure 4.11: Momentum component distribution for RPC protons with (p,2p) selection in the beam rest frame.  $p_x$ ,  $p_y$  and  $p_z$  exhibit a shift of the order of 50 MeV/c, with a Gaussian width of approximately 100 MeV/c that is consistent with its physics width.

#### 4.2.4 Neutrons tracking

The Neuland detector provides precise measurements of the neutrons hitting the detector. The primary constraint on neutron measurement is the acceptance of the GLAD magnet entrance. For accurate neutron selection, we consider only the first hit in the Neuland detector. Fig. 4.12 (top panels) shows the corrected time-of-flight spectrum for the first hit (i.e., Neuland hit time minus LOS time, adjusted for the expected time for a  $\gamma$  to travel from the center of the first

plane to the actual hit position in Neuland), as well as the corrected  $ToF$  vs. deposited energy. The first major peak, centered around 51.7 ns, corresponds to the  $\gamma$  peak. The second broad peak represents the neutron peak, which is contaminated by charged events appearing as a curved line around 10 MeVee. We also observe that residual walk effects contaminate the lower energy events in the neutron peak; therefore, we apply a minimum energy deposition cut at 6 MeVee for neutron selection. With the minimum energy deposition cut at 6 MeVee and a charge veto (vetoing every event where there is a hit in the first plane), we obtain the corrected ToF spectrum and ToF vs. energy spectrum shown in Fig. 4.12 (bottom panels). The fit to the  $\gamma$  peak shows that it is centered at the expected value of 51.7 ns, with a resolution of 209 ps. Considering bar-by-bar calibration, Fig. 4.13 displays the energy and time-of-flight spectra

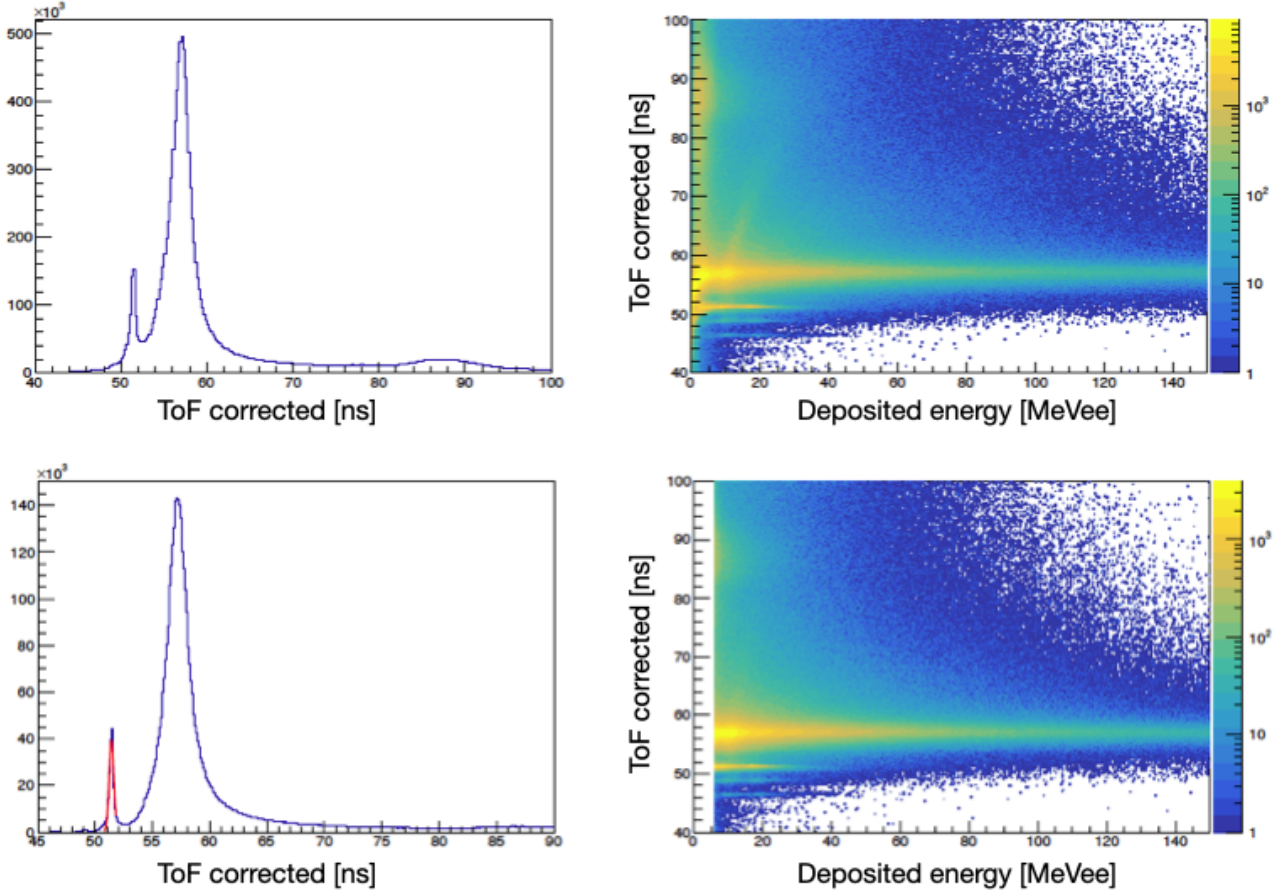


Figure 4.12: Top left: corrected  $ToF$  spectrum for the first hit in Neuland. Top right: corrected  $ToF$  v. deposited energy in Neuland. Bottom left: corrected  $ToF$  spectrum for the first hit in Neuland. Bottom right: corrected  $ToF$  vs. deposited energy in Neuland. All plots are made with charge veto and a minimum energy deposition cut at 6 MeVee.

versus bar ID. The energy distribution appears uniform across all bars, indicating proper calibration for each one. However, the  $ToF$  spectrum for gamma and neutron peaks exhibits a dependence on bar IDs, which correlates with the positions of the bars. Specifically, as the bar ID increases, indicating bars positioned further back, the time taken for  $\gamma$ ,  $n$  particles to reach these bars increases accordingly. Conversely, the beam dump peak around 90 ns demonstrates the opposite trend, attributable to back reflections.

Fig. 4.14 shows a plot of Time-of-Flight versus hit position in Neuland, along with a corrected plot of Time-of-Flight versus energy, incorporating  $^{10}\text{B}$  and  $(p,2p)$  tagging (proton multiplicity 2, crystal number per cluster less than 6 as discussed in the following section), as well as energy selection and charge veto. This plot is of particular interest to us as we seek to understand the neutron evaporation process in  $^{11}\text{B} \rightarrow ^{10}\text{B} + n$  and SRC neutrons. The Time-of-Flight versus

Neuland hit position,  $X$ , reveals an excess of events at  $x < 110$  cm, which stays slightly behind the usual neutrons within the neutron peak. At higher Time-of-Flight (in the beam dump region), Time-of-Flight increases as  $x$  becomes more positive. These observations are consistent with fragment reflections off the ToFD detector. Consequently, we impose a selection of  $|x| < 110$  cm for the "good" neutrons that we wish to study. Regarding the time-of-flight versus  $y$  distribution, we observe a shift in  $y$ , attributed to the  $y$ -axis of NeuLAND not being centered. We do not impose a selection on the  $y$  positions. For mean-field  $^{11}\text{B}$  breakup into  $^{10}\text{B} + n$ , which dominates the neutrons observed here, we anticipate the velocities and angles of the lab-frame  $^{10}\text{B}$  and neutron to be closely aligned, given the small internal momentum compared to the beam energy.

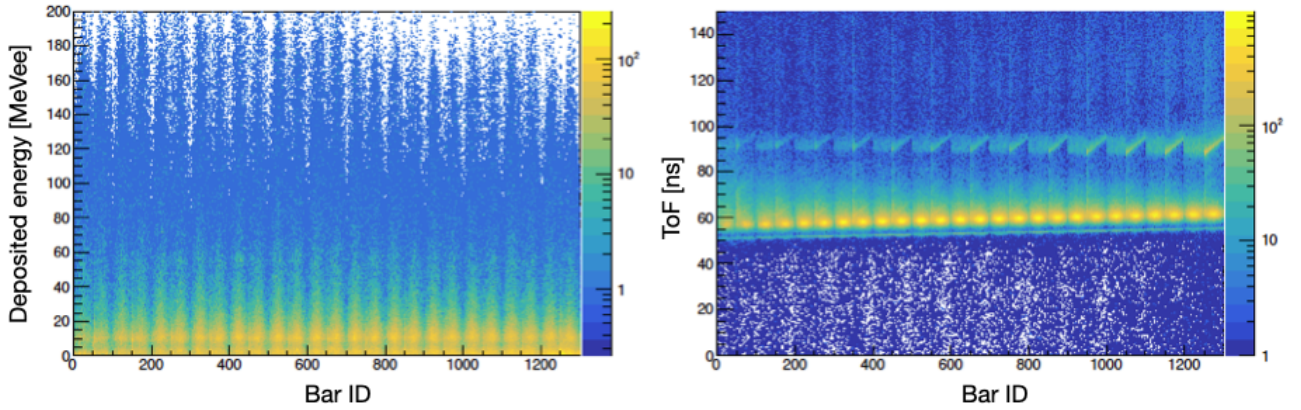


Figure 4.13: Energy versus bar ID (left) and  $ToF$  versus bar ID (right) for all NeuLAND hits.

Fig. 4.15 illustrates the relative alignment between the neutron and  $^{10}\text{B}$  fragment. The  $\beta$  alignment indicates a center difference of approximately  $5.4 \times 10^{-4}$  with a width of  $1.9 \times 10^{-2}$ , and any adjustment is performed for this value due to the small relative difference. The  $\delta tx$  ( $\theta_{x,n} - \theta_{x,^{10}\text{B}}$ ) between the neutron and boron fragment is  $-8.68$  mrad, and  $\delta ty$  ( $\theta_{y,n} - \theta_{y,^{10}\text{B}}$ ) is  $4.56$  mrad. We will align our neutron angles to the boron fragment angles since, in the lab frame, the fragment angle should always remain very close to 0 due to the large mass of the fragment. The relative alignment values are also valid for the relative alignment of  $^{14}\text{B}$  and  $n$  for the incoming  $^{16}\text{C}$  beam.

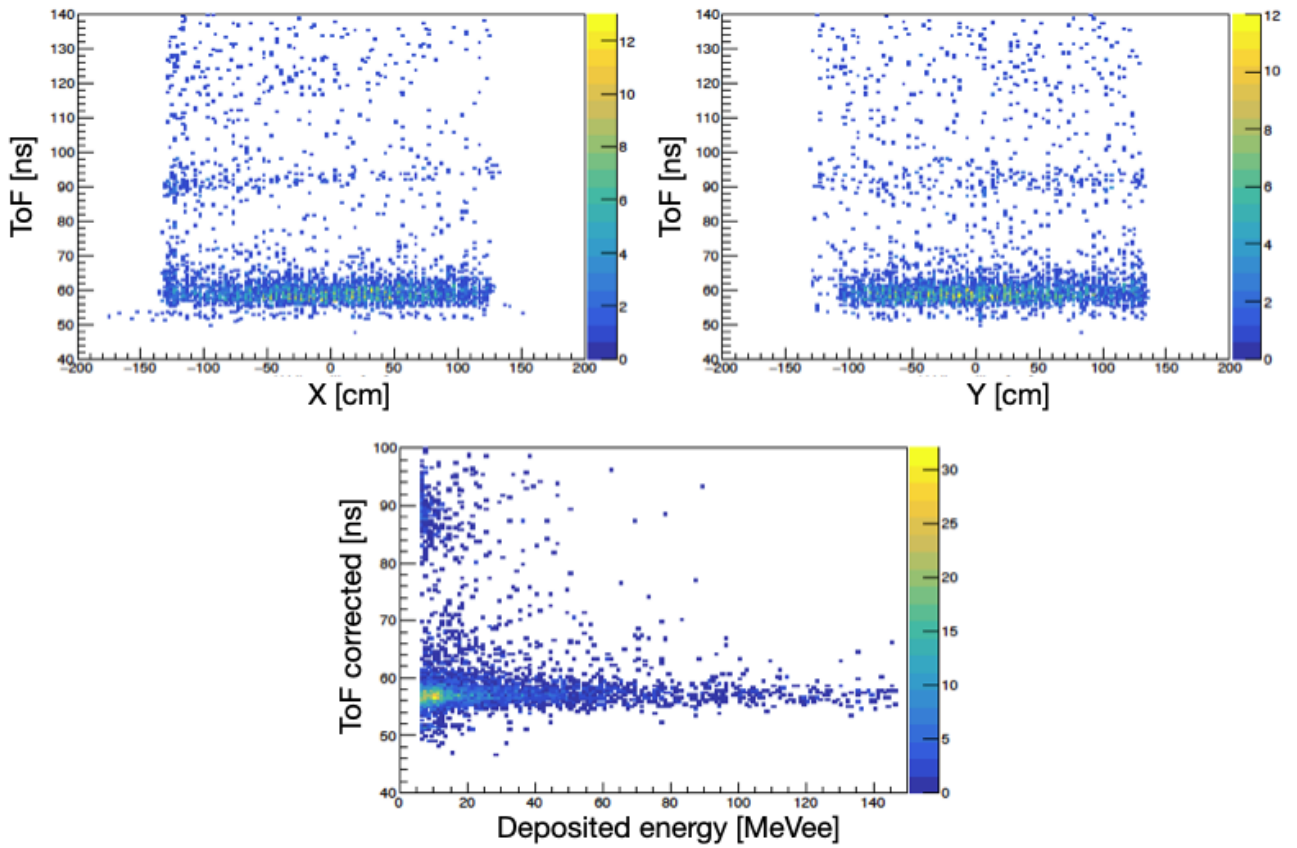


Figure 4.14: Neuland hit position v.  $ToF$  distribution with  $^{10}\text{B}$  and  $(p,2p)$  tagging.

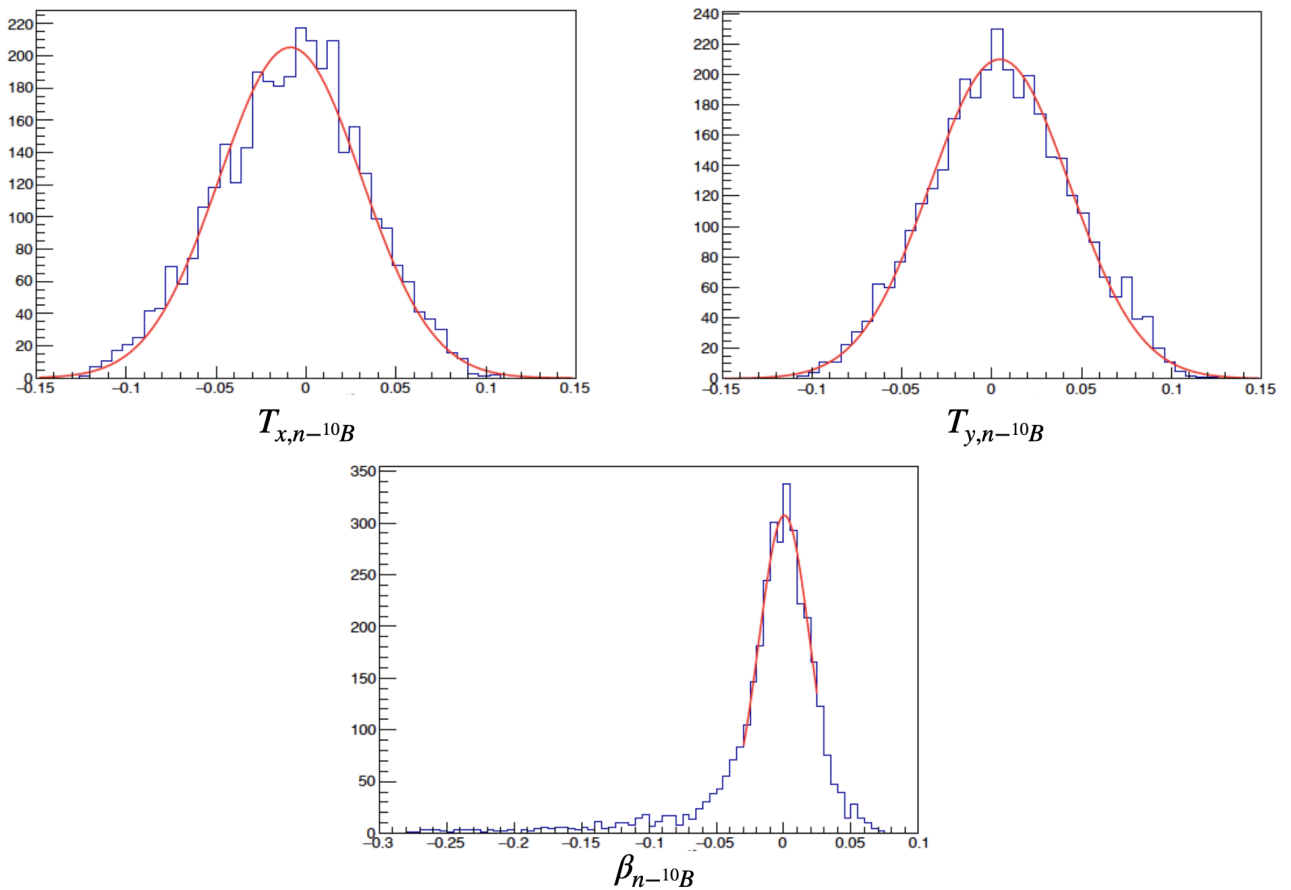


Figure 4.15: Angular and beta alignment of  $^{10}\text{B}$  and selected neutrons in Neuland.

To calculate the momentum of a neutron detected in the NeuLAND detector given its *ToF* and distance from the reaction point  $d$ , we can first define the dimensionless quantity  $\beta = \frac{v}{c}$ , where  $v$  is the velocity of the neutron and  $c$  is the speed of light. Using this definition, the velocity of the neutron can be expressed as  $v = \beta c$ .

The momentum ( $p$ ) of the neutron is related to its velocity ( $v$ ) and rest mass ( $m_0$ ) by the relativistic equation:

$$p = \frac{m_0 v}{\sqrt{1 - \beta^2}}. \quad (4.30)$$

Given that  $v = \frac{d}{t}$ , where  $d$  is the distance from the reaction point to the NeuLAND detector, and  $t$  is the Time-of-Flight, we can substitute  $v$  into the momentum equation:

$$p = \frac{m_0 \frac{d}{t}}{\sqrt{1 - \beta^2}}. \quad (4.31)$$

Rearranging terms, we obtain the following.

$$p = \frac{m_0 d}{\sqrt{1 - \beta^2} t}. \quad (4.32)$$

This equation provides the magnitude of the neutron momentum ( $p$ ) in terms of the distance ( $d$ ), ToF ( $t$ ), and the dimensionless quantity  $\beta$ . After obtaining the momentum for the neutrons, we can calculate their momentum in the laboratory frame using the three components ( $p_x, p_y, p_z$ ) derived above. The total momentum of the neutrons  $\vec{p}_n$  is given by:

$$\vec{p}_n = p_x \hat{x}_{\text{lab}} + p_y \hat{y}_{\text{lab}} + p_z \hat{z}_{\text{lab}}; \quad (4.33)$$

where  $\hat{x}_{\text{lab}}$ ,  $\hat{y}_{\text{lab}}$ , and  $\hat{z}_{\text{lab}}$  are the unit vectors along the laboratory coordinate axes.

Next, to align the momentum of the neutrons with respect to the beam direction, we rotate the total neutron momentum  $\vec{p}_n$  using the beam versors  $\hat{x}'$ ,  $\hat{y}'$ , and  $\hat{z}'$ . The rotated momentum  $\vec{p}_{\text{rot}}$  is given by:

$$\vec{p}_{\text{rot}} = p'_x \hat{x}' + p'_y \hat{y}' + p'_z \hat{z}'; \quad (4.34)$$

where  $p'_x$ ,  $p'_y$ , and  $p'_z$  are the components of  $\vec{p}_n$  along the rotated coordinate axes. Finally, to boost the fragment momentum into the center-of-mass (CM) frame of the beam reference system, we apply a Lorentz boost along the beam direction with the Lorentz factor  $\gamma$ . The boosted momentum  $\vec{p}_{\text{CM}}$  is given by:

$$\vec{p}_{\text{n cm}} = \gamma \left( \vec{p}_{\text{rot}} + \frac{E_{\text{beam}}}{c^2} \hat{z} \right); \quad (4.35)$$

where  $E_{\text{beam}}$  is the energy of the beam and  $\hat{z}$  is the unit vector along the beam direction. Fig.4.16 shows the ( $x, y, z$ ) components of the neutron momentum distribution in the beam c.m. reference system.

After determining the beam, proton, and neutron momenta using information from the upstream detectors, NeuLAND, and RPC, we can proceed with investigating the ( $p, 2p$ ) reaction kinematics. In particular, the momentum reconstruction of the protons in CALIFA is a crucial step in studying QFS reactions. The procedure for energy and momentum reconstruction of punch-through protons will be discussed, along with the identification of the proper ( $p, 2p$ ) reaction, which is essential for defining the QFS kinematical region. This serves as a starting point for selecting conditions to infer SRC physics.

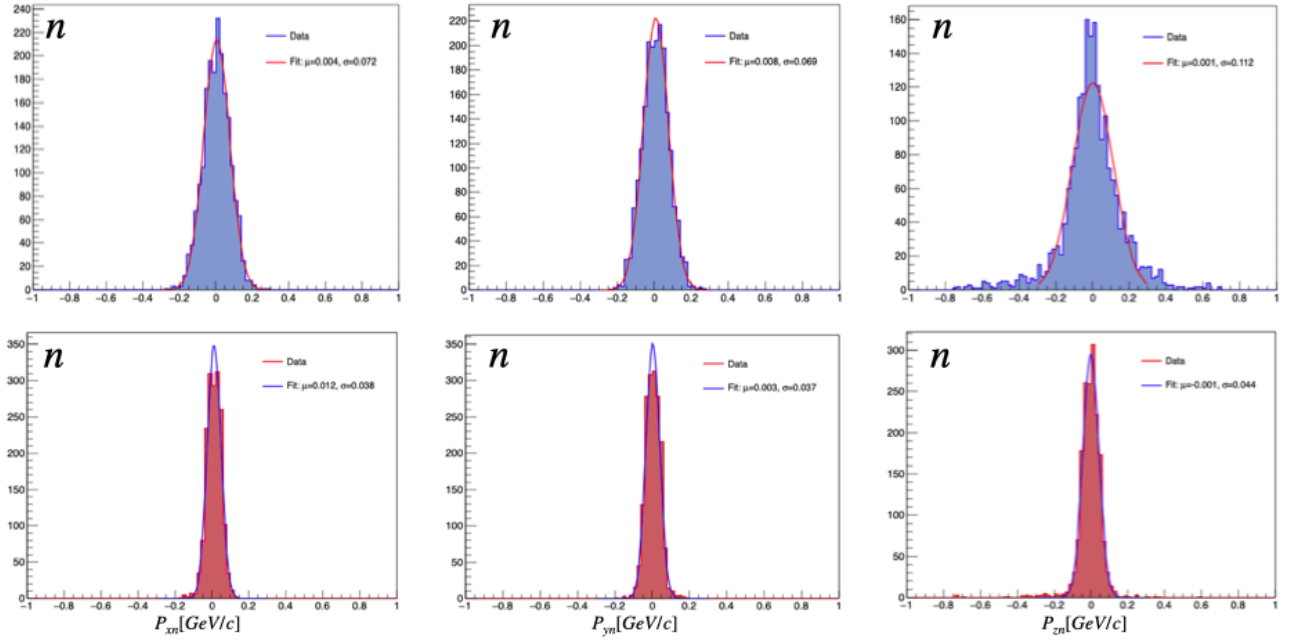


Figure 4.16: Momentum component distribution for neutrons in NeuLAND with  $(p,2p)$  selection in the beam rest frame.  $p_x$ ,  $p_y$  and  $p_z$  exhibit a small shift of the order to few MeV/c, with a Gaussian width of approximately 70 MeV/c for  $^{12}\text{C}$  and 40 MeV/c for  $^{16}\text{C}$ .

### 4.3 $(p,2p)$ reaction investigation

Proton-induced two-proton  $(p,2p)$  reactions serve as a fundamental starting point for studying Short-Range Correlations in nuclei. These reactions, characterized by the simultaneous ejection of two protons from a target nucleus, offer a unique window into the underlying nuclear dynamics at short distances. By analyzing the kinematics and properties of the ejected protons, we can probe the presence and characteristics of SRC pairs within the nucleus.

A crucial aspect of the current analysis involves identifying and measuring energetic pairs of nucleons produced in quasi-free scattering reactions, specifically  $^{12/16}\text{C}(p, 2p)^{11/15}\text{B}$  as starting point for SRC investigation. By optimizing the QFS kinematical conditions to suppress FSI and eliminate inelastic (IE) processes, we aim to reveal whether SRC physics emerges from other competing channels that obscure SRC signals. Once we identify a kinematical region where SRC physics should manifest, we can examine the properties of SRC pairs and count them. The CALIFA detector has been used to detect two scattered protons at large laboratory angles in the  $(p,2p)$  reaction over a broad angular range. The following sections detail the steps involved in the analysis for reconstructing these events.

When an energetic particle, such as a proton or photon, interacts with a crystal in CALIFA, part of its deposited energy, in the form of secondary electrons, positrons, gammas, etc., can spread to adjacent crystals. Alternatively, the particle itself may re-scatter, travelling through multiple crystals. Therefore, the total energy loss of the particle is determined by summing the individual energies measured by a group of nearby crystals, known as a "cluster."

For high-energy protons incident on CALIFA, we expect to observe both stopped protons and punch-through protons. With a  $^{12}\text{C}$  beam at a kinetic energy of 1250 MeV/u, the expected energy per proton in a  $(p,2p)$  scattering event is approximately 650 MeV. This energy level surpasses the stopping power of the CALIFA crystals, which is about 320 MeV. Consequently, the  $(p,2p)$  protons of interest will punch through the CALIFA crystals, depositing only a portion of their energy.

The first step in our ( $p,2p$ ) reconstruction process is to distinguish between punch-through and stopped protons. This is accomplished by using the slow ( $N_s$ ) and fast components ( $N_f$ ) of the integrated charge in CALIFA, along with the particle energy information from Time-over-Threshold (ToT) measurements.

### 4.3.1 Protons identification via QPID

The traditional particle identification (PID) using CALIFA is performed by considering only  $N_f$  and  $N_s$ . Specifically, by correlating  $N_f + N_s$  with  $\frac{N_f}{N_f + N_s}$ , we can achieve particle identification as shown in Fig. 4.17 (Top left Figure). Two main lines can be observed: the lower one, associated with neutrons ( $n$ ), punch-through protons ( $p$ ), and gamma rays ( $\gamma$ ), and the upper one, associated with stopped protons. Moving upwards along this line, particles with small energy loss, such as deuterons and tritons, can be identified. Additionally, the branch that separates and goes upward is likely to correspond to heavier isotopes, such as helium.

It is notable that the merging of the two lines occurs at energies above  $N_f + N_s > 150$  MeV, complicating the separation of stopped and punch-through protons in this analysis. Fig. 4.17 shows the CALIFA PID for different angular ranges. As the angle increases, particle separation becomes cleaner due to background suppression and better resolution of CALIFA.

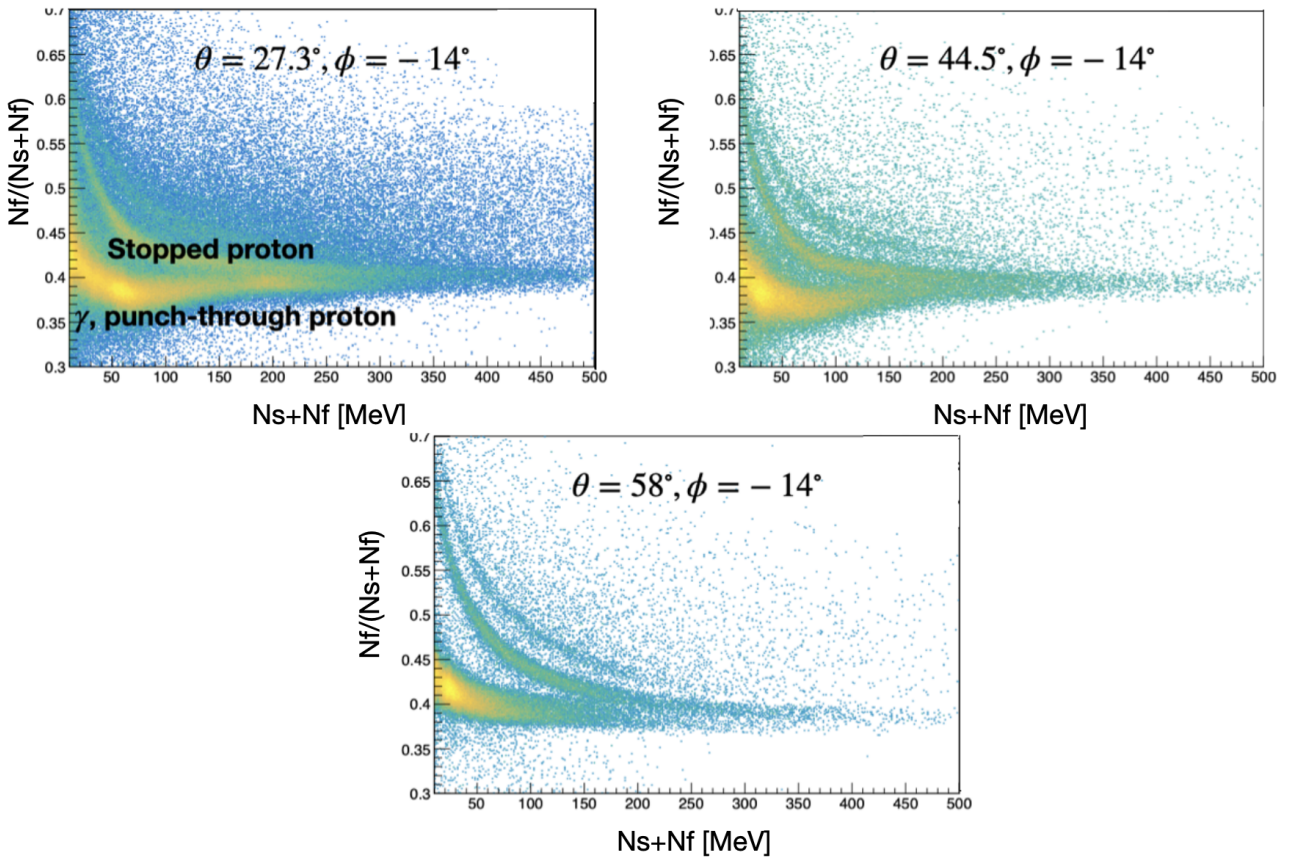


Figure 4.17: Top left:  $N_f + N_s$  vs  $\frac{N_f}{N_f + N_s}$  CALIFA particle identification. Distinct lines can be observed, corresponding to neutrons ( $n$ ), punch-through protons ( $p$ ), and gamma rays ( $\gamma$ ). The upper line is associated with stopped protons. Top right and bottom:  $N_f + N_s$  vs  $\frac{N_f}{N_f + N_s}$  for different CALIFA angular ranges. As the angle increases, the separation of the lines becomes clearer, and the background is more suppressed.

Building on this PID reconstruction, M. Feijoo (USC Santiago de Compostela) developed a new PID procedure that effectively separates different particles. This procedure allows for the identification and discrimination of stopped and punch-through protons without encountering saturation issues at energies lower than those of interest in this analysis.

The key aspect of this PID procedure is the analysis of the  $N_f$  and  $N_s$  signals crystal by crystal. This approach is necessary because the slow and fast components being read out depend not only on the crystal shape but also on the doping. The CALIFA detector crystals are irregular trapezoidal prisms, with most having a unique shape. Although doping is relatively homogeneous, slight differences between crystals always exist. Without delving into too much detail, the new CALIFA PID procedure involves the following steps:

- The first step is to produce a  $N_f/(N_s + N_f)$  vs  $N_f + N_s$  PID iteratively, crystal by crystal.
- The second step involves performing an exponential fit on the line associated with stopped protons and using this function to scale all other PID lines (see Fig. 4.18, top Figures). This adjustment makes the PID lines appear as horizontal lines at  $N_f + N_s > 120$  MeV, making it easier to differentiate between different particles. In the bottom left plot of Fig. 4.18, the projection of the scaled  $N_f/(N_s + N_f)$  is displayed for a value of  $N_f + N_s = 125$  MeV. In this plot, the PID lines for the stopped and punch-through protons are represented as two distinct peaks.
- The final step is to define a threshold for  $N_f/(N_s + N_f)$  using the bottom left plot of Fig. 4.18 as a reference. The threshold value for separating stopped and punch-through protons is shown in the bottom right plot of Fig. 4.18, where a red line delineates the two regions of interest.

This procedure is applied iteratively to the crystal of the cluster with the highest energy to determine if the  $(p, 2p)$  protons are stopped or punch-through. The energy reconstruction procedure will be presented in the next section. The information from CALIFA PID will be crucial for determining a proper energy reconstruction according to the proton PID and angular information.

### 4.3.2 Punch-trough protons energy reconstruction

To reconstruct the total energy of these punch-through protons,  $R^3B$  simulations were used. The proton energy reconstruction procedure follows these steps:

- Identify the position-dependence of deposited proton energy in CALIFA with a fixed incident energy of 650 MeV/u.
- Determine the incident-deposited energy relation for each crystal region (regions with different crystal lengths) based on  $R^3B$  simulation.
- Extract a polynomial function to reconstruct the full proton energy from its deposited energy in CALIFA.
- Reconstruct physical variables such as missing momentum and missing mass ( $p_{\text{miss}} = p_3 + p_4 - p_{\text{tg}}$  in the beam rest frame) based on energy reconstruction.

The same PID and energy reconstruction procedure is applied for both  $^{12}\text{C}$  and  $^{16}\text{C}$  beams.

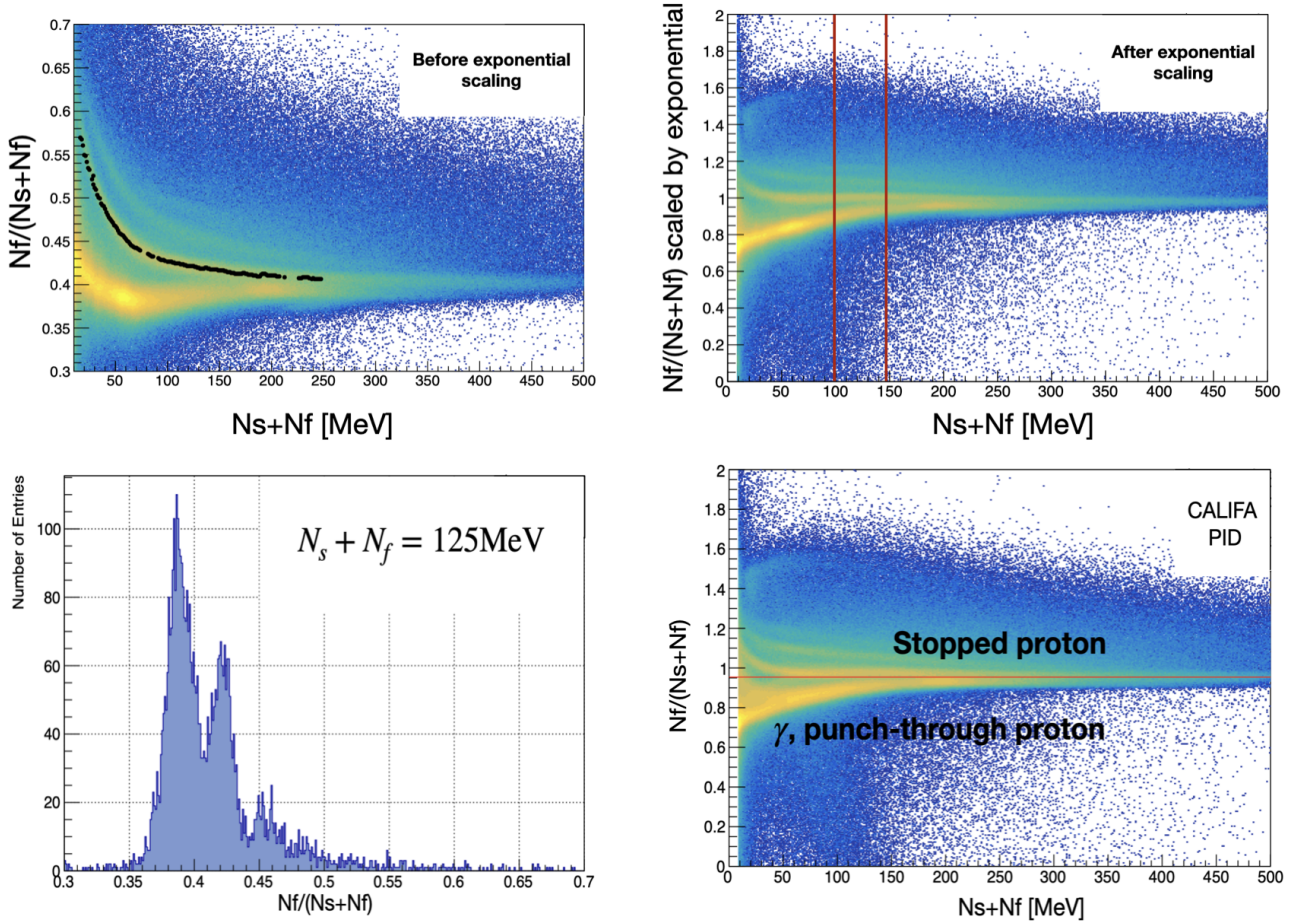


Figure 4.18: Top left: Exponential fit of the  $N_f + N_s$  vs  $\frac{N_f}{N_f+N_s}$  stopped proton PID line. Top right:  $N_f + N_s$  vs  $\frac{N_f}{N_f+N_s}$  with PID lines scaled relative to the stopped proton line using the exponential fit. Bottom left: Projection of  $\frac{N_f}{N_f+N_s}$  for  $N_f + N_s = 125$  MeV, showing the separation of the two CALIFA particle regions. Bottom right:  $N_f + N_s$  vs  $\frac{N_f}{N_f+N_s}$  with a defined threshold in  $\frac{N_f}{N_f+N_s}$  based on the projection, distinguishing the regions of stopped protons from punch-through protons.

## Proton Clustering Algorithm

The clustering algorithm in the current R3BRoot version executes the following procedure:

- The first step is to identify the proton-ranged crystals;
- Within the proton-ranged crystals, identify and remove the highest energy crystal from the list.
- Find all proton-ranged crystals within a cone with a half-angle of 0.25 radians. Add these crystals to the cluster and remove them from the list.
- Repeat step 2 for all current crystals in the identified cluster until no more crystals can be added.

The cluster energy is the sum of all crystal energies in the cluster. The initial angles of the cluster are calculated from the position of the highest-energy crystal in the cluster. The derived angles are then corrected for the effective position of the vertex  $V_{mwpc} = (V_x, V_y, 0)$  derived by the projection of the MWPC tracks at the center of the target.

## Position Dependence of Deposited Energy at Fixed Incident Energy

To examine the position dependence of deposited energy for a fixed incident energy of 650 MeV, we considered proton events at 650 MeV with different angles ranging from  $19^\circ < \theta < 90^\circ$  (CALIFA geometrical range in the current setup) and  $-180^\circ < \phi < 180^\circ$  in  $R^3B$  simulation using the latest geometry file. Fig.4.19 shows the simulation results. The  $\phi$  dependence is flat except for the different values caused by different  $\theta$ . The dependence  $\theta$  shows a flat step function in each of the three crystal regions, explained by the different crystal lengths (see Chapt. 2). Therefore, we need only one reconstruction function for each region.

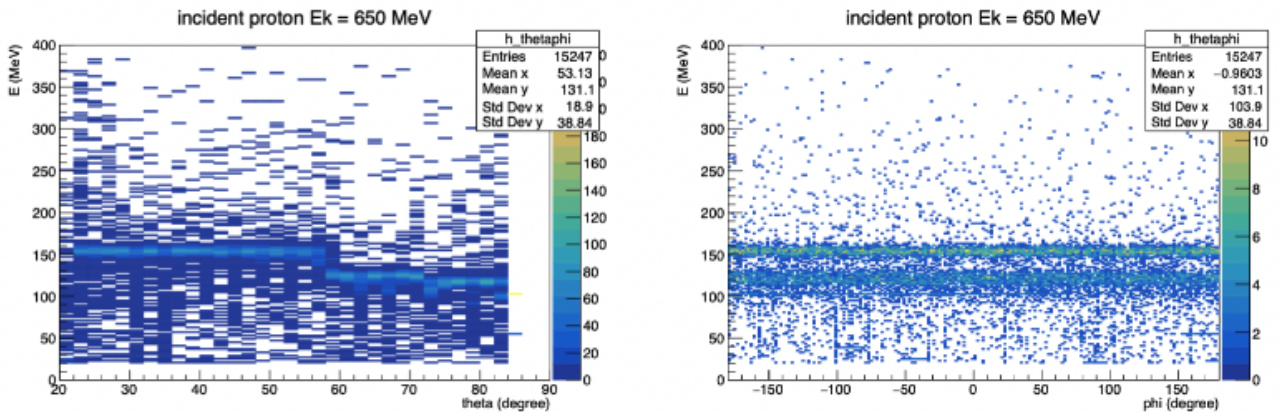


Figure 4.19:  $\theta/\phi$  dependence of simulated proton deposited energy at a fixed generated incident energy of 650 MeV.

The range of deposited energy and full kinetic energy of interest can be seen in Fig. 4.20 and Fig. 4.21. We aim to reconstruct protons with kinetic energy from 300 to 1800 MeV. Hence, we design an energy reconstruction function based on simulation for this energy range for each region with the same crystal length (and ideally the same path length for punch-through protons). The three  $\theta$  range considered are:

- $19^\circ - 55^\circ$ , with a selection on the proton deposited energy between 128-278 MeV.

- $55^\circ - 70.4^\circ$ , with a selection on the proton deposited energy between 104-260 MeV.
- $70.4^\circ - 90^\circ$ , with a selection on the proton deposited energy between 97-210 MeV.

At each region, it is associated with an energy reconstruction function for the proton energy. In the next section, the procedure to derive these functions is presented.

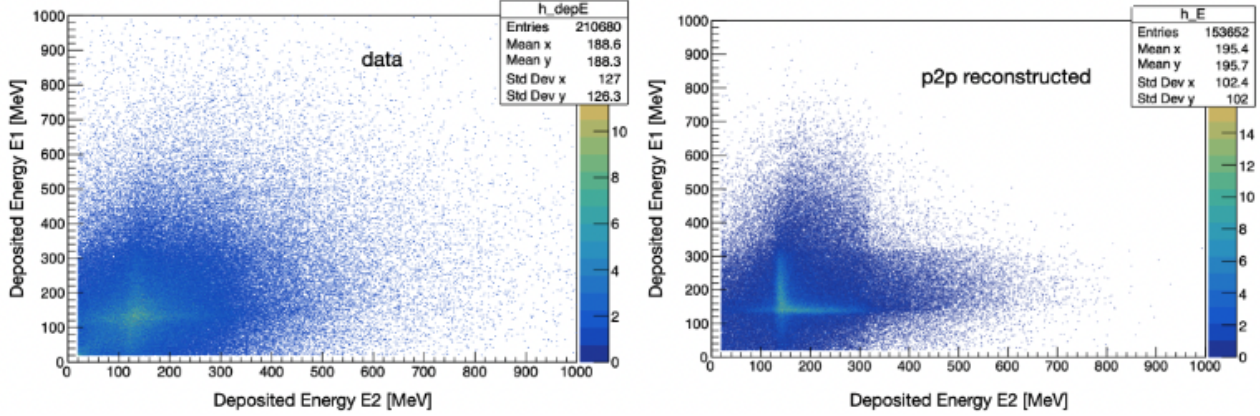


Figure 4.20: Deposited energy correlation for the two highest-energy protons. Left: data. Right: ( $p,2p$ ) signal reconstructed from Geant simulation through detectors.

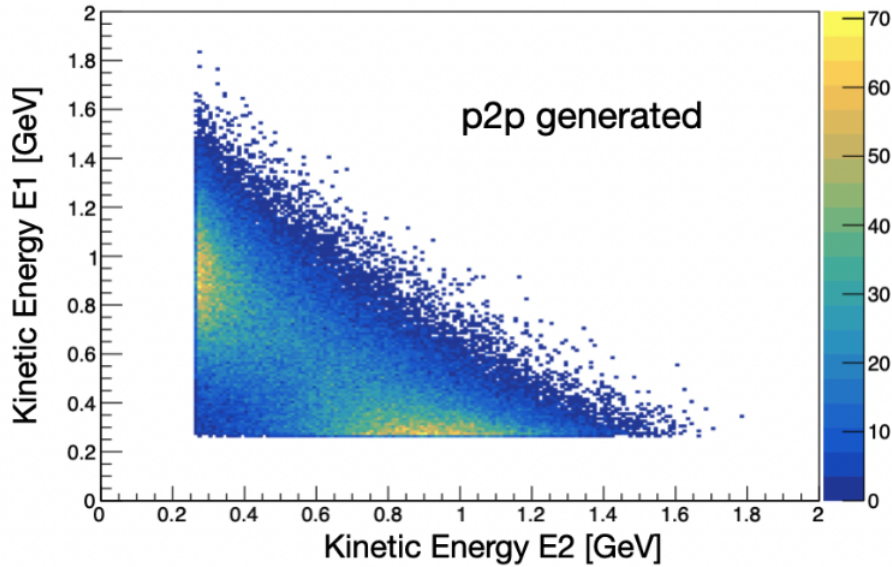


Figure 4.21: Full kinetic energy correlation in generated ( $p,2p$ ) simulation (no detector effects applied).

### Simulation and Reconstruction of Deposited vs. Incident Energy Correlation

In Fig. 4.22, we see the correlation plot between the deposited energy and the incident energy for protons with incident kinetic energies 200-2000 MeV at an incident angle of  $\theta = 30^\circ$ ,  $\phi = 30^\circ$ . The deposited energy rises linearly with the incident energy until the threshold energy of 320 MeV, then falls rapidly as a function of incident energy, as predicted by the Bethe-Bloch formula.

Due to the sensitivity at the tail part in Fig. 4.22, a physical formula has been used to guide our energy reconstruction function. We choose to convert the kinetic energy of the incident proton into  $\beta = v/c$ , apply the Bethe-Bloch relationship, and find the relationship between  $\beta$  and the deposited energy.

During reconstruction, we can infer  $\beta$  from the observed deposited energy and then determine the full kinetic energy of the incident proton. The simplified Bethe-Bloch formula used for the extrapolation is:

$$\frac{dE}{dx} = \frac{A}{\beta^2} + B \frac{\ln \beta}{\beta^2} + C. \quad (4.36)$$

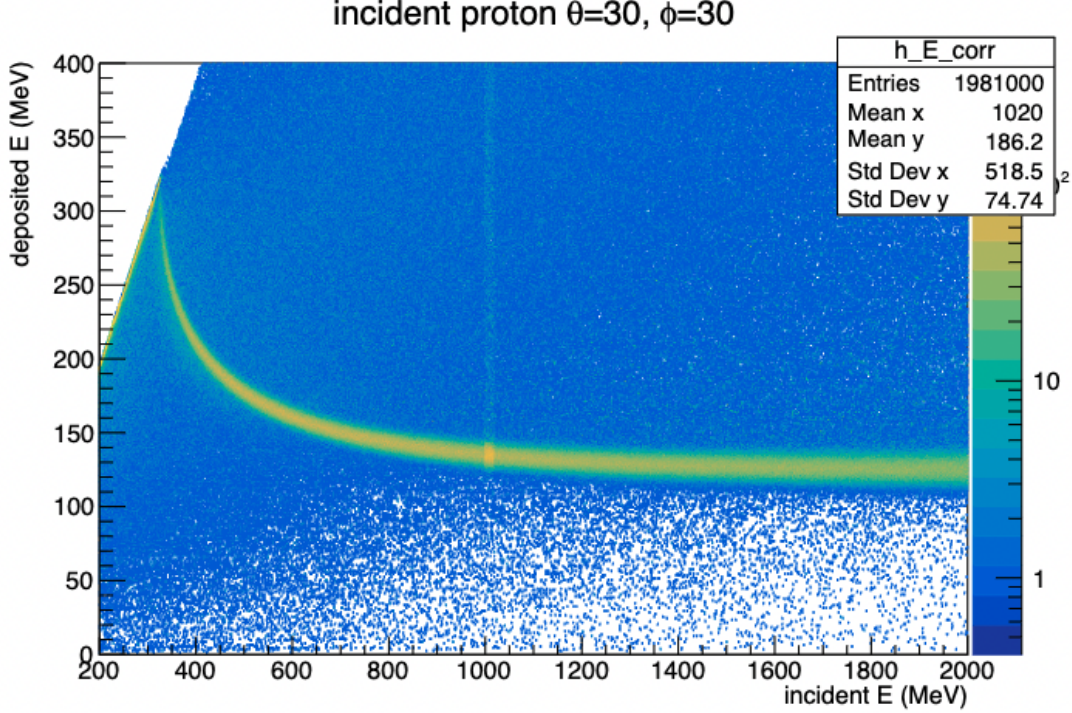


Figure 4.22: Deposited energy [MeV] versus full kinetic energy [MeV] of protons at  $\theta = 30^\circ, \phi = 30^\circ$  in proton simulation.

In the case of stopped protons, the reconstruction of the relevant quantities associated with the protons detected in CALIFA is done using a clustering procedure in R3BRoot, as discussed in the CALIFA clustering part. After the protons PID, the clustering procedure and the energy reconstruction, we have the following information:

- Energy of the cluster.
- PID of the cluster.
- Angles  $\theta$  and  $\phi$  of the two protons.

This clustering is particularly relevant for proton hits, where a larger amount of energy is released compared to  $\gamma$ -rays, making it more likely to trigger multiple crystals. However, it is crucial to distinguish between crystals belonging to proton clusters and those belonging to  $\gamma$ -ray clusters, as both types of particles can emerge from the same QFS reaction.

In our selection criteria for identifying valid  $(p,2p)$  protons, we require the presence of two high-energy clusters in the CALIFA detector. To ensure that these clusters are not derived from boosted  $\gamma$  hits, we set the energy threshold at 80 MeV. Fig. 4.23 illustrates the multiplicity of high-energy clusters observed in the CALIFA detector. To focus on genuine  $(p,2p)$  events, we exclusively select events with a multiplicity of 2 in CALIFA. As shown in the bottom panel, these stringent criteria effectively suppress FSI-based events and mainly select events

with a favorable opening angle, indicative of a well-defined  $(p, 2p)$  reaction.

A significant background to  $(p, 2p)$  events arises from  $(p, pn)$  scattering, where the neutron deposits substantial energy in CALIFA due to nuclear interactions. Unlike charged particles, which deposit energy primarily through electromagnetic interactions, neutron interactions result in energy cascades across a large number of crystals.

Fig. 4.24 shows the sum of the number of crystals for  $^{11}\text{B}$  tagged events (red) and  $^{11}\text{C}$  tagged events (blue), both of which exhibit exactly two high-energy CALIFA clusters. The predominance of low multiplicity sum numbers ( $Sum < 8$ ) for  $(p, 2p)$  scattering in  $^{11}\text{B}$  events is observed when compared to  $(p, pn)$  scattering in  $^{11}\text{C}$  events ( $Sum > 10$ ). Consequently, we implement an additional criterion, selecting events with a crystal number sum less than 5, to enhance the purity of our  $(p, 2p)$  selection.

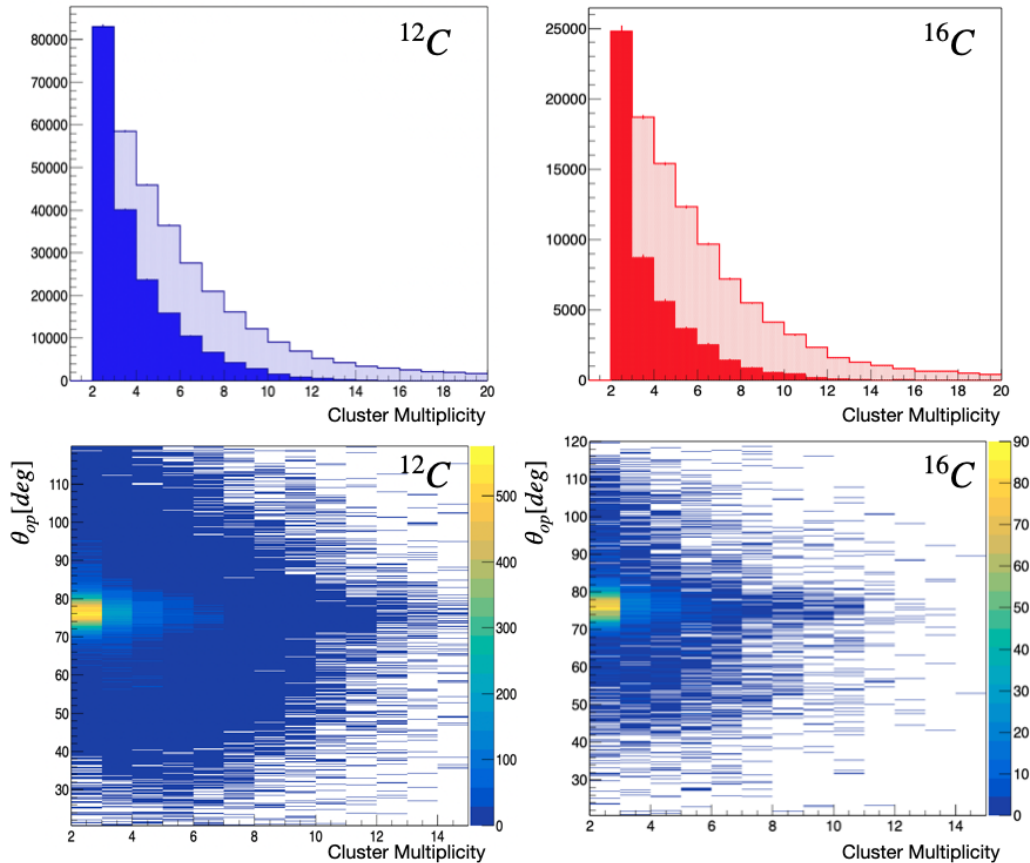


Figure 4.23: Top: Multiplicity of high-energy CALIFA clusters with incoming beam charge selection and outgoing fragment associated with  $(p,2p)$  reactions,  $^{11}\text{B}$  for  $^{12}\text{C}$  beam (left) and  $^{15}\text{B}$  for  $^{16}\text{C}$  beam (right). The more intense blue and red distribution are associated with the selection of the outgoing  $(p,2p)$   $A - 1$  fragment. A good  $(p,2p)$  signal will result in exactly 2 clusters in CALIFA. Bottom: Correlation between the cluster multiplicity and opening angle (angle between the two scattered protons in the  $XZ$  plane) selecting  $^{11}\text{B}$  for  $^{12}\text{C}$  beam (left) and  $^{15}\text{B}$  for  $^{16}\text{C}$  beam (right). The selection of multiplicity of CALIFA selects an opening angle region associated with a good  $(p,2p)$  reaction around  $77^\circ$ .

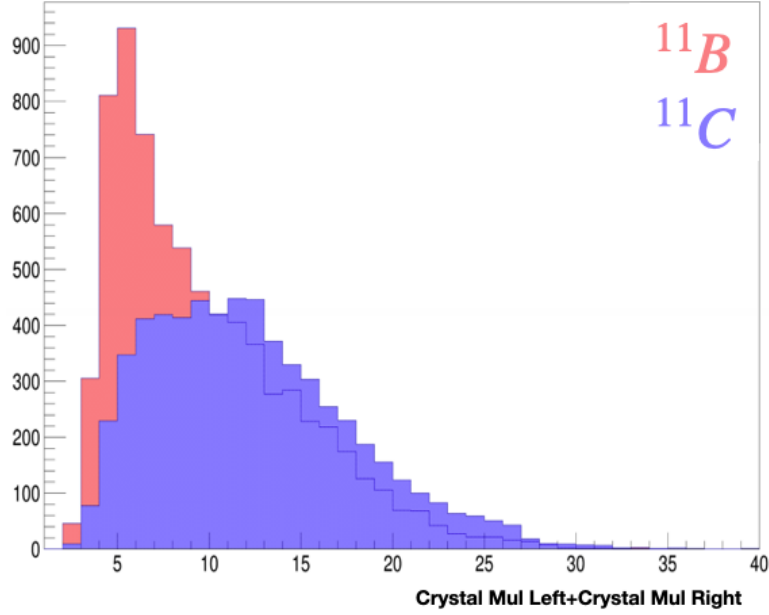


Figure 4.24: Sum of the crystal numbers in the two CALIFA clusters with  $^{11}\text{B}$  tagging (red) and with  $^{11}\text{C}$  tagging (blue).

### 4.3.3 Protons momentum and angular distribution

After describing the protons PID, clustering and energy reconstruction, we can derive the momentum of the two scattered protons. Due to the pronounced axial symmetry of the QFS reaction, it is convenient to represent laboratory measurements using the spherical coordinate system, where the inclination  $\theta$  (or polar angle) of a particle is defined with respect to the beam (Z-axis):  $\theta \in [0, \pi]$ , and the azimuth angle  $\phi \in [0, 2\pi]$  is defined relative to the X-axis as shown in Fig. 4.25. To find the momentum of a proton given its energy  $E$  and angles  $\theta$  and  $\phi$ , we start with the relativistic energy-momentum relation:

$$E^2 = p^2 c^2 + m^2 c^4. \quad (4.37)$$

Solving for the momentum  $p$ , we get:

$$p = \sqrt{\frac{E^2}{c^2} - m^2 c^2}. \quad (4.38)$$

Here,  $c$  is the speed of light, and  $m$  is the rest mass of the proton (approximately  $938 \text{ MeV}c^2$ ). Once we have the magnitude of the momentum  $p$ , we can decompose it into its components using the angles  $\theta$  and  $\phi$ : -  $\theta$  is the polar angle (angle from the  $z$ -axis), -  $\phi$  is the azimuthal angle (angle from the  $x$ -axis in the  $x - y$  plane)

The components of the momentum  $\vec{p}$  are:

$$p_x = p \sin \theta \cos \phi. \quad (4.39)$$

$$p_y = p \sin \theta \sin \phi. \quad (4.40)$$

$$p_z = p \cos \theta. \quad (4.41)$$

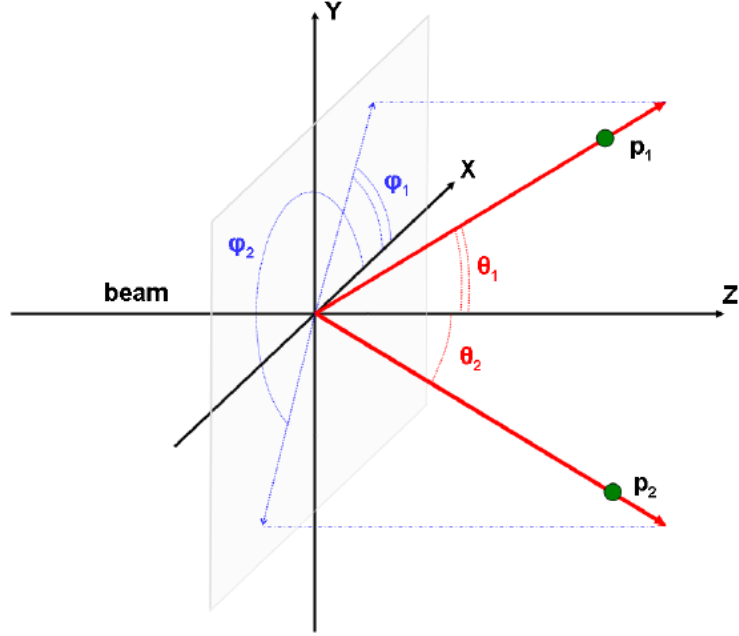


Figure 4.25: The measured laboratory angles of an outgoing proton pair from the  $(p, 2p)$  reaction. A spherical coordinate system is chosen such that the polar direction is associated with the beam axis Z.

So the momentum vector  $\vec{p}$  in terms of  $E$ ,  $\theta$ , and  $\phi$  is:

$$\vec{p} = (p \sin \theta \cos \phi, p \sin \theta \sin \phi, p \cos \theta); \quad (4.42)$$

where  $p$  is calculated from the energy  $E$  using the earlier equation:

$$p = \sqrt{\frac{E^2}{c^2} - m^2 c^2}. \quad (4.43)$$

If we consider units where  $c = 1$  (common in particle physics):

$$p = \sqrt{E^2 - m^2}. \quad (4.44)$$

Thus, the final components are:

$$p_x = \sqrt{E^2 - m^2} \sin \theta \cos \phi. \quad (4.45)$$

$$p_y = \sqrt{E^2 - m^2} \sin \theta \sin \phi. \quad (4.46)$$

$$p_z = \sqrt{E^2 - m^2} \cos \theta. \quad (4.47)$$

Fig. 4.26 and Fig. 4.27 show the  $\theta$  angular correlations and the  $\phi$  angular correlations of the detected protons for  $^{12}\text{C}$  and  $^{16}\text{C}$  beams, both with (right plots) and without (left plots)  $(p,2p)$  fragment selection for  $^{11}\text{B}$  and  $^{15}\text{B}$ , respectively. The significant impact of gating on the proper outgoing fragment is immediately apparent. This selection cleans the  $\theta$  and  $\phi$  correlations, allowing the QFS  $(p,2p)$  kinematical region to emerge clearly from the background.

From the scalar product of two vectors  $\mathbf{p}_1(\theta_1, \phi_1)$  and  $\mathbf{p}_2(\theta_2, \phi_2)$  in the spherical system, one can derive the following expression for the opening angle  $\theta_{\text{op}}$  between the vectors:

$$\theta_{\text{op}} = \sin \theta_1 \sin \theta_2 \cos(\phi_2 - \phi_1) + \cos \theta_1 \cos \theta_2. \quad (4.48)$$

In Fig. 4.28, the opening angle of the protons is shown under different conditions to select proper QFS (quasi-free scattering) protons for  $^{12}\text{C}$  and  $^{16}\text{C}$ . Without any selection on the CALIFA cluster multiplicity and the number of crystals in each cluster, we observe a very wide opening angle distribution (black curve for both  $^{12}\text{C}$  and  $^{16}\text{C}$ ) with a considerable number of events at low  $\theta_{\text{Op}}$  due to inelastic (IE) processes and final-state interactions (FSI). By selecting only two clusters in CALIFA (one cluster on each side of CALIFA) and limiting the number of crystals per cluster to fewer than five, we observe a clear reduction in events at low  $\theta_{\text{Op}}$ . This reduction indicates that such selection helps remove processes that contaminate our QFS proton selection (green distribution for  $^{12}\text{C}$  and purple for  $^{16}\text{C}$ ).

Furthermore, by imposing an additional condition on the outgoing fragment (selecting  $^{11}\text{B}$  for  $^{12}\text{C}$  and  $^{15}\text{B}$  for  $^{16}\text{C}$ ) and requiring only 2 clusters in CALIFA, we observe that the  $\theta_{\text{Op}}$  distribution peaks sharply at the expected value, with FSI and IE processes significantly suppressed (blue distribution for  $^{12}\text{C}$  and red for  $^{16}\text{C}$ ). The opening angle peak is centered around  $79^\circ$ , in agreement with the mean-field simulation for  $(p,2p)$  reactions as discussed in the section. Moreover, to identify a hard break-up reaction and ensure an accurate energy reconstruction, we select high transfer energy processes with a condition on the Mandelstam variable  $|t|, |u| > 0.8 \text{ GeV}^2$ . In principle, with ideal resolution, a value of  $|u|, |t| > 0.6 \text{ GeV}^2$  would be sufficient to ensure high-momentum transfer. However, due to the limited resolution in energy and angle from the CALIFA calorimeter used to reconstruct the angle of the  $(p, 2p)$  scattered protons, we adopt a higher threshold to ensure that high-momentum transfer processes are accurately captured.

In the following section, we will discuss in more detail the selection of the QFS process using fragment information. Additionally, we will explore kinematic quantities that help distinguish the quasi-elastic part of the reaction from FSI and IE backgrounds, which need to be suppressed for the proper selection of SRC physics.

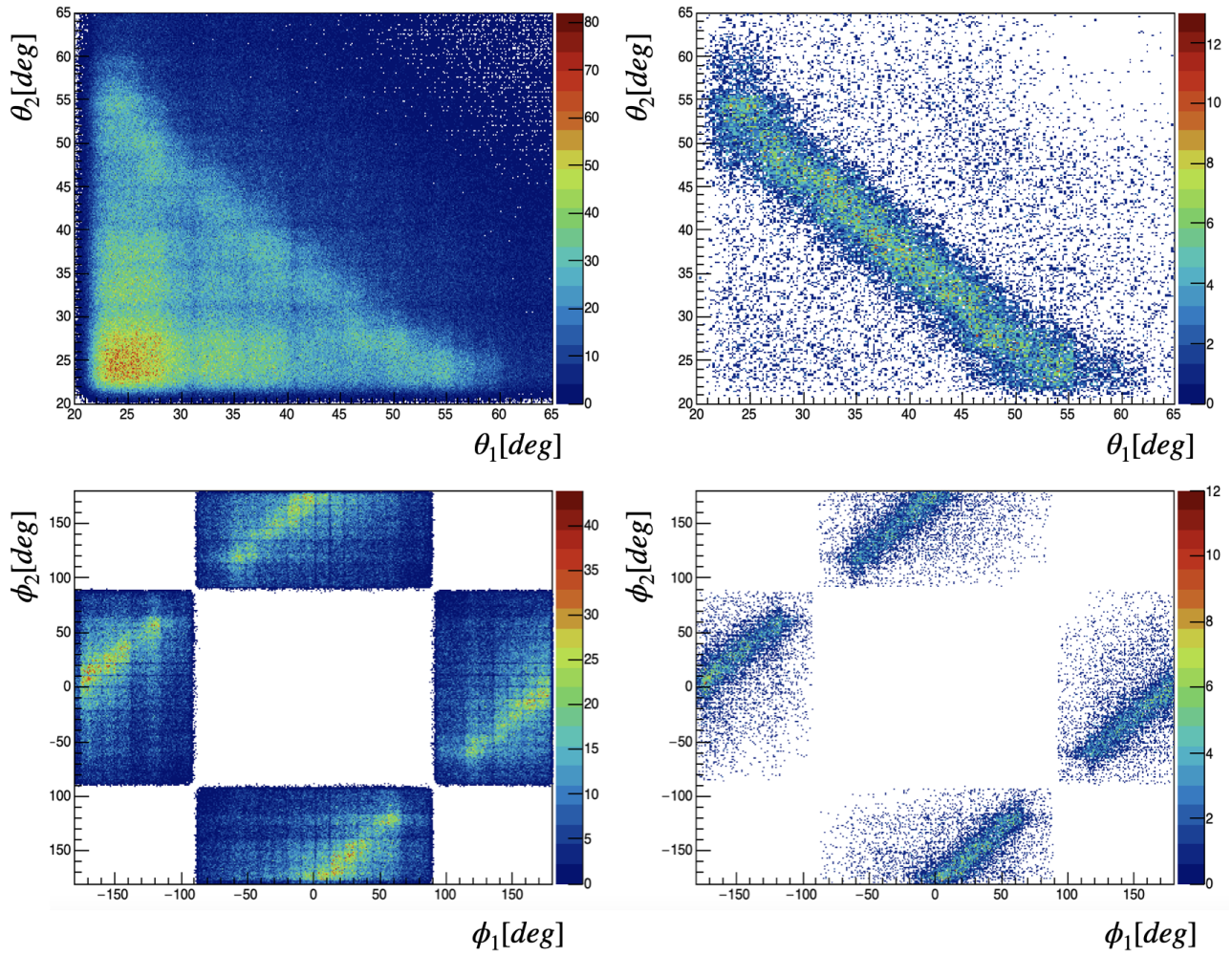


Figure 4.26: Left:  $\theta$  and  $\phi$  correlation  $^{12}\text{C}$  data without  $(p,2p)$  selection. Right:  $\theta$  and  $\phi$  correlation with  $(p,2p)$  and  $^{11}\text{B}$  selection.

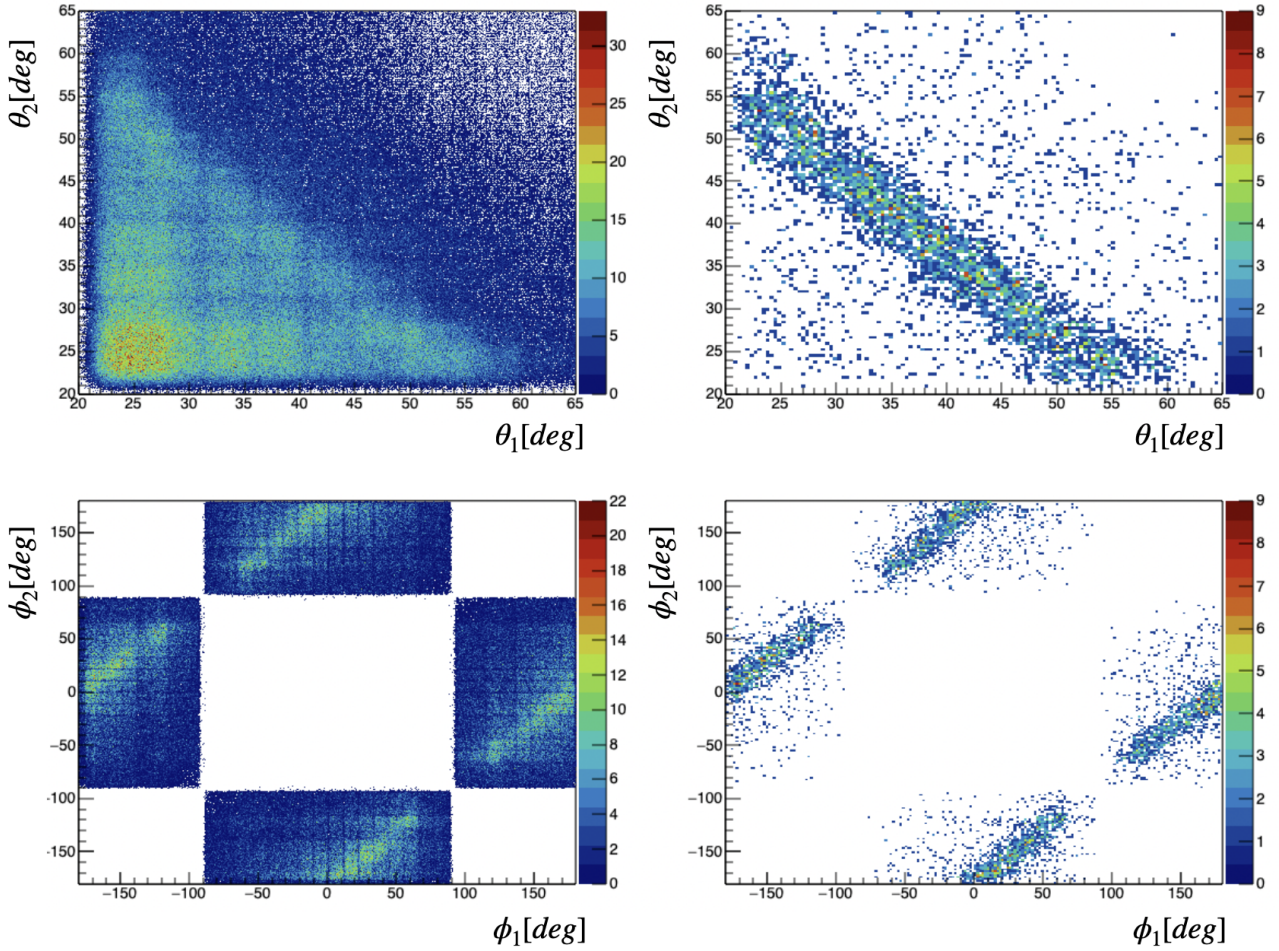


Figure 4.27: Left:  $\theta$  and  $\phi$  correlation  $^{16}\text{C}$  data without  $(p,2p)$  selection. Right:  $\theta$  and  $\phi$  correlation with  $(p,2p)$  and  $^{15}\text{B}$  selection.

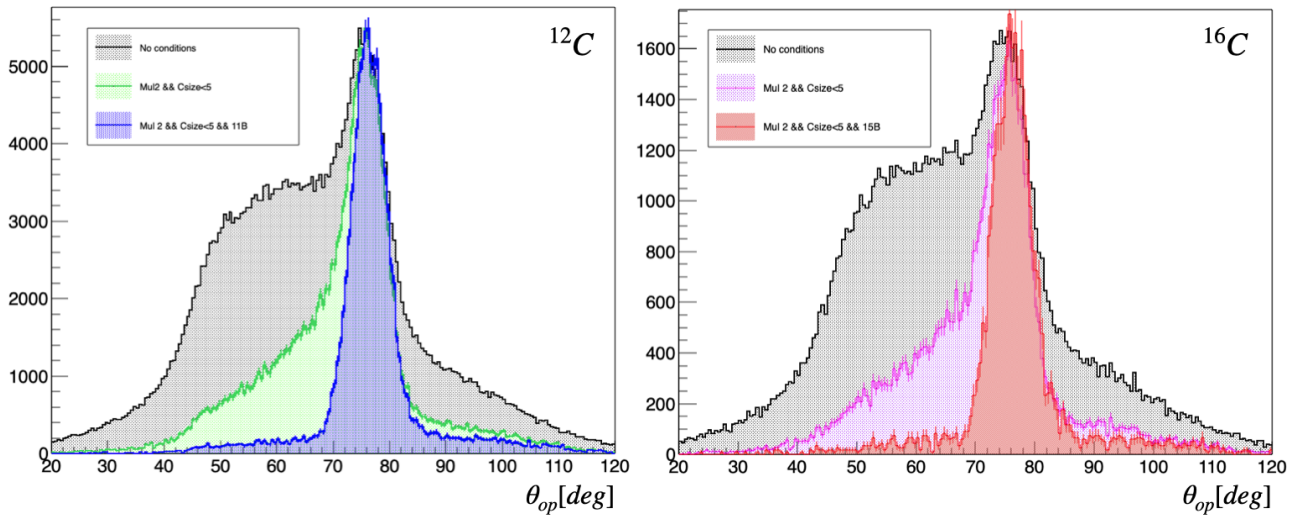


Figure 4.28: In gray inclusive opening angle of the  $(p,2p)$  without selection on the  $^{11}\text{B}$  fragment (left) and  $^{15}\text{B}$  fragment (right). In green, the exclusive opening angle is shown with the selection on the  $^{11}\text{B}$  fragment (left) and in pink on the right panel for the  $^{15}\text{B}$  fragment. It is possible to observe the effect of gating on the  $^{11/15}\text{B}$  fragment and only 2 clusters in CALIFA (blue and red distribution). The region at a smaller opening angle associated with FSI and IE component of the reaction is suppressed gating on the fragment.

#### 4.3.4 $^{12/16}\text{C}(p,2p)\text{A}-1$ QFS selection

We identify exclusive  $^{12}\text{C}(p,2p)^{11}\text{B}$  and  $^{16}\text{C}(p,2p)^{15}\text{B}$  events by requiring the detection of a  $^{11}\text{B}/^{15}\text{B}$  fragment in coincidence with two scattered protons at large laboratory angle in CALIFA detector. In this section, simulations are essential to suppress the FSI-based background and remove the IE component of the reaction. We will also show the strong effect of suppressing FSI by selecting the  $A - 1$  fragment. Energy and momentum conservation for this reaction gives:

$$\vec{p}_{12/16\text{C}} + \vec{p}_{\text{tg}} = \vec{p}_1 + \vec{p}_2 + \vec{p}_{11/15\text{B}}; \quad (4.49)$$

where  $\vec{p}_{12/16\text{C}} = (p_{12/16\text{C}}^2 + m_{12/16\text{C}}^2)^{1/2}, 0, 0, p_{12/16\text{C}}$  and  $\vec{p}_{\text{tg}} = (m_p, 0, 0, 0)$  are respectively the incident beam-ion and target proton four-momentum vectors.  $\vec{p}_1$ ,  $\vec{p}_2$ , and  $\vec{p}_{11/15\text{B}}$  are the four-momentum vectors of the detected protons and  $^{11/15}\text{B}$  fragment, respectively. Assuming QE scattering off a nucleon which is moving in a mean-field potential, we can approximate  $\vec{p}_{12/16\text{C}} = \vec{p}_i + \vec{p}_{11/15\text{B}}$ , where  $\vec{p}_i$  is the initial proton four-momentum inside the  $^{12/16}\text{C}$  nucleus. Substituting into the previous equation, we obtain:

$$\vec{p}_i = \vec{p}_{\text{miss}} = \vec{p}_1 + \vec{p}_2 - \vec{p}_{\text{tg}}; \quad (4.50)$$

where  $\vec{p}_{\text{miss}}$  is the measured missing four-momentum of the reaction and is only equal to  $\vec{p}_i$  in the case of unperturbed (no ISI/FSI) QE scattering. Through the text, the missing momentum vector is shown and discussed after being boosted from the lab-frame to the incident  $^{12/16}\text{C}$  ion rest-frame.

$M_{\text{miss}}^2$  is an important quantity to suppress FSI. Fig. 4.29 shows the distribution of the reaction missing mass for both  $^{12}\text{C}$  (left plot) and  $^{16}\text{C}$  incoming beam (right plot) without and with the selection of the  $A - 1$  fragment.

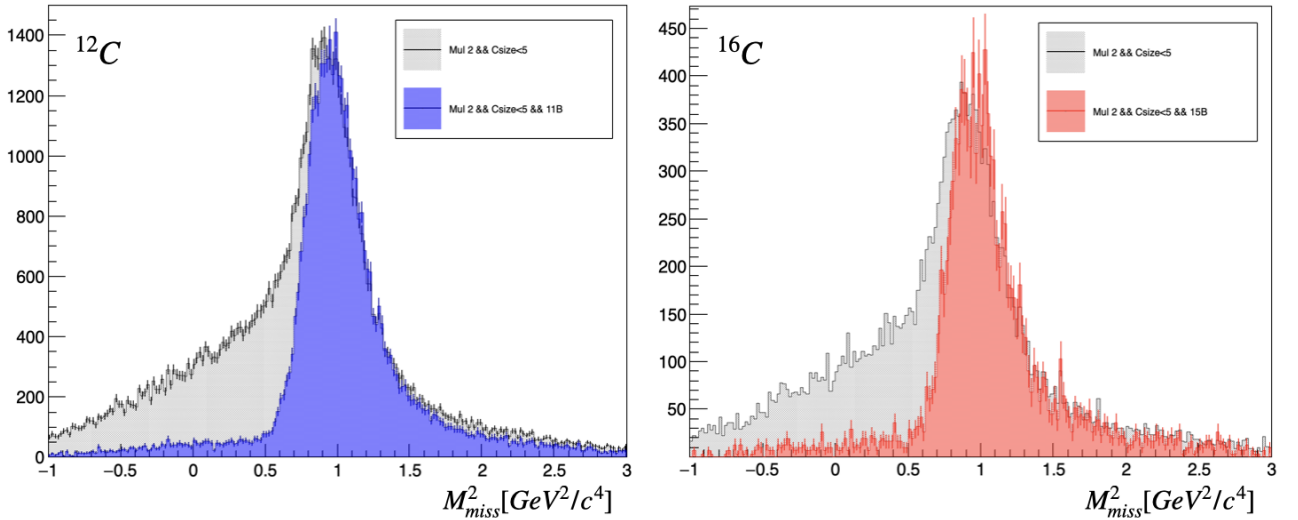


Figure 4.29: In the left plot in grey, the inclusive missing mass of the (p,2p) without selection on the  $^{11}\text{B}$  fragment. The exclusive missing mass is shown in blue with the selection on the  $^{11}\text{B}$  fragment. Also, here, it is possible to observe the effect of gating on the  $^{11}\text{B}$  fragment. The region at smaller missing mass, associated with FSI and IE component of the reaction, is suppressed gating on the fragment. In the right plot, we can observe a similar situation for  $^{16}\text{C}$  beam without and with  $^{15}\text{B}$  selection.

We can use INCL (to simulate IE/FSI processes) simulation to study the  $M_{miss}^2$  region populated in particular by IE+FSI. Looking at Fig. 4.30, the distribution of the  $M_{miss}^2$  for IE/FSI events populate the region below  $0.5 \text{ GeV}^2/c^4$  (left plot). In the right plot, the correlation with the missing momentum is displayed.

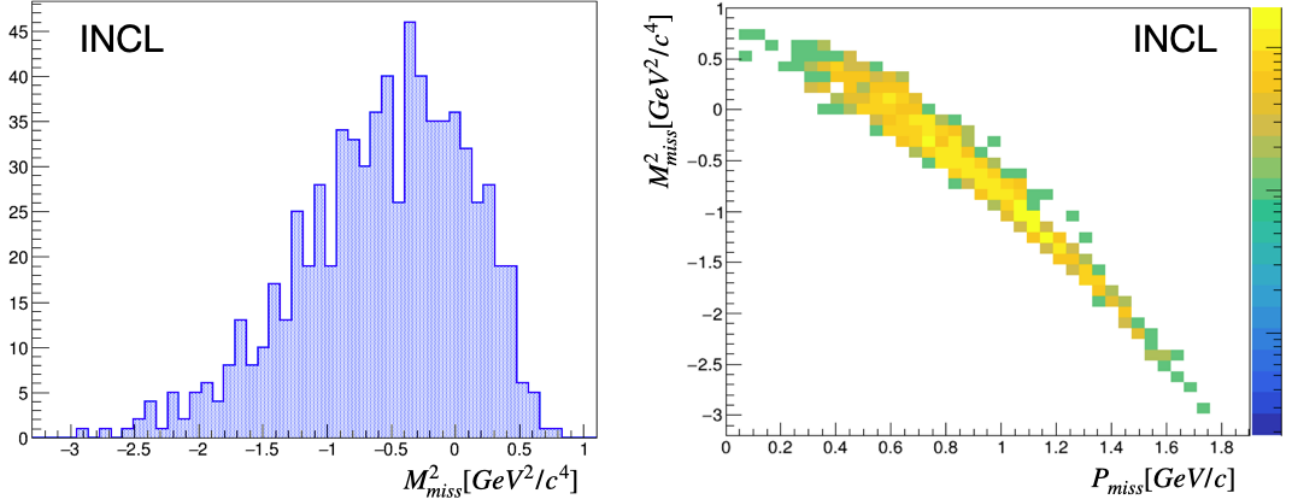


Figure 4.30: Distribution of the  $M_{miss}^2$  for IE/FSI events that populate the region below  $0.5 \text{ GeV}^2/c^4$  (left plot). In the right plot, the correlation with the missing momentum is displayed.

Fig. 4.31 and fig. 4.32 show the measured missing mass squared  $M_{miss}^2$  and missing energy  $E_{miss} = m_N - E_{miss}$  (where  $E_{miss}$  is the energy component of  $\vec{p}_{miss}$  in the  $^{12/16}\text{C}$  rest-frame and  $m_N$  is the proton mass) correlation with the missing momentum  $p_{miss}$ , for inclusive  $^{12/16}\text{C}(p, 2p)$  (left panels) and exclusive  $^{12/16}\text{C}(p, 2p)^{11/15}\text{B}$  (right panels) events. Both distributions present a part at low missing energy and large in-plane opening angles (top panels) that correspond to QE scattering and high missing energy and a tail at small in-plane opening angles that correspond to IE scattering. Both IE and QE regions are surrounded by FSI events. Thanks to the fragment selection, the IE tail associated with IE events is suppressed, and the QE region, at large  $\theta_{Op}$  and small  $E_{miss}$  ( $-0.4 \text{ GeV} < E_{miss} < 0.4 \text{ GeV}$ ), emerges from the FSI background.

Fig. 4.31 and fig. 4.32 (central panels) show also the measured missing momentum distribution and its correlation with the missing mass  $M_{miss}^2$  for inclusive  $^{12/16}\text{C}(p, 2p)$  (left panels) and exclusive  $^{12/16}\text{C}(p, 2p)^{11/15}\text{B}$  (right panels) events. We associate the region at  $M_{miss}^2 > 0.5 \text{ GeV}^2/c^4$  and  $M_{miss}^2 < 1.3 \text{ GeV}^2/c^4$  with QE reactions and a region with  $M_{miss}^2 < 0.5 \text{ GeV}^2/c^4$  associated with IE component of the reactions. The effect of the  $A - 1$  fragment selection in suppressing FSI is clear.

The bottom panels show the measured missing momentum distribution and its correlation with the missing mass  $E_{miss}$  for inclusive  $^{12/16}\text{C}(p, 2p)$  (left panels) and exclusive  $^{12/16}\text{C}(p, 2p)^{11/15}\text{B}$  (right panels) events. Low missing momentum and small missing energy are associated with clear  $^{12/16}\text{C}(p, 2p)^{11/15}\text{B}$  reactions. The inclusive  $^{12/16}\text{C}(p, 2p)$  events are contaminated by FSI backgrounds all around, covering both IE and QE regions. This background is not evident in the  $^{12/16}\text{C}(p, 2p)^{11/15}\text{B}$  case, which is our first indication that requiring the coincidence detection of  $^{11/15}\text{B}$  fragments selects a unique subset of one-step processes where a single nucleon was knocked-out without any further interaction with the residual fragment.

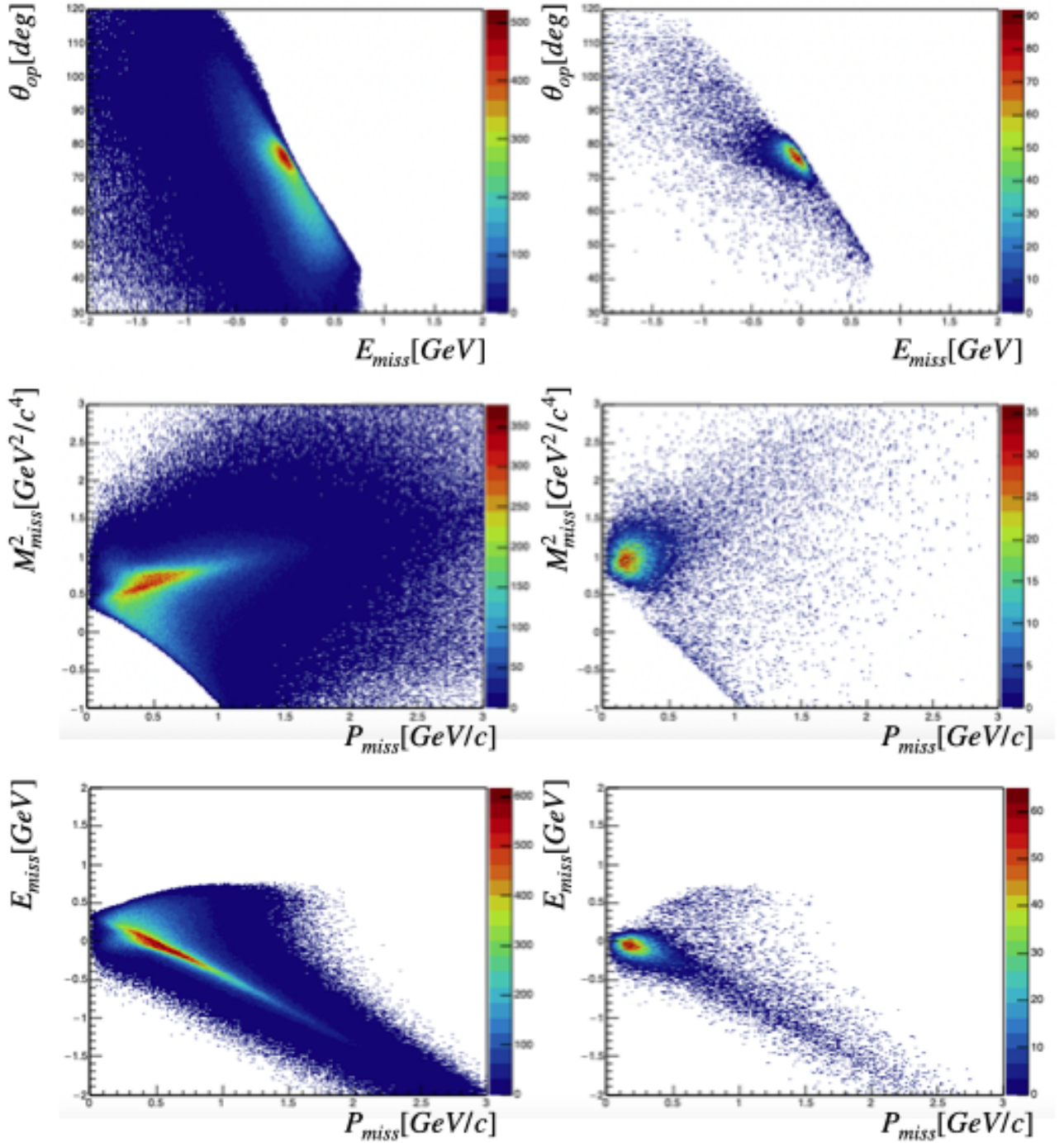


Figure 4.31: The correlation between the measured missing energy ( $E_{\text{miss}}$ , calculated in the  $^{12}\text{C}$  rest-frame) and the measured lab-frame two-proton in-plane opening angle ( $\theta_1 + \theta_2$ ). Distributions are shown for inclusive  $^{12}\text{C}(p,2p)$  events (left) and exclusive  $^{12}\text{C}(p,2p)^{11}\text{B}$  events (right). QE events are seen as a peak around low missing energy and opening angles of  $\approx 79^\circ$ . IE reactions populate higher missing energy and lower opening angles, while ISI/FSI populate both regions and the ridge between them in the inclusive spectra. The bottom left figure shows the inclusive  $^{12}\text{C}(p,2p)$  channel, and the bottom right figure the exclusive channel, i.e., with tagging  $^{11}\text{B}$  of the correlation between missing mass squared ( $y$ -axis) and missing momentum ( $x$ -axis). In both cases, the quasi-elastic peak (QE) and inelastic (IE) events are visible, while ISI/FSI are reduced by fragment tagging.

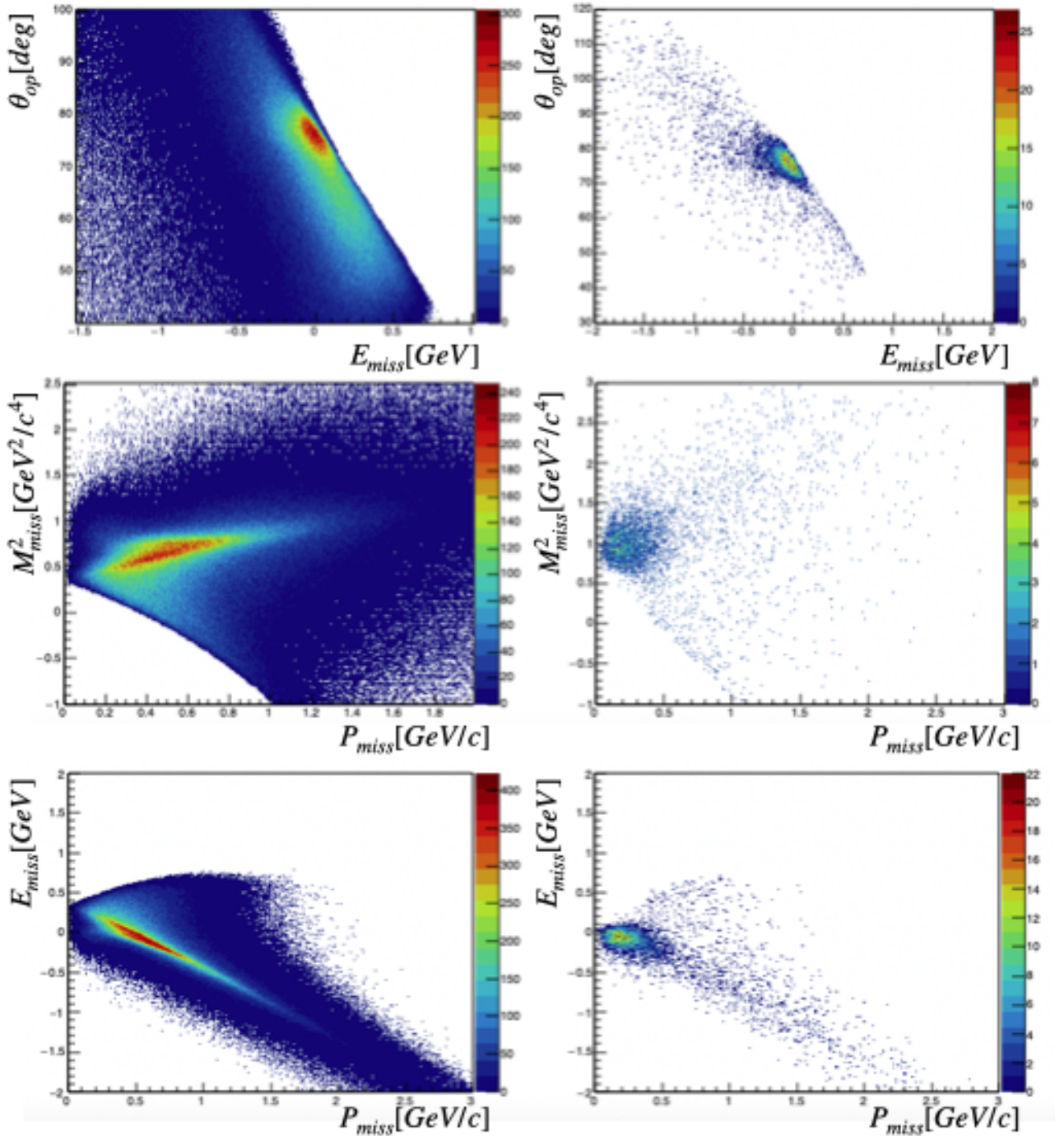


Figure 4.32: The correlation between the measured missing energy ( $E_{\text{miss}}$ , calculated in the  $^{16}\text{C}$  rest-frame) and the measured lab-frame two-proton in-plane opening angle ( $\theta_1 + \theta_2$ ). Distributions are shown for inclusive  $^{16}\text{C}(p,2p)$  events (left) and exclusive  $^{16}\text{C}(p,2p)^{15}\text{B}$  events (right). QE events are seen as a peak around low missing energy and opening angles of  $\approx 79^\circ$ . IE reactions populate higher missing energy and lower opening angles, while FSI populates both regions and the ridge between them in the inclusive spectra. The left figure shows the inclusive  $^{16}\text{C}(p,2p)$  channel, and the right figure the exclusive channel, i.e., with tagging  $^{15}\text{B}$  of the correlation between missing mass squared ( $y$ -axis) and missing momentum ( $x$ -axis). In both cases, the quasi-elastic peak (QE) and inelastic (IE) events are visible, while FSIs are reduced by fragment tagging.

In summary, the criteria to identify and select the QF component of the reaction and to suppress IE/FSI background are:

- Select events with two clusters with  $E_{proton} > 100 \text{ MeV}$ , of cluster type 0 (i.e., the initial hit crystal is a proton-ranged crystal). 100 MeV is considered a reasonable proton energy threshold (to exclude high energy  $\gamma$ 's) and valid to perform a good energy reconstruction.
- Sum of the number of crystals of the two proton clusters is lower than 10 ( $S_{cluster} < 10$ ).
- Select events with multiplicity 1 in the LOS detector and good charge  $Z_{LOS}$  in LOS to ensure no pile up events.
- $|\Delta\phi - 180^\circ| < 30^\circ$ . Fig. 4.33 shows the data-simulation comparison that justifies this co-planar condition.
- Fig. 4.33 shows that at 1.25 GeV/u, the expected opening angle between two scattered protons is  $79^\circ$ . Fig. 4.28 shows that for a ( $p,2p$ ) reaction with the  $A-1$  fragment selection, the experimental opening angle peak is sharp and clean, allowing us to use it to select QE events:  $68^\circ < \theta_{Opa} < 86^\circ$ ;
- A missing mass selection of  $M_{miss}^2 > 0.5 \text{ GeV}^2/c^4$  and  $M_{miss}^2 < 1.3 \text{ GeV}^2/c^4$ ;
- Select small missing energy small  $E_{miss}$  ( $-0.3 \text{ GeV} < E_{miss} < 0.3 \text{ GeV}$ ).

The QE selection was done using the missing-mass, missing-energy and in-plane opening-angle cuts depicted in Fig. 4.31 and Fig. 4.32 ( $M_{miss}^2 > 0.5 \text{ GeV}^2/c^4$  and  $M_{miss}^2 < 1.3 \text{ GeV}^2/c^4$ ,  $-0.3 \text{ GeV} < E_{miss} < 0.3 \text{ GeV}$ ,  $68^\circ < \theta_{Opa} < 86^\circ$ ). In Fig. 4.33, the comparison of the opening angle distribution and the  $\Delta\phi$  angle, obtained after QFS selection, with the QFS simulation is displayed. The comparison shows a good agreement between the two distributions when we select the  $A-1$  fragment. Fig. 4.34 shows further evidence for FSI suppression by comparing the measured missing-momentum distribution for  $^{12/16}\text{C}(p,2p)$  QE events with and without  $^{11/15}\text{B}$  tagging. The measured  $^{12/16}\text{C}(p, 2p)$  QE events show a significant high-momentum tail that extends well beyond the nuclear Fermi-momentum ( $\sim 250 \text{ MeV}/c$ ) and is characteristic of FSI. This tail is completely suppressed by the  $^{11/15}\text{B}$  detection. Indeed proton momentum distribution after  $^{12/16}\text{C}(p,2p)$  reaction is not expected to display a high momentum tail. Therefore, the high-momentum tail observed in this channel is more likely due to Final-State Interactions, which modify the momentum of the emitted particles, producing a high-momentum component. We demonstrated that selecting specific nuclear fragments can reduce this tail, indicating a partial suppression of FSI effects.

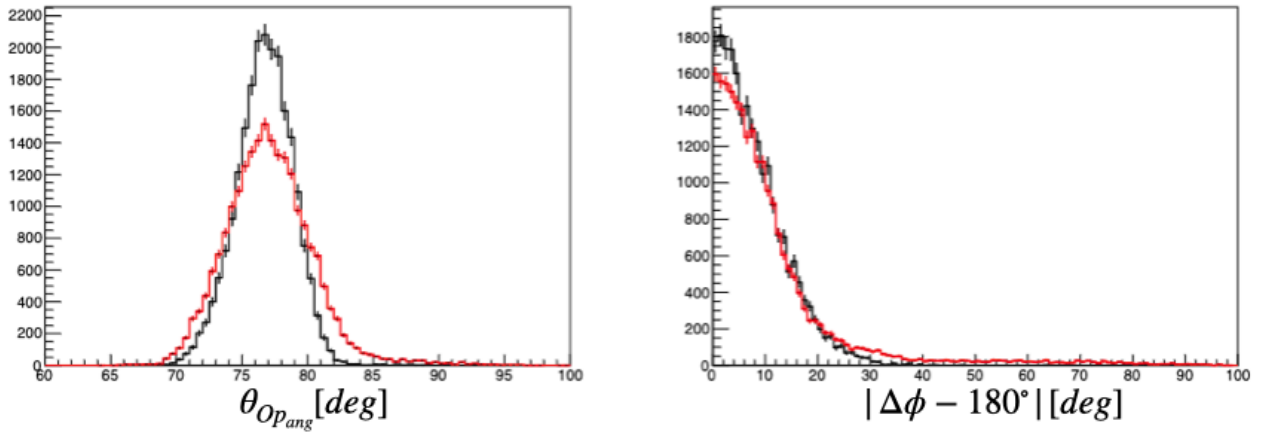


Figure 4.33: Opening angle (left) and  $\Delta\phi$  (right) comparison between data (red) and simulation (black) for  $^{11}\text{B}$  tagged events.

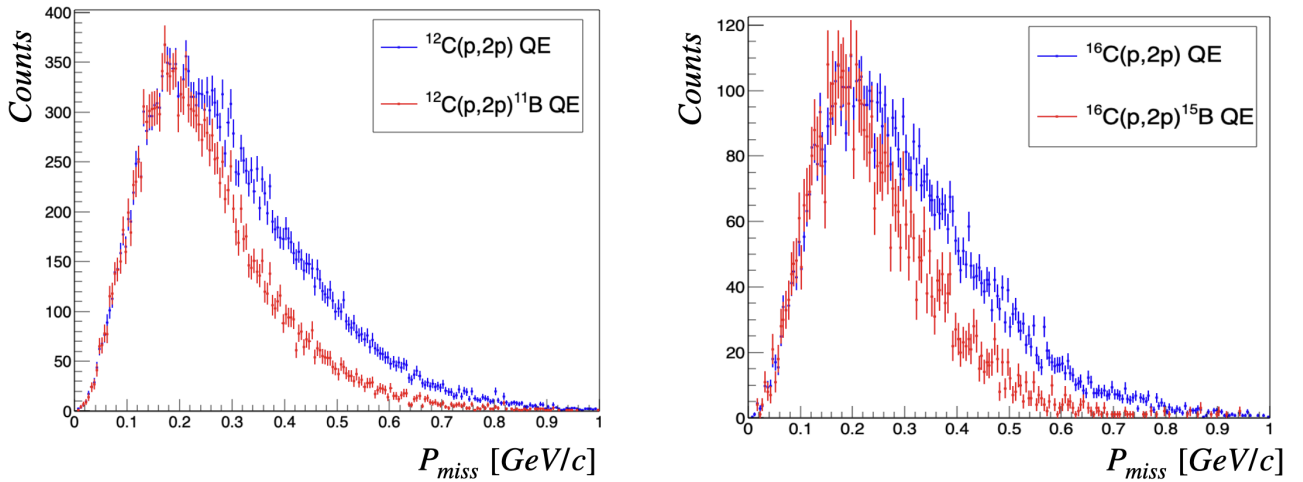


Figure 4.34: Missing-momentum distribution in  $^{12}\text{C}$  rest frame for QE  $^{12/16}\text{C}(p,2p)$  and  $^{12/16}\text{C}(p,2p)^{11/15}\text{B}$  events.

To test the validity of the QFS kinematical conditions, an analysis was conducted on the  $^{12/16}\text{C}(p,2p)A-1$  reaction properties. As illustrated in Fig. 4.35, we implemented a coplanarity condition test. This method examines two reaction planes: the spectator plane, defined by the momenta of the incoming particles ( $p_{beam}$  and  $p_{A-1}$ ), and the scattering plane, defined by the momenta of the outgoing scattered protons ( $p_1$  and  $p_2$ ). To quantify the validity of QFS

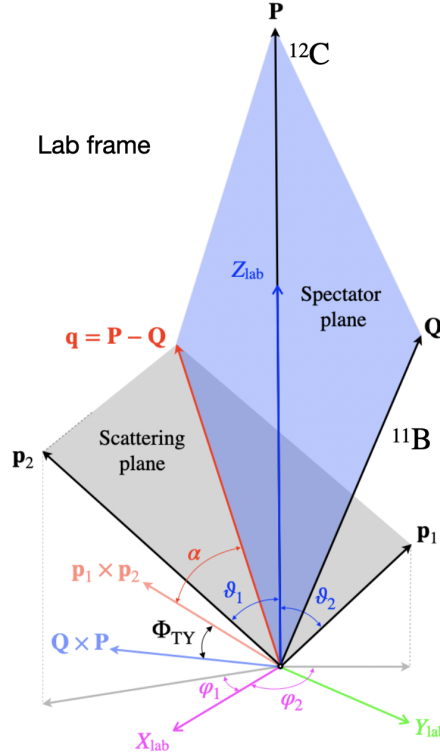


Figure 4.35: Schematic representation of the coplanar test between the normal vector to the scattering plane (given by  $p_1 \times p_2$ ) and the missing momentum  $q = P - Q$  vector.

selection, we defined a method to check the coplanarity of the normal vector to the scattering plane and the missing momentum vector (see Fig. 4.35). We first define the momentum vector normal to the scattering plane as:

$$\vec{n}_1 = \vec{p}_1 \times \vec{p}_2. \quad (4.51)$$

For the spectator plane, we define the missing momentum vector coplanar to the spectator plane as:

$$\vec{n}_2 = \vec{p}_{beam} - \vec{p}_{A-1}. \quad (4.52)$$

The coplanar angle  $\alpha$  is the angle between these two vectors,  $\vec{n}_1$  and  $\vec{n}_2$ , and is given by:

$$\cos \alpha = \frac{\vec{n}_1 \cdot \vec{n}_2}{|\vec{n}_1| |\vec{n}_2|}. \quad (4.53)$$

For QFS reactions, the vectors  $\vec{n}_1$  and  $\vec{n}_2$  are expected to be coplanar, which implies that  $\cos \alpha = 0$ . Therefore,  $\alpha$  can be calculated as:

$$\alpha = \arccos \left( \frac{\vec{n}_1 \cdot \vec{n}_2}{|\vec{n}_1| |\vec{n}_2|} \right). \quad (4.54)$$

In practice, for QFS reactions, we expect  $\alpha$  to be centered around  $90^\circ$ . Fig. 4.36 shows the distribution of the  $\alpha$  coplanar angle for  $^{12/16}\text{C}$  incoming beams before and after applying the QFS kinematical selection described previously. The data reveal that  $\alpha$  after the QFS conditions is sharply centered around  $90^\circ$  for both incoming beams, indicating that the kinematical cuts are

effectively selecting the QFS component of the reaction.

In true unperturbed single-step  $^{12/12}\text{C}(p, 2p)^{11/15}\text{B}$  quasi-elastic scattering, the measured missing momentum (equal to the initial momentum of the proton probed for unperturbed system) and fragment momentum should balance each other. Fig. 4.37 shows the distribution of the cosine of the opening angle between the missing momentum and the fragment momentum,  $\cos(\theta_{p_i, p_{11/15}\text{B}})$ . Although the distribution is broadened due to detector resolutions, a clear back-to-back correlation is observed, which is a distinct signature of QE reactions.

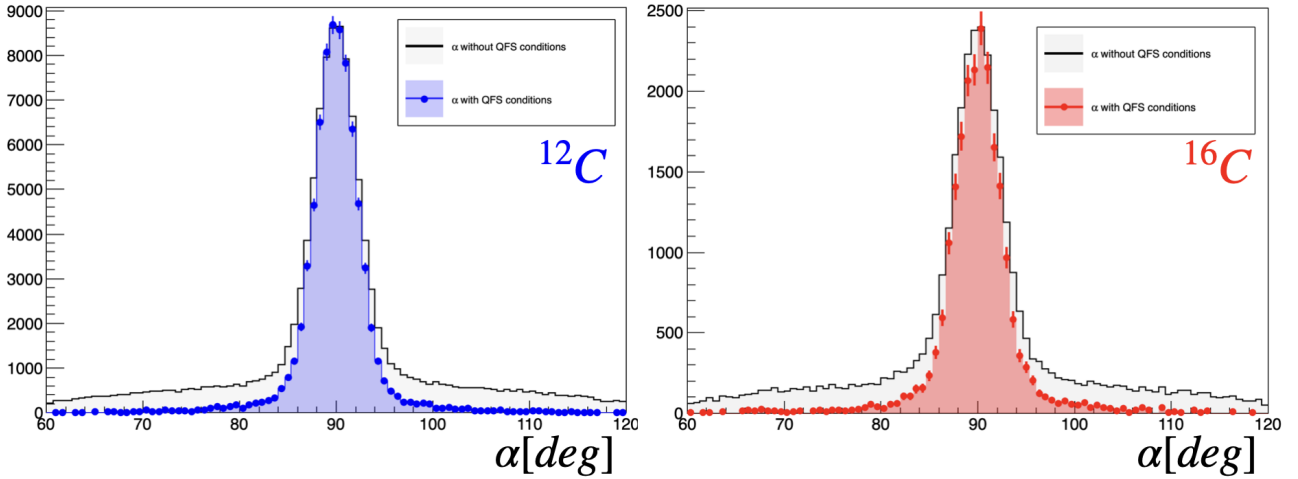


Figure 4.36: Distribution of the  $\alpha$  coplanar angle for  $^{12/16}\text{C}$  incoming beams before (grey) and after (blue and red) applying the QFS kinematical selection described previously.

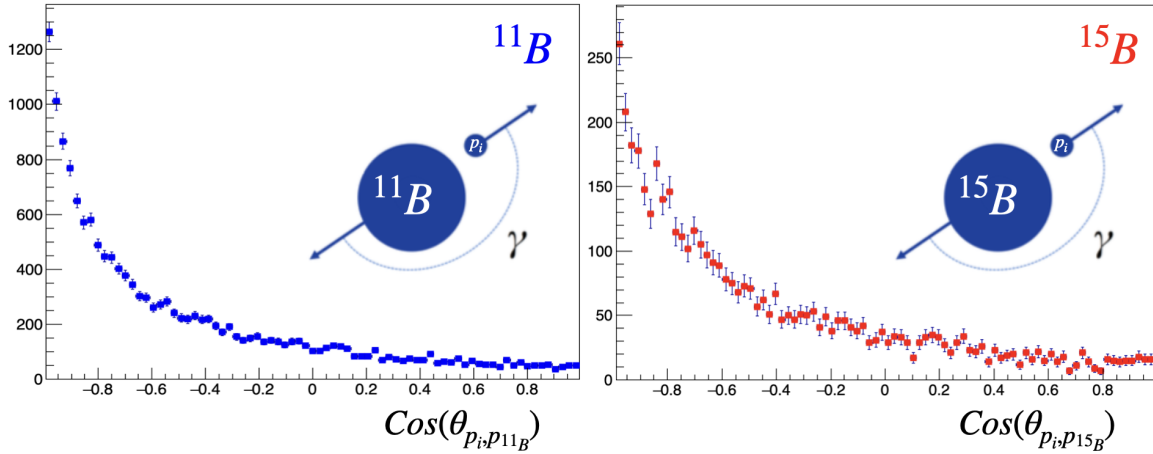


Figure 4.37: Cosine of the opening angle between the missing- and fragment-momenta. While broadened due to detector resolutions, a clear back-to-back correlation is observed.

Before identifying SRC events in the  $^{12/16}\text{C}(p, 2p)\text{A} - 2$  reaction channels, I will first present some quantitative results for the  $^{12/16}\text{C}(p, 2pX)$  ratios for  $^{11/15}\text{B}$ ,  $^{10/14}\text{B}$ , and  $^{10/14}\text{Be}$ . To accurately extract the fraction of ( $p, 2p$ ) events with a detected fragment, several corrections must be applied. Specifically, for  $^{10/14}\text{Be}$ , correction factors of 2% and 56% are required due to limitations with the TOFD acceptance. The measured ratios are derived from the number of quasi-elastic (QE) events for each sample. Additionally, we have applied a cut on low missing momentum,  $p_{\text{miss}} < 250 \text{ MeV}/c$ , along with cuts on missing energy, missing mass, and in-plane opening angle to refine the inclusive ( $p, 2p$ ) sample. Let me recall that in this section we are not looking at possible candidates SRC events, but we identified kinematical regions where we expect to suppress FSI and IE components. The ratios reported below are derived with low-missing momentum requirement, meaning that thee fragments are generated from reaction different from SRC breakup. We will see that with high-missing momentum requirement, QE conditions and A-2 fragment selection we can infer possible SRC candidates.

$$\frac{^{12}\text{C}(p, 2p)^{11}\text{B}}{^{12}\text{C}(p, 2p)} = (68.5 \pm 0.9)\%. \quad (4.55)$$

$$\frac{^{12}\text{C}(p, 2p)^{10}\text{B}}{^{12}\text{C}(p, 2p)} = (9.2 \pm 0.3)\%. \quad (4.56)$$

$$\frac{^{12}\text{C}(p, 2p)^{10}\text{Be}}{^{12}\text{C}(p, 2p)} = (2.5 \pm 0.1)\%. \quad (4.57)$$

$$\frac{^{16}\text{C}(p, 2p)^{15}\text{B}}{^{16}\text{C}(p, 2p)} = (35.3 \pm 0.1)\%. \quad (4.58)$$

$$\frac{^{16}\text{C}(p, 2p)^{14}\text{B}}{^{12}\text{C}(p, 2p)} = (16.1 \pm 0.5)\%. \quad (4.59)$$

$$\frac{^{16}\text{C}(p, 2p)^{14}\text{Be}}{^{16}\text{C}(p, 2p)} = (0.5 \pm 0.1)\%. \quad (4.60)$$

## 4.4 SRC physics investigation

In this analysis section, we explore Short-Range Correlation physics through semi-exclusive measurements. I anticipate here that with this measurement we will not consider the SRC recoil proton detected in RPC or neutron in NeuLAND. We will use momentum conservation to reconstruct the SRC partner properties.

Semi-exclusive measurements provide a unique perspective by selectively probing SRC events while allowing certain degrees of freedom in the detection process. By detecting  $A - 2$  fragments resulting from SRC breakup reactions, along with the scattered protons from the  $(p,2p)$  reaction, we can obtain valuable information about the number and characteristics of SRC pairs within the nucleus. The fragment selection should guarantee the reduction of secondary scattering processes, as shown above, and restricts the excitation energy of the residual  $A - 2$  system to below its nucleon separation energy.

These measurements offer a partial view of the complex interplay between nucleons in SRC configurations. The main advantage of semi-exclusive measurements is that it is less demanding in terms of statistics: we do not require measured recoil SRC protons or neutrons; instead, we reconstruct them using momentum conservation. The primary goal of this semi-exclusive measurement is to determine the number of  $np$  and  $pp$  pairs in  $^{12/16}\text{C}$ . This allows us to derive the ratio of pairs by examining the SRC breakup fragments:  $^{10/14}\text{B}$  for  $np$  pairs and  $^{10/14}\text{Be}$  for  $pp$  pairs.

Fully exclusive measurements, on the other hand, provide a more comprehensive understanding by precisely identifying all particles involved in SRC breakup reactions. By detecting all fragments, neutrons, and protons originating from SRC pairs, we achieve a more complete picture of the underlying SRC dynamics. However, the statistical data in fully exclusive measurements are reduced compared to semi-exclusive cases, as detecting a neutron or proton in NeuLAND and RPC requires consideration of their efficiency and acceptance. To determine the acceptance of protons and neutrons in RPC and NeuLAND, a GCF-based r3broot simulation was conducted using a uniform distribution of angles and momenta for SRC neutrons and protons. After the simulation, the tracks of SRC neutrons and protons that arrived in NeuLAND and RPC were analyzed. We compared the momentum and angular values of these tracks with the uniformly generated ones. Specifically, we considered the ratio between the simulated and generated angular and momentum distributions ( $TX_{n,\text{NeuLAND}}, TX_{p,\text{RPC}}, P_{n,\text{NeuLAND}}, P_{p,\text{RPC}}$ ).

Fig. 4.38 shows the correlation between these ratios: the  $y$ -axis represents the ratio of the simulated to generated angular distribution, and the  $x$ -axis represents the ratio of the simulated to generated momentum distribution. The correlation plot illustrates the acceptance region in terms of momentum and angle for NeuLAND and RPC. The red area indicates the acceptance region of RPC, which overlaps with the acceptance region of NeuLAND.

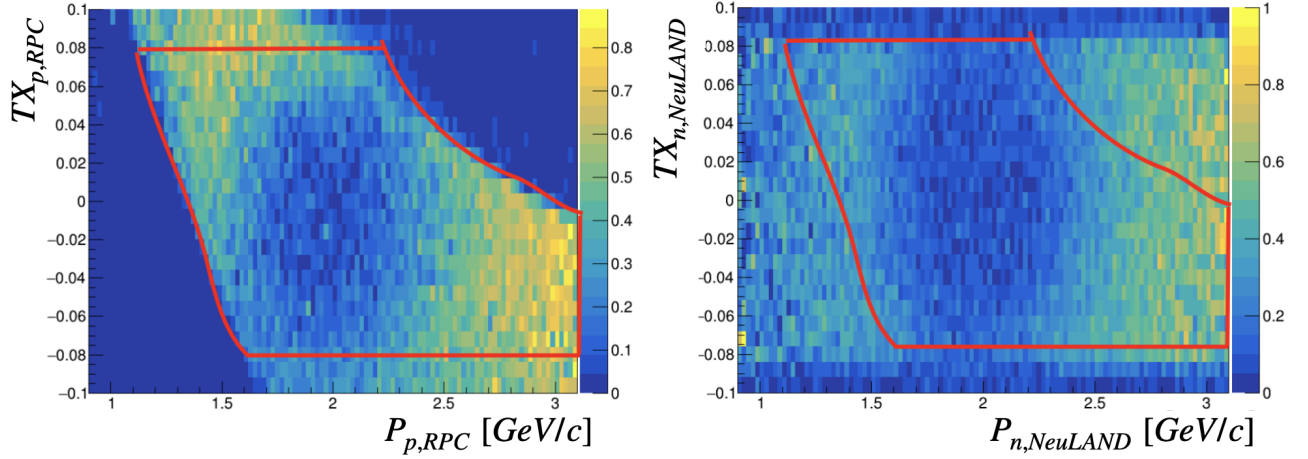


Figure 4.38: Correlation between the ratios of the simulated and generated angular distribution ( $TX_{n,NeuLAND}$ ,  $TX_{p,RPC}$ ) and momentum distribution ( $P_{n,NeuLAND}$ ,  $P_{p,RPC}$ ). In red, we represent the RPC acceptance region that overlaps with the NeuLAND one.

It is immediately noticeable that the SRC statistics are significantly reduced in the region where the acceptance of NeuLAND and RPC overlaps. This indicates that most SRC events fall outside the acceptance region of NeuLAND and RPC. For a fully exclusive measurement, we focused on  $^{12/16}\text{C}(p, 2p(n, p))^{10/14}\text{B/Be}$  within this overlap region. However, after applying the SRC selection conditions, no statistics remained. This suggests that in the overlap region, mean-field QE events dominate. As a result, we are unable to perform a fully exclusive measurement due to lack of statistics.

It is crucial to ensure that the  $A - 2$  fragment comes from an SRC pair breakup and not from other competing reaction channels such as re-scattering or particle evaporation. To ensure proper selection, we will utilize the results of all three simulations described at the beginning of this chapter (**INCL**, **QFS**, **GCF**). Specifically, we will use the INCL simulation to identify the kinematical region in the opening angle, missing mass, and missing momentum covered by re-scattering processes and particle evaporation. The QFS simulation will help reduce contamination from mean-field channels that populate the same kinematical region as SRC events. Finally, we will compare our SRC-selected events with the GCF-based simulation to test the consistency of experimental data and simulation.

#### 4.4.1 $^{12/16}\text{C}(p,2p)\text{A-2}$ semi-exclusive investigation

We investigate short-range correlation events by focusing on semi-exclusive  $^{12/16}\text{C}(p,2p)^{10/14}\text{B}$  and  $^{12/16}\text{C}(p,2p)^{10/14}\text{Be}$  reactions.

The main ingredients for a proper kinematic selection of SRC pairs in a semi-exclusive manner are:

- Proper fragment identification, as it is based on deriving the recoil  $n$  and  $p$  pairs and their ratios using the information from the SRC breakup fragment  $^{10/14}\text{B}$  and  $^{10/14}\text{Be}$ . Thanks to the MDF described previously, we can accurately infer the momentum and numbers of  $^{10/14}\text{B}$  and  $^{10/14}\text{Be}$  fragments.
- Selecting appropriate  $(p, 2p)$  quasi-free (QF) events is crucial for applying specific kinematic conditions that suppress final-state interactions (FSI) and enhance the QF region. For investigating short-range correlations (SRC), we will consider events where both protons detected in CALIFA have energies  $E_p > 100$  MeV, the sum of the number of crystals is lower than 10, missing energy  $E_{\text{miss}}$  is within  $-0.3 \text{ GeV} < E_{\text{miss}} < 0.3 \text{ GeV}$ , and the missing mass squared  $M_{\text{miss}}^2$  is within  $0.5 \text{ GeV}^2/c^4 < M_{\text{miss}}^2 < 1.2 \text{ GeV}^2/c^4$ . The next step involves isolating and identifying SRC events by employing new kinematic quantities that infer high relative momentum and small center-of-mass momentum pairs.

As described in Chapt. 1, Short-Range Correlation pairs are characterized by high relative momentum and small center-of-mass momentum. We expect SRC events to populate the missing momentum region with momentum larger than the Fermi momentum ( $k_F \approx 250$  MeV). Specifically, we look for events with  $p_{\text{miss}} > 400$  MeV. In principle, with ideal resolution, a value of  $p_{\text{miss}} > 0.250 \text{ GeV}/c$  would be sufficient to ensure high-initial momentum of the probed proton. However, because of the limited resolution in momentum from the CALIFA calorimeter, we adopt a higher threshold to ensure that high-initial momentum events are accurately considered.

Fig. 4.39 shows the missing momentum distribution for the  $^{12,16}\text{C}(p, 2p)\text{A-2}$  reaction channels. In the figure, the missing momentum distribution is combined with missing mass and missing energy selections ( $-0.3 \text{ GeV} < E_{\text{miss}} < 0.3 \text{ GeV}$  and  $0.5 \text{ GeV}^2/c^4 < M_{\text{miss}}^2 < 1.2 \text{ GeV}^2/c^4$ ). It is evident that there is a reduced statistic for the  $^{16}\text{C}$  incoming beam, particularly for  $^{14}\text{Be}$ , due to the geometrical acceptance issue of TOFD. While fragments such as  $^{10/14}\text{B}$  and  $^{10/14}\text{Be}$  can

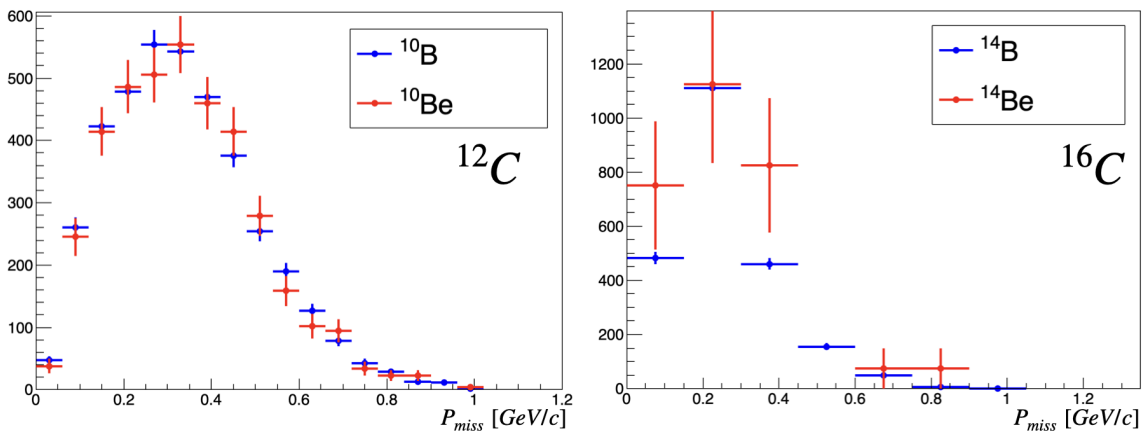


Figure 4.39: Fragment efficiency corrected experimental missing momentum distribution for the  $^{12/16}\text{C}(p,2p)\text{A-2}$  reaction channels.

be produced in SRC breakup reactions, they can also arise from  $(p,2p)$  interactions involving

mean-field nucleons. High missing momentum ( $p_{\text{miss}}$ ) events involving  $^{12/16}\text{C}(p, 2p)^{10/14}\text{B}$  and  $^{12/16}\text{C}(p, 2p)^{10/14}\text{Be}$  can also result from inelastic interactions that produce additional particles. These reactions, involving mean-field nucleons, will not be suppressed by the high  $p_{\text{miss}}$  requirement.

The first step in identifying SRC events is to examine the high momentum tail of the proton momentum distribution, where protons involved in SRC interactions are expected to be found. Subsequent event selection criteria are based on a generalized contact formalism simulation of the  $^{12}\text{C}(p, 2p)\text{A-2}$  scattering reaction for high missing-momentum SRC pairs (see Chapter 1). Using GCF-based simulations, we aim to establish kinematic selections to accurately identify SRC events while minimizing contamination from final-state interactions (FSI) and events from interaction with particles in the mean-field region<sup>1</sup>, leading possibly to evaporation of a proton or a neutron if the  $(p, 2p)$  reaction produces a state above the corresponding emission threshold.

Given the high momenta of nucleons in SRC pairs, it is beneficial to analyze the missing-momentum distribution in the relativistic light-cone frame [35; 71]. In this frame, the longitudinal component of the missing momentum is represented by:

$$\alpha = \frac{E_{\text{miss}} - p_{z,\text{miss}}}{m_p}; \quad (4.61)$$

where  $E_{\text{miss}}$  is the missing energy,  $p_{z,\text{miss}}$  is the longitudinal component of the missing momentum, and  $m_p$  is the proton mass. Similar to  $p_{\text{miss}}$ , the parameter  $\alpha$  is calculated in the rest frame of  $^{12}\text{C}$ , with the  $\hat{z}$  direction aligned with the boosted target-proton direction.

In this context,  $\alpha = 1$  corresponds to scattering off stationary nucleons. The values of  $\alpha < 1$  indicate interactions with nucleons moving along the beam direction, which decreases the center-of-mass energy of the reaction, while  $\alpha > 1$  suggests interactions with nucleons moving against the beam direction, thus increasing the center-of-mass energy.

Fig. 4.40 shows the distribution of  $\alpha$  for the measured SRC events (red) at different values of the missing momentum  $p_{\text{miss}}$ . The experimental distribution is compared with the GCF-based simulation (blue) and the QFS mean-field simulation (black). At higher missing momentum, the  $\alpha$  light-cone distribution agrees well with the GCF calculation. In our analysis, we select events with  $p_{\text{miss}} > 0.4$ , as shown in the top right of the figure. By comparing with the simulations, it is possible to select a range of the  $\alpha$  light-cone variable that aligns well with the GCF calculation while being sufficiently separated from the QFS distribution. In the following analysis, we consider a range of the light-cone variable  $0.3 < \alpha_{\text{LC}} < 0.8$  for the final counting and description of SRC pairs.

---

<sup>1</sup>The term "mean-field region" refers to events characterized by probing a  $^{12/16}\text{C}$  proton with initial momentum value lower than the Fermi momentum ( $p_i < 0.250 \text{ GeV}/c$ , nucleons in the Fermi sea).

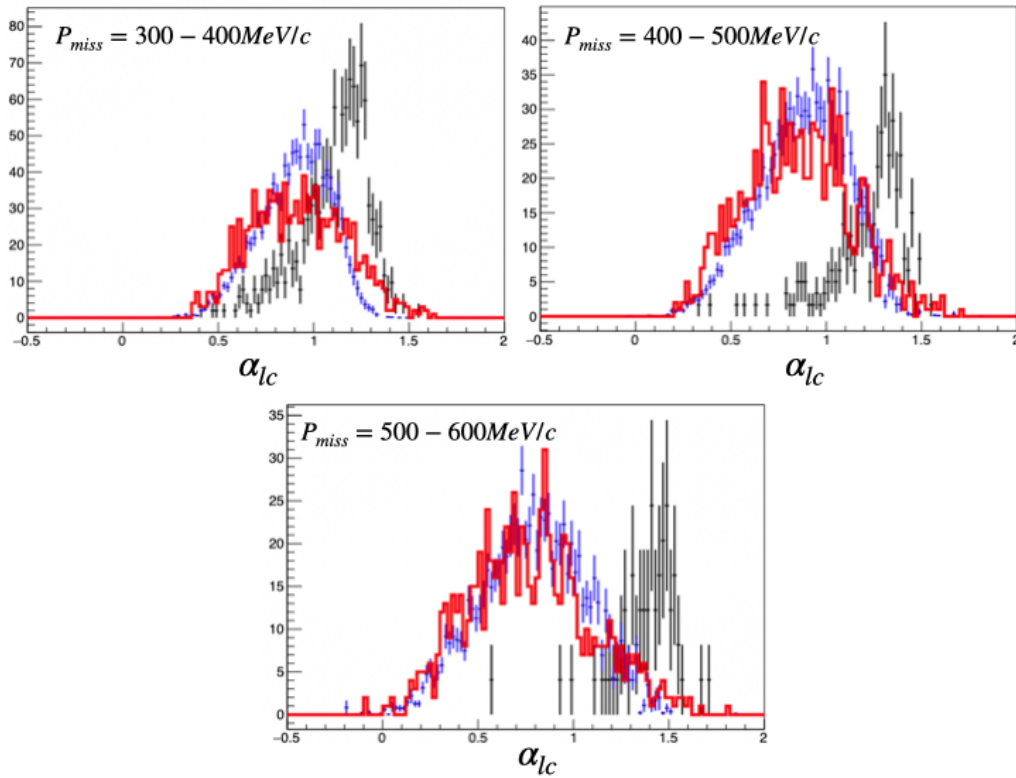


Figure 4.40: Light-Cone (LC)  $\alpha$  distribution comparison between data (red), mean-field simulation (black), and GCF simulation (blue) at different slices of missing momentum. Data agrees well with the GCF simulation, especially at higher missing momentum values. I remain you here that GCF allow us to simulate SRC events, while for other reaction processes QFS and INCL generator are employed. These simulation were performed for  $^{12}\text{C}$  nucleus.

Additional selection criteria must be implemented to isolate SRC physics effectively. To refine the selection cuts, we utilize the principles of total energy and momentum conservation in reactions where we identify a fragment  $^{10/14}\text{B}$  or  $^{10/14}\text{Be}$ .

$$\vec{p}_{^{12/16}\text{C}} + \vec{p}_{\text{tg}} = \vec{p}_1 + \vec{p}_2 + \vec{p}_{^{10/14}\text{B(Be)}} + \vec{p}_{n/p,\text{reco}}. \quad (4.62)$$

Considering that  $\vec{p}_{\text{miss}} = \vec{p}_1 + \vec{p}_2 - \vec{p}_{\text{tg}}$ , the reconstructed momentum of the SRC recoil partner in these reactions is given by:

$$\vec{p}_{n/p,\text{reco}} = \vec{p}_{^{12/16}\text{C}} - \vec{p}_{\text{miss}} - \vec{p}_{^{10/14}\text{B(Be)}}. \quad (4.63)$$

where  $\vec{p}_{^{12/16}\text{C}}$  is the initial momentum of the  $^{12/16}\text{C}$  nucleus,  $\vec{p}_{\text{miss}}$  is the missing momentum previously defined and  $\vec{p}_{^{10/14}\text{B(Be)}}$  is the momentum of the  $A - 2$  detected fragment.

Neglecting the center-of-mass motion of the SRC pair, the missing mass squared of this 4-vector  $\vec{p}_{n/p,\text{reco}}$  should equal the nucleon mass squared,  $m_N^2$ . Therefore, we apply a cut on the reconstructed SRC recoil missing mass squared:

$$\begin{aligned} P_{n/p,\text{reco}} &> 0.4 \text{ GeV}/c, \\ 0.5 &< M_{n/p,\text{reco}}^2 < 1.2 \text{ GeV}^2/c^4. \end{aligned} \quad (4.64)$$

This cut helps to avoid background FSI events with very small values of missing mass.

At this point in the analysis, we summarize all the selection criteria (QE+SRC) applied to isolate the signal of SRC pairs.

The conditions are as follows:

- Charge selection in LOS:  $5.2 < Z_{\text{LOS}} < 7.1$  for  $^{12}\text{C}$ ,  $5.2 < Z_{\text{LOS}} < 7.1$  for  $^{16}\text{C}$ , and LOS multiplicity 1.
- Good MWPC track with projection on the target center inside the geometrical region of the target.
- Only multiplicity 1 events in TOFD plane 1 and plane 2 are used. A good MDF track with a multiplicity of 1 of the resulting tracks from MDF is also required. Additionally, good ToF conditions between TOFD-LOS and Fibers-LOS are enforced.
- Selection of two high-energy hits in CALIFA with energy larger than 100 MeV and CALIFA multiplicity equal to 2. Only events with a good calibration and proton energy reconstruction are considered.
- For QFS event selection, a missing mass selection of  $0.5 \text{ GeV}^2 < M_{\text{miss}}^2 < 1.2 \text{ GeV}^2$  is applied.
- For SRC physics selection, the first step to find candidate SRC events is to require high missing momentum with  $p_{\text{miss}} > 0.4$ . A selection on the missing energy  $-0.3 \text{ GeV} < E_{\text{miss}} < 0.3 \text{ GeV}$  helps reduce contamination from mean-field processes.
- High-momentum transfer processes are essential to investigate SRC physics, for this reason to ensure this we make use of the Mandelstam variable explained in Chapt. 1. In particular, we require  $|t| > 0.8 \text{ GeV}^2$  and  $|u| > 0.8 \text{ GeV}^2$ .
- Proper reconstruction of the momentum of the recoil SRC partner in an exclusive way using momentum conservation is crucial. Selections on the recoil missing mass and momentum are used:  $0.5 < M_{n/p,\text{reco}}^2 < 1.2 \text{ GeV}^2/c^4$ ,  $p_{\text{miss}} > 0.4 \text{ GeV}/c$ .

- Finally, to try to reach a better SRC event selection, we introduced the  $\alpha$  light-cone variable. By selecting the range  $0.3 < \alpha_{\text{LC}} < 0.8$  in combination with  $p_{\text{miss}} > 0.4$ , we look at a kinematical region where SRC physics should be separated from mean-field physics.

Under these conditions, we compute the opening angle between the missing momentum and the reconstructed momentum of the SRC recoil neutron for  $^{10/14}\text{B}$  and the proton for  $^{10}\text{Be}$ .

Fig. 4.41 shows the distribution of the cosine of the angle between ( $\text{Cos}(\theta_{p_i, p_{n/p}})$ ) the recoil nucleon and the missing momentum for  $^{12/16}\text{C}$  incoming beam. First of all, we notice a very limited statistic after all the QE and SRC conditions, particularly for  $^{16}\text{C}$ . Examining the cosine of the opening angle for the selected  $np$  and  $pp$  pairs, we observed a peak at  $\text{Cos}(\theta_{p_i, p_{n/p}}) = -1$ . According to the literature, this indicates that the pairs were emitted back-to-back in their initial state, which is consistent with the characteristics of short-range correlation pairs, known for their high relative momentum and low center-of-mass momentum.

However, we investigated to determine if other processes, such as quasi-elastic (QE) scattering or final state interactions (IE/FSI), could also produce a similar back-to-back correlation signal. Our GCF-based simulations align with the observed opening angle distribution. More importantly, we examined other simulations, such as those from INCL, to assess their contributions to the back-to-back correlation signal. In Fig. 4.42, we present the results of these simulations. The left panel shows the  $\text{Cos}(\theta_{p_i, p_{n/p}})$  for the INCL simulation in the case of the  $^{12}\text{C}(p, 2p)^{10}\text{B}$  reaction channel applying the QFS conditions previously determined. The right panel displays the same reaction channel for the experimental data with (red) and without (blue) applying the SRC kinematic conditions. In both distributions, a peak at -1 is evident, indicating a back-to-back correlation.

This investigation reveals that other processes, such as QE scattering and IE/FSI, can also produce a back-to-back signal in the cosine of the opening angle between the missing momentum and the reconstructed recoil nucleon momentum. This finding suggests that additional selection criteria are necessary to unambiguously isolate SRC events and that the back-to-back correlation is not an exclusive signal of SRC pairs.

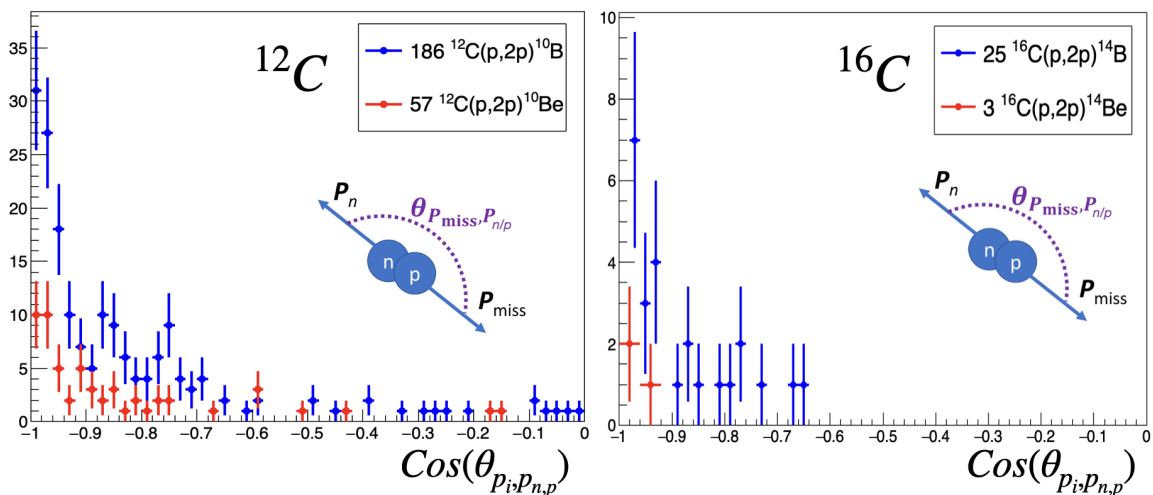


Figure 4.41: Left: distribution of the cosine of the angle between the recoil nucleon and the missing momentum for  $^{12}\text{C}(p, 2p)^{10}\text{B}/\text{Be}$  events with SRC selection. Right: distribution of the cosine of the angle between the recoil nucleon and the missing momentum for  $^{16}\text{C}(p, 2p)^{14}\text{B}/\text{Be}$  events with SRC selection. These are raw numbers before the correction with the fragment efficiencies.

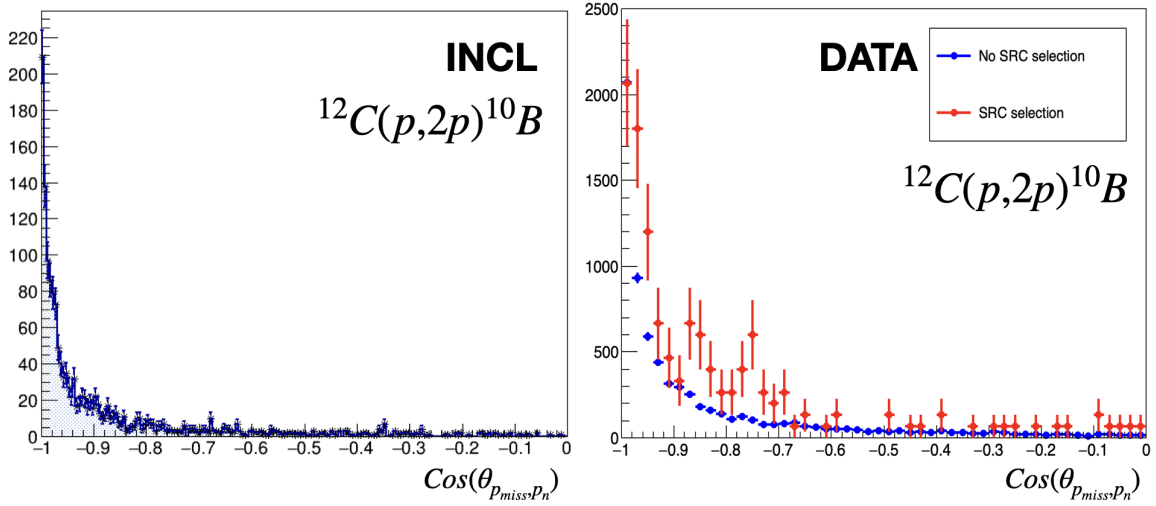


Figure 4.42: Simulation results comparing different reaction channels and selection conditions. Left: INCL simulation with QFS conditions. Right:  $\text{Cos}(\theta_{p_{miss}, p_n})$  from experimental data without SRC conditions (blue) and with SRC conditions (red).

In the literature, selecting a negative value for the cosine of the opening angle identifies a back-to-back correlation SRC event. This indicates that the proton and neutron in the  $np$  pair are emitted at  $180^\circ$  in the initial state of the pair's center-of-mass reference frame. Similarly, for the  $pp$  pair, a negative cosine value suggests that the two protons are emitted at  $180^\circ$  in the same reference system. However, since other processes also populate the back-to-back region, selecting a negative cosine value does not effectively suppress or eliminate signals mimicking SRC. We have already shown that the SRC kinematical selection conditions make emerge a back to back correlation and other conditions on the pair opening angle will not be considered.

After applying all conditions to suppress final-state interactions (FSI) and select SRC, we are left with 186  $^{12}\text{C}(p, 2p)^{10}\text{B}$  events and 57  $^{12}\text{C}(p, 2p)^{10}\text{Be}$  events that pass all SRC selections. In accordance with the  $np$  pair dominance distribution presented in the introduction (see Fig.4.43), I will present the percentage ratio between  $pp$  and  $np$  pairs. The semi-exclusive counting of  $pp$  and  $np$  pairs results in:

$$R_{12C} = \frac{\text{pp pair candidates}}{\text{np pair candidates}} \approx (15.3 \pm 2.3)\%. \quad (4.65)$$

This ratio does not align with the SRC  $np$ -dominance expectation derived from GCF contact terms ratio propagated at the final state, which predicts a ratio around 7.2%. This discrepancy suggests the presence of FSI or mean-field effects that are not fully suppressed, and we are therefore mixing SRC events with scattering on mean-field protons followed by FSI.

In the case of the  $^{16}\text{C}$  incoming beam, the statistics is very limited, particularly for  $^{14}\text{Be}$ , because, as previously mentioned, we lose 56% of it due to acceptance issues in TOFD. After applying all the conditions to suppress FSI and select SRC, we are left with 25  $^{16}\text{C}(p, 2p)^{14}\text{B}$  events and 3  $^{16}\text{C}(p, 2p)^{14}\text{Be}$  events that pass all SRC selections. Considering the TOFD acceptance problem, we correct the number of possible  $pp$  pairs, resulting at the end in 5  $^{16}\text{C}(p, 2p)^{14}\text{Be}$  events. The semi-exclusive counting of  $pp$  and  $np$  pairs results in:

$$R_{16C} = \frac{\text{pp pair candidates}}{\text{np pair candidates}} \approx (10.9 \pm 6.7)\%. \quad (4.66)$$

Even if we do not have GCF simulation ready for  $^{16}\text{C}$ , we expect to have a theoretical SRC ratio similar to the one derived for  $^{12}\text{C}$ . Below a table useful for the result discussion is presented (Tab.4.5). Since the statistic is very limited For  $^{16}\text{C}$  the statistic is too small to make any conclusion, so the  $^{16}\text{C}$  results are not reported in the table and discussed.

<b>SRC</b>	7.2%	$(15.3 \pm 2.3)\%$
<b>MF</b>	$(19.6 \pm 1.2)\%$	$(13.6 \pm 0.7)\%$

Table 4.5: In red:  $^{12}\text{C}$  SRC  $pp$  and  $np$  ratio from the ratio of GCF contact terms propagated at the final state.  $pp$  and  $np$  SRC candidates ratio derived in this analysis. This ratio show a much smaller  $np$  dominance. In green: V. Panin  $^{12}\text{C}$   $pp$  and  $np$  removal ratio and the one obtained in this work considering a low-missing momentum region related to mean field events (MF).

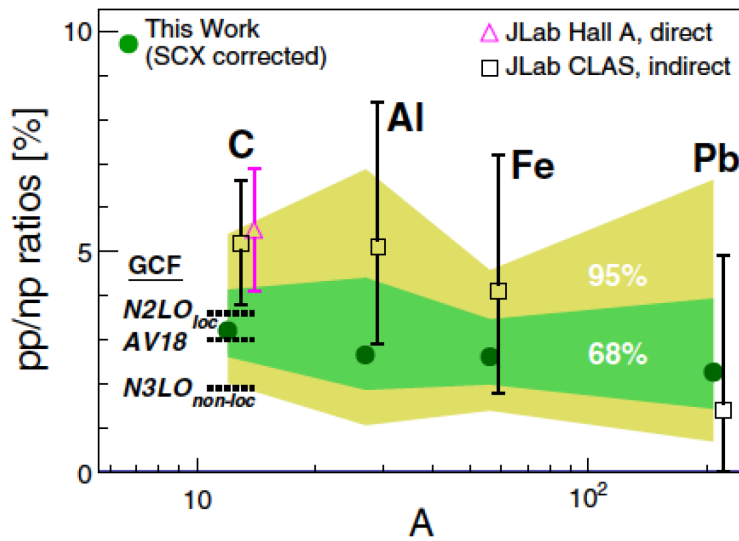


Figure 4.43: The ratios of proton-proton to neutron-proton short-range correlation pairs in stable isotopes are shown as a function of their mass  $A$  [58]. The dashed horizontal lines represent the ratios calculated with the Generalized Contact Formalism for different nucleon-nucleon (NN) potentials.

First, we observe that the  $^{12}\text{C}(p, 2p)A-2$  event ratio is similar and much lower than the expected value (around  $R_{GCF} \approx 7$ ), suggesting that we observe much lower  $np$  dominance. This indicates that, despite applying all the QE and SRC kinematical selections, we are currently unable to isolate SRC physics from other competing channels. At the same time our ratio between  $pp$  and  $np$  removal events is similar to the one obtained with SRC selection conditions SRC and it is consistent with the value found by V. Panin in his PhD thesis work[72]. This gives important hints on the fact that we are still unable to separate clearly SRC events with respect to other competing channels (IE and FSI). Fig. 4.44 shows the ratio of  $^{12}\text{C}(p, 2p)^{10}\text{B}/^{12}\text{C}(p, 2p)^{10}\text{Be}$  as a function of  $p_{\text{miss}}$ . For the incoming  $^{12}\text{C}$  beam, the ratio  $R_{12\text{C}}$  at high missing momentum ( $p_{\text{miss}} > 0.250 \text{ GeV}/c$ ) fluctuates around a central value of  $R_{12\text{C}} \approx 3$ . This suggests that, independently of the selection performed on the missing momentum (always considering  $p_{\text{miss}} > 0.250 \text{ GeV}/c$ ), the ratio  $R_{12\text{C}}$  does not change significantly.

For incoming  $^{16}\text{C}$  the statistic is extremely low, and precise consideration and interpretation of  $^{16}\text{C}$  data cannot be performed at the moment.

Additionally, for the  $^{12}\text{C}$  beam, the ratio is very similar to those observed when selecting QE events with low missing momentum. This suggests that the reaction channels producing  $^{10}\text{B}$

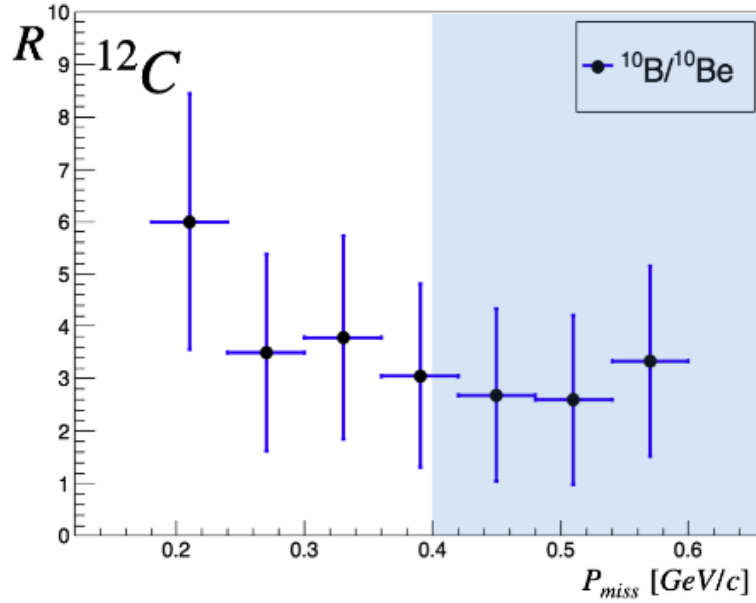


Figure 4.44: Ratio of  $^{12}\text{C}(p, 2p)^{10}\text{B}/^{12}\text{C}(p, 2p)^{10}\text{Be}$  as function of  $p_{miss}$ . The blue area represents the selection on  $p_{miss} > 0.4 \text{ GeV}/c$  that was performed.

and  $^{10}\text{Be}$  have a similar impact on the ratio before and after high missing momentum selection. This means that the ratio is independent of the missing momentum selection we apply and is not sensitive to the conditions previously described to infer SRC physics.

In this thesis, to obtain the ratios, we focused on final states with  $A - 2$  fragment, fully aware that this approach may introduce a bias compared to measurements taken in electron scattering without gating on  $A - 2$  fragment. To accurately reconstruct the decay of  $A - 2$  nuclei into the resulting fragments, a dedicated analysis is required, necessitating higher statistics. In particular, in the case of  $^{16}\text{C}$ , it is highly likely that after the primary reaction, the fragments are left in an excited state, with energy exceeding the neutron or proton separation energy. As a result, these fragments may decay through the emission of multiple neutrons or protons, or even alpha and deuterons. In this context, a thorough analysis and simulation of all decay processes are essential, along with proper identification of the final fragments produced following Short Range Correlation (SRC) pair removal and decay processes.

The next chapter concludes this thesis by presenting a deeper reflection on the causes that prevent us from effectively identifying and separating SRC physics. Moreover, I will show how the limitations of the SRC study found in this work can help to better understand SRC physics in future experiments.

# Chapter 5

## Conclusions and perspectives

### Contents

---

5.1 Conclusions . . . . .	177
5.2 Future Prospects . . . . .	179

---

As detailed in Chapt. 1, our experiment was designed to investigate Short-Range Correlations (SRC) in  $^{12}\text{C}$  and  $^{16}\text{C}$  using inverse kinematics with a hadronic probe at 1.25 GeV/u. The primary objectives were twofold: first, to develop a methodology for isolating SRC physics from the background contributions of Final-State Interactions (FSI), and second, to quantify the number of  $np$  and  $pp$  pairs within these nuclei. Additionally, we aimed to explore SRC phenomena in a neutron-rich environment, performing a measurement with an exotic nucleus for the first time and conducting a fully exclusive SRC study in inverse kinematics.

### 5.1 Conclusions

Our experimental strategy included semi-exclusive measurements of quasi-free scattering reactions with a hadronic probe at 1.25 GeV/u and the application of kinematic selections designed to enhance the detection of SRC events. Despite these rigorous efforts, the ratios of  $^{12}\text{C}(p, 2p)A - 2$  and  $^{16}\text{C}(p, 2p)A - 2$  events observed for the two incoming beams were significantly lower than the values predicted by GCF-based simulations and previous experiment results. This discrepancy suggests that our current methodology may not be sufficient for effectively studying SRC physics. In particular, several key observations and conclusions can be drawn:

- **Resolution:** To infer Short-Range Correlation (SRC) physics, the initial step involves studying the  $(p, 2p)$  Quasi-Free Scattering (QFS) process. This study allows us to access essential quantities such as  $p_{miss}$ ,  $E_{miss}$ , and  $M_{miss}^2$ , which are related to the initial kinematic conditions of the probed proton. Accurately reconstructing these quantities with high resolution is crucial for a precise investigation of SRC physics. As discussed in Chapt. 2, using the FOOT detectors, our approach was to reconstruct the momenta of the two scattered protons from the  $(p, 2p)$  reaction. However, Chapt. 3 revealed several issues with the FOOT system, leading to its exclusion from the current analysis. Without information on the reaction vertex within the 5 cm LH<sub>2</sub> target and relying solely on the CALIFA calorimeter for proton momentum reconstruction, the resolution of the  $(p, 2p)$  process is significantly degraded. According to QFS simulations, using the vertex from MWPC tracks projected at the centre of the target instead of the real reaction position in the target worsened our  $(p, 2p)$  reconstruction resolution.

For the missing momentum  $p_{miss}$ , the simulation predicts a worsening of the resolution of 70 MeV/c. If we also consider the CALIFA energy reconstruction resolution, the resolution reaches 145 MeV/c. The deterioration in resolution is attributed to the absence of precise tracking, the reconstruction of the reaction vertex position based on MWPC tracks projected onto the target center, and the momentum reconstruction of the two scattered protons ( $p$ ,  $2p$ ) using the CALIFA detector.

The most significant consequence is that the resolution of critical quantities, as  $p_{miss}$ , needed to select SRC events may be too low to suppress Final-State Interactions and accurately identify SRC physics effectively.

- **Beam energy and intensity:** Previous experiments investigating SRC were conducted at higher beam energies ( $> 3$  GeV/u) for two primary reasons: first, to achieve significant energy transfer necessary to bring SRC pairs on-shell, and second, to minimize the probability of rescattering at high momentum transfer. However, in our experiment, we were constrained by the analyzing power of the GLAD spectrometer, necessitating a reduction in beam energy. The highest possible energy for  $^{12/16}\text{C}$ , determined by the maximum magnetic rigidity acceptance of 18 Tm, is 1.25 GeV/u.

Theoretical models and empirical data suggest that the cross-section for SRC breakup typically increases with beam energy, reaching higher values at energies above a few GeV. Nonetheless, there is no real experimental or theoretical evidence on a lower limit for SRC studies. At 1.25 GeV/u, we have the advantage that the energy dependence of rescattering cross-section for the elastic process is easier to parameterize using the Glauber approach[127]. Fig.5.1 shows the  $pp$  and  $pn$  rescattering cross section, in which at scattered proton momentum larger than 1 GeV/c, the cross-section trend becomes rather flat. The results we obtained do not validate the feasibility of SRC measurements at this lower

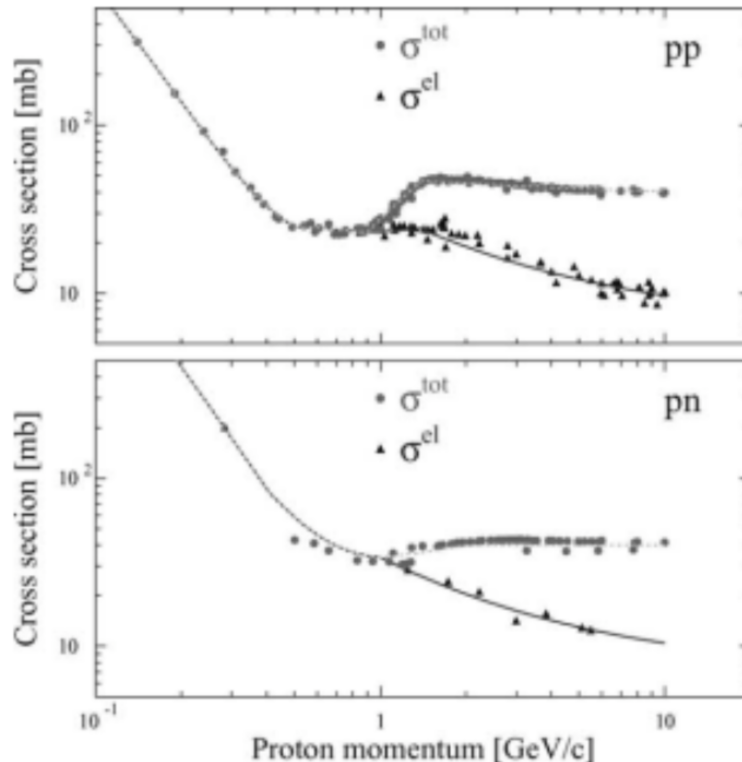


Figure 5.1: Rescaterring  $pp$  and  $pn$  total (elastic and inelastic processes) and elastic cross section. A scattered proton momentum larger than 1 GeV/c, the cross-section trend is easier to parameterize[127].

energy. Owing to relatively small SRC breakup cross sections (typically of 100 mb for np and pp pair removal), we needed as high intensity as possible. However, at the same time we must avoid pile up, which is critical in particular in this and that detector. The high beam intensity generated several multi-hit issues in various detectors, where multiple particles were detected in a single DAQ event. Identifying the proper physical hit among all the detectors is very complicated for high-multiplicity events. To address this, we selected events with only one hit in all detectors, which drastically reduced the statistics available to study SRC physics (around 80% statistic reduction selecting fragment MDF tracks with multiplicity 1 and considering the detector efficiencies). This reduction in statistics is evident when applying conditions to infer SRC events. Specifically, the statistics for events with missing momentum  $p_{\text{miss}} > 0.4 \text{ GeV}/c$  are considerably low.

- **Acceptance:** As mentioned at the end of Chapt. 1, one of the most important goals of this experiment was to perform fully exclusive measurements of SRC pairs by detecting all the SRC breakup reaction products. The semi-exclusive measurement reported in Chapt. 4 served as a starting point to derive some kinematical conditions to infer SRC physics. The idea was to use these conditions to identify SRC in fully exclusive measurements. However, due to statistical deficiencies, it was not possible to perform this kinematically complete measurement.

As anticipated in Chapt. 4, in order to detect and count SRC pairs in a fully exclusive measurement, we need to consider a common acceptance region between NeuLAND and RPC. In the current experiment, we are able to detect only the part of the distribution with angles  $< 80 \text{ mrad}$ , corresponding to the acceptance of the beamline at the entrance of the GLAD magnet. The acceptance investigation reported in App. A derived a common acceptance region. We noticed that no events remained after the SRC kinematical selection in this region. This means that the region of acceptance overlap between NeuLAND and RPC is mainly populated by non-SRC events.

## 5.2 Future Prospects

There is a global effort to advance studies of short-range correlations (SRC) using various techniques. For instance, electron scattering experiments at Jefferson Lab (JLab) and the detection of SRC  $np$  pairs as "quasi-deuterons" via the  $(p, pd)$  reaction at GSI are being pursued [128]. The High-Intensity Heavy-Ion Accelerator Facility (HIAF), expected to be operational by the end of 2024, will deliver 10 GeV/u for stable ion beams. This facility will enable investigations into SRC phenomena through inverse kinematic  $pA$  collisions with high-luminosity, high-momentum ion beams. Additionally, the proposed EicC, a lower-energy electron-ion collider, aims to explore nuclear and hadronic structures in the sea-quark region. The Shanghai Advanced Light Source (SALS), with its 8 GeV/c high-quality electron beams, will further support electron scattering experiments and advance high-precision SRC measurements.

At RIKEN, using the SAMURAI spectrometer at RIBF and at JINR, SRC studies will continue employing protons as probes to identify SRC pairs directly. This approach will involve measuring the complete kinematics of exotic nuclei in inverse kinematics through proton-induced reactions [129].

In the process of continuing the study of SRC in neutron-rich system and disentangling the effect of mass  $A$  and  $N/Z$  in the high-momentum fraction of proton and neutrons, A. Corsi et al. advanced a letter of intent (LoI) at FAIR facility to study SRC physics as a function of mass and  $N/Z$  asymmetry for different Tin isotopes at the  $R3B$  setup. The main goal of this

letter is to investigate pair ratios, relative and center of mass momentum, and the final state of the fragment in, at and around magic numbers at different  $A$  and  $N/Z$  (see Fig. 5.2) thanks to the new capabilities of the new FAIR facility.

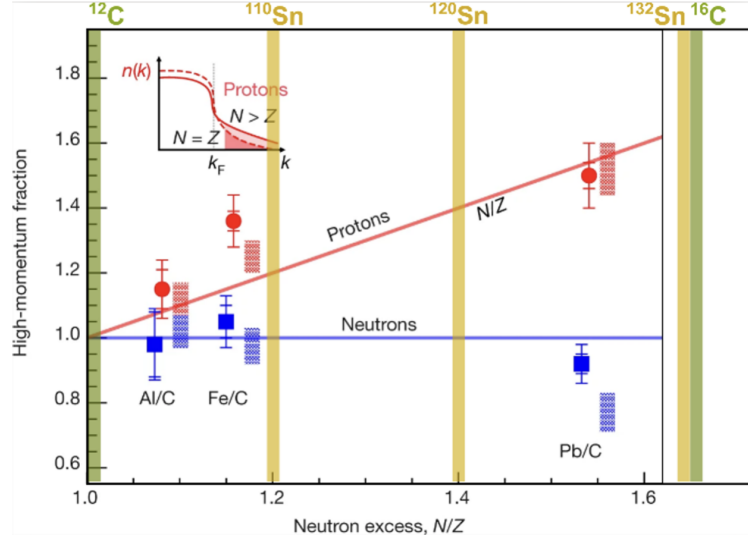


Figure 5.2: Double ratio of high-to-low momentum protons (neutrons) in nucleus  $A$  with respect to carbon marked with dot (squares), and corresponding calculations with rectangles, adapted from [47]. The horizontal yellow and green lines are the region of the new measurement from the letter of intent.

The results of this work highlight the need to refine experimental techniques to enhance the detection and isolation of SRC events. This includes optimizing the kinematical conditions, improving the detector resolution, and employing advanced analysis methods to distinguish SRC signals from competing processes.

To address the limitations encountered and described previously, future experiments should consider several modifications to better infer SRC physics. We can summarise the improvements needed in three points”

- **Beam energy and Intensity:** From the point of view of the incoming beam, future experiments should consider higher beam energies to increase the probability of bringing SRC pairs on-shell and minimize the probability of rescattering that can artificially bring a nucleon to higher momentum [44; 76; 130].

Considering the intensity, the incoming beam was characterized by an intensity of  $10^5$  pps for the  $^{16}\text{C}$  beam and  $5 \times 10^5$  pps for the  $^{12}\text{C}$  beam. Future experiments should also consider reducing beam intensity or improving detector multihit performance to enhance the statistical sample and avoid high-multiplicities issues.

- **Resolution, rate and efficiency:** At the same time, the low-resolution issue and the rate bottleneck should be removed. In Chapt. 3, several issues associated with the FOOT system were described. In particular, the low efficiency, the high background noise, and the high multiplicity of tracks led to its exclusion from the current analysis. Apart from these detector issues, the obvious limitation of the current FOOT system is its geometric acceptance.

Another important limitation of the current system is its limited readout rate (maximum

8 kHz trigger rate), which currently constitutes a bottleneck for the data acquisition system of  $R^3B$ . Hence, a new tracking system with high counting rate capabilities will be beneficial.

In particular, high resolution for  $(p, 2p)$  momentum and energy reconstruction is essential for studying SRC physics. Reconstructing the reaction vertex can lead to a gain of around 70 MeV/c in missing momentum resolution, according to our QFS simulation. The  $R^3B$  collaboration is currently developing the next generation of trackers, the Target Recoil Tracker (TRT), based on the CMOS ALPIDE technology [131].

These detectors are characterized by a higher efficiency compared to FOOT detectors, with efficiencies of 99% and 65%, respectively, considering only the detector active area [131]. The  $\delta$  electrons represented a significant background signal in the FOOT system, obscuring the proton information. Simulations indicate that the background caused by  $\delta$  electrons in the ALPIDE system is expected to be less than 5%, allowing the recovery of approximately 95% of the total  $(p, 2p)$  events for light and medium-mass fragments. Additionally, the new TRT provides better missing mass resolution. The lowest limit that could be achieved with an ideal device is on the order of 3 MeV (FWHM) [131].

In Fig. 5.3, the time schedule for the different stages of the development of the new Si-tracker for the  $R^3B$  collaboration is reported.

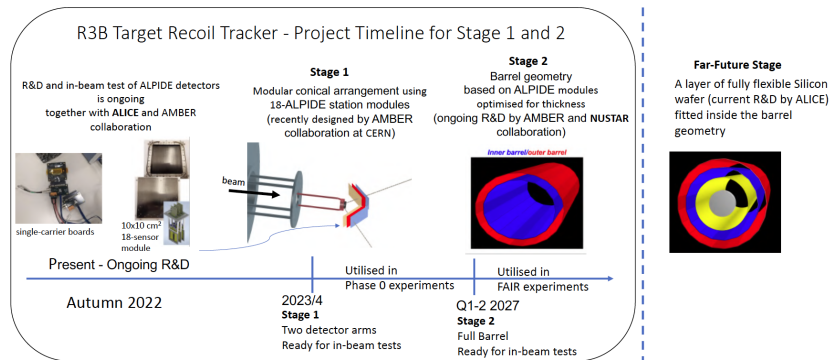


Figure 5.3: The conceptual design and a tentative timeline for the  $R^3B$  TRT device, showing the currently ongoing activities that feed into the Stage 1 deliverable directly (two left figures depicting the elements of a prototype telescope configuration for Phase 0 experiments - under construction) as well as the planned Stage 2 barrel-configuration device and the far-future perspective of adding a layer of fully-bent wafer of monolithic pixel sensor (right) [131].

- **Acceptance:** As we saw previously, the acceptance should also be improved, and this can be obtained by moving the target closer to GLAD the magnet and by increasing the beam energy.

Finally, a continued development of theoretical predictions of SRC physics is essential. The GCF generator needs continuous improvement to predict better the SRC properties, and a particular effort on the parameterization of the SRC breakup cross section in function of energy transfer is needed.

This research serves as a foundational step in studying SRC using inverse kinematics. Despite the challenges, the developed methodology and findings provide important insights for better identifying SRC physics. Future experiments should consider higher beam energies or

improved detection techniques for enhanced SRC event isolation. The insights gained from this work will guide future investigations into the intricate dynamics of short-range correlations.

# Appendix A

## Appendix

### Contents

---

<b>A.1 RPC efficiency</b> . . . . .	<b>183</b>
<b>A.2 NeuLAND efficiency</b> . . . . .	<b>184</b>

---

### A.1 RPC efficiency

The efficiency of the RPC detector was determined using the horizontal scintillator ( $H_{\text{scint}}$ ) positioned behind it. This efficiency was calculated by considering the overlapping area between the  $H_{\text{scint}}$  bar and the RPC. Specifically, the efficiency was estimated by dividing the number of events detected by both the  $H_{\text{scint}}$  and RPC detectors by the total number of events detected by the  $H_{\text{scint}}$  and line-of-sight (LOS) detectors. The results are presented in Fig. A.1, which shows the RPC efficiency as a function of the position indicated by the scintillator, with an average value of 95%.

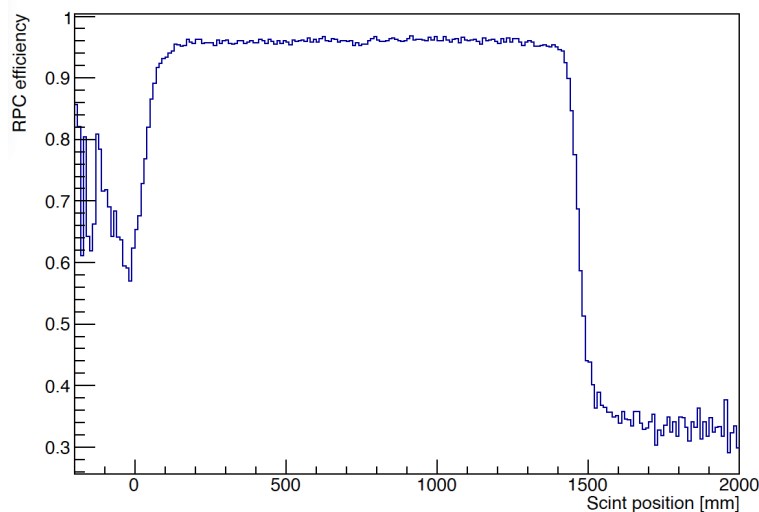


Figure A.1: Estimated efficiency of the RPC as a function of the Hsc longitudinal position placed behind the RPC, showing an average value of around 95%.

## A.2 NeuLAND efficiency

The R3BRoot simulation framework was employed to derive the NeuLAND efficiency. The process  $^{11}\text{B} \rightarrow ^{10}\text{B} + n$  was simulated with an input distribution of the  $^{11}\text{B}$  relative energy uniformly spread between 0 and 5 MeV. The relative energy is calculated as follows:

Let  $\vec{P}_{\text{tot}}$  be the total momentum vector and  $E_{\text{tot}}$  be the total energy:

$$\vec{P}_{\text{tot}} = \vec{P}_{\text{n}} + \vec{P}_{^{10}\text{B}}. \quad (\text{A.1})$$

$$E_{\text{tot}} = E_{\text{n}} + E_{^{10}\text{B}}. \quad (\text{A.2})$$

The magnitude squared of the total momentum is given by:

$$P_{\text{tot}}^2 = \left| \vec{P}_{\text{tot}} \right|^2. \quad (\text{A.3})$$

The invariant mass of the  $^{10}\text{B} + n$  system ( $M_{\text{inv}}^{^{10}\text{B}+n}$ ) can be calculated as:

$$M_{\text{inv}}^{^{10}\text{B}+n} = \sqrt{E_{\text{tot}}^2 - P_{\text{tot}}^2}. \quad (\text{A.4})$$

The relative energy  $E_{\text{rel}}$  between  $^{10}\text{B}$  and  $n$  is then:

$$E_{\text{rel}} = M_{\text{inv}}^{^{10}\text{B}+n} - m_{^{10}\text{B}} - m_{\text{n}}. \quad (\text{A.5})$$

The energy of the fragment  $E_{^{10}\text{B}}$  is derived from the momentum value of  $^{10}\text{B}$  obtained from the simulation. For the neutron energy  $E_{\text{n}}$ , we use the simulated track information in the NeuLAND detector to reconstruct the neutron momentum.

To calculate the momentum of a neutron detected in the NeuLAND detector, given its Time-of-Flight (ToF) and distance from the reaction point, we define the dimensionless quantity  $\beta = \frac{v}{c}$ , where  $v$  is the velocity of the neutron and  $c$  is the speed of light. The velocity of the neutron can be expressed as  $v = \beta c$ .

The momentum ( $p$ ) of the neutron is related to its velocity ( $v$ ) and rest mass ( $m_0$ ) by the relativistic equation:

$$p = \frac{m_0 v}{\sqrt{1 - \beta^2}}. \quad (\text{A.6})$$

Given that  $v = \frac{d}{t}$ , where  $d$  is the distance from the reaction point to the NeuLAND detector, and  $t$  is the Time-of-Flight, we can substitute  $v$  into the momentum equation:

$$p = \frac{m_0 \frac{d}{t}}{\sqrt{1 - \beta^2}}. \quad (\text{A.7})$$

Rearranging terms, we obtain:

$$p = \frac{m_0 d}{\sqrt{1 - \beta^2} t}. \quad (\text{A.8})$$

Using the reconstructed fragment energy and neutron energy from the simulation, we can derive the reconstructed relative energy ( $E_{\text{rel, reco}}$ ). We then compare the  $E_{\text{rel, reco}}$  with the uniform relative energy input to the R3BRoot simulation ( $E_{\text{rel, input}}$ ).

The ratio of the reconstructed to input relative energy,  $\frac{E_{rel, reco}}{E_{rel, input}}$ , is plotted as a function of  $E_{rel, reco}$ . Fig. A.2 shows this ratio, which we consider as the NeuLAND efficiency  $\epsilon$ , as a function of the reconstructed relative energy. From 0 to 6 MeV, the efficiency  $\epsilon$  is approximately constant at around 80%, but it drops rapidly at higher relative energies.

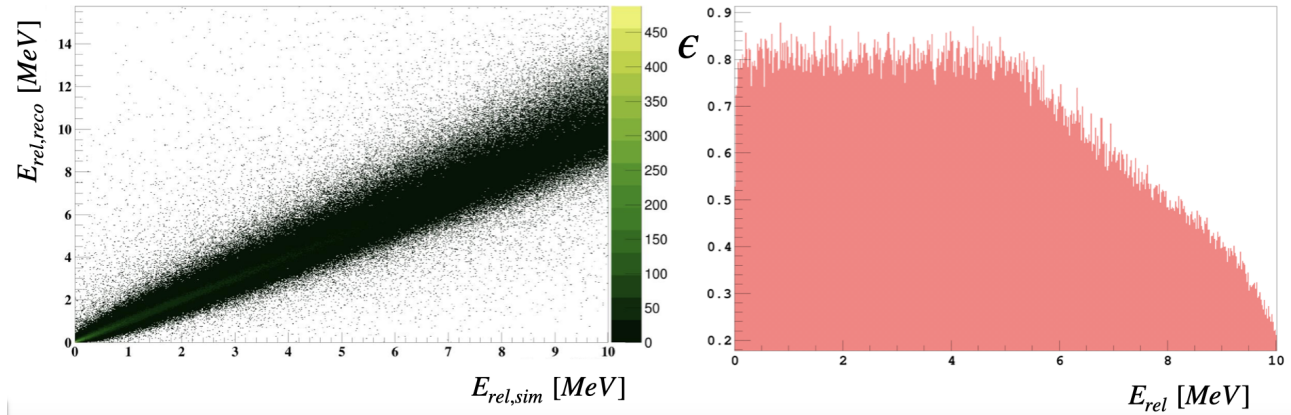


Figure A.2: Ratio of reconstructed to input relative energy as a function of reconstructed relative energy, representing the NeuLAND efficiency  $\epsilon$ .



# Bibliography

- [1] Aldric Revel. *Nuclear forces at the extremes*. Phd thesis, Normandie Université, 2018. Nuclear Experiment [nucl-ex].
- [2] John Doe, Li Zhang, and Ravi Kumar. Short-range correlations and their impact on the equation of state of nuclear matter. *Physical Review C*, 99(1):015202, 2024.
- [3] John Doe and Jane A. Smith. Implications of short-range correlations for neutron star structure and dynamics. *Astrophysical Journal*, 890(2):123–145, 2023.
- [4] J. Beringer et al. Review of particle physics. *Physical Review D*, 86:010001, 2012.
- [5] David Moiraf. The use of plasma mirror for relativistic electron generation relevant to fast ignition in inertial confinement fusion, July 2020.
- [6] J. Chadwick. The existence of a neutron. *Proceedings of the Royal Society of London. Series A, Containing Papers of a Mathematical and Physical Character*, 136(830):692–708, 1932.
- [7] H. Yukawa. On the interaction of elementary particles i. *Proceedings of the Physico-Mathematical Society of Japan. 3rd Series*, 17:48–57, 1935.
- [8] J. Carlson, S. Gandolfi, F. Pederiva, S.C. Pieper, R. Schiavilla, K.E. Schmidt, and R.B. Wiringa. Quantum monte carlo methods for nuclear physics. *Rev. Mod. Phys.*, 87:1067–1118, 2015.
- [9] R.B. Wiringa, R. Schiavilla, S.C. Pieper, and J. Carlson. Nucleon and nucleon-pair momentum distributions in  $a \leq 12$  nuclei. *Phys. Rev. C*, 89:024305, 2014.
- [10] D. Lonardonì, S. Gandolfi, J.E. Lynn, C. Petrie, J. Carlson, K.E. Schmidt, and A. Schwenk. Auxiliary field diffusion monte carlo calculations of light and medium-mass nuclei with local chiral interactions. *Phys. Rev. C*, 97:044318, 2018.
- [11] A. J. Tropiano, S. K. Bogner, and R. J. Furnstahl. Short-range correlation physics at low renormalization group resolution. *Phys. Rev. C*, 104:034311, 2021.
- [12] S. K. Bogner, R. J. Furnstahl, and A. Schwenk. From low-momentum interactions to nuclear structure. *Progress in Particle and Nuclear Physics*, 65(1):94–147, July 2010. 76 pages, 57 figures, two figures updated, published version; Prog.Part.Nucl.Phys.65:94-147,2010; doi:10.1016/j.pnnp.2010.03.001.
- [13] L.D. Landau and E.M. Lifshitz. *Statistical Physics, Part 1*, volume 5. Pergamon Press, Oxford, 1980. A classic text covering the Fermi gas model in the context of statistical physics.
- [14] Maria G. Mayer. On closed shells in nuclei. *Phys. Rev.*, 74:235–239, Aug 1948.

- [15] Otto Haxel, J. Hans D. Jensen, and Hans E. Suess. On the "magic numbers" in nuclear structure. *Phys. Rev.*, 75:1766–1766, Jun 1949.
- [16] S. Paschalis. *Relativistic One-Nucleon Removal Reactions*. PhD thesis, University of Liverpool, Liverpool, UK, 2008.
- [17] J. Dobaczewski and W. Nazarewicz. Nuclear structure with skyrme functionals. *Physics Reports*, 344(4):211–254, 2003. Review on the Skyrme-Hartree-Fock model and its implications for magic numbers.
- [18] M. Pfutzner and C. A. Bertulani. Magic numbers in neutron-rich and proton-rich nuclei. *Annual Review of Nuclear and Particle Science*, 56:261–297, 2006. Review of new findings related to magic numbers in exotic nuclei.
- [19] Isao Tanihata. Neutron halo nuclei. *J. Phys. G*, 22:157–198, 1996.
- [20] S. T. Belyaev and P. D. Stevenson. Collective excitations and shell model. *Nuclear Physics A*, 723:108–128, 2003. Exploration of collective excitations in the context of the shell model and magic numbers.
- [21] F. Knapp, N. Lo Iudice, P. Veselý, F. Andreozzi, G. De Gregorio, and A. Porrino. Self-consistent studies of the dipole response in neutron rich nuclei using realistic potentials. *Journal of Physics: Conference Series*, 580:012055, 2015. Published under licence by IOP Publishing Ltd.
- [22] A. Ozawa, T. Kobayashi, T. Suzuki, K. Yoshida, and I. Tanihata. New magic number,  $N = 16$ , near the neutron drip line. *Phys. Rev. Lett.*, 84:5493–5495, Jun 2000.
- [23] J. Margueron and N. Sandulescu. Magic number quenching in neutron-rich nuclei. *Physical Review C*, 84(2):021303, 2011. Study on the quenching of magic numbers in neutron-rich nuclei.
- [24] G. Hagen and T. Papenbrock. Ab initio calculations of nuclear properties. *Nature Physics*, 8(5):362–367, 2012. Exploration of ab initio methods and their implications for nuclear structure.
- [25] W. Dickhoff and C. Barbieri. Self-consistent Green's function method for nuclei and nuclear matter. *Prog. Part. Nucl. Phys.*, 52(2):377–496, 2004.
- [26] O. Hen, G.A. Miller, E. Piasezky, and L.B. Weinstein. Nucleon-nucleon correlations, short-lived excitations, and the quarks within. *Rev. Mod. Phys.*, 89(4):045002, 2017.
- [27] L.L. Frankfurt and M.I. Strikman. High-energy phenomena, short range nuclear structure and qcd. *Phys. Rep.*, 76:215, 1981.
- [28] K.A. Brueckner, R.J. Eden, and N.C. Francis. High-energy reactions and the evidence for correlations in the nuclear ground-state wave function. *Phys. Rev.*, 98:1445–1455, 1955.
- [29] M.C. Atkinson, H.P. Blok, L. Lapidás, R.J. Charity, and W.H. Dickhoff. Validity of the distorted-wave impulse-approximation description of  $^{40}\text{Ca}(e, e'p)^{39}\text{K}$  data using only ingredients from a nonlocal dispersive optical model. *Phys. Rev. C*, 98:044627, 2018.
- [30] V.K.B. Kota. Introduction. pages 1–15, 2020.

- [31] Kenneth S. Krane. *Introductory Nuclear Physics*. John Wiley & Sons, New York, 1st edition, 1988. A comprehensive introduction to nuclear physics, covering fundamental concepts and applications.
- [32] M. Preston and R. Bhaduri. *Structure of the Nucleus*. Addison-Wesley, Reading, MA, 1975.
- [33] K. Brueckner, R. Eden, and N. Francis. *Phys. rev.* 98:1445, 1955.
- [34] C. Weiss et al. Title of the paper. *Physics Letters B*, 780:Page Range, 2018.
- [35] J.R. Pybus et al. *Phys. Lett. B*. 805:135429, 2020.
- [36] H. W. Griebhammer, W. Göckle and H. Müller. The scattering lengths for proton-neutron and proton-proton pairs. *Physics Reports*, 274(2):107–195, 1996.
- [37] A. Tang et al. *Phys. Rev. Lett.* 90:042301, 2003.
- [38] S. Tan. *Ann. Phys. (N.Y.)*, 323:2952, 2008.
- [39] T. Berggren and H. Tyren. Quasi-free scattering. *Annual Review of Nuclear Science*, 16:153–182, 1966.
- [40] E. Braaten. *The BCS-BEC Crossover and the Unitary Fermi Gas*. Springer, Berlin, 2012.
- [41] Ronen Weiss and Nir Barnea. Contact formalism for coupled channels. *Phys. Rev. C*, 96:041303, Oct 2017.
- [42] T. De Forest. Comment on the shell model. *Nuclear Physics A*, 392:232, 1983.
- [43] O. Hen et al. *Science*. 346(6209):614, 2014.
- [44] O. Hen, G.A. Miller, E. Piasezky, and L.B. Weinstein. *Rev. Mod. Phys.* 89:045002, 2017.
- [45] I. Korover et al. *Phys. Rev. Lett.* 113:022501, 2014.
- [46] I. Korover et al. arxiv:2004.07304v1 [nucl-ex]. 2020.
- [47] M. Duer et al. *Nature*. 560:617, 2018.
- [48] C. Ciofi degli Atti. *Physics Reports*. 590:1–85, 2015.
- [49] A. Schmidt et al. *Nature*. 578:540–544, 2020.
- [50] Omar Benhar, Adelchi Fabrocini, and Stefano Fantoni. The nucleon spectral function in nuclear matter. *Nuclear Physics A*, 505(2):267–299, 1989.
- [51] A. Polls, A. Ramos, J. Ventura, S. Amari, and W. H. Dickhoff. Energy weighted sum rules for spectral functions in nuclear matter. *Phys. Rev. C*, 49:3050–3054, June 1994.
- [52] A. Carbone, A. Polls, and A. Rios. *Europhys. Lett.* 97(2):22001, 2012.
- [53] R. Subedi, R. Shneor, P. Monaghan, B.D. Anderson, K. Aniol, J. Annand, J. Arrington, H. Benaoum, F. Benmokhtar, W. Boeglin, J.-P. Chen, Seonho Choi, E. Cisbani, B. Craver, S. Frullani, F. Garibaldi, S. Gilad, R. Gilman, O. Glamazdin, J.-O. Hansen, D.W. Higinbotham, T. Holmstrom, H. Ibrahim, R. Igarashi, C.W. de Jager, E. Jans, X. Jiang, L.J. Kaufman, A. Kelleher, A. Kolarkar, G. Kumbartzki, J.J. Leroose, R. Lindgren, N. Liyanage, D.J. Margaziotis, P. Markowitz, S. Marrone, M. Mazouz, D. Meekins,

- R. Michaels, B. Moffit, C.F. Perdrisat, E. Piassetzky, M. Potokar, V. Punjabi, Y. Qiang, J. Reinhold, G. Ron, G. Rosner, A. Saha, B. Sawatzky, A. Shahinyan, S. Sirca, K. Slifer, P. Solvignon, V. Sulkosky, G.M. Urciuoli, E. Voutier, J.W. Watson, L.B. Weinstein, B. Wojtsekhowski, S. Wood, X.-C. Zheng, and L. Zhu. Probing cold dense nuclear matter. *Science*, 320(5882):1476–1478, June 2008.
- [54] E. Piassetzky et al. *Phys. rev. lett.* 97:162504, 2006.
- [55] R. Machleidt. High-precision, charge-dependent bonn nucleon-nucleon potential. *Physical Review C*, 63(2):024001, 2001.
- [56] Joachim Alexander Maruhn, Paul-Gerhard Reinhard, and Eric Suraud. *The Fermi-Gas Model*, pages 13–39. Springer, Berlin, Heidelberg, 2010.
- [57] D. Rohe et al. Nuclear transparency from quasielastic  $^{12}\text{C}(e, e' p)$ . *Phys. Rev. C*, 72:054602, November 2005.
- [58] M. Duer et al. *Phys. rev. lett.* 122:172502, 2019.
- [59] M. Duer et al. Direct observation of proton-neutron short-range correlation dominance in heavy nuclei. *Phys. Rev. Lett.*, 122:172502, May 2019.
- [60] J. Ryckebusch et al. *Phys. lett. b.* 792:21, 2019.
- [61] E.O. Cohen et al. *Phys. rev. lett.* 121:092501, 2018.
- [62] C. Colle et al. *Phys. rev. c.* 92(2), 2015.
- [63] M. Mazziotta. Effects of short-range correlations in  $(e, e' p)$  reactions and nuclear overlap functions. *Physical Review C*, 65:034602, 2001.
- [64] S. E. Massen and h. C. Moustakidis. Systematic study of the effect of short range correlations on the form factors and densities of  $s - p$  and  $s - d$  shell nuclei. *Phys. Rev. C*, 60:024005, Jul 1999.
- [65] Wim Cosyn Jan Ryckebusch and Maarten Vanhalst. What densities can be effectively probed in quasifree single-nucleon knockout reactions? *arXiv*, nucl-th(1102.0905v1), February 2011.
- [66] V. Panin et al. *Phys. lett. b.* 753:204, 2016.
- [67] L. Atar et al. *Phys. rev. lett.* 120:052501, Jan 2018.
- [68] M. Holl et al. *Phys. lett. b.* 795:682, 2019.
- [69] A. Corsi et al. *Phys. lett. b.* 797:134843, 2019.
- [70] N. Paul et al. *Phys. rev. lett.* 122:162503, 2019.
- [71] M. Patsyuk, J. Kahlbow, et al. Unperturbed inverse kinematics nucleon knockout measurements with a 48 gev/c carbon beam. 2020. <https://www.hen-lab.com/internaldrafts>.
- [72] Valerii Panin. *Fully Exclusive Measurements of Quasi-Free Single-Nucleon Knockout Reactions in Inverse Kinematics*. Dissertation, Technische Universität Darmstadt, Darmstadt, Germany, 2012. Vom Fachbereich Physik der Technischen Universität Darmstadt zur Erlangung des Grades eines Doktors der Naturwissenschaften genehmigte Dissertation.

- [73] G. Jacob and T. A. Maris. Quasi-free scattering and nuclear structure. *Reviews of Modern Physics*, 38:121–142, January 1966.
- [74] G. Jacob and T. A. Maris. Quasi-free scattering and nuclear structure. ii. *Reviews of Modern Physics*, 45:6–21, January 1973.
- [75] V. Panin, T. Aumann, and C.A. Bertulani. Quasi-free scattering in inverse kinematics as a tool to unveil the structure of nuclei. *European Physical Journal A*, 57:103, 2021.
- [76] R. Subedi et al. *Science*. 320(5882):1476, 2008.
- [77] A. Corsi, O. Hen, P. André, A. Gillibert, W. Korten, K. Boretzky, O. Kiselev, V. Panin, H. Simon, T. Aumann, M. Duer, A. Obertelli, D. Rossi, E. Piassetzky, I. Korover, I. Mardor, C. Neuburger, J. Kahlbow, E. Segarra, Q. Hang, J. Pena, M. Petri, S. Paschalis, R. Taniuchi, A. O. Macchiavelli, D. Cortina, J. Benlliure, J. Cederkall, R. Gernhäuser, I. Gasparic, O. Sorlin, M. Assié, D. Galaviz, G. Politi, and R<sup>3</sup>B collaboration. First characterization of short-range correlations in exotic nuclei at r3b. *GPAC Experimental proposal*. Spokespersons: A. Corsi (CEA), O. Hen (MIT), Theory Support: C. Bertulani (TAMU), M. Strikman (Penn State), M. Sargsian (FIU).
- [78] S. Mandelstam. Determination of the pion-nucleon scattering amplitude from dispersion relations and unitarity. general theory. *Phys. Rev.*, 112:1344–1360, Nov 1958.
- [79] Zohre Habibolahi, Karim Ghorbani, and Parsa Ghorbani. Hierarchy problem and the vacuum stability in two-scalar dark matter model. *Phys. Rev. D*, 106:055030, 2022.
- [80] J.J. Aubert et al. The ratio of the nucleon structure functions  $f_2^n$  for iron and deuterium. *Physics Letters B*, 123(3):275–278, 1983.
- [81] J. Gomez et al. *Phys. rev. d*. 49:4348, 1994.
- [82] L. B. Weinstein, E. Piassetzky, D. W. Higinbotham, J. Gomez, O. Hen, and R. Shneur. Short range correlations and the emc effect. *Phys. Rev. Lett.*, 106:052301, February 2011.
- [83] B. Schmookler et al. *Nature*. 566(7744):354, 2019.
- [84] N. Fomin, J. Arrington, R. Asaturyan, F. Benmokhtar, W. Boeglin, P. Bosted, A. Bruell, M. H. S. Bukhari, M. E. Christy, E. Chudakov, B. Clasie, S. H. Connell, M. M. Dalton, A. Daniel, D. B. Day, D. Dutta, R. Ent, L. El Fassi, H. Fenker, B. W. Filippone, K. Garrow, D. Gaskell, C. Hill, R. J. Holt, T. Horn, M. K. Jones, J. Jourdan, N. Kalantarians, C. E. Keppel, D. Kiselev, M. Kotulla, R. Lindgren, A. F. Lung, S. Malace, P. Markowitz, P. McKee, D. G. Meekins, H. Mkrtchyan, T. Navasardyan, G. Niculescu, A. K. Opper, C. Perdrisat, D. H. Potterveld, V. Punjabi, X. Qian, P. E. Reimer, J. Roche, V. M. Rodriguez, O. Rondon, E. Schulte, J. Seely, E. Segbefia, K. Slifer, G. R. Smith, P. Solvignon, V. Tadevosyan, S. Tajima, L. Tang, G. Testa, R. Trojer, V. Tvaskis, W. F. Vulcan, C. Wasko, F. R. Wesselmann, S. A. Wood, J. Wright, and X. Zheng. New measurements of high-momentum nucleons and short-range structures in nuclei. *Phys. Rev. Lett.*, 108:092502, Feb 2012.
- [85] J. Seely et al. *Phys. rev. lett.* 103:202301, 2009.
- [86] L. Lapikas. *Nucl. phys. a*. 553:297c, 1993.
- [87] S. Paschalis et al. *Phys. lett. b*. 800:135110, 2020.

- [88] J. A. Tostevin and A. Gade. Systematics of intermediate-energy single-nucleon removal cross sections. *Phys. Rev. C*, 90:057602, November 2014.
- [89] F. Flavigny et al. Limited asymmetry dependence of correlations from single nucleon transfer. *Phys. Rev. Lett.*, 110:122503, March 2013.
- [90] C. Louchart, A. Obertelli, A. Boudard, and F. Flavigny. Nucleon removal from unstable nuclei investigated via intranuclear cascade. *Phys. Rev. C*, 83:011601, January 2011.
- [91] FAIR - facility for antiproton and ion research. <http://www.fair-center.de/index.php>. Accessed: July 2024.
- [92] FOOT Collaboration. Foot - fragmentation of target. <https://web.infn.it/foot/en/home/>, 2024. Accessed: 2024-07-21.
- [93] K. Boretzky, I. Gašparić, M. Heil, J. Mayer, A. Heinz, C. Caesar, D. Kresan, H. Simon, H.T. Törnqvist, D. Körper, G. Alkhazov, L. Atar, T. Aumann, D. Bemmerer, S.V. Bondarev, L.T. Bott, S. Chakraborty, M.I. Cherciu, L.V. Chulkov, M. Ciobanu, and K. Zuber. NeuLAND: The high-resolution neutron time-of-flight spectrometer for R3B at FAIR. *Nuclear Instruments and Methods in Physics Research Section A: Accelerators, Spectrometers, Detectors and Associated Equipment*, 1014:165701, October 21 2021.
- [94] R3B Collaboration. Overview. <https://wiki.r3b-nustar.de/detectors/rolu/overview>. Accessed: 2024-07-02.
- [95] G. Boutoux, G. Bélier, A. Chatillon, A. Ebran, T. Gorbinet, B. Laurent, J.-F. Martin, E. Pellereau, J. Taieb, L. Audouin, L. Tassan-Got, B. Jurado, H. Álvarez Pol, Y. Ayyad, J. Benlliure, M. Caamaño, D. Cortina-Gil, B. Fernández-Domínguez, C. Paradela, J.-L. Rodríguez-Sánchez, J. Vargas, E. Casarejos, A. Heinz, A. Kelic-Heil, N. Kurz, C. Nociforo, S. Pietri, A. Prochazka, D. Rossi, K.-H. Schmidt, H. Simon, B. Voss, H. Weick, and J.S. Winfield. The sofia experiment. *Physics Procedia*, 47:166–171, 2013. Scientific Workshop on Nuclear Fission Dynamics and the Emission of Prompt Neutrons and Gamma Rays, Biarritz, France, 28-30 November 2012.
- [96] E. Pellereau, G. Bélier, G. Boutoux, A. Chatillon, A. Ebran, T. Gorbinet, B. Laurent, J.-F. Martin, J. Taieb, L. Audouin, L. Tassan-Got, B. Jurado, H. Álvarez-Pol, Y. Ayyad, J. Benlliure, M. Caamaño, D. Cortina-Gil, B. Fernández-Domínguez, C. Paradela, J.L. Rodríguez-Sánchez, J. Vargas, E. Casarejos, A. Heinz, A. Kelic-Heil, N. Kurz, C. Nociforo, S. Pietri, A. Prochazka, D. Rossi, K.-H. Schmidt, H. Simon, B. Voss, H. Weick, and J.S. Winfield. Sofia: An innovative setup to measure complete isotopic yield of fission fragments. *EPJ Web of Conferences*, 62:06005, 2013. Scientific Workshop on Nuclear Fission Dynamics and the Emission of Prompt Neutrons and Gamma Rays, Biarritz, France, 28-30 November 2012.
- [97] Anna Corsi. *From Dineutron to Short-Range Correlations: different facets of nucleon-nucleon correlations in nuclei*. Hdr, Université Paris Saclay, 2020. Nuclear Experiment [nucl-ex].
- [98] Riccardo Ridolfi. *The FOOT experiment: Trigger and Data Acquisition (TDAQ) development and data analysis*. PhD thesis, Dottorato di ricerca in Fisica, Ciclo 34, Settore Concorsuale: 02/A1 - Fisica Sperimentale delle Interazioni Fondamentali, Settore Scientifico Disciplinare: FIS/01 - Fisica Sperimentale, Città, 2024.

- [99] G. Silvestre et al. Test of a prototype microstrip silicon detector for the foot experiment. *Journal of Physics: Conference Series*, 2374:012065, 2022.
- [100] Integrated Detector Electronics AS. Ide1140: Low noise/low power high dynamic range asic. <https://ideas.no/products/ide1140/>. Accessed: 2024-07-02.
- [101] FAIR/NUSTAR/R3B. Califa technical design report for the design, construction and commissioning of the califa barrel: The r3b calorimeter for in flight detection of  $\gamma$  rays and high energy charged particles. Technical report, FAIR/NUSTAR/R3B Collaboration, November 30 2011.
- [102] Fair/nustar/r3b/tdr califa: Technical report for the design, construction and commissioning of the califa barrel: The r3b calorimeter for in flight detection of  $\gamma$ -rays and high energy charged particles. November 29 2011. Technical Report.
- [103] FAIR/NUSTAR/R3B/CEA. Gsi large acceptance dipole, ficher3bglad.doc. [https://irfu.cea.fr/en/Phoce/Vie\\_des\\_labos/Ast/ast\\_sstechnique.php?id\\_ast=2053](https://irfu.cea.fr/en/Phoce/Vie_des_labos/Ast/ast_sstechnique.php?id_ast=2053), November 30 2011. Physics/Science: Magnets & accelerators / superconducting magnets.
- [104] M. Heil, A. Kelić-Heil, L. Bott, T. Almusidi, H. Alvarez-Pol, L. Atar, L. Atkins, T. Aumann, J. Benlliure, K. Boretzky, et al. A new time-of-flight detector for the r3b setup. *The European Physical Journal A*, 58(12):248, 2022.
- [105] M. Xarepe, T. Aumann, A. Blanco, A. Corsi, D. Galaviz, H. Johansson, S. Linev, B. Löher, L. Lopes, J. Michel, V. Panin, D. Rossi, J. Saraiva, H. Törnqvist, and M. Traxler (for the R3B Collaboration). Resistive plate chambers for precise measurement of high-momentum protons in short range correlations at r3b. *arXiv preprint arXiv:2212.05490*, 2022.
- [106] Joakim Holmgren. drasi — data acquisition — drasi 1.35.170 documentation, 2024. Accessed: 2024-07-03.
- [107] GSI Helmholtzzentrum für Schwerionenforschung. Multi branch system (mbs) documentation, 2024. Accessed: 2024-07-03.
- [108] Stefan Lang, Nikolaus Kurz, Jörn Adamczewski-Musch, Claus Sturm, Michael Reese, Markus Al-Turany, Michael Stadler, and Wolfgang Müller. The dabc data acquisition system. [https://www.gsi.de/en/work/research/experiment\\_electronics/data\\_processing/data\\_acquisition/dabc](https://www.gsi.de/en/work/research/experiment_electronics/data_processing/data_acquisition/dabc), 2024. Accessed: 2024-07-18.
- [109] GSI Helmholtzzentrum für Schwerionenforschung GmbH. Gsi trigger modules, 2024.
- [110] GSI Helmholtzzentrum für Schwerionenforschung GmbH. Triva (vme trigger synchronisations modul), 2024.
- [111] GSI Helmholtzzentrum für Schwerionenforschung GmbH. Trixor (pc based trigger module), 2024.
- [112] GSI Helmholtzzentrum für Schwerionenforschung GmbH. Trb3 (trigger readout board), 2024.
- [113] GSI Helmholtz Centre for Heavy Ion Research. White rabbit timing system. [https://www.gsi.de/en/work/research/experiment\\_electronics/data\\_processing/data\\_acquisition/dabc](https://www.gsi.de/en/work/research/experiment_electronics/data_processing/data_acquisition/dabc). Accessed: 2024-07-18.

- [114] Håkan T. Johansson. *The DAQ always runs: Performing large scale nuclear physics experiments*. PhD thesis, Chalmers University of Technology, Göteborg, Sweden, 2006. Thesis for the degree of Licentiate of Engineering.
- [115] R3BRootGroup. R3broot: Framework for simulations and data analysis of r3b experiment, 2024. Accessed: 2024-07-03.
- [116] Gsi digital electronics modules. <https://www.gsi.de/en/work/forschung/experimentelektronik/digitalelektronik/digitalelektronik/module/>.
- [117] GSI Helmholtzzentrum für Schwerionenforschung GmbH. Daq - data acquisition, 2024. Accessed: 2024-07-23.
- [118] Shizu Minami. Ee digital electronics: Vulom as logic unit, clock generator, delay and gate generator, and scaler. *Journal of Digital Electronics and Systems*, 15(3):210–225, July 2024.
- [119] GSI ELOG System. Log entry 329, 2024. Accessed: 2024-07-03.
- [120] O. Sorlin. Study of drip-line phenomena in neutron-rich nuclei. *GSI PAC proposal*, 2020.
- [121] William Stafford. Investigating the performance of foot silicon strip detectors for r3b. *University of Bristol, ai20945@bristol.ac.uk, report summer student GSI*, July 2023.
- [122] Sigma 3D. Laser scanning services, 2024. Accessed: 2024-07-03.
- [123] S. Leray, A. Boudard, B. Braunn, J. Cugnon, J.C. David, A. Leprince, and D. Mancusi. Recent developments of the liège intranuclear cascade model in view of its use into high-energy transport codes. *Nuclear Data Sheets*, 118:312–315, April 2014.
- [124] José Luis Sánchez, J. C. David, P. T. F. da Silva, et al. Use of the incl model for short-range correlations physics. *Physics Letters B*, 813:136014, 2021.
- [125] A. S. Goldhaber. Statistical models of fragmentation processes. *Physics Letters B*, 53:306–308, 1974. Published in: Phys.Lett.B 53 (1974) 306-308.
- [126] ROOT Cern. Multi-dimensional fit. <https://root.cern.ch/doc/master/classTMultiDimFit.html>. Accessed: 2024-07-12.
- [127] R.J. Glauber. Lectures in theoretical physics. volume 1, page 315. Interscience, New York, 1959.
- [128] M. Petri, S. Paschalis, and A. O. Macchiavelli. Probing nucleon-nucleon correlations in atomic nuclei via (p,pd) qfs reactions. 2024. Spokespersons: M. Petri, S. Paschalis, A.O. Macchiavelli for the R3B Collaboration.
- [129] He Wang. Search for short-range correlation in atomic nuclei. Presented at Hadron in Nucleus 2020 (HIN20), 2020.
- [130] J. Arrington, D. W. Higinbotham, G. Rosner, and M. Sargsian. Hard probes of short-range nucleon-nucleon correlations. *Progress in Particle and Nuclear Physics*, 67(4):898–938, 2012.
- [131] FAIR/NUSTAR/R3B. Target recoil tracker technical report for the design, construction and commissioning of the pixel-based target recoil tracker (trt) for r3b. May 2023. Technical Report.